

Effect of additives on bio-inspired mineralization of CaCO_3 and application of its composites

A Dissertation

Submitted in partial fulfillment for the degree of

Doctor of Philosophy



Debojit Paul

(Roll No. 176122026)

Thesis Supervisor: Prof. Gopal Das

Department of Chemistry

Indian Institute of Technology Guwahati

Assam -781039, India

Effect of additives on bio-inspired mineralization of CaCO_3 and application of its composites

A Dissertation

*Submitted in partial fulfillment for the degree of
Doctor of Philosophy*



Debojit Paul

(Roll No. 176122026)

Thesis Supervisor: Prof. Gopal Das

Department of Chemistry

Indian Institute of Technology Guwahati

Assam-781039, India



DEDICATED TO MY

FAMILY & FRIENDS



INDIAN INSTITUTE OF TECHNOLOGY GUWAHATI

Department of Chemistry

STATEMENT

I do hereby declare that the matter embodied in this thesis is the result of investigations carried out by me in the Department of Chemistry, Indian Institute of Technology Guwahati, Assam – 781039, India, under the supervision of Dr. Gopal Das, Professor, Department of Chemistry, Indian Institute of Technology Guwahati, Assam – 781039, India. In keeping with the general practice of reporting scientific observations, due acknowledgements have been made wherever this work is based on the findings of other investigators.

Date: 2022

(Debojit Paul)

Place: IIT Guwahati



INDIAN INSTITUTE OF TECHNOLOGY GUWAHATI

Department of Chemistry

CERTIFICATE

This is to certify that **Mr. Debojit Paul** (Roll No. 176122026) has been working under my supervision since July, 2017 as a regular registered Ph. D. student. His thesis entitled “**Effect of additives on bio-inspired mineralization of CaCO₃ and application of its composites**” is an authentic record of the results obtained from the research work carried out under my supervision in the Department of Chemistry, Indian Institute of Technology Guwahati, Assam - 781039, India. I am forwarding his thesis to submit for the award of degree of Doctor of Philosophy, from this institute. I hereby certify that he has fulfilled all the requirements, according to the rules of this institute regarding the investigations embodied in his thesis and this work has not been submitted elsewhere for a degree.

Dr. Gopal Das

(Thesis Supervisor)

Professor, Department of Chemistry

IIT Guwahati, Assam - 781039, India

The thesis entitled “**Effect of additives on bio-inspired mineralization of CaCO₃ and application of its composites**” is categorized into eight chapters based on the results obtained by experimental works performed during the research period.

Chapter 1: Introduction

Biom mineralization is a fundamental life process that leads to the formation of mass and structure in almost all life forms. This biogenic process leads to the formation of hierarchically structured organic-inorganic hybrid composites, popularly termed biominerals, which are widely prevalent among almost all living organisms.[1–3] The organisms exploit the properties of these materials, such as mechanical, optical, magnetic, etc., for a variety of purposes.[4,5] The organisms undergo evolution in the biomineral structures based on their requirements and to adapt to specific environmental challenges. It is fascinating to observe the ability possessed by the organisms to optimize the shape, size, structure, orientation, texture, and overall morphology of the biominerals. The scientists have involved themselves in understanding this biological phenomenon and more so have engulfed themselves in understanding the mystery behind this art. Till today, decades since the onset of the preliminary studies, a fairly large number of questions related to biominerals still remain unexplored. The scientific efforts in the field of materials science, clubbed together with the understanding of chemistry, have enabled scientists to mimic the design and synthesize various biogenic materials, of which the biominerals commandingly stand out as one of them.[6–8]

The study of biom mineralization is a multidisciplinary prospect that engages researchers from biology, chemistry, materials science, geology, and beyond.[9] The key role played by chemistry in biom mineralization research can broadly be divided into three main areas; in studying the chemical composition, biochemistry, and crystallography of the materials, in designing *in vitro* model systems to understand the interactions between the organic and the inorganic phases to understand the actual mechanism in biological systems and in developing new synthetic techniques by mimicking the biological systems to generate organic-inorganic composites with enhanced mechanical properties.

Among others, the factor that stands out is the ability of CaCO₃ to exhibit polymorphism. For over a century, CaCO₃ has been known to exist in three main anhydrous crystalline forms; calcite, aragonite, and vaterite, two hydrated crystalline forms; calcium carbonate monohydrate (monohydrocalcite) (CaCO₃·1H₂O) and calcium carbonate hexahydrate (ikaite) (CaCO₃·6H₂O), and also in the amorphous state as amorphous calcium carbonate (ACC).[10]

The crystal morphology, polymorphism, and materials properties of the biominerals can be controlled by the introduction of templates and additives. The introduction of a template to influence the nucleation step during CaCO_3 crystallization is fundamentally referred to as heterogeneous nucleation and the effect induced by it is known as the templating effect. Since its discovery in 1965, the presence and also the distribution of intracrystalline molecules in various marine organisms,[11] the researchers working on biomimetic materials based on biominerals have moved a long way in their study of the incorporation of species within the composite. These incorporated species are known as additives and they play a crucial role in determining the properties of the composite.

CaCO_3 is a very important material for industries. The biomimetic method of its synthesis can give us any of the polymorphs, ACC, calcite, vaterite and aragonite, or a mixture and accordingly, various morphologies can be synthesized of nano to micro sized particles. These *in vitro* biomineralized CaCO_3 have a wide range of applications, including as drug delivery vehicles, bone grafting, protein immobilization, catalysis, biosensors, CO_2 capture and release and water treatment.

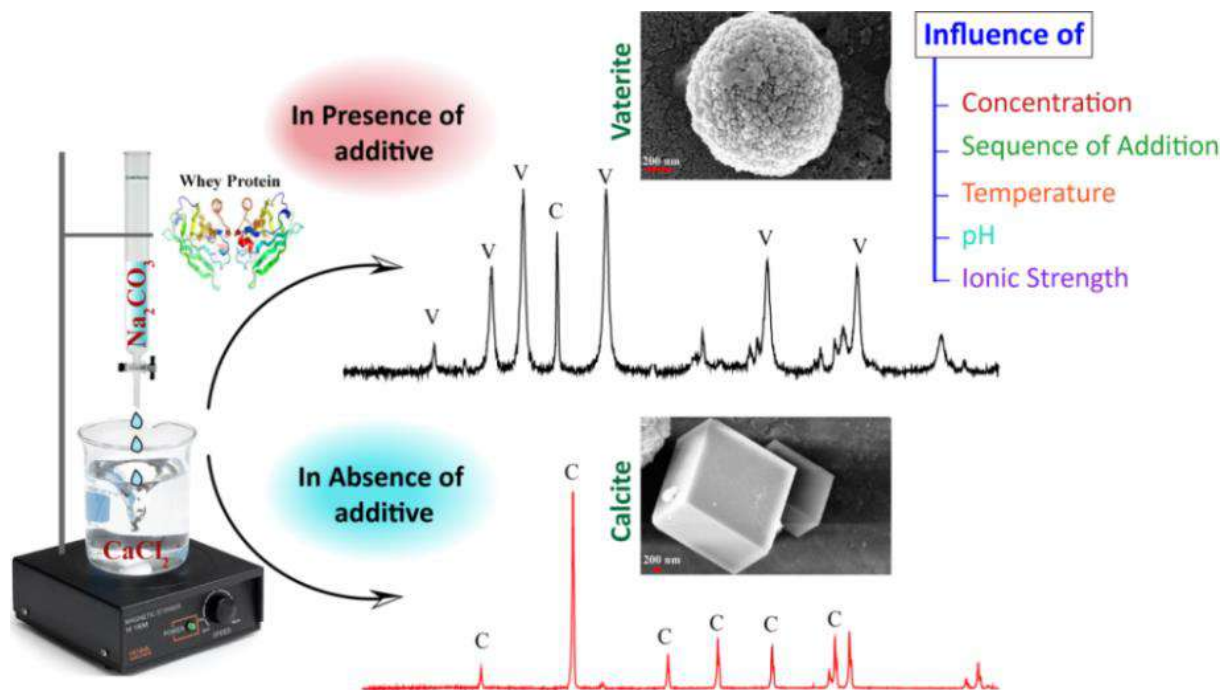
Chapter 2: Experimental Methods and Characterization

This chapter provides comprehensive information about the materials and different methodologies adopted for the synthesis and characterization of the biominerals and their composites, followed by their subsequent applications. Specification of analytical instruments used along with different experimental conditions adopted in the study of the materials and their applications have been elaborately discussed.

Chapter 3: Whey protein directed *in vitro* biomineralization of vaterite: A study on the influence of external parameters on CaCO_3 phase transformation (*Colloid Interfac. Sci. Comm.*, 2020, **36, 100255)**

This chapter demonstrates the role of a complex biopolymer, the organic biomolecule whey protein as an additive *in vitro* biomineralization of CaCO_3 . Whey protein is composed of five major components, α -lactalbumin, β -lactoglobulin, glycomacropeptide, serum albumin, and immunoglobulins. As a complex biopolymer, whey protein exhibits a random conformation in solution and in its role in the process of *in vitro* biomineralization of CaCO_3 ; its adsorption on the initial nanocrystals of CaCO_3 via weak interactions influenced the kinetic crystallization pathway, hence selectively forming the metastable vaterite phase rather than the most stable calcite phase. The study was extended to understand the influence of the change in parameters

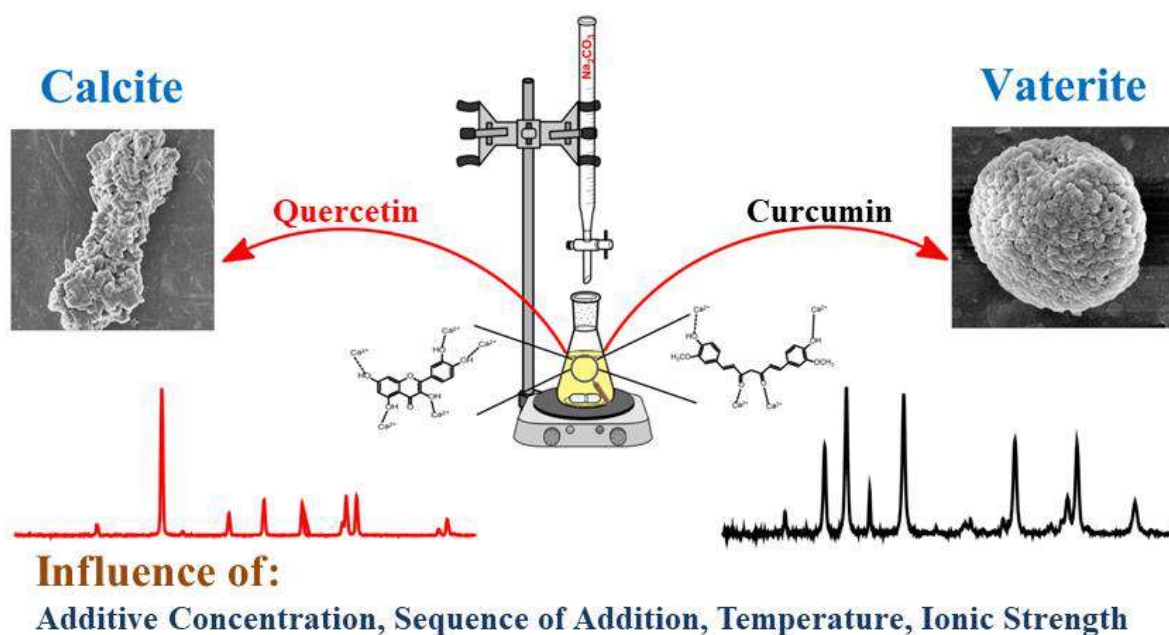
such as the concentration of the additive, sequence of addition, temperature, pH and ionic strength of the solution on phase transformation and to justify the role of whey protein in assisting the formation of the metastable vaterite particles.



Scheme 1: A pictorial illustration of the research work covered in **Chapter 3**.

Chapter 4: Role of curcumin and quercetin as additives in the *in vitro* biomineralization of CaCO_3 : A comparative study on phase modulation (*Ceram. Int.*, 2021, **47**, 12334-12341)

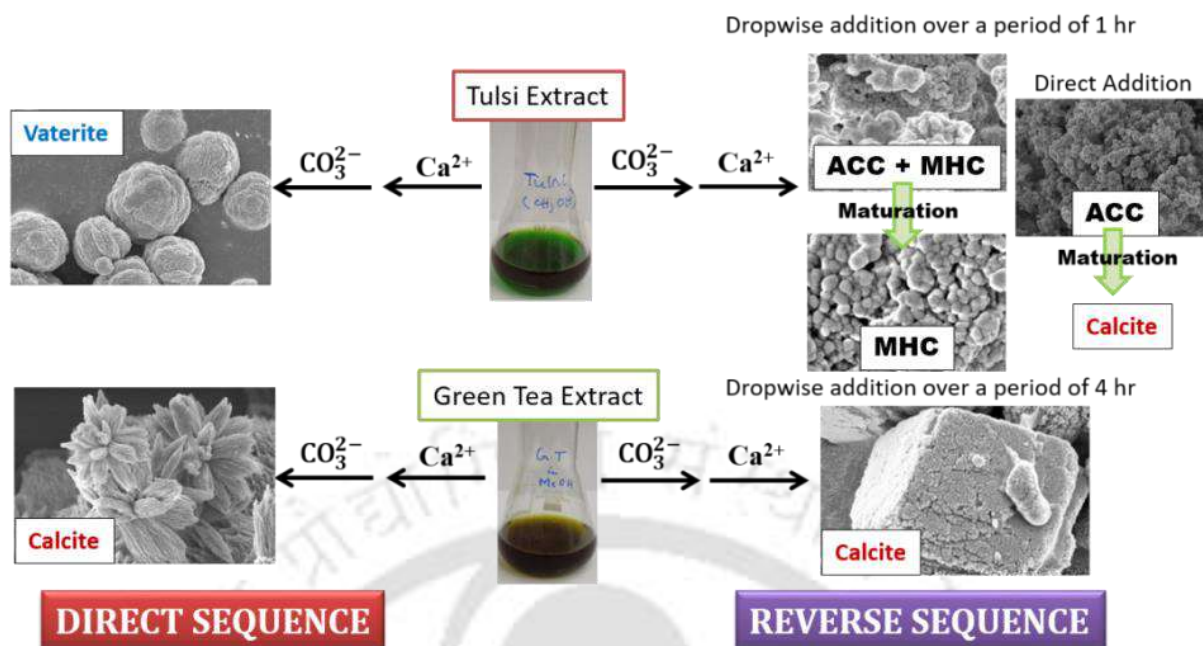
The use of low molecular weight organic molecules as additives in the *in vitro* biomineralization of CaCO_3 was discussed in this chapter. A comparative mode of study was performed between two polyphenolic additives, curcumin and quercetin; both of them being bio-friendly with numerous health benefits. The additive curcumin was able to stabilize the metastable vaterite phase and with quercetin, an interesting observation was made in terms of the morphology of the calcite particles formed. A dumbbell-shaped morphology, different from the usual rhombohedral morphology of the calcite crystals, was obtained. Additionally, the maturation of the CaCO_3 crystals in solution with time was studied to observe any changes in phase and morphology. Also, extended studies were performed to investigate the influence of the change in parameters such as; template concentration, the sequence of addition, temperature and ionic strength on the phase, morphology and size of the particles in the presence of both the additives.



Scheme 2: A pictorial illustration of the research work covered in **Chapter 4**.

Chapter 5: Tuning of CaCO₃ phase and morphology directed by plant-based *in vitro* model systems: A thorough insight into the formation of monohydrocalcite (*New J. Chem.*, 2021, 45, 18337–18348)

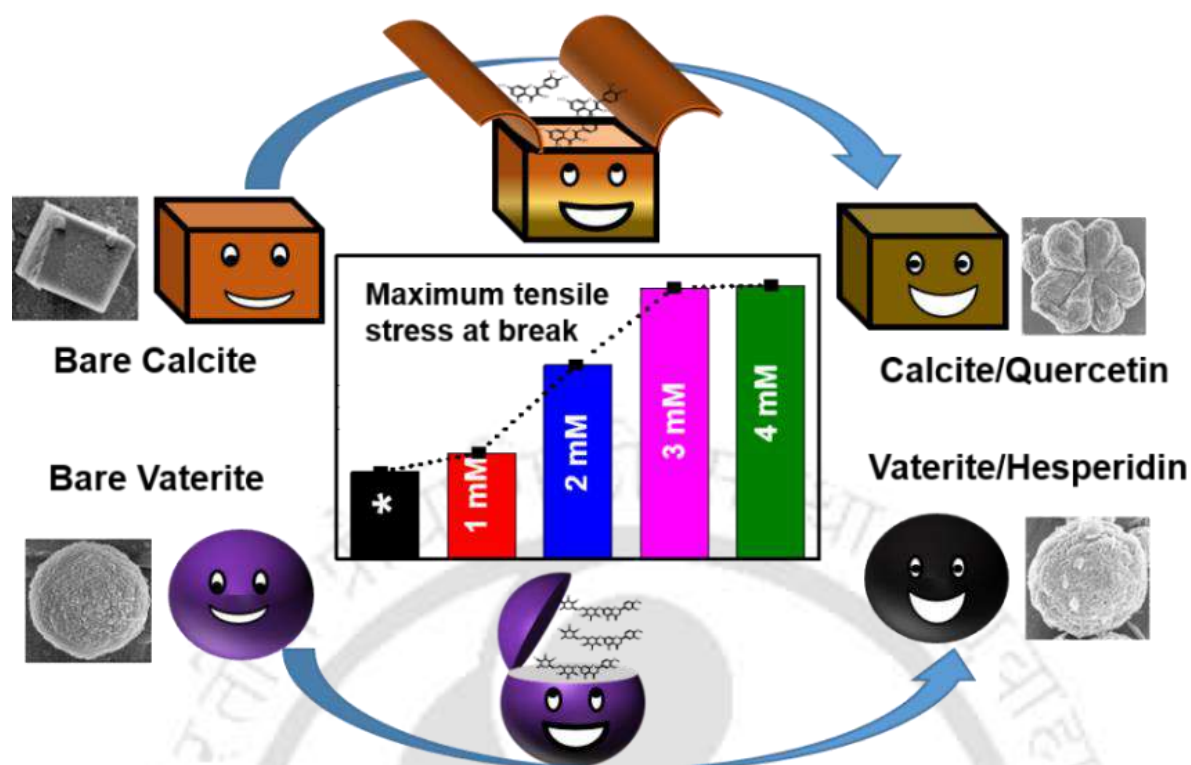
In this chapter, an *in vitro* study on the modulation of phases and polymorphism of CaCO₃ utilizing some naturally available and biological friendly additives was performed. The study was based on Tulsi and Green tea extracts in methanol and water. In the first part of the study, metastable vaterite particles and calcite particles with highly captivating and elegant floral morphology viz. rose-like and daffodil-like, were successfully synthesized. The second part involved reversing the sequence of addition of the Ca²⁺ and CO₃²⁻ ions where we could isolate the highly unstable amorphous calcium carbonate and one of the rare hydrated phases of CaCO₃, the monohydrocalcite phase. The formation of monohydrocalcite was obtained by controlling the addition of the Ca²⁺ ions, and the subsequent transformation of the monohydrocalcite particles to the thermodynamically stable calcite phase at high temperatures was studied. In short, the *in vitro* transformation of CaCO₃ from the unstable amorphous precursor to the stable calcite phase via the hydrated monohydrocalcite phase was reported with experimental evidences including crystallographic studies and well defined morphologies.



Scheme 3: A pictorial illustration of the research work covered in **Chapter 5**.

Chapter 6: Incorporation of flavonoids into CaCO_3 and their influence on the phase, morphology and mechanical strength of the composites: A bio-inspired approach (*Colloids Surf. A: Physicochem. Eng. Asp.*, 2022, **642**, 128720)

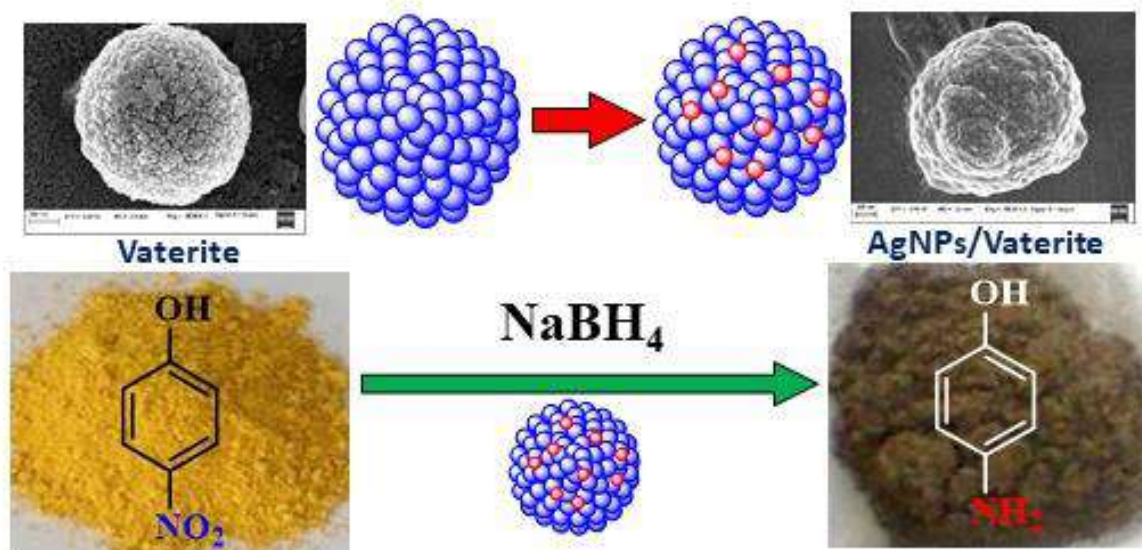
Biomaterials are composite materials that exhibit remarkable mechanical strength and properties and the organic molecules associated with the inorganic crystalline phase stand out as one of the most important reasons for this phenomenon. The work discussed in this chapter involves *in vitro* synthesized biomaterials based on the flavonoids quercetin and hesperidin. In the first part of this study, the influence of these organic molecules on the resulting CaCO_3 composites in terms of phase and morphology is illustrated. Subsequently, in the second part, it is demonstrated how by tuning the concentration of the incorporated organic phase, constituted by the flavonoid molecules, the mechanical toughness of the composite could be varied. The interaction between the organic and inorganic phases and their influence on the mechanical properties of the composite for both calcite and metastable vaterite is described. The mechanical strength of the composites was evaluated post their doping into gelatin films. The maximum tensile stress attained by the CaCO_3 incorporated with quercetin and hesperidin was 2728 kPa and 3152 kPa, respectively, in contrast to the low value of 1140 kPa, which was observed for bare CaCO_3 .



Scheme 4: A pictorial illustration of the research work covered in **Chapter 6**.

Chapter 7a: *In vitro* biomineralized vaterite as a solid-support for silver nanoparticles: A highly efficient catalyst for the reduction of 4-Nitrophenol (*Mol. Catal.*, 2021, **504, 111433)**

In this work, the spherical morphology and porous surface texture of biomineralized vaterite were utilized by subjecting it as an inert solid support for silver nanoparticles. The resulting composite material was used as a catalyst for the reduction of 4-Nitrophenol. The methods assigned were eco-friendly and one of the stand out features was the very even and dense distribution of the silver nanoparticles with sufficient spacing between the neighbouring particles such that the question of agglomeration between particles could be neglected. The majority of the silver nanoparticles embedded were of ultrafine size, with an average diameter of 3.5 nm, which can be attributed to the porous surface texture of vaterite. The composite catalyst showed excellent catalytic activity towards the reduction and remained unaltered for at least five consecutive cycles. The high rate constant of $2.2 \times 10^{-2} \text{ s}^{-1}$ and an impressive turnover frequency of $2.36 \times 10^{-2} \text{ mmol mg}^{-1} \text{ s}^{-1}$ are the highlights of this nanoparticle-based catalyst. Additionally, the effectiveness of this catalyst towards the reduction of 4-Nitrophenol were also studied in water from natural sources; tap water and lake water. The results attained were highly impressive, suggesting that the material promises to be highly efficient as a potential catalyst for the industrial treatment of wastewater and can be deployed for large-scale purposes.

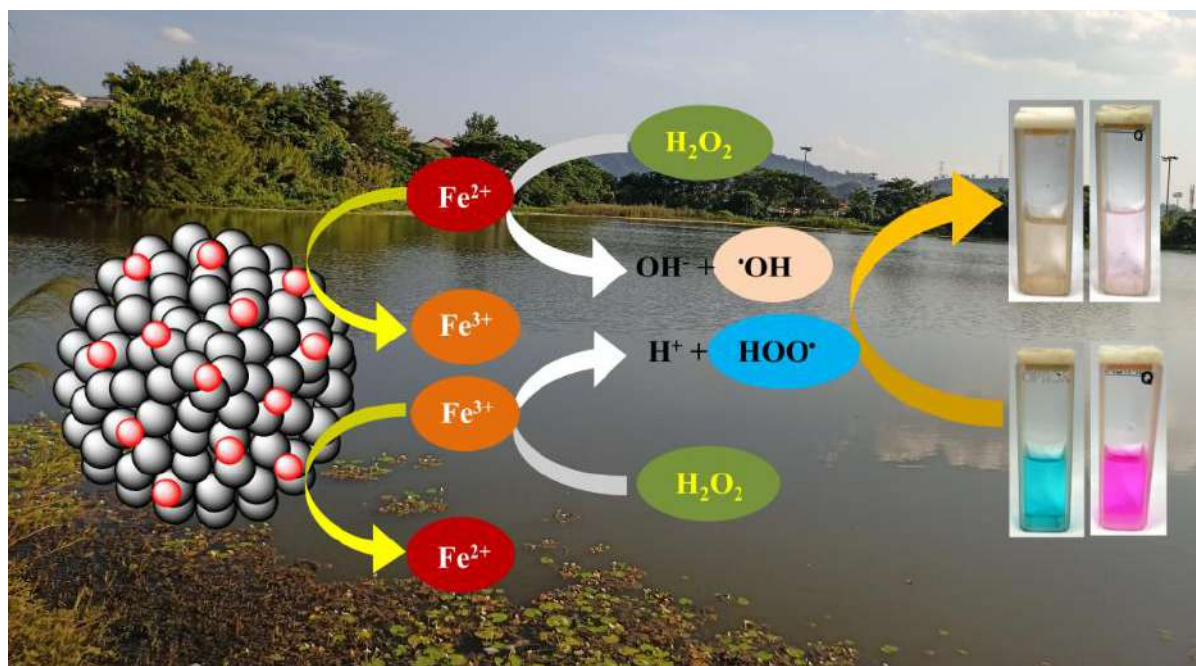


Scheme 5: A pictorial illustration of the research work covered in **Chapter 7a**.

Chapter 7b: Vaterite and calcite based magnetite composites: A comparative study on the catalytic performance during spontaneous Fenton-like dye degradation
(*J. Environ. Chem. Eng.*, 2022, **10**, 107558)

This chapter is based on an advanced oxidation process (AOP), the Fenton-like degradation of dyes. AOPs have been adopted to address the increasing threat of wastewater discharge from industries. In this work, an attempt was made to improve the performance of magnetite (Fe_3O_4) nanoparticles when subjected as catalysts in Fenton-like dye-degradation. *In vitro* biomineralized vaterite was used as solid support for Fe_3O_4 nanoparticles, and the resulting composite was utilized as a heterogeneous catalyst to perform the degradation of potentially toxic organic dyes, Methylene Blue (MB) and Rhodamine B (RhB). With bare Fe_3O_4 , degradation of 60% and 58% of MB and RhB was observed in two hours, whereas, with the vaterite-supported Fe_3O_4 , almost complete degradation, 96%, of MB and 86% degradation of RhB was achieved. As a comparison, the commercially available form of CaCO_3 , the calcite phase, was also used as a support for Fe_3O_4 and the composite, when used as a catalyst, resulting in 81% and 73% degradation of MB and RhB. The comparative studies revealed that the use of solid supports had improved the catalytic activity of the material. The biomineralized vaterite microspheres behaved as better support, and therefore, high rate constants of $3.15 \times 10^{-2} \text{ min}^{-1}$ and $1.82 \times 10^{-2} \text{ min}^{-1}$, respectively, were achieved for the degradation reactions of MB and RhB performed using the catalysts based on them. Further, the magnetic nature of the catalyst made it a great prospect for reusability. Experimentally we observed that the catalysts retained their

complete efficiency even after five consecutive cycles. Also, the versatility of the catalyst was proved by its ability to perform in natural water sources; tap water, lake water and river water.

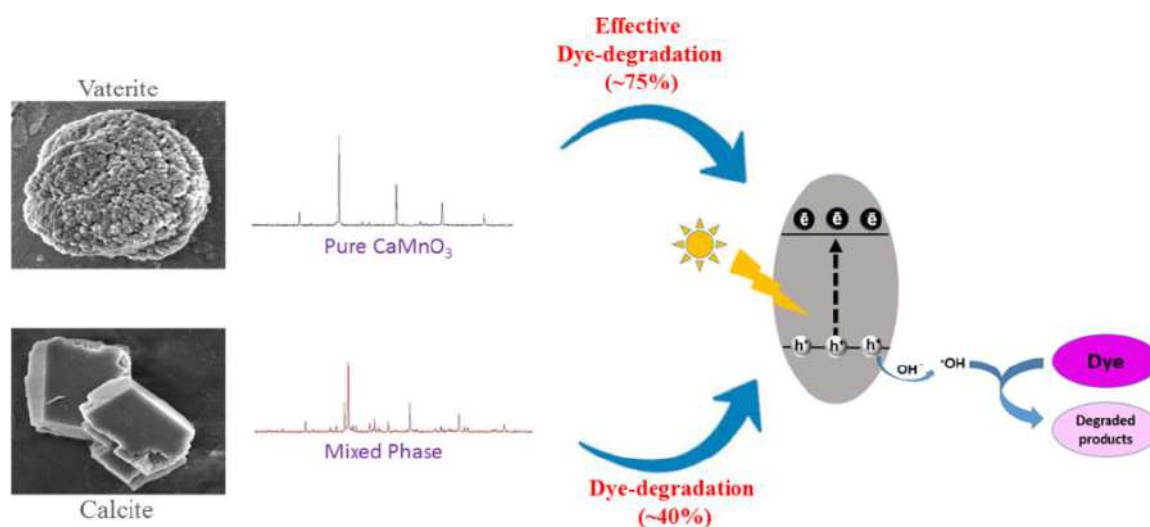


Scheme 6: A pictorial illustration of the research work covered in **Chapter 7b**.

Chapter 8: *In vitro* biomineralized vaterite derived efficient solid-state synthesis of pure CaMnO_3 perovskite as a useful photocatalyst (*CrystEngComm.*, 2021, **23**, 4050-4058)

The perovskite materials have attracted immense popularity in recent years due to their role in energy-based applications. Calcium manganese oxides are analogous to the systems that perform water-splitting in the natural photosynthesis process. Herein, we discuss a convenient method to synthesize the perovskite CaMnO_3 . Biomineralized vaterite was used as the calcium source to synthesize pure CaMnO_3 efficiently. In contrast, commercially available CaCO_3 comprising of the calcite phase led to the formation of a mixture of calcium manganese oxides. The bandgap energy of pure CaMnO_3 was found out to be 1.21 eV. This low value suggested that the material would easily absorb visible light, rendering it highly suitable to be used as a photocatalyst. Hence, it was subjected as a photocatalyst to catalyze the photolytic degradation of the toxic dyes viz. Rhodamine 6G, Rhodamine B, Methylene blue and Methyl orange. The photocatalytic degradation of Rhodamine 6G was studied in detail, where 72% of dye degradation was observed within 2 hrs in the presence of pure CaMnO_3 in contrast to 46% in the presence of the mixed-phase calcium manganese oxide. The mechanistic pathway of degradation was also studied, from which we could infer that the photo-generated $\cdot\text{OH}$ and h^+ were the species responsible for the degradation of Rh 6G. To validate the effectiveness of the catalyst towards

wastewater treatment, the degradation experiments were performed in lake water and river water, and the results obtained were impressive.



Scheme 7: A pictorial illustration of the research work covered in **Chapter 8**.

Conclusion and future plans and perspectives

To summarise, all the aspects of biomineralization broadly covered by a chemistry have been addressed in the experimental works, leading to the preparation of the thesis. The characterization of the crystallography and composition of the materials to study the phase and morphology of the biominerals; designing *in vitro* model systems to understand biomineralization where both small and large molecules, as well as plant extracts, were used; and in the development of new methods to improve the material properties, the incorporation of flavonoids to improve the mechanical strength was performed; also the biomineralized materials were subjected as solid supports for metal nanoparticles and converted to perovskite materials to perform wastewater treatment related applications. Further, the utilization of the *in vitro* biomineralized CaCO_3 particles in biological applications such as drug delivery and a similar approach with another calcium-based biomineral hydroxyapatite are in the reckoning. The results attained through the course of work show how biologically useful molecules and plant extracts can participate in Ca-based biomineralization and hence, generating scope for their utilization in the broader picture concerning these materials, such as in applications involving drug delivery vehicles, bone grafting, etc. In addition to the applications performed in the experiments leading to this thesis, the numerous polymorphs of CaCO_3 synthesized here can be utilized in other medical and environmental applications.

References:

1. L. Addadi and S. Weiner, A Pavement of Pearl, *Nature*, 1997, **389**, 912-913.
2. M. D. Brasier, O. R. Green, A. P. Jephcoat, A. K. Kleppe, M. J. Van Kranendonk, J. F. Lindsay, A. Steele and N. V. Grassineau, Questioning the Evidence for Earth's Oldest Fossils, *Nature*, 2002, **416**, 76–81.
3. A.-W. Xu, Y. Ma and H. Cölfen, Biomimetic Mineralization, *J. Mater. Chem.*, 2007, **17**, 415–449.
4. H. A. Lowenstam and S. Weiner, *On Biomineralization*, Oxford University Press, 1989.
5. S. I. Stupp, G. C. Mejicano and J. A. Hanson, Organoapatites: Materials for Artificial Bone. II. Hardening Reactions and Properties, *J. Biomed. Mater. Res.*, 1993, **27**, 289–299.
6. M. Viani, T. E. Scha, J. B. Thompson, N. A. Frederick, J. Kindt and P. K. Hansma, *Molecular Mechanistic Origin of the Toughness of Natural Adhesive Fibers and Composites*, 1999, **399**, 761–763.
7. S. Mann, Synthesis of Barium Sulfate from Surfactant – Inorganic Nanoparticles
REVIEWS The Chemistry of Form, *Angew.Chem.Int.Ed*, 2000, **39**, 3392–3406.
8. H. Du, U. Steiner and E. Amstad, Nacre-Inspired Hard and Tough Materials, *Chimia (Aarau)*, 2019, **73**, 29–34.
9. L. A. Estroff, Introduction : Biomineralization, *Chem. Rev.*, 2008, **108**, 10–12.
10. N. A. J. M. Sommerdijk and G. de With, Biomimetic CaCO₃ Mineralization Using Designer Molecules and Interfaces, *Chem. Rev.*, 2008, **108**, 4499–4550.
11. N. Watabe, Studies on Shell Formation, *J. Ultrastruct. Res.*, 1965, **12**, 351–370.

ACKNOWLEDGEMENT

This thesis represents not only my work in the lab, but it is a milestone in more than half a decade of work at IITG and specifically within CHL-201. My experience at IITG has been nothing short of amazing. Since my first day here I have felt at home. I have been given unique opportunities and been fortunate enough to make the most out of it. Throughout these years I have learned that there are some who build tools, some who use them and also some who do a bit of both. This thesis presents the lessons that I have learned in making some and also using a few: “Effect of additives on bio-inspired mineralization of CaCO_3 and application of its composites”. This thesis is the result of work by a number of people, who I wish to thank. But this thesis is also the result of many experiences I have encountered at IITG from dozens of remarkable individuals who I also wish to acknowledge.

First and foremost, I wish to thank my supervisor, Professor Gopal Das. The biggest reason why this journey has been so remarkable is because of his never ending support and his calm and composed nature which I wish to imbibe in my personality. Being a student of science it gives me immense pleasure to have been fortunate enough to work in this unique area of specialization "Biom mineralization". And during the most difficult times while performing the experiments and writing this thesis, he gave me the moral support and the freedom I needed to move on. My thesis committee members guided me through all these years. Thank you, Prof. Lal Mohan Kundu, Prof. Sandip Paul and Dr. Dipankar Srimani, for being my major advisors and being a constant source of support. I would also like to thank our department HODs (during my PhD tenure), Prof. T. Punniyamurthy and Prof. Gopal Das, all the faculty members, scientific officers, technical and non-technical staffs in the Department of Chemistry, IIT Guwahati. I sincerely appreciate all the staffs and instrument operators of Central Instrument Facility, IIT Guwahati for providing all the necessary instrumental facilities required during my research work.

Dozens of people have helped and taught me immensely at this lab throughout these years. The following people have been a source of support and energy ever since and an amazing help all this time, Nilotpall Da, Utsab Da, Biswajit Da, Rupinder Bhaiya, Bishu Da, Arnab Da, Jayakrishnan Bhaiya, Santanu Da, Senjuti, Deepa Di, Alesh, Megha, Sagnik, Debolina, Pampi, Pegu, Rubi and Neha. Thank you to everyone at the lab for many years of tea, snacks, parties, movies, outings and fun while working on the thesis! Also thank you to everyone at the department/campus/hostel, who has helped with the project and supported me in many ways.

ACKNOWLEDGEMENT

A special group of friends is not mentioned yet, because they deserve their own part. I wish to thank them for their support, inspiration and camaraderie: Sourav and Subhamoy. Thank you for teaching me about the subject; about professionalism needed when creating new things; and most importantly for standing beside me when I needed you the most. A special mention to another special friend Sujit for being an integral part of this journey.

I have special friends to thank, going back to my pre-IITG days. I have to especially thank Rupayan whom I consider my best friend since high school and Rahul, who has been a very special friend. A special mention to the person, Sourav Da, who had encouraged and motivated me in all possible ways to begin this journey and has continued his unconditional support to me all these years. I wish to acknowledge a friendship that began at the onset of my journey towards research and became ripe throughout my years at IITG because of their respective contribution towards the completion of my thesis: thank you to Anup and Prayasee.

I would also like to extend my gratitude to my all teachers/faculties and friends from my school, Bachelor's and Master's. Although they were far apart during this tenure, their direct or indirect support and motivation has guided me to reach this far. It is difficult to weave all the names in a single piece of writing. So, any omission in this brief acknowledgement does not mean lack of gratitude.

I finish with my pillars of strength, where the most basic source of my life energy resides: my family. Their support has been unconditional all these years; they have given up many things for me to be where I am in my life right now; they have cherished with me every great moment and supported me whenever I needed it. This thesis belongs to the family, special mention to my maternal uncles, aunties and cousins. It is a combination of all the knowledge that my father (Debabrata Paul) gave me, coupled with the love and wonderful personality that my mother (Shikha Paul) has. And thanks to Indrani Purkayastha, for being there through thick and thin, for always cheering me up so that I could continue my hustle at IITG and beyond in this journey called life.

Lastly, I wish to acknowledge the force that drives this universe, the almighty. I take this opportunity to praise and thank God, for the wisdom he bestowed upon me, the strength, peace of mind, good health and countless blessing in every step of this research and its subsequent completion in due time.

Debjit

Table of Content

Chapter 1: Introduction

1.1 Inspiration from living organisms	1
1.2 The chemistry of CaCO ₃	1
1.3 Different stages of crystal maturation	3
1.3.1 Nucleation	3
1.3.1.1 Homogeneous nucleation	3
1.3.1.2 Heterogeneous nucleation	5
1.3.2 Crystal growth	6
1.3.2.1 Growth controlling factors	6
1.3.2.2 Role of additives	7
1.3.2.3 Role of Templates	10
1.3.2.3 Oriented nucleation	11
1.4 Polymorph control (formation of metastable phases)	11
1.5 Mechanical properties	13
1.6 Wastewater treatment	14
Objectives of the thesis	15
References	16

Chapter 2: Experimental Details and Characterization

2.1 Materials and Instruments	25
2.2 Experimental methods and characterization	26
2.2.1 Synthesis of CaCO ₃ in the presence of whey protein	26
2.2.2 Synthesis of CaCO ₃ in the presence of the additives curcumin and quercetin	27
2.2.3 Tulsi and Green tea extracts as additives	28
2.2.3.1 Preparation of the leaf extracts	28
2.2.3.2 In vitro crystallization of CaCO ₃ in the presence of leaf extracts	29
2.2.3.3 The reverse sequence of addition	29
2.2.4 Mechanical Strength of CaCO ₃ composites	30
2.2.4.1 Synthesis of CaCO ₃ in the presence of the additives quercetin and hesperidin	30
2.2.4.2 Fabrication of gelatin films	31
2.2.4.3 Mechanical testing	31

Contents

2.2.5	<i>Ag NPs/Vaterite catalyst for reduction of 4-Nitrophenol</i>	32
2.2.5.1	<i>Synthesis of Ag NPs/Vaterite catalyst</i>	32
2.2.5.2	<i>Catalytic reduction of 4-NP</i>	33
2.2.6	<i>Vaterite and Calcite based Magnetite composites</i>	33
2.2.6.1	<i>Synthesis of Fe₃O₄ nanoparticles</i>	33
2.2.6.2	<i>Synthesis of Fe₃O₄/Vaterite nanoparticles</i>	34
2.2.6.3	<i>Synthesis of Fe₃O₄/Calcite nanoparticles</i>	34
2.2.6.4	<i>Degradation of dyes by Fenton-like process</i>	35
2.2.7	<i>Biominederalized Vaterite derived CaMnO₃ as photocatalysts</i>	36
2.2.7.1	<i>Synthesis of CaMnO₃</i>	36
2.2.7.2	<i>Degradation of Rhodamine 6G and the other dyes</i>	38
References		39

Chapter 3: Whey protein directed *in vitro* biomineralization of vaterite: A study on the influence of external parameters on CaCO₃ phase transformation

3.1	Introduction	41
3.2	Results and Discussions	42
3.2.1	<i>Influence of Whey Protein on CaCO₃ precipitation</i>	42
3.2.2	<i>Effect of Variation in Parameters</i>	45
3.2.2.1	<i>Effect of Whey Protein concentration</i>	45
3.2.2.2	<i>Effect of Sequence of addition</i>	46
3.2.2.3	<i>Effect of Temperature</i>	47
3.2.2.4	<i>Effect of pH</i>	49
3.2.2.5	<i>Effect of Ionic strength</i>	50
3.3	Conclusion	52
References		53
Annexure-Chapter 3		56

Chapter 4: Role of curcumin and quercetin as additives in the *in vitro* biomineralization of CaCO₃: A comparative study on phase modulation

4.1	Introduction	65
-----	--------------	----

4.2 Results and Discussions	66
4.2.1 <i>Influence of Curcumin and Quercetin in CaCO₃ biomineralization</i>	66
4.2.1.1 <i>CaCO₃ Phase Maturation</i>	69
4.2.2 <i>Effect of Variation in Parameters</i>	72
4.2.2.1 <i>Effect of additive concentration</i>	72
4.2.2.2 <i>Effect of Sequence of addition</i>	73
4.2.2.3 <i>Effect of Temperature</i>	74
4.2.2.4 <i>Effect of Ionic strength</i>	75
4.3 Conclusion	76
References	77
Annexure-Chapter 4	80
Chapter 5: Tuning of CaCO₃ phase and morphology directed by plant-based <i>in vitro</i> model systems: A thorough insight into the formation of monohydrocalcite	
5.1 Introduction	91
5.2 Results and Discussions	92
5.2.1 <i>Normal sequence of addition</i>	92
5.2.1.1 <i>Crystallization of CaCO₃ in the presence of tulsi and green tea extracts in methanol</i>	93
5.2.1.2 <i>Crystallization of CaCO₃ in the presence of tulsi and green tea extracts in water</i>	94
5.2.1.3 <i>Reusability of tulsi extract in methanol and the effectiveness of the mixture of tulsi and green tea extracts in methanol</i>	97
5.2.2 <i>Reverse sequence of addition</i>	97
5.3 Conclusion	109
References	109
Annexure-Chapter 5	113

Chapter 6: Incorporation of flavonoids into CaCO₃ and their influence on the phase, morphology and mechanical strength of the composites: A bio-inspired approach

6.1 Introduction	121
------------------	-----

Contents

6.2 Results and Discussions	122
6.2.1 <i>Incorporation of quercetin and hesperidin in CaCO₃ crystals</i>	122
6.2.2 <i>Quantification of the incorporation of quercetin and hesperidin in CaCO₃ crystals</i>	126
6.2.3 <i>Effects of incorporated organic compounds on CaCO₃</i>	127
6.2.4 <i>Determination of mechanical strength</i>	131
6.2.5 <i>Characterization of the films</i>	133
6.3 Conclusion	133
References	134
Annexure-Chapter 6	136

Chapter 7a: *In vitro* biomineralized vaterite as a solid-support for silver nanoparticles: A highly efficient catalyst for the reduction of 4-Nitrophenol

7a.1 Introduction	143
7a.2 Results and discussion	145
7b.2.1 <i>General characterizations of the materials</i>	145
7b.2.2 <i>Reduction of 4-NP</i>	150
7a.3 Conclusion	155
References	156
Annexure-Chapter 7a	160

Chapter 7b: Vaterite and calcite based magnetite composites: A comparative study on the catalytic performance during spontaneous Fenton-like dye degradation

7b.1 Introduction	167
7b.2 Results and Discussions	168
7b.2.1 <i>General characterizations of the materials</i>	168
7b.2.2 <i>Dye degradation studies</i>	173
7b.2.3 <i>Resuability of the catalyst</i>	178
7b.2.4 <i>Mechanism of the Fenton-like dye degradation</i>	179
7b.3 Conclusion	181

Contents

References	182
Annexure-Chapter 7b	186

Chapter 8: *In vitro* biomineralized vaterite derived efficient solid-state synthesis of pure CaMnO_3 perovskite as a useful photocatalyst

8.1 Introduction	195
8.2 Results and Discussions	197
8.2.1 <i>General characterizations of the materials</i>	197
8.2.2 <i>Photocatalytic dye-degradation</i>	200
8.3 Conclusion	206
References	206
Annexure-Chapter 8	211
Conclusion and Future Perspective	215
Curriculum Vitae	217

Introduction



1.1 Inspiration from living organisms

Biom mineralization is a fundamental life process that leads to the formation of mass and structure in almost all life forms. The hierarchically structured organic-inorganic hybrid composites, popularly termed biominerals, formed during this biogenic process are widely prevalent among almost all living organisms, ranging from the unicellular marine organisms to shells in tiny mollusks to the highly complex skeleton in higher organisms including the bones and teeth in the human body.^{1.1-1.3} The properties of these materials, such as mechanical, optical, magnetic, etc., are exploited by the organisms for a variety of purposes.^{1.4,1.5} The ability possessed by the organisms to optimize the shape, size, structure, orientation, texture, and overall morphology of the biominerals is fascinating. Ever since the beginning of the era when scientists involved themselves in understanding this biological phenomenon, they have been thrilled by this special ability and, therefore, have engulfed themselves into understanding the mystery behind this art. Till today, decades since the onset of the preliminary studies, a fairly large number of questions related to biominerals remain unexplored. The scientific efforts in the field of materials science clubbed together with the understanding of chemistry have enabled scientists to mimic the design and synthesize various biogenic materials, of which the biominerals commandingly stand out as one of them.^{1.6-1.8} However, to date, they have not attained success in synthesizing minerals that possess superior properties to their biological counterparts. The quest to obtain the biological standard is still on.

1.2 The chemistry of CaCO₃

The organization of the inorganic crystals over the organic matrix is responsible for the exceptional properties of the biominerals.^{1.9-1.12} Simultaneously, with this organization, the authority over polymorphism and crystallographic arrangement are the additional factors that substantially determine the properties of these materials. As it is evident that the interaction of the organic and inorganic phases is essential in the *in vivo* generation, both soluble and insoluble directing species have been comprehensively studied. However, a complete understanding of the correlation between these agents and the crystallographic structure and properties of the resulting material is yet to be accomplished.^{1.13-1.16}

In this thesis, we have focussed on the biomimetic synthesis of CaCO₃ to understand the factors that influence the formation of the different polymorphs. CaCO₃ being the most abundant biomineral covers a large part of the biomineral world and is also a material of industrial importance as it finds application in the generation of commercial and personal care

products.^{1.17,1.18} Among the inorganic materials, CaCO_3 has extensive biomedical applications owing to its availability, low cost, safety, biocompatibility, pH sensitivity, and biodegradability.^{1.19} It has been used as a carrier for targeted drug delivery and as a template for biodegradable polymer capsules for applications in nanomedicine.^{1.20–1.22}

The study of biomineralization is a multidisciplinary prospect that engages researchers from biology, chemistry, materials science, geology, and beyond.^{1.23} The key role played by chemistry in biomineralization research can broadly be divided into three main areas, in studying the chemical composition, biochemistry, and crystallography of the materials; in designing *in vitro* model systems to understand the interactions between the organic and the inorganic phases to understand the actual mechanism in biological systems; in developing new synthetic techniques by mimicking the biological systems to generate organic-inorganic composites with enhanced mechanical properties.

The primary source of CaCO_3 in nature is the remains from the skeletons of marine organisms that have accumulated over millions of years. These remains can be seen in the form of chalk, limestone, etc., and these minerals are also involved in the global carbon cycle.^{1.9,1.10,1.24} Being the most abundant biomineral, with an alluring science of its formation and characteristic toughness, makes it a very special prospect among chemists and material scientists. The ability of CaCO_3 to exhibit polymorphism is another factor that stands out. CaCO_3 is known to exist in three main anhydrous crystalline forms; calcite, aragonite, and vaterite, they are the most prevalent; two hydrated crystalline forms; calcium carbonate monohydrate (monohydrocalcite) ($\text{CaCO}_3 \cdot \text{H}_2\text{O}$) and calcium carbonate hexahydrate (ikaite) ($\text{CaCO}_3 \cdot 6\text{H}_2\text{O}$), and also in the amorphous state as amorphous calcium carbonate (ACC).^{1.10} Recently, one more hydrated crystalline form has been reported by Zou et al. as calcium carbonate hemihydrate $\text{CaCO}_3 \cdot \frac{1}{2}\text{H}_2\text{O}$.^{1.25} Calcite is the most stable and has a rhombohedral crystallographic unit cell; aragonite, which is comparatively unstable, is orthorhombic and the metastable vaterite is hexagonal.^{1.26} It is the Wull's Rule, which predicts the morphology of the crystals.^{1.27} For calcite, it was observed both experimentally and theoretically that it has a rhombohedral crystal structure. Aragonite has an orthorhombic crystal structure and the metastable vaterite has a hexagonal crystal structure. The first member of the hydrated crystal group, calcium carbonate hexahydrate, crystallizes with a monoclinic crystal structure.^{1.28} The crystal structure of monohydrocalcite with trigonal symmetry was determined in 1981.^{1.29} Zou et al. reported the newest phase, calcium carbonate hemihydrate to exist with a monoclinic crystal structure.^{1.25}

The formation of matured crystals in nature and also during *in vitro* studies goes via the nucleation and crystallization mechanisms and CaCO_3 is often considered as a reference model

system for studying this phenomenon.^{1.30,1.31} What makes CaCO_3 even more special is its sensitivity towards template effects that makes it applicable for elementary studies on template-mineral interactions. When synthesized under ambient conditions without any template or additive, it attains the thermodynamically most-stable calcite phase and appears as rhombohedral crystals, whereas, in the presence of templates or additives, the polymorphs can be tuned from one form to the other based on the synthetic requirements or to understand the dynamic mechanism of formation of CaCO_3 .

1.3 Different stages of crystal maturation

1.3.1 Nucleation

It is the first step in the crystallization of inorganic minerals in which a small number of constituting species such as ions, atoms, or molecules organize themselves in a pattern characteristic of a crystalline solid, following which a new phase (solid) is formed from the previous (liquid) phase.^{1.32} The process begins by the formation of tiny metastable clusters within the liquid phase where the clusters are in a continuous state of growth and disintegration, which is dictated by a balancing act between the increasing surface energy associated with the increased surface area and the lowering of bulk energy associated with the formation of a crystal lattice.^{1.10,1.33} Eventually, there arises an instance where the bulk energy neutralizes the surface energy and a critical size is attained. Following this, the subsequent growth causes a reduction in the Gibbs energy of the system as the further decrease of the lattice energy overcompensates the increase in surface energy. These clusters then grow until they reach a critical size and by overcoming an energy barrier which ultimately leads to the generation of a stable nucleus. According to the classical nucleation theory,^{1.34} homogeneous nucleation is directed by elevated supersaturations and heterogeneous nucleation, on the contrary, is induced by the presence of substrates that behave as active sites and govern the whole process.

1.3.1.1 Homogeneous nucleation

Over the period, there has been an evolution in the theories of nucleation. Since the very beginning, the model featuring the nucleation of ions (or pair of ions) has been successfully used to explain many attributes of the nucleation process.^{1.35-1.37} However, a drawback of this model lies in the fact that it considers only the energy aspects while neglecting the structural information. As a result, this model has been reviewed over time.^{1.38,1.39}

The Gibbs energy associated with nucleus formation is contributed by the Gibbs energy gained by the formation of a nucleus from the supersaturated solution and the energy lost in the formation of a new surface and is represented as;

$$\Delta G = -nkT \ln S + \sigma A \quad (1)$$

Where n is the size of the nucleus formed, k is the Boltzmann's constant, T is the temperature, S is the supersaturation, σ is the interfacial Gibbs energy for nucleation, and A is the surface area. The supersaturation S can be determined from the solubility product K_{sp} and the activities a of the species involved, here $a(\text{Ca}^{2+})$ and $a(\text{CO}_3^{2-})$, via

$$\ln S = \ln[a(\text{Ca}^{2+}) a(\text{CO}_3^{2-})]/K_{sp} \quad (2)$$

As homogeneous nucleation is directed by elevated supersaturations, the chemical parameters such as the Ca^{2+} ion activity $a(\text{Ca}^{2+})$ and the CO_3^{2-} ion activity $a(\text{CO}_3^{2-})$ determine the nucleation. In any CaCO_3 formation reaction, K_{sp} is temperature-dependent and varies depending on the CaCO_3 phase. The activity of the constituting ions and hence, the supersaturation ratio is influenced by the conditions, such as temperature, pH, and ionic strength of the system per the Debye-Huckel law. The precipitation kinetics of the reactions is considerably affected by the operating conditions mentioned above, that is why the different crystalline phases, vaterite, aragonite, and calcite, are obtained. The most stable phase at any temperature is calcite, while the other two are metastable phases. According to the study performed by Rodriguez-Blanco et al.,⁹ the crystallization mechanism of CaCO_3 could be divided into two main stages. The initial stage where the transformation of unstable ACC to metastable vaterite phase and in the second stage, the subsequent transformation of metastable vaterite to stable calcite. These observations are in tandem with other reports along the same line; for example, Bots et al.^{1.40} observed the mechanistic features of the transformation of ACC to vaterite and merged their observations with those obtained by Rodriguez-Blanco et al. to understand the complete abiotic transformation mechanism from the amorphous phase to the stable calcite via vaterite. Ogino et al.,^{1.41} in their work, pointed out that the rate-determining step of this whole transformation is the dissolution of vaterite, leading to the growth of calcite. Another study reported by Dickinson et al.,^{1.42} illustrated the effect of chemical parameters such as the Ca^{2+} ion activity $a(\text{Ca}^{2+})$ and CO_2 partial pressure $p\text{CO}_2$ on nucleation. They varied $a(\text{Ca}^{2+})$ and $p\text{CO}_2$ and observed that at low $a(\text{Ca}^{2+})$, the process being thermodynamically controlled, the rhombohedral calcite crystals formed were stepped multinucleated. Here, the amount of CO_2 determined the amount of calcite formed. At comparatively higher values of $a(\text{Ca}^{2+})$, they obtained perfect rhombohedral crystals of calcite and in this case, the process was a balance between kinetic and thermodynamic factors. At even higher $a(\text{Ca}^{2+})$, it becomes a kinetically controlled reaction and a biphasic

product, where $\sim 1/3$ calcite and $\sim 2/3$ vaterite was formed and from then on, with further increase in $a(\text{Ca}^{2+})$ and $p\text{CO}_2$, the proportion of the vaterite phase would increase.

1.3.1.2 Heterogeneous nucleation

This type of nucleation involves the introduction of a substrate in the reaction medium. The pre-critical nucleus interacts with the substrate and this interaction is said to lower the surface Gibbs energy in most cases which reduce the barrier otherwise set for the development of the critical nucleus. Therefore, the nucleation taking place at the interface is favored over the one occurring in bulk (homogeneous nucleation). This is also the basis for the formation of oriented crystals as the interaction with the surface advocates the nucleation on a specific crystal plane.

For homogeneous nucleation, the relevant Gibbs energy σ_{hom} equals the Gibbs energy γ_{nl} associated with the nucleus (n)-liquid (l) interface,

$$\text{i.e., } \sigma_{hom} = \gamma_{nl} \quad (3)$$

For heterogeneous nucleation, the relevant interfacial Gibbs energy σ_{het} is the sum of the Gibbs energies for the nucleus-liquid and nucleus-substrate interfaces minus that for the liquid-substrate interface,

$$\text{i.e., } \sigma_{het} = (\gamma_{ns} - \gamma_{ls})(I - \zeta) + \gamma_{nl}\zeta \quad (4)$$

where, ζ is the ratio of nucleus-liquid area versus total area.

On introducing the contact angle θ between the substrate and the pre-nucleation cluster, the relation between ΔG_{het}^* and ΔG_{hom}^* can be expressed as,

$$\Delta G_{het}^* = \kappa f(\theta) \Delta G_{hom}^* \quad (5)$$

where $*$ denotes the critical state.

The contact angle and the shape of the nucleus determines the function $f(\theta)$, while the function κ contains the interface energy γ_{cf} between the growing cluster and the fluid.

It should be noted that some assumptions are to be made before applying the heterogeneous nucleation model.^{1,10}

- i. The substrate should be rigid.
- ii. The nucleating species is all individual ions.
- iii. The system is thermodynamical for the nucleus with constant interface energies and solubility products.

However, several drawbacks are associated with the classical heterogeneous nucleation model; for example, it considers the substrate flat and the nucleus to be a spherical cap. This approach makes the model very rigid and it was found to be difficult to correlate with systems associated with different shapes of the substrate and nucleus. Hence, modifications have been made where

Liu et al.^{1.36} put forward a new model considering the substrate geometry to be spherical and the concept of a faceted nucleus has been given by Travaille et al.^{1.37} Therefore, despite the possible shortcomings, the classical heterogeneous nucleation model has been used either directly or post-modification to understand the various aspects of nucleation.

1.3.2 Crystal growth

The nucleation process is accompanied by crystal growth which can be classified into two main steps, mass transfer of the constituting ions/species from the bulk (solution) to the crystal surface and surface integration of the crystal unit in the crystal lattice.

In general, the process of crystal growth may or may not be influenced by foreign species such as ions or organic compounds. However, in biomineralization, these species known as additives play a huge part in the crystal growth process, such as determination of the phase and morphology by influencing the crystallographic parameters of the growing crystal. In the following section, a detailed discussion on the role played by these species on the crystal growth process has been elaborately discussed.

1.3.2.1 Growth controlling factors

This special kind of organization attributed to the hierarchical arrangement is responsible for the outstanding mechanical properties of the biominerals, such as high crack resistance. In biominerals, the organic phase makes up from as low as 0.05 to as high as 40% of the composite.⁴ As a result of prolonged research in the field of biomineralization, it is now evident that the organic phase plays a huge role in directing mineral growth.^{1.43} The localization of the organic molecules within the biominerals leads to two subdivisions; intercrystalline and intracrystalline. The biominerals in which the organic phase (molecules) occupies the crystal surface are classified as “intercrystalline” and the ones in which these molecules are incorporated inside a single crystal are classified as “intracrystalline”.^{1.44} The reports related to intracrystalline molecules are mostly associated with CaCO₃. It is of absolute interest to researchers how the macromolecules are successfully incorporated within the dense inorganic host-crystals; what may be the advocating criteria for a specific molecule to be incorporated within a specific crystal; and finally, to know the biological function of the resulting intracrystalline composite. In **Fig. 1.1**, we represent all the different pathways of crystallization.

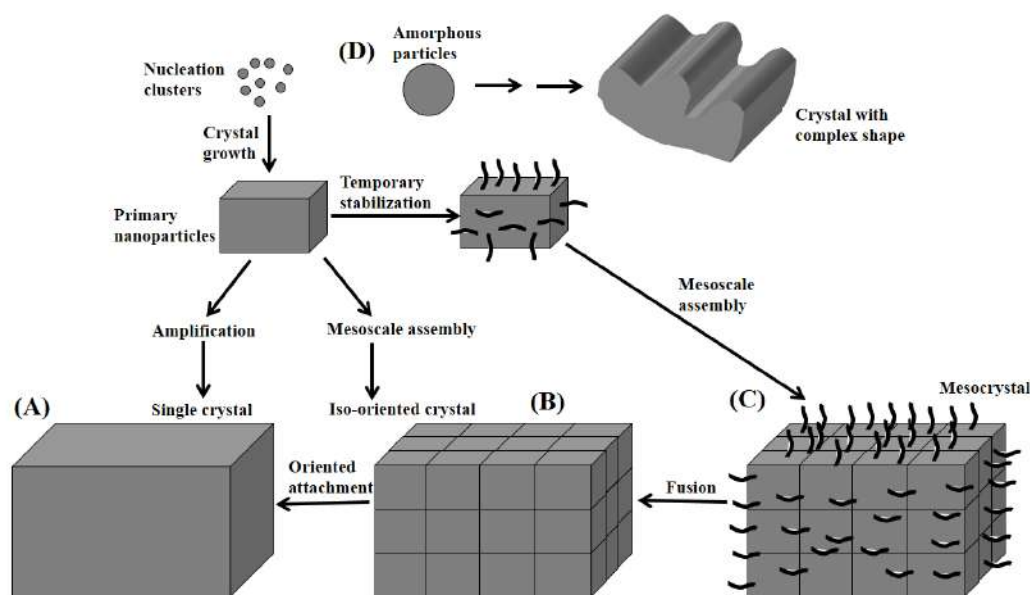


Figure 1.1: Schematic representation of different pathways of crystallization. Pre-nucleation clusters grow to produce a critical nucleus which grows further into a primary nanoparticle. (A) The primary nanoparticles then mature into a single crystal by the addition of ions; (B) The primary nanoparticles mature into a single crystal by oriented attachment of multiple particles; (C) The additives attach to the surface of primary nanoparticle to form mesocrystals; (D) The pre-nucleation clusters lead to the formation of amorphous particles which crystallize either with or without interaction with an additive to produce different crystal morphologies.

1.3.2.2 Role of additives

It was in 1965 when a study performed by Norimitsu Watabe reported the presence and also the distribution of intracrystalline molecules in various marine organisms for the first time.^{1.45} Since then, taking a cue from the biological specimens, the researchers working on biomimetic materials based on biominerals have moved a long way in their study on the incorporation of species within the composite. It has been demonstrated that not just organic but also inorganic additives play a crucial role in determining the properties of the composite.^{1.46} As for the intercrystalline composites, the additives adsorbed to the surface of the primary particles prevent the formation of the critical nucleus by facilitating the growth of the different faces. These additives can also promote the growth of crystals by altering the surfaces properties of crystals post adsorption or can form a bridge between several crystalline units. For the intracrystalline ones, the incorporated additives inside the mineral promote their solubility and also raise the limit in size essential for the development of stable particles. These effects boost the aggregation of smaller units, therefore, forming either randomly organized polycrystalline entities or well-organized, larger aggregates. There are instances where the additive adsorption takes place post the nucleation stage and in this case, they influence the formation of the crystal by hindering the

growth at specific crystal faces.^{1.47} As a result, the formation of the equilibrium morphology is disturbed and this will, in turn, affect the structure of the crystallographic unit cell, thereby influencing the overall phase and morphology of the system.

Kim et al. performed an experimental study to understand the role of additives on the early stages of calcite crystal growth.^{1.48} The experiments in this study were based on the fact that the crystallization process advances much slowly in small volumes as compared to large volumes. They investigated the role of two soluble additives, Mg^{2+} and poly (styrene sulfonate), on the initial stages of calcite crystal growth from an amorphous precursor (ACC). Interestingly, they reported that the first crystals of calcite that were observed in each case were perfectly rhombohedral and the soluble additives did not influence the morphology till the sizes of the crystals were 100 nm for Mg^{2+} and 1 μm for poly (styrene sulfonate). Based on their findings, they also stated that the concentration, additive binding strength, and supersaturation are the factors that determine the size of the growing calcite crystal at which the additive would start to affect the morphology.

Kim et al. studied the combined effects of Sr(II) and poly (acrylic acid) in the precipitation of $CaCO_3$ by diffusion of CO_2 , generated from $(NH_4)_2CO_3$ into an aqueous solution of $CaCl_2$.^{1.49} They found that the morphology of the calcite crystals was different from the typical rhombohedral morphology. Liu et al. performed the precipitation of $CaCO_3$ in the presence of egg white and Cu^{2+} .^{1.50} They reported that copper(II) could induce the formation of metastable vaterite. Du et al. successfully showed the influence of many organic and inorganic additives, low-molecular-weight additives such as glycine, citric acid, acrylic acid, and magnesium chloride hexahydrate; and high low-molecular-weight additives such as poly (acrylic acid), poly (sodium 4-styrene sulfonate), and poly (allylamine) on the crystallization of amorphous $CaCO_3$ when they are exposed to humid environments and elevated pressures.^{1.51} Stepic et al. used aspartic acid and its derivatives as models of biomolecules to study their interactions with calcite.^{1.52} Wada et al. demonstrated the effect of electric field combined with the additive polylysine on the crystallization of calcite.^{1.53} They found that on changing the concentration of polylysine coupled with polarization treatment, calcite crystals with different morphologies were formed. Bahrom et al. synthesized $CaCO_3$ with toroidal-like morphology by the use of poly (styrene sulfonate) sodium and dextran sodium sulfate as organic additives.^{1.19} Zhu et al. used N-stearoyl L-glutamic acid, an amphiphile, as the organic additive and reported an aggregation-based crystal growth of $CaCO_3$, different from the usual mode of solution crystallization.^{1.54}

Sun et al., by tuning the concentration of the additive adipic acid, controlled the morphology and surface area of the vaterite particles.^{1.55} Marzec et al. subjected both amino acids and dye

molecules as additives and showed how multiple organic additives co-operatively work in the case of biomineralization, to control the structure and properties of the composites.^{1.56} Kim et al. synthesized calcite crystals by the occlusion of block copolymers based on poly (methacrylic acid) (PMAA) and poly (benzyl methacrylate) (PBzMA). [57] Different structures were obtained by varying the concentration of the block copolymers used, **Fig. 1.2**. In another work, Kim et al., with the help of a series of copolymer nanoparticles based on the hydrophobic poly (2-hydroxypropyl methacrylate) subjected as additives during CaCO_3 precipitation, studied the crystal habit modification and nanoparticle occlusion within calcite crystals.^{1.58} Wang et al. reported the selective formation of metastable vaterite by subjecting alkanolamide 6502 as an additive to study its influence on the morphology of the precipitating CaCO_3 .^{1.59} Zou et al. performed experimental studies to recognize the influence of acidic macromolecule, poly (aspartic acid) during the mineralization of CaCO_3 .^{1.60} They reported that at a low concentration of the additive, the inhibition was more pronounced for the vaterite phase; hence

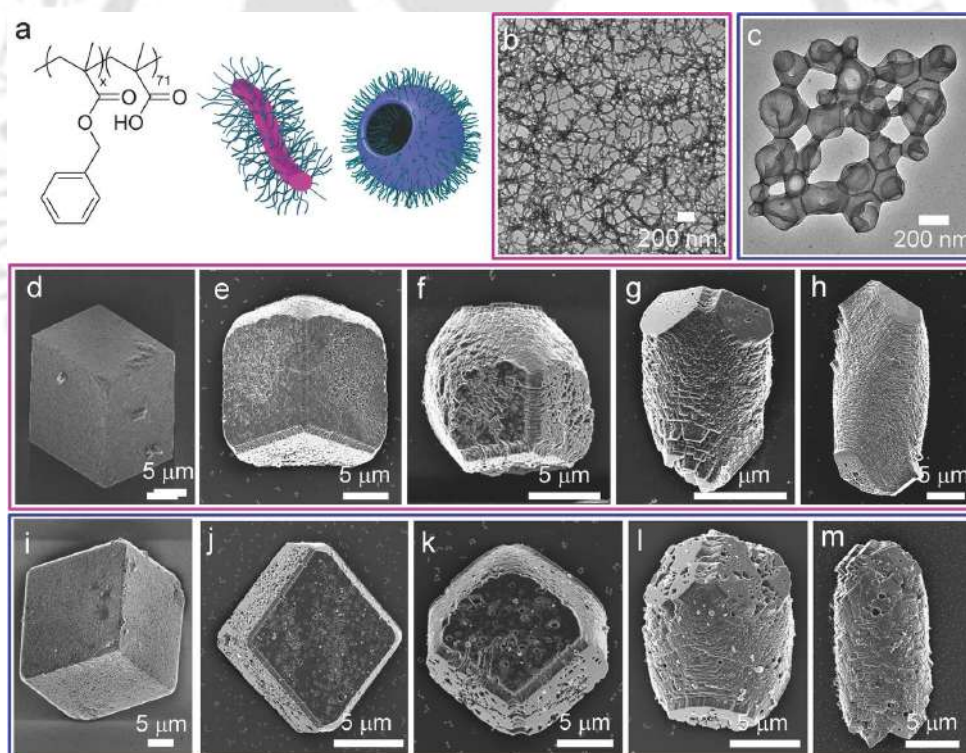
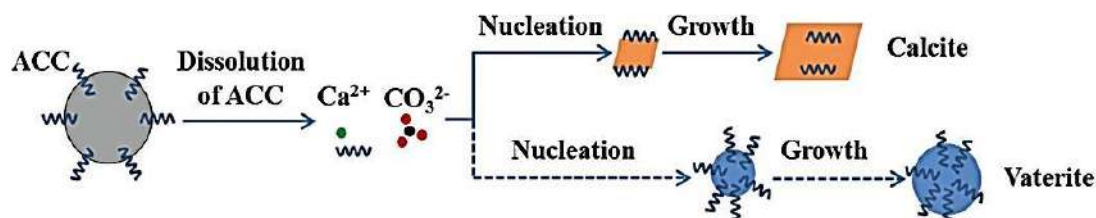


Figure 1.2: a) The chemical structure of the poly (methacrylic acid)-poly (benzyl methacrylate) (PMAA-PBzMA) diblock copolymer particles, where $x = 98$ and $y = 71$ for the worm particles and $x = 300$ and $y = 71$ for the vesicle particles, and schematics of worm and vesicle nano-objects. b,c) TEM images of (b) copolymer worms and (c) copolymer vesicles. SEM images of calcite crystals precipitated in the presence of d–h) vesicles and i–m) worms at fixed $[\text{Ca}^{2+}] = 1.25 \times 10^{-3} \text{ M}$ at copolymer concentrations of (d) $20 \mu\text{g mL}^{-1}$, (e) $50 \mu\text{g mL}^{-1}$, (f) $125 \mu\text{g mL}^{-1}$, (g) $250 \mu\text{g mL}^{-1}$, (h) $500 \mu\text{g mL}^{-1}$, (i) $20 \mu\text{g mL}^{-1}$, (j) $50 \mu\text{g mL}^{-1}$, (k) $125 \mu\text{g mL}^{-1}$, (l) $250 \mu\text{g mL}^{-1}$, and (m) $500 \mu\text{g mL}^{-1}$, where these show that the crystal morphologies change with increasing copolymer in solution.^{1.57} (Reprinted with permission from John Wiley and Sons)

the calcite phase was more favored. At higher concentrations, the amorphous precursor (ACC) was stabilized for a longer duration which facilitated vaterite formation via the pseudomorphic transformation. **Fig. 1.3** represents a schematic illustration of the role of poly (aspartic acid) during the crystallization of ACC in solution.

(a) Dissolution and reprecipitation



(b) Pseudomorphic transformation

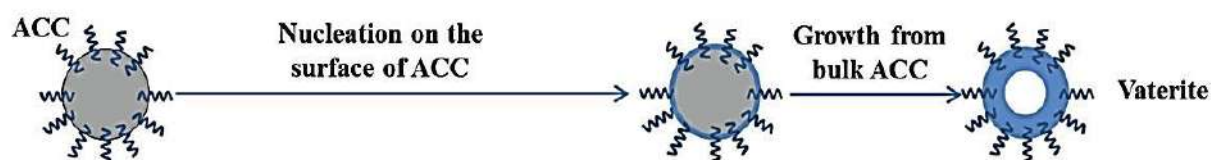


Figure 1.3: Schematic illustration of ACC crystallization in solution. (a) In presence of a low concentration of poly (aspartic acid), calcite and vaterite form via a dissolution and reprecipitation process. (b) At a high concentration of poly (aspartic acid), stabilization of ACC for a longer time allows the vaterite formation via a pseudomorphic transformation process.^{1,60} (Reprinted with permission from John Wiley and Sons)

1.3.2.3 Role of Templates

The introduction of a substrate to influence the nucleation step during CaCO_3 crystallization is fundamentally what is referred to as heterogeneous nucleation. The substrate involved here is called the template and the effect induced by it is known as the templating effect. The process of CaCO_3 nucleation on templates is generally explained by three mechanisms: epitaxy, charge/polarization matching, and mutual templating.^{1,10}

In epitaxy, it is the complementarity in terms of the crystallographic structure of the nucleus and the template. This mechanism assumes the template to have a rigid structure and that the template and the forming crystal have a structural surface-repetitive, complimentary basis for pattern recognition.^{1,61} Owing to these constraints, it becomes difficult to use this model to explain the nucleation process in all systems. However, a close structural match between the template surface and the nucleating crystal enables a significant level of control over crystallization. In the second mechanism, charge/polarization matching, the distribution of charges on the nucleus or the template is complemented by the opposite charge on the other. As

can be understood, the pre-requisite factors here determining the nucleation process are much more considerate on the interface structure as compared to the epitaxy mechanism. However, there are instances where nucleation occurs, but the charge/polarization mechanism cannot be used to explain the process. As a result, another mechanism, the mutual templating mechanism, to comprehensively understand the templating process was developed. In a mutual templating mechanism, the structure of the nucleus and the template mutually influence each other to achieve an optimum interface, both structurally and energetically. This phenomenon has been justified by molecular dynamics studies.^{1.62} The experimental studies have shown that the growth rate is influenced by the flexibility of the substrate and low interface energy between the template and the nucleus promotes the growth rate.^{1.63}

1.3.2.4 Oriented nucleation

We have seen how the formation of a crystal (CaCO_3) takes place, the constituting ions assemble to form the pre-nucleation clusters, which lead to the formation of the nucleus upon further addition of ions, and the nucleus above the critical size further develops to generate a crystal. The organic molecules and surfaces if introduced play a significant role where they influence the stabilization of a particular polymorph or a specific crystal face. This stabilization of a specific crystal face on a template surface is referred to as oriented nucleation.^{1.10} Describing the role of templates in CaCO_3 formation, we can say that the organic surfaces provided by the templates during the crystallization process encourage heterogeneous nucleation by lowering the surface free energy of the developing nuclei and; aids in the formation of a particular polymorph by stabilizing a specific crystal face.

1.4 Polymorph control (formation of metastable phases)

The factors responsible for the formation of metastable phases have already been discussed. The introduction of organic molecules (additives) or surfaces (templates) enables us to successfully isolate the metastable phase like spherical vaterite by terminating the growth of the crystals to the rhombohedral calcite. This is achieved by either of the two ways; the introduction of a suitable surface, raises the ΔG_n of calcite as compared of that of vaterite and ultimately facilitating the formation of the metastable vaterite.^{1.64,1.65} In a second way, the organic additives simply bind to specific crystal faces of the growing crystal post the nucleation process and prevent the crystal from further maturation.

Kanoje et al. studied the influence of template based on surfactant-polymer on the morphology of CaCO_3 .^{1.66} The co-operative effect of the surfactant and the polymer contributed to the formation of different polymorphs and morphology, as a result, spherical, bone-like, and cluster-like morphologies of CaCO_3 were obtained. Abeywardena et al. studied the precipitation of CaCO_3 in which they extracted calcium from dolomite using sucrose solution.^{1.67} In the next part of the study, they performed the crystallization of CaCO_3 using sucrate ($\text{Sucrose} + \text{OH}^- = \text{Sucrate}^-$) and sodium dodecyl sulphate individually and also in combination as the templates. Rianasari et al. synthesized lamellar stacks of CaCO_3 single-crystal sheets under the influence of the template poly(acrylic) acid.^{1.68} They had taken calcium acetate as the CaCO_3 precursor.

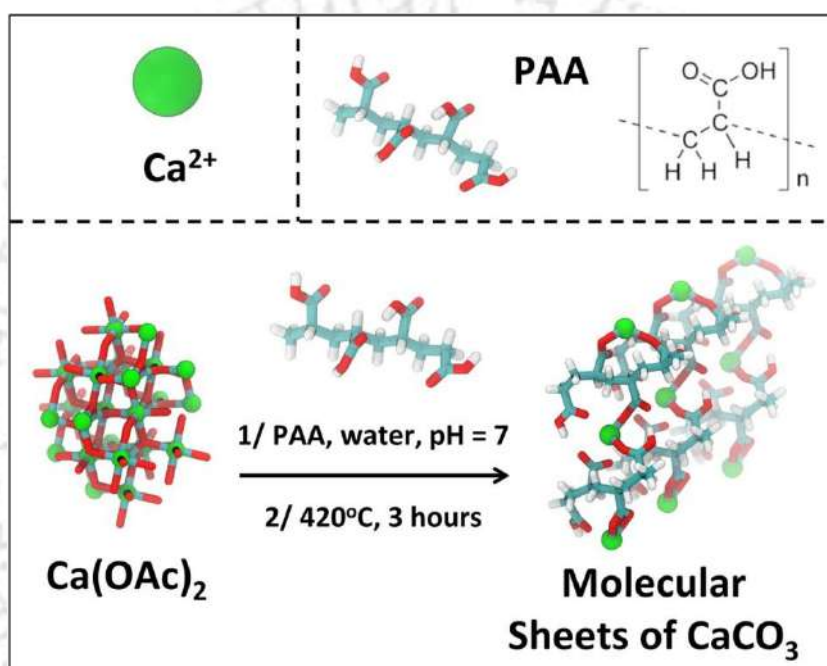


Figure 1.4: Schematic representation of the molecular sheets of CaCO_3 formation using a two-step process. A nacre-like lamellar structure of molecular sheets of CaCO_3 interleaved with organic material, (amorphous carbon) are produced using a formulation of poly(acrylic) acid (PAA) and calcium acetate (Ca-Ac) using a chemical template technique and followed by calcination.^{1.68} (Reprinted with permission from Springer Nature)

The variation in the concentration of the precursor and the template ($\text{Ca}^{2+}/\text{COO}^-$) allowed the control in the morphology of CaCO_3 and produced molecular sheets of unit cell dimensional. **Fig. 1.4** schematically represents the formation of CaCO_3 molecular sheets using a two-step process.

Lopez-Berganza et al. studied the combined effects of additives and surface templates on CaCO_3 formation.^{1.69} Two different poly-electrolyte films, poly (ethylene imine) and a two-layer film composed of poly (allylamine hydrochloride) and poly (acrylic acid), were subjected as templates and the organic additives used were amino acids and monosaccharides. The

experimental observations followed by the kinetic studies on the precipitation process provided insights into understanding the mechanisms of mineralization.

From a recent work performed by Wei et al., we can understand the role of biological cells as templates in the precipitation of CaCO_3 .^{1.70} In this work, they subjected three types of microbial cells as templates; *Escherichia coli*, *Staphylococcus aureus*, and Beer Yeast. In the presence of the bare cells, the precipitated CaCO_3 particles were a mixture of calcite and vaterite, with the ratio of the latter being higher. With the encapsulated cells, *Escherichia coli* and *Staphylococcus aureus* gave similar results, but with yeast, the ratio of calcite was more than that of vaterite. The difference in polymorphism observed was due to the differences in cell wall components of the cells used as templates.

1.5 Mechanical properties

The skeletal support and protection stand out as the trademark feature of the biominerals.^{1.71} In the invertebrates, calcium carbonate is responsible for these functions. The complex and hierarchical structures of these composite biominerals are the essential features responsible for superior mechanical properties such as hardness and crack resistance.^{1.72–1.75} As a result, material chemists have been fascinated and have always been in the quest of synthesizing materials that would match the properties of the biominerals such that they could be utilized for various applications.^{1.76} To understand the mechanical properties of the biogenic composites, it is essential to take cognizance of the microstructure, properties and morphologies of the individual constituents. Therefore, understanding the composition of the biominerals was of first-hand importance, whereby it was observed that in the organic-inorganic hybrid composites, the inorganic mineral phase is closely associated with organic molecules. These organic molecules were either present between the crystal units or embedded within single crystals, suggesting that the occlusion of generally very low levels of organic species contributed to the superior mechanical properties of the biominerals as compared to their synthetic inorganic counterparts.^{1.77}

The biogenic calcite single-crystal is reported to possess better mechanical strength as compared to the geologic calcite single-crystal available in the form of Iceland spar. Kunitake et al. performed a comparative study on the mechanical properties of biogenic calcite from the outer shell of the mollusk *Atrina rigida* and the geologic calcite from Iceland spar.^{1.78} The shell of *Atrina rigida* is made up of two layers containing mineral crystals with neighboring organic matrices. The mineral in the inner layer is constituted by aragonite “tablets,” and in the outer layer, it is calcite present as elongated single-crystal “prisms”. They reported that these calcite

prisms in *Atrina rigida* are harder than the geologic calcite in Iceland spar and summarised that the difference in the hardness could be due to factors such as the occluded organic molecules, Mg^{2+} , residual defects arising out of the formation process, etc. Based on similar studies, which revealed the properties of the biogenic minerals and the possible reasons responsible for their superiority, the incorporation of organic molecules, especially with calcite single crystals has been a subject of considerable interest. Kim et al. incorporated functionalized polystyrene within calcite single crystals and investigated the mechanical properties of the composite.^{1.79} The real highlight of the incorporation was in terms of the improvement acquired in the fracture behavior attributed to the strong association of the polymer particles with the crystal. In another study, Kim et al. reported the role of incorporated amino acids on the hardness of the resulting calcite composite.^{1.80} The two amino acids used were glycine and aspartic acid. A significant increase in the hardness of the crystals was observed on varying the concentration of the incorporated species.

1.6 Wastewater treatment

The release of industrial effluents into the environment is a major threat to the ecosystem and this crisis is being encountered across the globe. In recent times, due to the increase in demand for commercial products as well as pharmaceutical requirements, the production of goods has increased manifold and eventually, the release of toxic by-products evolved during their synthesis poses an additional threat to the environment, especially the water bodies. Industries such as textiles, cosmetics, plastics, leather, etc., use toxic organic dyes to impart color to their products.^{1.81,1.82} The most common and widely used dye in textile industries for dyeing wool, silks, and cotton is methylene blue. Methyl orange is a very common water-soluble azo dye used in industries such as textile, paper, printing, and food and is mostly discharged in industrial wastewater.^{1.83,1.84} Rhodamine B is widely used for industrial purposes, such as printing and dyeing in textile, paper, paints, leathers etc. Rhodamine 6G is widely used in the cosmetics industry for making products such as lipsticks.^{1.85} These dyes are highly soluble in water and the color associated with them prevents the penetration of light through water, hindering photosynthesis in aquatic plants, and disturbing the ecological balance. In short, based on recent reports, the major threats posed by the dyes that are discharged into the water bodies include lowering the aesthetic quality of water bodies, increasing the biochemical and chemical oxygen demand (BOD and COD), impairment of photosynthesis, making way into the food chain and thereby posing the threats of toxicity and carcinogenicity.^{1.86} The reagents used in pharmaceuticals such as 4-Nitrophenol released into water bodies pose a severe threat, even in

trace amounts, they are hazardous, causing potential damage to the human central nervous system, kidney, liver, etc.

The current techniques implemented for dye removal include adsorption, oxidation/reduction, biological activity, etc.^{1,87} More efforts are being put into the advance oxidation processes (AOPs). The in-situ generation of reactive oxygen species significantly enhances the degradation process. Photocatalysis is another effective method for environmental remediation applications, especially in recent times; they are considered one of the best remedies. The photocatalysts are designed to utilize light energy to initiate the processes and also to maintain their uniqueness to perform its task more efficiently. However, in organic transformations involving metal nanoparticles aimed at remediation of the hazardous reagents and the AOPs involving metal oxide nanoparticles, the challenge lies in designing a catalyst with high efficiency and the ability to run for several cycles as the tiny nanoparticles are highly susceptible to agglomeration. A platform in the form of support is very important to prevent them from agglomerating and also immobilizing. In most cases, it is the solid support coupled with the method assigned for the fabrication of NPs that determines the size of the NPs and the catalytic activity. Several materials have been subjected as solid supports such as SiO₂, carbon nanofibers, graphene oxide, TiO₂, etc.^{1,88,1,89} The spherical vaterite particles, with a surface porous texture, seem to be a perfect candidate to perform the role of a solid-support for metal-based nanoparticles to be utilized in the above-mentioned remediation processes. However, the present literature suggests that they have not been explored much. Hence, one of the major objectives of this thesis is to utilize the potential of the vaterite particles as a solid-support for metal and metal-based nanoparticles.

Objectives of the thesis

In our efforts to study the biomineralization process, in this thesis we plan to utilize the tools provided by chemistry, as discussed earlier, to understand the process and to develop materials inspired by the biogenic process with enhanced properties to be utilized for different applications. The objectives of the thesis are presented in the following points:

- Additive directed synthesis of CaCO₃.
- To study the influence of external parameters.
- *In vitro* model system-based study of the mechanistic pathways of polymorph transformation.
- Tuning the mechanical properties of CaCO₃.

- Utilization of the biomineralized CaCO_3 as inert solid support and a precursor for the synthesis of materials with advanced functional properties.

References:

- 1.1. L. Addadi and S. Weiner, A Pavement of Pearl, *Nature*, 1997, **389**, 912–913.
- 1.2. M. D. Brasier, O. R. Green, A. P. Jephcoat, A. K. Kleppe, M. J. Van Kranendonk, J. F. Lindsay, A. Steele and N. V. Grassineau, Questioning the Evidence for Earth's Oldest Fossils, *Nature*, 2002, **416**, 76–81.
- 1.3. A.-W. Xu, Y. Ma and H. Cölfen, Biomimetic Mineralization, *J. Mater. Chem.*, 2007, **17**, 415–449.
- 1.4. H. A. Lowenstam and S. Weiner, *On Biomineralization*, Oxford University Press, 1989.
- 1.5. S. I. Stupp, G. C. Mejicano and J. A. Hanson, Organoapatites: Materials for Artificial Bone. II. Hardening Reactions and Properties, *J. Biomed. Mater. Res.*, 1993, **27**, 289–299.
- 1.6. M. Viani, T. E. Scha, J. B. Thompson, N. A. Frederick, J. Kindt and P. K. Hansma, *Molecular Mechanistic Origin of the Toughness of Natural Adhesive Fibers and Composites*, 1999, **399**, 761–763.
- 1.7. S. Mann, Synthesis of Barium Sulfate from Surfactant – Inorganic Nanoparticles REVIEWS The Chemistry of Form, *Angew. Chem. Int. Ed*, 2000, **39**, 3392–3406.
- 1.8. H. Du, U. Steiner and E. Amstad, Nacre-Inspired Hard and Tough Materials, *Chimia (Aarau)*, 2019, **73**, 29–34.
- 1.9. L. B. Gower, Biomimetic Model Systems for Investigating the Amorphous Precursor Pathway and Its Role in Biomineralization, *Chem. Rev.*, 2008, **108**, 4551–4627.
- 1.10. N. A. J. M. Sommerdijk and G. de With, Biomimetic CaCO_3 Mineralization Using Designer Molecules and Interfaces, *Chem. Rev.*, 2008, **108**, 4499–4550.
- 1.11. K. K. Sand, C. S. Pedersen, S. Sjöberg, J. W. Nielsen, E. Makovicky and S. L. S. Stipp, Biomineralization: Long-Term Effectiveness of Polysaccharides on the Growth and Dissolution of Calcite, *Cryst. Growth Des.*, 2014, **14**, 5486–5494.
- 1.12. J. W. Shen, C. Li, N. F. A. Van Der Vegt and C. Peter, Understanding the Control of Mineralization by Polyelectrolyte Additives: Simulation of Preferential Binding to Calcite Surfaces, *J. Phys. Chem. C*, 2013, **117**, 6904–6913.
- 1.13. B. T. Kato, Polymer / Calcium Carbonate Layered Thin-Film Composites, 2010, **12**, 1543–1546.
- 1.14. H. Du and E. Amstad, Water: How Does It Influence the CaCO_3 Formation?, *Angew.*

- Chemie - Int. Ed.*, 2020, **59**, 1798–1816.
- 1.15. L. B. Mao, H. L. Gao, H. Bin Yao, L. Liu, H. Cölfen, G. Liu, S. M. Chen, S. K. Li, Y. X. Yan, Y. Y. Liu and S. H. Yu, Synthetic Nacre by Predesigned Matrix-Directed Mineralization, *Science*, 2016, **354**, 107–110.
 - 1.16. X. R. Xu, A. H. Cai, R. Liu, H. H. Pan, R. K. Tang and K. Cho, The Roles of Water and Polyelectrolytes in the Phase Transformation of Amorphous Calcium Carbonate, *J. Cryst. Growth*, 2008, **310**, 3779–3787.
 - 1.17. D. B. Trushina, T. V. Bukreeva, M. V. Kovalchuk and M. N. Antipina, CaCO₃ Vaterite Microparticles for Biomedical and Personal Care Applications, *Mater. Sci. Eng. C*, 2014, **45**, 644–658.
 - 1.18. B. Cantaert, D. Kuo, S. Matsumura, T. Nishimura, T. Sakamoto and T. Kato, Use of Amorphous Calcium Carbonate for the Design of New Materials, *Chempluschem*, 2017, **82**, 107–120.
 - 1.19. H. Bahrom, A. A. Goncharenko, L. I. Fatkhutdinova, O. O. Peltek, A. R. Muslimov, O. Y. Koval, I. E. Eliseev, A. Manchev, D. Gorin, I. I. Shishkin, R. E. Noskov, A. S. Timin, P. Ginzburg and M. V. Zyuzin, Controllable Synthesis of Calcium Carbonate with Different Geometry: Comprehensive Analysis of Particle Formation, Cellular Uptake, and Biocompatibility, *ACS Sustain. Chem. Eng.*, 2019, **7**, 19142–19156.
 - 1.20. Y. Svenskaya, B. Parakhonskiy, A. Haase, V. Atkin, E. Lukyanets, D. Gorin and R. Antolini, Anticancer Drug Delivery System Based on Calcium Carbonate Particles Loaded with a Photosensitizer, *Biophys. Chem.*, 2013, **182**, 11–15.
 - 1.21. H. Yang, Y. Wang, T. Liang, Y. Deng, X. Qi, H. Jiang, Y. Wu and H. Gao, Hierarchical Porous Calcium Carbonate Microspheres as Drug Delivery Vector, *Prog. Nat. Sci. Mater. Int.*, 2017, **27**, 674–677.
 - 1.22. S. Mofakhami and E. Salahinejad, Biphasic Calcium Phosphate Microspheres in Biomedical Applications, *J. Control. Release*, 2021, **338**, 527–536.
 - 1.23. L. A. Estroff, Introduction : Biomineralization, *Chem. Rev.*, 2008, **108**, 10–12.
 - 1.24. J. W. Beck, R. L. Edwards, E. Ito, F. W. Taylor, J. Recy, F. Rougerie, P. Joannot and C. Henin, Sea-Surface Temperature from Coral Skeletal Strontium/Calcium Ratios, *Science*, 1992, **257**, 644–647.
 - 1.25. Z. Zou, W. J. E. M. Habraken, G. Matveeva, A. C. S. Jensen, L. Bertinetti, M. A. Hood, C.-Y. Sun, P. U. P. A. Gilbert, I. Polishchuk, B. Pokroy, J. Mahamid, Y. Politi, S. Weiner, P. Werner, S. Bette, R. Dinnebier, U. Kolb, E. Zolotoyabko and P. Fratzl, A Hydrated Crystalline Calcium Carbonate Phase: Calcium Carbonate Hemihydrate,

- Science*, 2019, **363**, 396–400.
- 1.26. N. H. De Leeuw and S. C. Parker, Surface Structure and Morphology of Calcium Carbonate Polymorphs Calcite, Aragonite, and Vaterite: An Atomistic Approach, *J. Phys. Chem. B*, 1998, **102**, 2914–2922.
 - 1.27. G. Wulff, Zur Frage Der Geschwindigkeit Des Wachstums Und Der Auflösung Der Krystallflächen, *Zeitschrift Für Krist., Cryst. Mater.*, 1901, **34**, 449–530.
 - 1.28. B. Dickens and W. E. Brown, The Crystal Structure of Calcium Carbonate Hexahydrate at $\sim -120^\circ$, *Inorg. Chem.*, 1970, **9**, 480–486.
 - 1.29. H. Effenberger, Kristallstruktur und Infrarot-Absorptionsspektrum von synthetischem Monohydrocalcit, $\text{CaCO}_3 \cdot \text{H}_2\text{O}$, *Monatshefte für Chem.*, 1981, **112**, 899.
 - 1.30. D. Gebauer, A. Völkel and H. Cölfen, Stable Prenucleation Calcium Carbonate Clusters, *Science*, 2008, **322**, 1819–1822.
 - 1.31. M. H. Nielsen, S. Aloni and J. J. De Yoreo, In Situ TEM Imaging of CaCO_3 Nucleation Reveals Coexistence of Direct and Indirect Pathways, *Science*, 2014, **345**, 1158–1162.
 - 1.32. F. Liendo, M. Arduino, F. A. Deorsola and S. Bensaid, Nucleation and Growth Kinetics of CaCO_3 Crystals in the Presence of Foreign Monovalent Ions, *J. Cryst. Growth*, 2022, **578**, 126406.
 - 1.33. H. Cölfen, Bio-Inspired Mineralization Using Hydrophilic Polymers, in *Biomaterialization II*, Springer Berlin Heidelberg, pp. 1–77.
 - 1.34. N. Spanos and P. G. Koutsoukos, Kinetics of Precipitation of Calcium Carbonate in Alkaline pH at Constant Supersaturation. Spontaneous and Seeded Growth, *J. Phys. Chem. B*, 1998, **102**, 6679–6684.
 - 1.35. A. E. Nielsen, Kinetics of Precipitation, *Oxford Pergamon Press*, 1964.
 - 1.36. X. Y. Liu and S. W. Lim, Templating and Supersaturation-Driven Anti-Templating: Principles of Biomineral Architecture, *J. Am. Chem. Soc.*, 2003, **125**, 888–895.
 - 1.37. A. M. Travaille, E. G. A. Steijven, H. Meekes and H. Van Kempen, Thermodynamics of Epitaxial Calcite Nucleation on Self-Assembled Monolayers, *J. Phys. Chem. B*, 2005, **109**, 5618–5626.
 - 1.38. P. C. Rieke, Application of Van Oss-Chaudhury-Good Theory of Wettability to Interpretation of Interfacial Free Energies of Heterogeneous Nucleation, *J. Cryst. Growth*, 1997, **182**, 472–484.
 - 1.39. D. Gebauer, How Can Additives Control the Early Stages of Mineralisation?, *Minerals*, 2018, **8**.
 - 1.40. P. Bots, L. G. Benning, J. D. Rodriguez-Blanco, T. Roncal-Herrero and S. Shaw,

- Mechanistic Insights into the Crystallization of Amorphous Calcium Carbonate (ACC), *Cryst. Growth Des.*, 2012, **12**, 3806–3814.
- 1.41. T. Ogino, T. Suzuki and K. Sawada, The Rate and Mechanism of Polymorphic Transformation of Calcium Carbonate in Water, *J. Cryst. Growth*, 1990, **100**, 159–167.
 - 1.42. S. R. Dickinson, G. E. Henderson and K. M. McGrath, Controlling the Kinetic versus Thermodynamic Crystallisation of Calcium Carbonate, *J. Cryst. Growth*, 2002, **244**, 369–378.
 - 1.43. S. Weiner and W. Traub, Macromolecules in Mollusc Shells and Their Functions in Biomineralization., *Philos. Trans. R. Soc. London, Ser. B*, 1984, **304**, 425–434.
 - 1.44. E. Weber and B. Pokroy, Intracrystalline Inclusions within Single Crystalline Hosts: From Biomineralization to Bio-Inspired Crystal Growth, *CrystEngComm*, 2015, **17**, 5873–5883.
 - 1.45. N. Watabe, Studies on Shell Formation, *J. Ultrastruct. Res.*, 1965, **12**, 351–370.
 - 1.46. F. C. Meldrum and S. T. Hyde, Morphological Influence of Magnesium and Organic Additives on the Precipitation of Calcite, *J. Cryst. Growth*, 2001, **231**, 544–558.
 - 1.47. H. H. Teng, P. M. Dove, C. A. Orme and J. J. De Yoreo, *Thermodynamics of Calcite Growth: Baseline for Understanding Biomineral Formation*, *Science*, 1998, **282**, 724–727.
 - 1.48. Y.-Y. Kim, C. L. Freeman, X. Gong, M. A. Levenstein, Y. Wang, A. Kulak, C. Anduix-Canto, P. A. Lee, S. Li, L. Chen, H. K. Christenson and F. C. Meldrum, The Effect of Additives on the Early Stages of Growth of Calcite Single Crystals, *Angew. Chemie*, 2017, **129**, 12047–12052.
 - 1.49. H. Y. Kim, T. Yang, W. Huh, Y. Kwark, Y. Lee and I. W. Kim, The Combined Effects of Sr (II) and Poly (Acrylic Acid) on the Morphology of Calcite, *Materials*, 2019, **12**, 1–8.
 - 1.50. X. Liu, K. Li, C. Wu, Z. Li, B. Wu, X. Duan, Y. Zhou and C. Pei, Influence of Copper (II) on Biomineralization of CaCO₃ and Preparation of Micron Pearl-like Biomimetic CaCO₃, *Ceram. Int.*, 2019, **45**, 14354–14359.
 - 1.51. H. Du, C. Courrégelongue, J. Xto, A. Böhlen, M. Steinacher, C. N. Borca, T. Huthwelker and E. Amstad, Additives: Their Influence on the Humidity- And Pressure-Induced Crystallization of Amorphous CaCO₃, *Chem. Mater.*, 2020, **32**, 4282–4291.
 - 1.52. R. Stepić, L. Jurković, K. Klementyeva, M. Ukrainczyk, M. Gredičak, D. M. Smith, D. Kralj and A. S. Smith, Adsorption of Aspartate Derivatives to Calcite Surfaces in Aqueous Environment, *Cryst. Growth Des.*, 2020, **20**, 2853–2859.

- 1.53. N. Wada, N. Horiuchi, M. Nakamura, K. Nozaki, A. Nagai and K. Yamashita, Calcite Crystallization on Polarized Single Calcite Crystal Substrates in the Presence of Poly-Lysine, *Cryst. Growth Des.*, 2018, **18**, 872–878.
- 1.54. G. Zhu, S. Yao, H. Zhai, Z. Liu, Y. Li, H. Pan and R. Tang, Evolution from Classical to Non-Classical Aggregation-Based Crystal Growth of Calcite by Organic Additive Control, *Langmuir*, 2016, **32**, 8999–9004.
- 1.55. R. Sun, T. Willhammar, E. Svensson Grape, M. Strømme and O. Cheung, Mesoscale Transformation of Amorphous Calcium Carbonate to Porous Vaterite Microparticles with Morphology Control, *Cryst. Growth Des.*, 2019, **19**, 5075–5087.
- 1.56. B. Marzec, D. C. Green, M. A. Holden, A. S. Coté, J. Ihli, S. Khalid, A. Kulak, D. Walker, C. Tang, D. M. Duffy, Y. Y. Kim and F. C. Meldrum, Amino Acid Assisted Incorporation of Dye Molecules within Calcite Crystals, *Angew. Chemie - Int. Ed.*, 2018, **57**, 8623–8628.
- 1.57. Y. Y. Kim, M. Semsarilar, J. D. Carloni, K. R. Cho, A. N. Kulak, I. Polishchuk, C. T. Hendley, P. J. M. Smeets, L. A. Fielding, B. Pokroy, C. C. Tang, L. A. Estroff, S. P. Baker, S. P. Armes and F. C. Meldrum, Structure and Properties of Nanocomposites Formed by the Occlusion of Block Copolymer Worms and Vesicles Within Calcite Crystals, *Adv. Funct. Mater.*, 2016, **26**, 1382–1392.
- 1.58. Y. Y. Kim, L. A. Fielding, A. N. Kulak, O. Nahi, W. Mercer, E. R. Jones, S. P. Armes and F. C. Meldrum, Influence of the Structure of Block Copolymer Nanoparticles on the Growth of Calcium Carbonate, *Chem. Mater.*, 2018, **30**, 7091–7099.
- 1.59. J. Wang, J. Song, Z. Ji, J. Liu, X. Guo, Y. Zhao and J. Yuan, *The Preparation of Calcium Carbonate with Different Morphologies under the Effect of Alkanolamide 6502*, *Colloids Surfaces A Physicochem. Eng. Asp.*, 2020, **588**, 124392.
- 1.60. Z. Zou, L. Bertinetti, Y. Politi, P. Fratzl and W. J. E. M. Habraken, Control of Polymorph Selection in Amorphous Calcium Carbonate Crystallization by Poly(Aspartic Acid): Two Different Mechanisms, *Small*, 2017, **13**, 1–11.
- 1.61. J. H. Van der Merwe, Misfit Dislocations in Epitaxy, *Metall. Mater. Trans. A Phys. Metall. Mater. Sci.*, 2002, **33**, 2475–2483.
- 1.62. D. M. Duffy, A. M. Travaille, H. Van Kempen and J. H. Harding, Effect of Bicarbonate Ions on the Crystallization of Calcite on Self-Assembled Monolayers, *J. Phys. Chem. B*, 2005, **109**, 5713–5718.
- 1.63. S. J. Cooper, R. B. Sessions and S. D. Lubetkin, Role of Interfacial Tension in Nucleation beneath Monolayer Films, *Langmuir*, 1997, **13**, 7165–7172.

- 1.64. H. Tong, W. Ma, L. Wang, P. Wan, J. Hu and L. Cao, Control over the Crystal Phase, Shape, Size and Aggregation of Calcium Carbonate via a L-Aspartic Acid Inducing Process, *Biomaterials*, 2004, **25**, 3923–3929.
- 1.65. W. Hou and Q. Feng, Morphology and Formation Mechanism of Vaterite Particles Grown in Glycine-Containing Aqueous Solutions, *Mater. Sci. Eng. C*, 2006, **26**, 644–647.
- 1.66. B. Kanoje, D. Patel and K. Kuperkar, Morphology Modification in Freshly Precipitated Calcium Carbonate Particles Using Surfactant-Polymer Template, *Mater. Lett.*, 2017, **187**, 44–48.
- 1.67. M. R. Abeywardena, R. K. W. H. M. K. Elkaduwe, D. G. G. P. Karunarathne, H. M. T. G. A. Pitawala, R. M. G. Rajapakse, A. Manipura and M. M. M. G. P. G. Mantilaka, *Surfactant Assisted Synthesis of Precipitated Calcium Carbonate Nanoparticles Using Dolomite: Effect of PH on Morphology and Particle Size*, *Adv. Powder Technol.*, 2020, **31**, 269–278.
- 1.68. I. Rianasari, F. Benyettou, S. K. Sharma, T. Blanton, S. Kirmizialtin and R. Jagannathan, A Chemical Template for Synthesis of Molecular Sheets of Calcium Carbonate, *Sci. Rep.*, 2016, **6**, 1–10.
- 1.69. J. A. Lopez-Berganza and R. M. Espinosa-Marzal, Mechanistic Approach to Predict the Combined Effects of Additives and Surface Templates on Calcium Carbonate Mineralization, *Cryst. Growth Des.*, 2016, **16**, 6186–6198.
- 1.70. Y. Wei, H. Xu, S. Xu, H. Su, R. Sun, D. Huang, L. Zhao, Y. Hu, K. Wang and X. Lian, Synthesis and Characterization of Calcium Carbonate on Three Kinds of Microbial Cells Templates, *J. Cryst. Growth*, 2020, **547**, 125755.
- 1.71. F. C. Meldrum and H. Cölfen, Controlling Mineral Morphologies and Structures in Biological and Synthetic Systems, *Chem. Rev.*, 2008, **108**, 4332–4432.
- 1.72. S. Weiner, L. Addadi and H. D. Wagner, Materials Design in Biology, *Mater. Sci. Eng. C*, 2000, **11**, 1–8.
- 1.73. M. A. Meyers, P. Y. Chen, A. Y. M. Lin and Y. Seki, Biological Materials: Structure and Mechanical Properties, *Prog. Mater. Sci.*, 2008, **53**, 1–206.
- 1.74. S. Kamat, X. Su, R. Ballarini and A. H. Heuer, Structural basis for the fracture toughness of the shell of the conch *Strombus gigas*, *Nature*, 2000, **405**, 1036.
- 1.75. J. Aizenberg, J. C. Weaver, M. S. Thanawala, V. C. Sundar, D. E. Morse and P. Fratzl, Materials Science: Skeleton of *Euplectella* Sp.: Structural Hierarchy from the Nanoscale to the Macroscale, *Science*, 2005, **309**, 275–278.

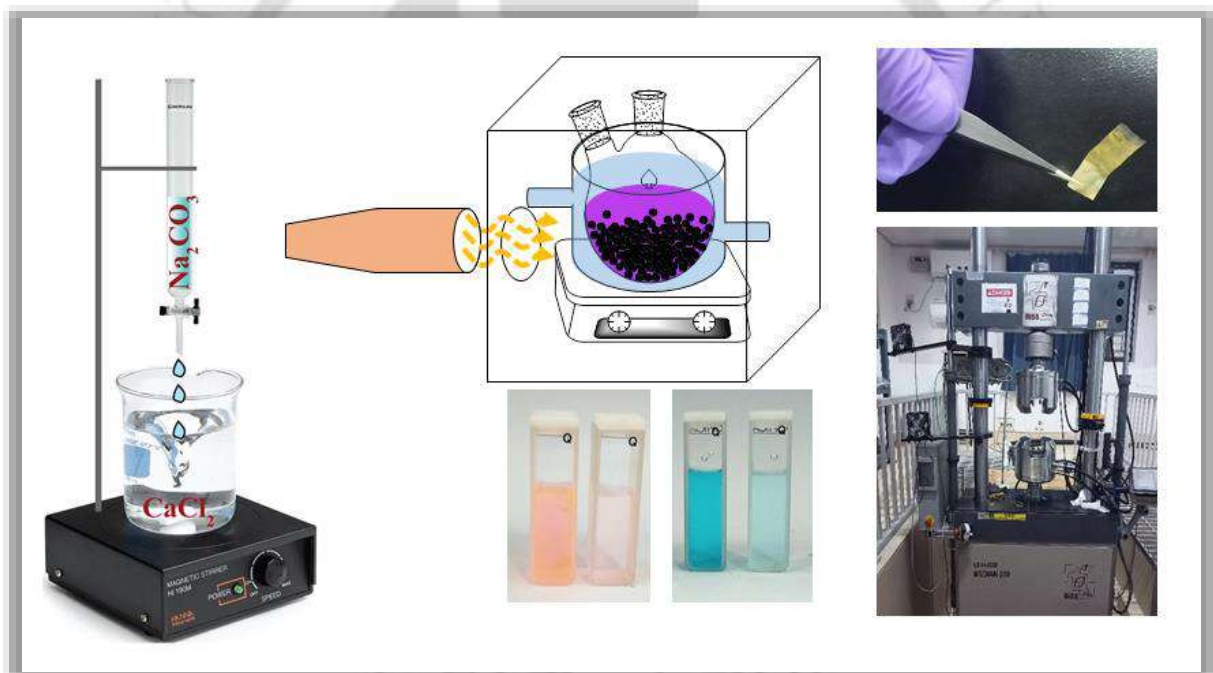
- 1.76. S. Weiner and L. Addadi, Design Strategies in Mineralized Biological Materials, *J. Mater. Chem.*, 1997, **7**, 689–702.
- 1.77. A. Berman, J. Hanson, L. Leiserowitz, T. F. Koetzle, S. Weiner and L. Addadi, Biological Control of Crystal Texture: A Widespread Strategy for Adapting Crystal Properties to Function, *Science*, 1993, **259**, 776–779.
- 1.78. M. E. Kunitake, L. M. Mangano, J. M. Peloquin, S. P. Baker and L. A. Estroff, Evaluation of Strengthening Mechanisms in Calcite Single Crystals from Mollusk Shells, *Acta Biomater.*, 2013, **9**, 5353–5359.
- 1.79. Y. Y. Kim, L. Ribeiro, F. Maillot, O. Ward, S. J. Eichhorn and F. C. Meldrum, Bio-Inspired Synthesis and Mechanical Properties of Calcite-Polymer Particle Composites, *Adv. Mater.*, 2010, **22**, 2082–2086.
- 1.80. Y. Y. Kim, J. D. Carloni, B. Demarchi, D. Sparks, D. G. Reid, M. E. Kunitake, C. C. Tang, M. J. Duer, C. L. Freeman, B. Pokroy, K. Penkman, J. H. Harding, L. A. Estroff, S. P. Baker and F. C. Meldrum, Tuning Hardness in Calcite by Incorporation of Amino Acids, *Nat. Mater.*, 2016, **15**, 903–910.
- 1.81. V.K. Saharan, M.P. Badve and A.B. Pandit, Degradation of reactive red 120 dye using hydrodynamic cavitation, *Chem. Eng. J.*, 2011, **178**, 100–107.
- 1.82. U.G. Akpan and B.H. Hameed, Parameters affecting the photocatalytic degradation of dyes using TiO₂-based photocatalysts: a review, *J. Hazard. Mater.*, 2009, **170**, 520–529.
- 1.83. Z.Z. Vasiljevic, M.P. Dojcinovic, J.D. Vujancevic, I. Jankovic-Castvan, M. Ognjanovic, N.B. Tadic, S. Stojadinovic, G.O. Brankovic and M. V. Nikolic, Photocatalytic degradation of methylene blue under natural sunlight using iron titanate nanoparticles prepared by a modified sol–gel method, *R. Soc. Open Sci.*, 2020, **7**, 200708.
- 1.84. P. Dey and R. Das, Enhanced photocatalytic degradation of methyl orange dye on interaction with synthesized ligand free CdS nanocrystals under visible light illumination, *Spectrochim. Acta A*, 2020, **231**, 118122.
- 1.85. M.N. Ghazzala, H. Kebaili and M. Joseph, Photocatalytic degradation of Rhodamine 6G on mesoporous titania films: combined effect of texture and dye aggregation forms, *Appl. Catal. B Env.*, 2012, **115**, 276–284.
- 1.86. B. Lellis, C.Z. Fávoro-Polonio, J.A. Pamphile and J.C. Polonio, Effects of textile dyes on health and the environment and bioremediation potential of living organisms, *Biotechnol. Res. Innov.*, 2019, **3**, 275–290.
- 1.87. E. Kusiak-Nejman and A.W. Morawski, TiO₂/graphene-based nanocomposites for water treatment: a brief overview of charge carrier transfer, antimicrobial and photocatalytic

- performance, *Appl. Catal. B: Environ.*, 2019, **253**, 179–186.
- 1.88. P. Zhang, C. Shao, Z. Zhang, M. Zhang, J. Mu, Z. Guo and Y. Liu, In situ assembly of well-dispersed Ag nanoparticles (AgNPs) on electrospun carbon nanofibers (CNFs) for catalytic reduction of 4-nitrophenol, *Nanoscale*, 2011, **3**, 3357–3363.
- 1.89. M. Wang, D. Tian, P. Tian, L. Yuan, Synthesis of micron-SiO₂@nano-Ag particles and their catalytic performance in 4-nitrophenol reduction, *Appl. Surf. Sci.*, 2013, **283**, 389–395.





Experimental Details and Characterization



This chapter provides comprehensive information about the materials and different methodologies adopted for the synthesis and characterization of the biominerals and their composites followed by their subsequent applications. Specification of analytical instruments used along with different experimental conditions adopted in the study of the materials and their applications are elaborately discussed.

2.1 Materials and Instruments

All of the reagents and solvents were available from commercial suppliers and used hereafter without further purification. $\text{CaCl}_2 \cdot 2\text{H}_2\text{O}$ (Emplura), Na_2CO_3 anhydrous (Emplura), CaCO_3 (Emsure) and $\text{Ca}(\text{OH})_2$ (Emparta), NaOH pellets (Emsure), ammonia solution (about 30% GR), $\text{FeSO}_4 \cdot 7\text{H}_2\text{O}$ (Emsure), $\text{Fe}(\text{NO}_3)_3 \cdot 9\text{H}_2\text{O}$ (Emsure) and sodium lauryl sulphate were purchased from Merck. $\text{Mn}(\text{OH})_2$ (purity 99%) was purchased from Nanoshel. Whey protein isolate was purchased from Glanbia Nutritionals (Provon 292). α -lactalbumin, β -lactoglobulin, serum albumin, curcumin (purity $\geq 99\%$) and quercetin (purity $\geq 99\%$), silver nitrate (purity $\geq 99\%$), α -D-Glucose, 4-Nitrophenol (purity $\geq 99\%$) and 2-Nitrophenol (purity $\geq 98\%$), triethylamine (purity $\geq 99.5\%$), sodium azide (purity $\geq 99.5\%$), tert Butanol (purity $\geq 99\%$), p-Benzoquinone (purity $\geq 98\%$), potassium oxalate monohydrate (purity $\geq 98\%$) were purchased from Sigma Aldrich. The dyes Rh 6G (purity $\geq 99\%$), MB (purity $\geq 97\%$), MO (ACS reagent) and Rh B (purity $\geq 95\%$) were purchased from Sigma-Aldrich.

The samples synthesized were characterized by a number of spectroscopic and microscopic techniques. The techniques used were; *Fourier Transform-Infrared spectroscopy* (FT-IR) in Perkin Elmer-Spectrum One FT-IR spectrometer; *Powder X-Ray Diffraction* (PXRD) and the quantitative analysis results in Rigaku Smartlab X-ray Spectrophotometer with $\text{Cu-K}\alpha$ ($\lambda=1.54 \text{ \AA}$), source running at a power of 9 kW; *Field Emission Scanning Electron Microscope* (FESEM) in Sigma 300 FESEM (Carl Zeiss); *Dynamic Light Scattering* (DLS) in Anton Paar Litesizer 500 instrument, Circular Dichroism (CD) in JASCO J-1500 spectropolarimeter (Jasco Analytical Instruments, Easton, US); Thermogravimetric Analysis/Derivative Thermogravimetry (TGA/DTG) in Netzsch, STA449F3A00; Energy Dispersive X-Ray Spectroscopy (EDX) element analysis and EDX mapping in Sigma (Zeiss); Solid-state Nuclear Magnetic Resonance (ssNMR) in a JEOL-400 spectrometer at 100.61 MHz for ^{13}C NMR; Universal Testing Machine (UTM) in BISS Median 250; Atomic Absorption Spectroscopy (AAS) in Varian AA240, Field Emission Transmission Electron Microscope (FETEM), High Resolution TEM (HRTEM) and EDX mapping analysis were performed in JEOL 2100F;

Brunauer–Emmett–Teller (BET) surface area analysis was performed in Quantachrome Quadrasorb evo surface area analyzer; X-ray Photoelectron Spectroscopy (XPS) in ESCALAB Xi+(Thermo Fisher Scientific Pvt. Ltd., UK); Vibrating-Sample Magnetometer (VSM) in Lakeshore (7410 series); Ultraviolet-vis diffuse reflectance spectra (DRS) in Perkin-Elmer Lambda 750 UV/Vis Spectrophotometer. Absorption measurements in the different experiments were carried out on a Perkin-Elmer Lambda-750 UV-Vis Spectrophotometer.

2.2 Experimental methods and characterization

2.2.1 Synthesis of CaCO_3 in the presence of whey protein

To a 20 ml solution of whey protein (2.5 mg/ml, pH =7), 20 ml of 0.25 M of CaCl_2 solution was added. Both the solutions were prepared in Millipore water. The concentration of whey protein was maintained as such in all other experiments unless otherwise stated. The resulting solution was slowly stirred for 5 minutes before the dropwise addition of the 0.25 M Na_2CO_3 solution (20 ml, Millipore water) was started under slow but continuous stirring conditions at 100 r.p.m. The frequency of addition was maintained at 4 drops/minute. Once the supersaturation state had reached, the precipitation of CaCO_3 was observed. After the addition was complete, the resulting solution was filtered using regular filter paper. The residue was washed several times with deionized water. It was then allowed to dry under normal conditions at room temperature for 24 hours. The dried CaCO_3 was then collected and subjected to investigation such as FT-IR, PXRD, FESEM, and DLS measurements. The filtrate obtained was preserved and subjected to another cycle. As a control, CaCO_3 was synthesized without the addition of whey protein, keeping all the parameters as same.

Keeping all the conditions the same, the precipitation was performed in the presence of the individual components of whey protein; α -lactalbumin, β -lactoglobulin and serum albumin. The study was further subjected to several variations in conditions followed by the characterization of the CaCO_3 particles thus obtained:

The concentration of whey protein: The formation of CaCO_3 was studied at two different concentrations of whey protein: 30 mg (1.5 mg/ml) and 50 mg (2.5 mg/ml).

Reverse addition: Na_2CO_3 was first allowed to interact with whey protein, followed by the dropwise addition of CaCl_2 to the mixture.

Temperature: The process was carried out at three different temperatures: room temperature 25 °C, 60 °C and 10 °C, maintaining all other conditions the same.

pH: The experiments were performed at pH 7, 5 and 4, keeping all other conditions the same.

Ionic Strength: Two different sets were performed; in the absence of any electrolytes and in the presence of 100 mM NaCl.

Characterization methods

The FT-IR spectra of the dried compounds were recorded with KBr pellets in the range 1100–400 cm^{-1} , this was followed by the PXRD and the quantitative analysis of the samples. The particle sizes and zeta potential were measured by DLS experiments at pH 7.4 and temperature 25 °C. The morphology of the species was investigated by using FESEM imaging studies by the drop (1 mM/ 2 μl) cast method on glass plates covered with Al-foil. CD spectra of whey protein were obtained for the initial solution (2.5 mg/ml) and the filtrate after the first and the second cycle of the *in vitro* biomineralization. The solutions were prepared by drawing 20 μl of whey protein solution from the initial solution (2.5 mg/ml) and diluting it to 2 ml. The pH of the solution was 7. Similarly, for the 2nd and the 3rd cycles, the whey protein (20 μl) was taken from the respective filtrates obtained and diluted to 2 ml. A quartz cell of path length 10 mm was used for measurement. The spectra were obtained in the wavelength range of 195-260 nm.

2.2.2 Synthesis of CaCO_3 in the presence of the additives curcumin and quercetin

The concentration of curcumin was maintained at 3 mM in a 10 ml solution of 0.25 M CaCl_2 in Millipore water (curcumin was dissolved in a small amount of acetone). The solution was slowly stirred for 5 minutes in order to facilitate the interaction between the Ca^{2+} and binding centres of curcumin. This was followed by the dropwise addition of 0.25 M Na_2CO_3 solution (10 ml, Millipore water) under continuous stirring conditions at 100 r.p.m (4 drops/min). The solution was subjected to stirring in order to maintain the uniformity in the interaction between the additive bound Ca^{2+} and the incoming carbonate anions. On completion of the addition, the resulting solution was filtered through regular filter paper. The residue was washed several times with Millipore water followed by acetone to remove curcumin. The CaCO_3 particles were dried at room temperature for 48 hours. Similarly, for the experiments using *quercetin*, the concentration of quercetin in solution was maintained at 3 mM and all other conditions and procedures were kept the same. CaCO_3 in the dried state was then collected and assigned for characterization such as FT-IR, PXRD, FESEM, and DLS measurements. The biomineralization process was studied by varying certain parameters. Initially, the concentration of curcumin and quercetin was doubled to 6 mM to understand the role of additive concentration and the rest of the procedure remained the same. The effect of the reverse sequence of addition of the ions in

the mineralization was also studied. Na_2CO_3 was first allowed to interact with the additive, followed by the dropwise addition of CaCl_2 to the mixture. Then, the *in vitro* biomineralization process was carried out at different temperatures; 10 °C, 25 °C and 80 °C to study the effect of temperature. Also, two different sets of experiments were performed, one in the absence of any electrolytes and the other in the presence of 100 mM NaCl to understand the role of ionic strength in the mineralization process.

Characterization methods

The FT-IR spectra of the compounds were obtained with the assistance of KBr pellets in the range 4000–400 cm^{-1} , followed by the PXRD and quantitative analysis of the samples. The particle sizes and zeta potential were measured by DLS experiments at pH 7.4 and temperature 25 °C. The morphology of the aggregated species was investigated by using FESEM imaging studies by the drop (1 mM/ 2 μl) cast method on glass plates covered with Al-foil.

2.2.3 Tulsi and Green tea extracts as additives

2.2.3.1 Preparation of the leaf extracts

The leaf extracts were prepared by following an efficient method already available in the literature.^{2.1,2.2}

Preparation of Tulsi extract in methanol and water

Fresh leaves were collected in their blooming stage from several spots at IIT Guwahati campus. The leaves were thoroughly washed with water so as to remove the external impurities and dried at room temperature for 48 hours. The dried leaves were then powdered, and in each extraction process, 2 grams of the dried powder was subjected to reflux in 50 ml of methanol and water, respectively. The extracts were then collected by filtering through regular filter paper.

Preparation of Green tea extract in methanol and water

Green tea in its purest form and of the finest quality was obtained from the local tea gardens of Assam. The powdered leaves, 3 grams, were subjected to reflux as such in 50 ml of methanol and water, respectively, followed by filtration through regular filter paper to obtain the pure extracts.

2.2.3.2 In vitro crystallization of CaCO₃ in the presence of leaf extracts

In each experiment, 5 ml of the extracts (tulsi or green tea in methanol/water) were used as additives. In a 10 ml solution of 0.25 M CaCl₂ (in Millipore water), 5 ml of the extract was added, and the solution was slowly stirred for 15 minutes to allow the interaction between the additive molecules and Ca²⁺, following which, Na₂CO₃ (0.25 M in 10 ml Millipore water) was added to the solution in a dropwise manner (4 drops/minute), maintaining continuous stirring at 100 r.p.m. It was observed that on super-saturation, the precipitate has started to fall, and on complete addition of the Na₂CO₃ solution, the resulting suspension was filtered through a regular filter paper. The residue was washed several times with water and methanol and allowed to dry at room temperature for 48 hours.

Reusability of tulsi extract in methanol and the effectiveness of the mixture of tulsi and green tea extracts in methanol

In the reusability experiment, the crystallization process using tulsi extract in methanol was studied to observe whether the additive retains its effectiveness even after several cycles. In this experiment, the filtrate that was obtained on filtering the suspension after the crystallization process was used to perform its role for the next cycle; all other steps in the procedure were kept the same. A total of three cycles were performed to study the effects of reusing the extract. In another experiment, both the tulsi and the green tea extracts in methanol were mixed in a ratio of 1:1 (2.5 ml each). They were used as additives in the crystallization process to observe their role in a mixture.

2.2.3.3 The reverse sequence of addition

As an extension of this work, the methanol extracts of tulsi and green tea were used to study the phase transformation of CaCO₃ w.r.t the *in vitro* crystallization. Here, the sequence of addition was reversed such that the CO₃²⁻ ions (Na₂CO₃) were allowed to interact with the extract followed by the addition of Ca²⁺ ions (CaCl₂).

Characterization methods

The synthesized particles were initially characterized by FT-IR spectroscopy to determine the phase, where the spectra of the dried compounds were recorded in the range 1800–400 cm⁻¹. This was followed by the PXRD analysis. The morphology of the particles was obtained from the FESEM imaging technique. TGA/DTG were performed in the range of 25-800 °C in increments of 10 °C/min to justify the formation of the hydrated and anhydrous phases. EDX

element analysis and EDX mapping were performed for the monohydrocalcite phase to prove the presence of Mg along with the other elements of CaCO_3 . The hydrodynamic diameter and zeta potential of the particles were measured by DLS experiments at pH 7 and temperature 20 °C.

2.2.4 Mechanical Strength of CaCO_3 composites

2.2.4.1 Synthesis of CaCO_3 in the presence of the additives quercetin and hesperidin

The composites were synthesized by varying the concentration of the additives, quercetin and hesperidin, as 1 mM, 2 mM, 3 mM and 4 mM. In each precipitation experiment, the concentration of $\text{CaCl}_2 \cdot 2\text{H}_2\text{O}$ was taken as 0.20 M (10 ml in Millipore water) and to it, the additive (dissolved in a small amount of MeOH) was added. The solution was gently stirred for 10 mins, after which the dropwise addition of 0.20 M Na_2CO_3 (10 ml in Millipore water) was started under controlled stirring conditions at 150 r.p.m. The number of drops was maintained at 3 drops/min. Once the addition was complete, the resulting colloidal solution was filtered and washed, initially with methanol to remove any excess amount of organic additive, followed by water (several times). The composite particles were thus obtained as the residue was dried at room temperature for 24 hours before subjecting them to characterizations. As a control, CaCO_3 without any additive was precipitated, all the steps were maintained the same except for the addition of the additives.

Characterization methods

The FT-IR spectra of the dried compounds were recorded in the range 1100–400 cm^{-1} . The PXRD and the quantitative analysis results of the samples were obtained to determine the polymorph. The morphology of the particles (powdered composite) and the films were investigated by using FESEM imaging studies. Solid-state NMR experiments of the composite materials were carried out at room temperature (298 K) using a 4 mm MAS probe. The ^{13}C NMR spectra were recorded using the single pulse at a spinning speed of 10 kHz. The TGA analyses were performed in the range of 25–800 °C with increments of 10 °C/min. XPS analyses were performed to determine the influence of the incorporated flavonoid molecules on the composite.

2.2.4.2 Fabrication of gelatin films

The casting technique was followed to fabricate thin gelatin films.^{2,3} For this purpose, 2 g gelatin powder (Sigma, U.S.A.) was mixed with 100 ml of deionized water at 60 °C under vigorous stirring until completely dissolved. 1.5 ml of 2 % (w/v) gelatin solution was then thoroughly mixed with 2 mg of various additive powders (CaCO₃ composites) in 2 ml micro-centrifuge tubes maintaining the temperature at 60 °C that avoided the sol-gel transition of gelatin. Thereafter, the mixed gelatin solution was poured on top of the polydimethylsiloxane (PDMS) (Dow Corning Corporation, Midland, MI U.S.A.) molds (4 cm x 4 cm) and spreaded uniformly. The casted gelatin solution was then allowed to dry overnight at room temperature (RT 25 °C). The gelatin solution without any additive was used to fabricate control films. The dried films were then peeled off the PDMS molds and investigated for mechanical testing. The images of all the fabricated films, the control and the ones with the incorporated CaCO₃ composites are shown in **Fig. 2.1**.

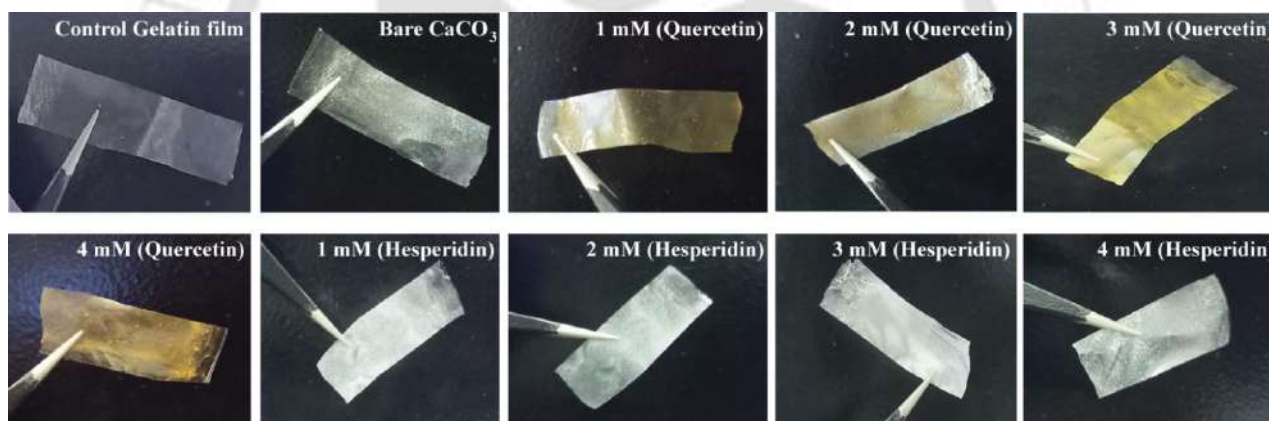


Figure 2.1: Images of all the fabricated films.

2.2.4.3 Mechanical testing

Tensile mechanical properties of gelatin films were tested using UTM equipped with a 100 N load cell and examined at a crosshead speed of 1 mm.min⁻¹. Films (4 cm long and 1 cm wide) were used to determine the maximum tensile stress and elongation at break. The gauge length between two clamps was set at 3 cm.^{2,4} The maximum tensile stress and elongation at break of the films were calculated from the obtained stress-strain curve.

2.2.5 Ag NPs/Vaterite catalyst for reduction of 4-Nitrophenol

2.2.5.1 Synthesis of Ag NPs/Vaterite catalyst

The vaterite particles were first synthesized in the presence of whey protein as the additive, the procedure presented elaborately in *section 2.2.1*. The loading of Ag NPs on the spherical vaterite particles was done using a modified Tollens reaction.^{2.5,2.6} In this method, 20 mg of the biomineralized vaterite particles was added to a solution of 25 mL AgNO₃ (1×10^{-3} mol L⁻¹) and 25 mL (5.10×10^{-3} mol L⁻¹) NH₄OH. The solution was maintained at a pH of 11.5 using NaOH. The solution was incubated with shaking at 120 rpm for 1h at 30 °C. This was followed by the addition of 10 mL of α -D-Glucose (1×10^{-2} mol L⁻¹). The solution was again shaken for 15 minutes. The resulting solution was centrifuged for 1 minute at 4000 rpm and washed three times with deionized water to separate the Ag NPs/Vaterite from any unreacted species. The supernatant was collected for AAS to precisely determine the amount of Ag deposited on the vaterite surface. The resulting Ag NPs embedded vaterite particles were dried at room temperature. Four different experiments were performed by changing the concentration of AgNO₃ and keeping the amount of vaterite constant. This was done to determine the extent of Ag NPs loaded on a constant amount of vaterite. From the AAS experiments, it was observed that the weight percentage (wt. %) of Ag NPs on Ag NPs/Vaterite increased significantly up to 1×10^{-3} mol L⁻¹ (concentration of AgNO₃) after which the wt. % remained more or less the same. Hence the concentration of AgNO₃ for all the synthesis of Ag NPs/Vaterite throughout this work was fixed at 1×10^{-3} mol L⁻¹.

Characterization methods

The biomineralized vaterite microspheres were subjected to the PXRD technique to confirm the crystalline phase. The morphology of the species was investigated by using FESEM imaging study by the drop (1 mM/ 2 μ l) cast method on glass plates covered with Al-foil. For the Ag NPs/Vaterite catalyst, the crystal phase was determined using the PXRD technique. The morphology after the fabrication of Ag NPs was studied using FESEM, following the same procedure as mentioned above and compared with that of the bare vaterite particles and the bare Ag NPs. The structure, size and extent of loading of the Ag NPs on vaterite were studied in detail by the FETEM. Under this, various techniques such as FETEM images, HRTEM and EDS mapping were adopted to provide a clear picture of the fabrication. EDX element analysis was performed to confirm the presence and the extent of Ag NPs on the nanocomposite. TGA analysis was performed to study the structural weight loss with respect to the components of the

nanocomposite. The surface area of the biomineralized vaterite particles before and after the fabrication of Ag NPs was obtained and compared using the BET specific surface area technique. The percentage of Ag NPs loaded on vaterite was determined quantitatively by the AAS analysis.

2.2.5.2 Catalytic reduction of 4-NP

The experiment to determine the catalytic activity of Ag NPs/Vaterite on the reduction of 4-NP to 4-AP in the presence of an excess of NaBH₄ was performed in a standard quartz cuvette at room temperature. The catalytic activity of the catalyst and simultaneous reduction of 4-NP was monitored by a UV-Vis spectrophotometer. 1 µl of 4-NP was introduced into the quartz cuvette from a stock solution of 4-NP of strength 0.2 M and 100 µl of NaBH₄ from a stock solution of strength 0.2 M. The solution in the quartz cuvette was filled to 1 ml with deionized water such that the strength of 4-NP and NaBH₄ in the final solution to be studied for the catalytic activity was 0.2 mM and 20 mM respectively. Hence all the standard experiments were performed with 1 mg of the catalyst. 1 mg of the Ag NPs/Vaterite was added to the solution in the quartz cuvette and the UV-Vis spectra were recorded immediately (time, t= 0 min), followed by 1 minute intervals in the scanning range of 275-500 nm. Subsequently, an equal amount of 4-NP (1 µl) was added to observe the catalytic activity in the second cycle and so on for five cycles. Since the volume of 4-NP is negligible as compared to the volume of the solution and NaBH₄ was added in large excess, the concentration of 4-NP with respect to that of NaBH₄ is considered unchanged for all five cycles. The optimization experiments were performed to determine the amount of nanocomposite that was to be used for maximum efficiency of the catalyst. Three different amounts of the catalyst, 0.5 mg, 1 mg and 1.5 mg were studied and eventually, it was observed that the best catalytic activity was attained in the case where 1 mg of the nanocomposite catalyst was used. Absorption measurements were carried out using 10 mm path length quartz cuvettes in the wavelength range of 250-500 nm.

2.2.6 Vaterite and Calcite based Magnetite composites

2.2.6.1 Synthesis of Fe₃O₄ nanoparticles

10 ml each of 0.1 M FeSO₄ and Fe(NO₃)₃ solution were mixed and stirred for 30 mins in a round bottom flask.^{2,7} A 10 ml of 3 mM sodium lauryl sulphate, used as the nanoparticle stabilizer, was added to the mixture and stirred for another 30 mins. This was followed by the dropwise addition of Triethylamine under vigorous stirring. The pH of the solution was maintained at ~2.0 to 3.0 before the addition of the base. The resulting dark brown mixture was kept under

continuous stirring for another 2 hours, after which the mixture turned into a complete black suspension. The black suspension was collected after centrifugation at 10000 rpm for 10 mins. The black-colored mass was then resuspended by sonication in a mixture of water and methanol and washed several times for the removal of impurities and the excess base. Finally, the product obtained was dried overnight under vacuum conditions and subjected to characterization and further experiments.

2.2.6.2 Synthesis of Fe_3O_4 /Vaterite nanoparticles

Here, we adopted a method previously reported by us along the lines of additive assisted synthesis of $CaCO_3$, where we could successfully isolate the vaterite phase.^{2,8} In a 10 ml solution of 0.1 M $CaCl_2 \cdot 2H_2O$, 10 mg of whey protein was added under stirring conditions (500 rpm). The solution was stirred for another 15 mins, following which the synthesized Fe_3O_4 nanoparticles were added. The mixture was then stirred for another 15 mins to allow the nanoparticles to suspend uniformly. This was followed by the dropwise addition of 10 ml, 0.1 M Na_2CO_3 solution. On completion of the addition process, the resulting precipitate was collected by centrifugation at 6000 rpm for 10 mins. The precipitate was then resuspended by sonication (in a mixture of water and methanol) and washed twice to remove the impurities. The product was obtained by drying under vacuum and subjected to characterization and dye-degradation experiments. Three different syntheses were performed by changing the amount of the Fe_3O_4 nanoparticles, 5 mg, 10 mg, and 20 mg, such that in the resulting composite, Fe_3O_4 /Vaterite, the ratio of the magnetite nanoparticles to the solid-support vaterite would be 0.5:10, 1:10, and 2:10.

2.2.6.3 Synthesis of Fe_3O_4 /Calcite nanoparticles

In this method, whey protein was not used, as the desired solid support for the Fe_3O_4 nanoparticles here was calcite. All the other methods, including the concentration of the substrates, followed during the synthesis were the same as mentioned above for Fe_3O_4 /Vaterite. The calcite and vaterite particles were also synthesized as a control to compare their phase and morphology with the Fe_3O_4 loaded versions. In these precipitation processes, the methods followed were the same as mentioned above except for the addition of the Fe_3O_4 nanoparticles.

Characterization methods

All three materials were initially subjected to PXRD analysis to study the diffraction patterns and XPS to identify the elements and their electronic states. The morphology of the materials was obtained from the FESEM technique by placing the powdered samples directly on the stub

with the assistance of a double-headed carbon tape before loading them in the instrument for imaging. FETEM images of the solid-supported materials were obtained. The samples for imaging were prepared by the drop cast method (1 mM/ 2 μ l) on a copper grid, 300 mesh \times 83 μ m pitch. The Brunauer-Emmett-Teller (BET) surface area measurements were performed to obtain the specific surface area of the materials, Fe₃O₄/Vaterite and Fe₃O₄/Calcite, by using the N₂-gas adsorption method. The materials were subjected to degassing for 12 h at 60°C under a high vacuum before the sorption analysis. The zeta potential of the particles was obtained at pH= 7 and at 25 °C. TGA/DTG of the materials was performed in order to justify the loading of the magnetite nanoparticles on the CaCO₃ phases. These studies were performed in the range of 25-800 °C with increments of 10 °C/min. EDX element analysis and EDX elemental mapping of the materials were performed to determine the extent of loading of the Fe₃O₄ nanoparticles. The magnetic properties of the materials were obtained from the VSM experiments where the magnetization saturation (M_s) of the materials was obtained from VSM analysis.

2.2.6.4 Degradation of dyes by Fenton-like process

The synthesized Fe₃O₄, Fe₃O₄/Calcite, and Fe₃O₄/Vaterite were used as catalysts in the heterogeneous Fenton-like degradation of dyes. All the experiments were performed in a 100 ml round bottom flask, where, to a 50 ml of the dye solution of strength 1 \times 10⁻⁵ M, a certain amount of the catalyst was added, followed by the addition of H₂O₂ under constant stirring conditions and at room temperature. The amount of catalyst and H₂O₂ to be added was optimized by performing the reactions with varying amounts to ascertain the optimum conditions for maximum degradation. Among the three different materials subjected as catalysts, Fe₃O₄/Vaterite was used as the standard to optimize the reaction conditions. The amount of catalyst (Fe₃O₄/Vaterite) was varied as 10 mg, 20 mg, 30 mg, 40 mg, 50 mg, and 60 mg and the concentration of hydrogen peroxide was varied between 3-6 mM. Post the optimization process, the amount of the other catalysts was fixed. The organic dyes MB and RhB were used as model dyes. The reactions were performed for 2 hours during which, aliquots of 2 ml were collected every 15 minutes and centrifuged. To study the degradation process, the supernatant was analyzed by Ultraviolet-Visible (UV-Vis) absorption spectroscopy in the wavelength range of 525-725 nm for MB,^{2,9,2.10} and 450-650 nm for RhB.^{2.11,2.12} To justify the results, the extent of degradation of MB was also determined from the COD and the total organic carbon (TOC) measurement. The activity of the catalyst (Fe₃O₄/Vaterite) was examined at different pH conditions (pH = 5,6,7,8 and 9) by performing the degradation of MB. The pH of the solution

was adjusted by adding suitable amounts of HCl and NaOH, maintaining all other conditions the same as mentioned above.

Determination of Chemical Oxygen Demand (COD)

Two different solutions, 'Solution 1' (mercuric sulfate and sulfuric acid) and 'Solution 2' for low range COD (silver sulfate, chromic acid, sulfuric acid and demineralized water) were purchased from HACH, USA. In a typical COD determination experiment, 2 mL of the dye solution is mixed with 0.25 mL of 'Solution 1' and 2.8 mL of 'Solution 2'. In this work, we had to take two different dye solutions, one with the initial concentration of MB and the other being the supernatant after the degradation process. The individual mixture solutions were then digested in a COD digester (ECO25 Thermoreactor) for 2 hours at 150 °C. The digested samples were analyzed after cooling them to room temperature with the help of a UV-Vis spectrophotometer at 420 nm (HACH, USA; DR 900) for the COD measurement of the samples.

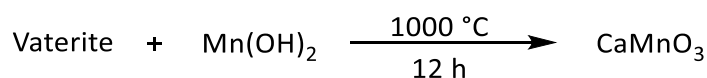
Preparation of Dye solution for Fenton-like degradation

Initially, a stock solution of both the dyes was prepared in 100 ml of Millipore water. The concentration of the stock solution was 1 mM and for this, 32 mg of MB and 48 mg of RhB were dissolved in 100 ml of Millipore water. For the dye degradation studies, the dye solutions were diluted according to the required concentration, where the final volume was 50 ml. Therefore, for 1×10^{-5} M of 50 ml MB solution, 250 μ l from the stock solution was taken and diluted to 50 ml. Similarly, for 1×10^{-5} M of 50 ml RhB solution, 250 μ l from the stock solution was taken and diluted to 50 ml. 2 ml of these 1×10^{-5} M solution were collected and analyzed by UV-Vis absorption spectroscopy in the wavelength range of 525-725 nm for MB and 450-650 nm for RhB to determine the initial absorbance, A_0 , of the dyes.

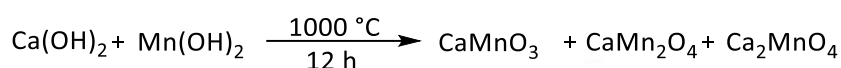
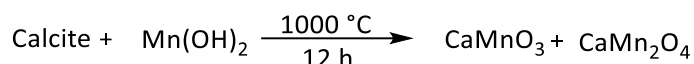
2.2.7 Biomineralized Vaterite derived CaMnO_3 as photocatalysts

2.2.7.1 Synthesis of CaMnO_3

The *in vitro* biomineralized vaterite was synthesized using curcumin as the additive, the procedure mentioned elaborately in section 2.2.2. Following this, the Ca and Mn precursors, biomineralized vaterite (CaCO_3), and $\text{Mn}(\text{OH})_2$ (1:1) were ground in a mortar and pestle to make a homogeneous mixture. The mixture was heated at 1000 °C for 12 hours in the furnace. Heat treatment below this temperature of 800 °C led to the formation of a small amount of mixed-phase CMOs alongside a large amount of manganese oxide.



Additionally, two different syntheses were performed, varying the Ca precursor. In both cases, a similar experimental condition was followed.



Characterization methods

All the materials thus obtained were subjected to PXRD analysis. In a typical analysis, around 50 mg of the powdered sample was placed on the glass sample holder. Two of the oxides, synthesized using (i) Biomineralized Vaterite and Mn(OH)_2 ; (ii) Commercial CaCO_3 and Mn(OH)_2 were studied thoroughly. The morphologies of the particles were obtained from the FESEM technique. The samples in the powdered form were directly placed on the sample stub with the assistance of a double-headed carbon tape before loading them in the instrument for imaging. The specific surface area of the materials was obtained from the BET surface area measurements by using the N_2 -gas adsorption method. Before the sorption analysis, the degassing of the compound was carried out at 100°C under a high vacuum for 12 h. The UV-vis DRS of the materials were performed using BaSO_4 as an internal standard. The absorption spectra were converted into the Tauc plot of $(\alpha h\nu)^2$ versus $h\nu$, where α is the optical absorption coefficient, h is the Planck's constant, and ν is the photon's frequency. HRTEM of the material obtained using biomineralized vaterite was performed to confirm the formation of CaMnO_3 by comparing the fringe spacing with the theoretical inter-planar spacing of the (h,k,l) planes of CaMnO_3 . Here, the sample subjected for imaging was prepared by drop cast method (1 mM/ 2 μl) on a copper grid, 300 mesh \times 83 μm pitch. The wavelength spectrum of the light source (200 W Halogen lamp) was obtained from Spectroradiometer CS-200 (Konica Minolta). The experiment was performed by keeping the light source at a distance of 2 m from the spectroradiometer. The intensity of the light was found out to be 11507.13 cd/m^2 and the wavelength spectrum was obtained in the range of 380-780 nm, **Fig. 2.2**.

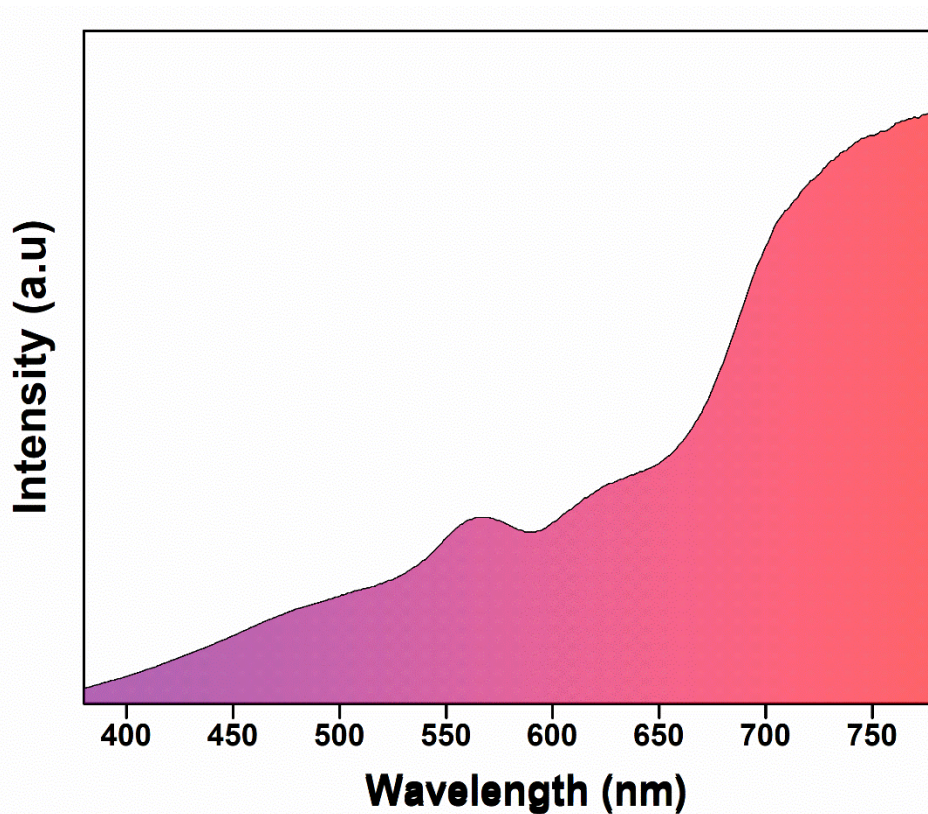


Figure 2.2: Wavelength spectrum of the 200 W Halogen lamp.

2.2.7.2 Degradation of Rhodamine 6G and the other dyes

The synthesized CMOs were used as photocatalysts to perform the photocatalytic dye-degradation of the toxic organic pollutants. In the case of Rh 6G, two separate dye-degradation experiments were performed, one with the calcium manganese oxide synthesized using biomineralized vaterite and the other with commercially available CaCO_3 . In a standard photocatalytic dye-degradation experiment, 20 mg of CMO powder was added to an aqueous solution of Rh 6G (100 mL, 5 ppm). The same concentration was used for the other dyes also. The solution was then kept under stirring in the dark for 1 hour to ensure that the adsorption equilibrium is reached, following which, the suspension was irradiated with simulated sunlight for 2 hours to study the photolytic reaction. A 200 W Halogen lamp was used as the light source. Aliquots of 2 ml were collected at intervals of 10 minutes and centrifuged. The supernatant was analyzed by UV-Vis absorption spectroscopy using 10 mm path length quartz cuvettes in the wavelength range of 460-600 nm. The degradation of the other dyes, RhB, MB and MO was studied, maintaining all the conditions, including the concentration of the dye and the catalyst, the same. The recyclability and reusability of CaMnO_3 were also tested for five consecutive cycles for each dye. The photocatalyst was recovered and dried at the end of each cycle after centrifugation, followed by removing the dye solution. The recycled material was reused as a

photocatalyst to perform another cycle of dye-degradation. A schematic representation of the device set up has been illustrated in **Fig. 2.3**.

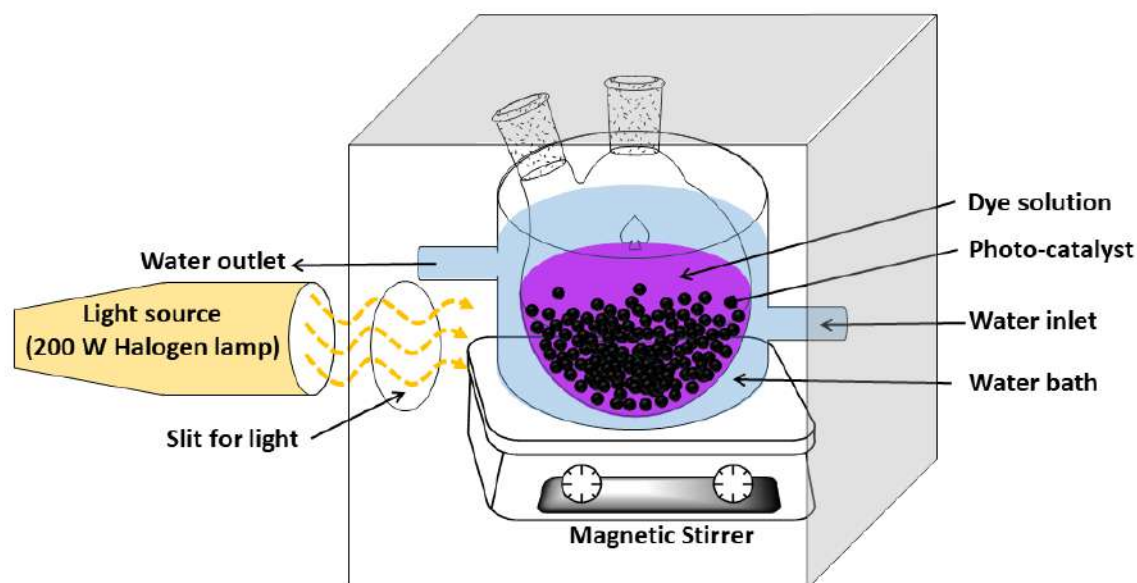


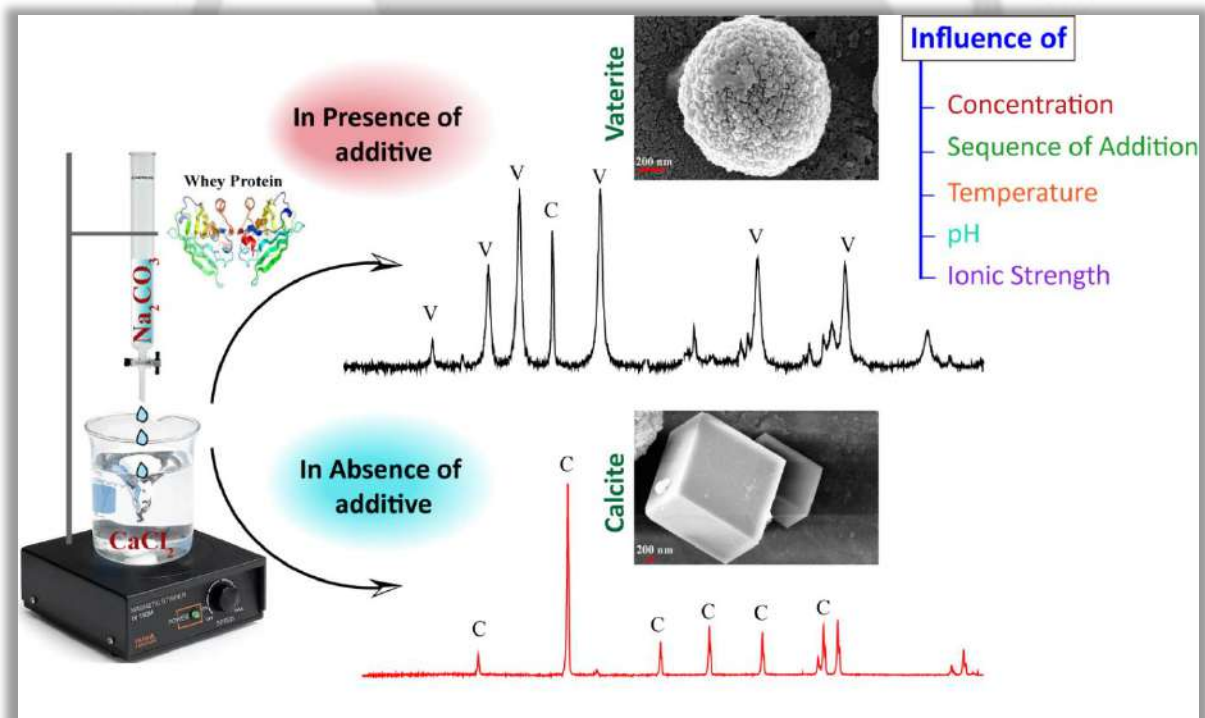
Figure 2.3: Illustration of the photocatalytic device set up.

References:

- 2.1. R. Borah and S. P. Biswas, Tulsi (*Ocimum sanctum*), excellent source of phytochemicals, *IJEAB*, 2018, **3**, 1732-1738.
- 2.2. E. W. C. Chan, Y. Y. Lim and Y. L. Chew, Antioxidant activity of *Camellia sinensis* leaves and tea from a lowland plantation in Malaysia, *Food Chemistry*, 2007, **102**, 1214-1222.
- 2.3. N. Suderman, M. I. N. Isa and N. M. Sarbon, Characterization on the mechanical and physical properties of chicken skin gelatin films in comparison to mammalian gelatin films. *IOP Conf. Ser.: Mater. Sci. Eng.*, 2018, **440**, 12033.
- 2.4. Y. P. Singh, J. C. Moses, B. K. Bhunia, S. K. Nandi, and B. B. Mandal, Hierarchically structured seamless silk scaffolds for osteochondral interface tissue engineering. *J. Mater. Chem. B*, 2018, **6**, 5671-5688.
- 2.5. P. C. Sahoo, F. Kausar, J. H. Lee and J. I. Han, Facile fabrication of silver nanoparticle embedded CaCO_3 microspheres via microalgae-templated CO_2 biomineralization: application in antimicrobial paint development, *RSC Adv.*, 2014, **4**, 32562-32569.
- 2.6. L. Kvitek, M. Vanickova, A. Panacek, J. Soukupova, M. Dittrich, E. Valentova, R. Prucek, M. Bancirova, D. Milde and R. Zboril, Initial Study on the Toxicity of Silver Nanoparticles (NPs) against *Paramecium caudatum*, *J. Phys. Chem.*, 2009, **113**, 4296.

- 2.7. B. Saha, S. Das, J. Saikia and G. Das, Preferential and Enhanced Adsorption of Different Dyes on Iron Oxide Nanoparticles: A Comparative Study, *J. Phys. Chem. C*, 2011, **115**, **16**, 8024–8033.
- 2.8. D. Paul, S. Halder and G. Das, Whey protein directed in vitro vaterite biomineralization: Influence of External Parameters on Phase Transformation. *Colloids Interface Sci. Commun.*, 2020, **36**, 100255.
- 2.9. M. F. A. Messih, A. E. Shalan, M. F. Sanad and M. A. Ahmed, Facile approach to prepare ZnO@SiO₂ nanomaterials for photocatalytic degradation of some organic pollutant models. *J. Mater. Sci.: Mater. Electron.*, 2019, **30**, 14291–14299.
- 2.10. J. Xu, T. Zhang and J. Zhang, Photocatalytic degradation of methylene blue with spent FCC catalyst loaded with ferric oxide and titanium dioxide, *Sci. Rep.*, 2020, **10**, 12730.
- 2.11. M. S. Ansari, K. Raees, M. A. Khan, M. Z. A. Rafiquee and M. Otero, Kinetic Studies on the Catalytic Degradation of Rhodamine B by Hydrogen Peroxide: Effect of Surfactant Coated and Non-Coated Iron (III) Oxide Nanoparticles, *Polymers*, 2020, **12**, 2246.
- 2.12. P. Liu, J. Zhang, D. Gao and W. Ye, Efficient visible light-induced degradation of Rhodamine B by W(N_xS_{1-x})₂ nanoflowers. *Sci. Rep.*, 2017, **7**, 40784.

Whey protein directed *in vitro* biomineralization of vaterite: A study on the influence of external parameters on CaCO_3 phase transformation



3.1 Introduction

Calcium carbonate in the anhydrous crystalline phase exists in three different polymorphs; calcite, aragonite, and vaterite. The vaterite phase being the least stable among these three. Hence the occurrence of vaterite in nature is limited due to its unstable nature under normal conditions of temperature, pressure, pH, etc. The size of the spheres ranges from 1-10 μm .^{3.1} The formation and isolation of vaterite is, therefore, a topic of utmost interest in the field of research not only due to its unstable nature but also because of its utility in several applications such as a carrier for active compounds in the field of medicine, as a template for biodegradable polymer capsules for applications in nanomedicine.^{3.2,3.3} The vaterite particles also find utility in commercial and personal care products such as abrasives, adsorbents, anticaking agents, buffers, dyes, etc.^{3.4} Also used in microrheology and microfluidics due to its unique optical properties.^{3.5,3.6}

In our effort to understand the mechanism of biomineralization in this study, we had subjected the organic biomolecule whey protein to assist the *in vitro* biomineralization of CaCO_3 . Being one of the two main constituents of milk protein, it is inexpensive, easily available and highly soluble in water. The isoelectric point, pI 4.5, of whey protein indicates that it possesses a net negative charge which will allow it to interact with Ca^{2+} ions in an aqueous solution near-neutral pH and at room temperature. It is difficult to comment on the specificity of the role played by polymeric molecules in crystallization since they mostly occur in random coil conformation.^{3.7,3.8} In this case, the biopolymer whey protein has been assigned the job to influence the crystallization pathway of CaCO_3 . Its role just like any other polymeric molecule assisting the stabilization of a particular phase may be due to either nucleation or adsorption of the polymer or both.^{3.9} Arresting a particular phase during CaCO_3 phase transformation by crystallization requires the proper alignment of the binding groups that facilitates nucleation.^{3.10} Whey protein is composed of five major components, α -lactalbumin, β -lactoglobulin, glycomacropeptide (GMP), serum albumin, and immunoglobulins.^{3.11} As a complex biopolymer, whey protein exhibits a random conformation in solution and therefore, talking about its role in this process we also consider the adsorption of the protein on the initial nanocrystals of CaCO_3 via weak interactions which would influence the kinetic crystallization pathway hence selectively forming the metastable vaterite phase rather than the most stable calcite phase. In addition to studying the precipitation of CaCO_3 in the presence and absence of whey protein, we also observed the results by reversing the sequence of addition of the Ca^{2+} and the CO_3^{2-} to compare the percentage of vaterite formation in each case. The study was further subjected to

certain changes in parameters such as the concentration of protein, temperature, pH and ionic strength to monitor their effect on vaterite formation in the presence of whey protein.

3.2 Results and Discussions

The morphology and phases of the CaCO_3 were investigated using FESEM, powder XRD, FT-IR spectroscopy and subsequently, the hydrodynamic diameter and the zeta potential of the particles were obtained using DLS measurements. The effect of various parameters on the phase transformation is explained.

3.2.1 Influence of Whey Protein on CaCO_3 precipitation

The *in vitro* biomineralization of CaCO_3 under controlled conditions in the absence of protein resulted in the formation of the rhombohedral calcite phase, the most stable polymorph of CaCO_3 , without any trace of the other two polymorphs vaterite and aragonite. The percentage of calcite formation was 100%, obtained from the quantitative analysis result, Fig. A3.1(A). This was supported by the FT-IR spectrum, Fig. 3.1(B), where only two peaks at 712 cm^{-1} and 875 cm^{-1} , the characteristic peaks for the calcite phase were observed. In the PXRD pattern, Fig. 3.1(A), peaks at 2θ values equal to 23.08, 29.32, 35.87, 39.31, 43.18, 47.42 and 48.53 identical to the characteristic peaks for the calcite phase corresponding to (012), (104), (110), (11-3), (202), (018) and (11-6) planes, respectively were observed and these peaks matched well with the standard PDF data for calcite (ICSD 00-047-1743). The hydrodynamic diameter and the zeta potential, Fig. A3.7, of the calcite, thus obtained, was found to be 1028.4 nm and -14.2 mV, respectively. The FESEM images, Fig. 3.2(A) and (B), showed the formation of rhombohedral calcite crystals in clusters and also as individual particles. The biomineralization carried out in the presence of whey protein resulted in the selective formation of the most unstable phase of CaCO_3 , vaterite, with a very minimal amount of calcite. The percentage of vaterite obtained was 90.03%, and that of calcite was 9.97%, Fig. A3.1(B). When the FT-IR spectrum obtained, Fig. 3.1(B), was observed, it was seen that the peaks due to vaterite at 745 cm^{-1} , 875 cm^{-1} , and 1085 cm^{-1} were high in intensity whereas the peak at 712 cm^{-1} due to calcite was very weak. Similarly, in the PXRD pattern, Fig. 3.1(A), the peaks due to vaterite at 2θ values equal to 21.09, 25.57, 27.25, 33.17, 43.98 and 50.43, corresponding to (002), (100), (101), (102), (110) and (104) planes, respectively, were stronger whereas the peak resulting from calcite at 2θ value equal to 29.65 due to the (104) plane was weak in intensity and these peaks matched well with the standard PDF data for the vaterite and the calcite phase of CaCO_3 (ICSD 00-060-0483 and 00-047-1743 respectively). The hydrodynamic diameter and the zeta potential of the CaCO_3 thus

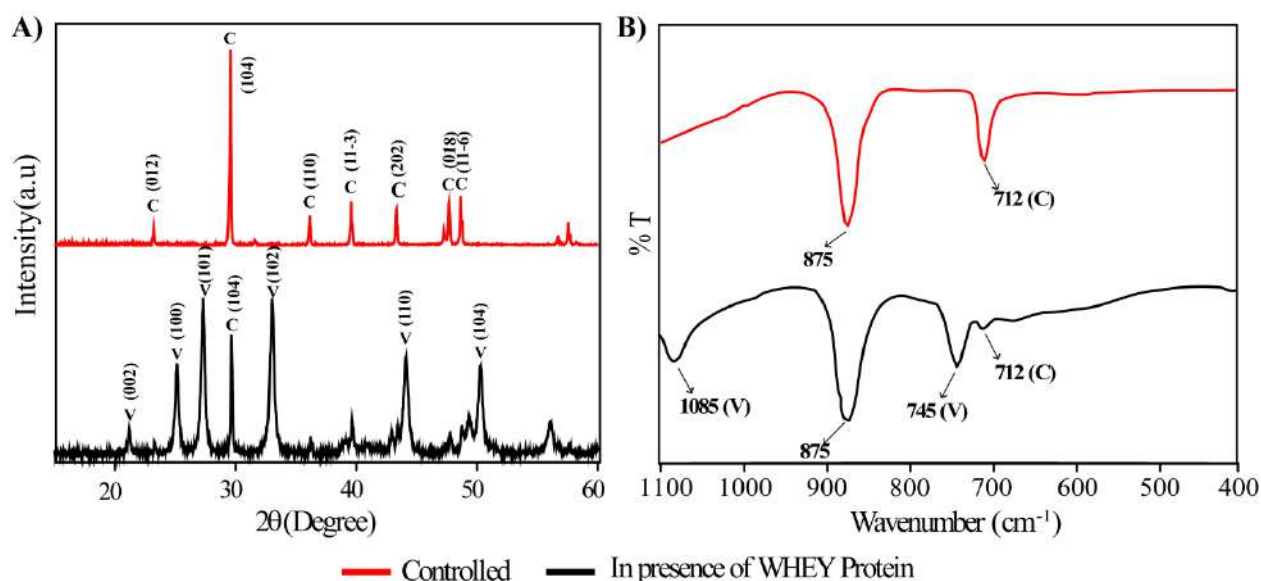


Figure 3.1: A) PXRD pattern and B) FT-IR spectra of CaCO_3 minerals **under controlled conditions** and in the **presence of whey protein**.

obtained were 1086.5 nm and -13.8 mV, respectively, Fig. A3.7. The FESEM images, Fig. 3.2(C) and 2(D), showed the formation of spherical vaterite particles.

The above results clearly show that whey protein assists the *in vitro* biomineralization of vaterite during CaCO_3 precipitation.^{3,12-3,15} Being highly soluble in water and possessing a net negative charge at around the neutral pH range and at room temperature, it will selectively bind to Ca^{2+} ions and direct the nucleation of the vaterite phase by raising the free energy of nucleation, ΔG_n of calcite making it relatively higher than that of vaterite, and therefore, vaterite particles precipitate out first even though they are the least stable among all the polymorphs.^{3,16} Under controlled conditions in the absence of the protein, the free energy of crystallization, ΔG_n of calcite is lower than that of vaterite. This leads to the formation of calcite on supersaturation. In addition to this, whey protein also influences the kinetic crystallization pathway by adsorption on to the pre-clusters or the initial nanocrystals via weak interactions such as electrostatic interactions, hydrogen bonding and hydrophobic interactions. Hence stabilizing the metastable vaterite phase.

In living organisms, the role of proteins and organic molecules during biomineralization is not restricted to a single cycle, rather it should be able to direct the process over multiple cycles. From our experiment, it was obvious that whey protein fits into this category quite clearly due to its ability to retain its structure and hence assist the purpose of vaterite formation. This was justified by the circular dichroism experiment of the initial whey protein solution and the whey protein solutions obtained in the form of filtrate after the first and the second cycle.^{3,17,3,18} A

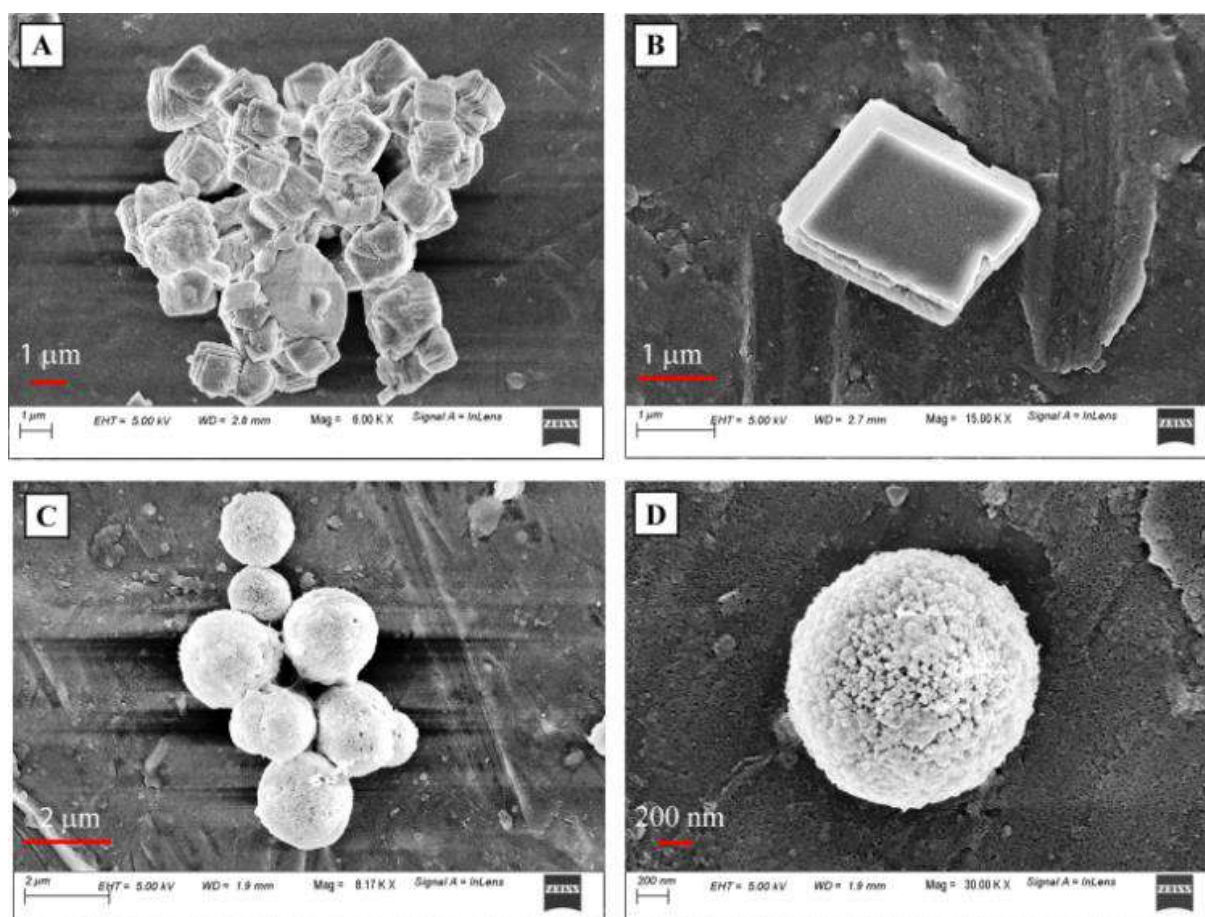


Figure 3.2: FESEM Images (A) and (B) of CaCO_3 under controlled conditions; (C) and (D) in the presence of whey protein.

careful analysis of the spectra, Fig. A3.13 would suggest that whey protein had not undergone any change in the secondary structure, therefore, its role only in facilitating the stabilization of the vaterite phase and not taking part in the reaction itself has been confirmed. Also, the PXRD pattern, Fig. A3.14, and the FESEM image, Fig. A3.15, clearly suggests the formation of spherical vaterite particles on reusing the protein after the first cycle. This experiment confirms the ability of whey protein to be reused for a multiple number of cycles.

In an aqueous solution, at room temperature and near-neutral pH whey protein is highly soluble and the individual component proteins remain in the dissociated state. At higher temperature around $60\text{ }^\circ\text{C}$, it undergoes denaturation and the component protein molecules aggregate. Similarly at pH 4.5, the isoelectric point of whey protein, the electrostatic forces of attraction are minimum and the protein-protein interaction increases and hence they aggregate.^{3.19} The percentage composition of the five major components of whey protein are; α -lactalbumin (25%), β -lactoglobulin (65%), serum albumin (8%), glycomacropeptide (GMP) and immunoglobulins. Most of these components have an excellent binding affinity for calcium ion.^{3.20-3.22} Although it

is known that protein plays a key role in determining the phase transformation in biomineralization, the role of α -lactalbumin, β -lactoglobulin and serum albumin during the precipitation of CaCO_3 were studied separately to compare their role as individual molecules with whey protein in assisting the highly selective formation of the metastable vaterite phase. The experiments with the individual components were performed maintaining all the conditions the same as in the experiment with whey protein. It was observed from the PXRD pattern (ICSD 00-060-0483 and 00-047-1743 for vaterite and calcite respectively), Fig. A3.16, and the quantitative analysis result, Fig. A3.17, that the percentage of vaterite had dropped in each case where the proteins were used independently compared to the very high 90% that was obtained in the case of whey protein. With α -lactalbumin, the percentage of vaterite obtained was 58%, with β -lactoglobulin it was 70% and with serum albumin it was 40%.

3.2.2 Effect of Variation in Parameters

3.2.2.1 Effect of Whey Protein concentration

The effect of whey protein concentration on the formation of the polymorphs was studied at two different concentrations 30 mg (1.5 mg/ml) and 50 mg (2.5 mg/ml). At 30 mg, Fig. A3.1(C), the amount of vaterite obtained was 69.7%, whereas at, 50 mg, the amount of vaterite obtained was 90.3%, Fig. A3.1(B). From the FT-IR spectrum, Fig. A3.2(B), it was observed that the peak at 712 cm^{-1} due to the calcite was more intense at 30 mg (1.5 mg/ml) as compared to that in the case of 50 mg (2.5 mg/ml). Similarly, in the PXRD pattern, Fig. A3.2(A), characteristic peaks for vaterite were more intense in the second case but not so in the first case and matches well with the standard PDF data of the vaterite and the calcite phase (ICSD 00-060-0483 and 00-047-1743 respectively). The morphology of the particles obtained using FESEM, are mostly spherical with occasional rhombohedral particles. At 30 mg, Fig. 3.3(A), (B), and (C), the rhombohedral calcite appeared with the spherical vaterite at a ratio close to that obtained from the quantitative analysis result. At 50 mg, Fig. 3.3(D), (E) and (F), the spherical vaterite phase was almost formed explicitly with a minimal representation of calcite. The hydrodynamic diameters are 1086.5 nm and 2365.3 nm, respectively and the zeta potential -16.7 mV and -13.8 mV, respectively, Fig. A3.8. Hence, the effect of whey protein concentration is clearly visible. On lowering the concentration, the goal of attaining the least stable phase, vaterite highly selectively was affected and therefore the percentage of vaterite formation had reduced quite significantly. Since the goal of this study is to obtain the metastable vaterite particles, this experiment helped us to determine the amount of whey protein that was to be used for our

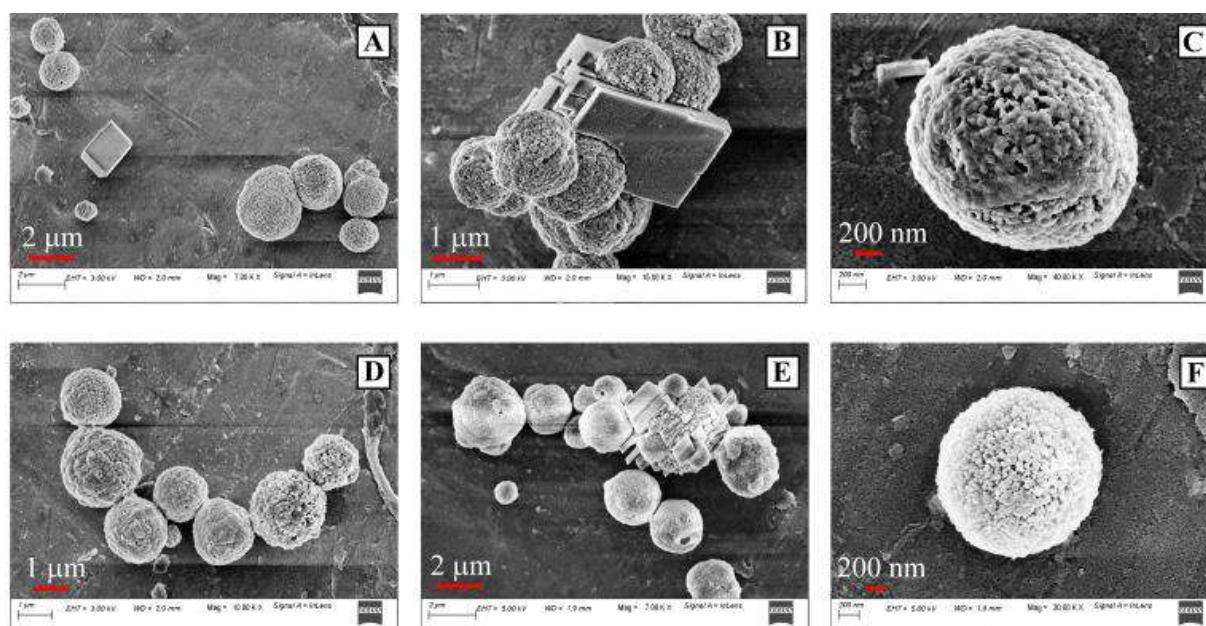


Figure 3.3: FESEM Images (A) (B) and (C) of CaCO_3 at 30 mg of whey protein; (D) (E) and (F) at 50 mg of whey protein.

further studies that were to be carried out subjecting certain changes in parameters. Therefore the amount of whey protein was fixed at 2.5 mg/ml of solution for all the successive experiments.

3.2.2.2 Effect of Sequence of addition

On reversing the sequence of addition, the calcite phase dominated with a minimal amount of vaterite. The FT-IR spectrum, Fig.A3.3(B) shows that the characteristic peak for calcite at 712 cm^{-1} is more intense as compared to the peak at 745 cm^{-1} for vaterite. In the PXRD pattern, Fig.A3.3(A), the characteristic peak for calcite is intense whereas the vaterite peaks are almost negligible and the pattern matches well with the vaterite and the calcite phase of CaCO_3 (ICSD 00-060-0483 and 00-047-1743 respectively). The morphology, obtained from the FESEM images, Fig. 3.4(A) and (B), is that of the rhombohedral calcite crystals, which are very distinct in a cluster and also as individual particles. The hydrodynamic diameter obtained was 2594.1 nm and the zeta potential, -20.9 mV. From the quantitative analysis result, Fig.A3.1(D), the percentage of calcite and vaterite were 76% and 24%, respectively. The protein played a pivotal role in assisting the formation of vaterite. Under the normal sequence of addition, the formation of vaterite is more than 90%, Fig. A3.1(B), whereas on reversing, the percentage drops down to just 24%.

This justifies the interaction of the Ca^{2+} with the protein before precipitating down to CaCO_3 .

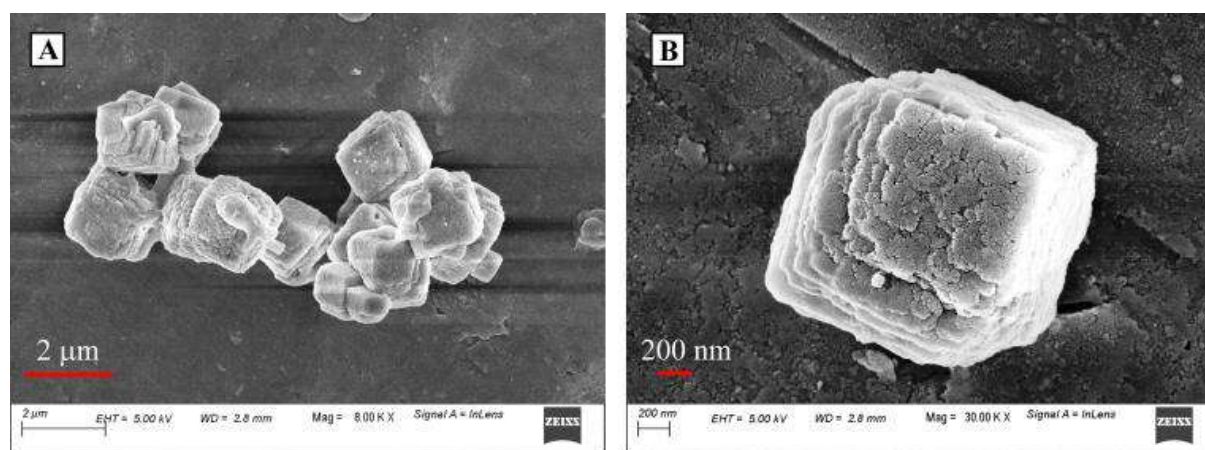


Figure 3.4: FESEM Images (A) and (B) of CaCO_3 due to **reverse addition**.

When protein assists in selective formation of the vaterite phase by increasing the free energy of nucleation of calcite, ΔG_n . The 24% of vaterite that had formed on reversing the sequence of addition is due to the adsorption of the protein on the CaCO_3 pre-clusters via weak interactions such as electrostatic interactions, therefore, affecting the kinetic crystallization pathway.

3.2.2.3 Effect of Temperature

To determine the influence of temperature on the formation of different polymorphs of CaCO_3 , the *in vitro* biomineralization was performed at three different temperatures. From the quantitative analysis results, Fig. A3.1(B), Fig. A3.1(E), Fig. A3.1(F) that the percentage formation of vaterite was 90.03, 93, 0.03 when the temperature was maintained at room temperature 25 °C, 60 °C, and 10 °C, respectively. The FT-IR spectra, Fig. A3.4(B), for the CaCO_3 formed at room temperature, showed the characteristic peaks for vaterite at 745 cm^{-1} and 1085 cm^{-1} with a very sharp intensity and a very weak signal at 712 cm^{-1} for the formation of calcite. Similarly, the PXRD pattern, Fig. A3.4(A) supported the formation of vaterite selectively over calcite with high-intensity peaks for the vaterite phase and the PXRD pattern matches with the standard PDF data for both the vaterite and the calcite phase (ICSD 00-060-0483 and 00-047-1743 respectively). From the FESEM images, the shape of the particles was found to be spherical as that of vaterite, Fig. 3.3(D), (E) and (F). When performed at 60 °C, it showed even higher selective formation of the least stable polymorph vaterite, whereby the FT-IR spectra, Fig. A3.4(B), gave only the characteristic peaks for vaterite at 745 cm^{-1} and 1085 cm^{-1} with high intensity and no peak for calcite, and similarly, the PXRD pattern showed only the peaks for vaterite at very high intensity whereas the peaks for calcite were almost negligible (ICSD 00-060-0483). The FESEM images, Fig. 3.5(D), (E), and (F) showed spherical shaped vaterite particles both in a cluster and also individually. The biomineralization, when carried out

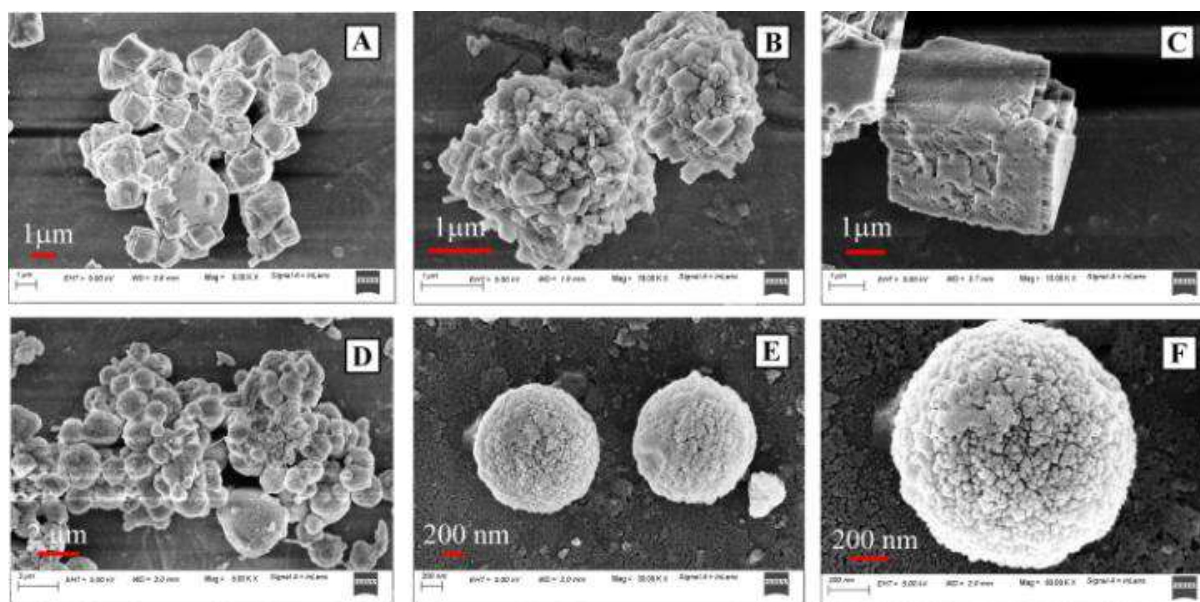


Figure 3.5: FESEM Images (A) (B) and (C) of CaCO_3 at $10\text{ }^\circ\text{C}$; (D) (E) and (F) at $60\text{ }^\circ\text{C}$ rhombohedral calcite particles. The DLS experiment for each case gave us the hydrodynamic diameter and the zeta potential for the CaCO_3 formed at room temperature, $60\text{ }^\circ\text{C}$ and $10\text{ }^\circ\text{C}$ as 1086.5 nm, 2816.4 nm, and 2480.9 nm; -13.8 mV, -20.4 mV and -18.1 mV respectively, Fig. A3.10(A) and (B).

at $10\text{ }^\circ\text{C}$, showed opposite results to that at higher temperatures. Here the phase obtained is calcite with a negligible amount of vaterite. The FT-IR spectrum, Fig. A3.4(B), showed no peak for the vaterite particles but only the signals at 712 cm^{-1} and 875 cm^{-1} due to calcite. Similarly, the PXRD pattern, Fig. A3.4(A), showed only the formation of calcite phase (ICSD 00-047-1743) and the morphology obtained from the FESEM images, Fig. 3.5(A), (B) and (C) were rhombohedral calcite particles. The DLS experiment for each case gave us the hydrodynamic diameter and the zeta potential for the CaCO_3 formed at room temperature, $60\text{ }^\circ\text{C}$ and $10\text{ }^\circ\text{C}$ as 1086.5 nm, 2816.4 nm, and 2480.9 nm; -13.8 mV, -20.4 mV and -18.1 mV respectively, Fig. S10(A) and S10(B).

The influence of temperature on the polymorph obtained in the biomineralization of CaCO_3 has been studied previously.^{3,23,3,24} It was suggested that lower temperature around $0\text{ }^\circ\text{C}$ favors the formation of calcite and higher temperature around $60\text{ }^\circ\text{C}$ comparatively gives a better result for vaterite formation. In this study, we have seen that the introduction of whey protein plays an important role in the formation of the least stable polymorph vaterite specifically over calcite at room temperature. At high temperature, $60\text{ }^\circ\text{C}$, the individual components of whey protein especially β -lactoglobulin is broken down into smaller fractions from dimer to monomer.^{3,19,3,25} Hence the number of particles that are available to influence the Ca^{2+} precipitation or the kinetic crystallization pathway by adsorption on the CaCO_3 pre clusters are more than that at lower

temperatures. This leads to the formation of the least stable polymorph vaterite almost specifically, at a percentage even higher than 90% as in the case of room temperature. Low temperatures are highly favorable for the formation of the calcite phase and also the solubility of whey protein at 10 °C is very low which restricts it from interacting with the particles in solution. As a result, the role played by the protein in influencing the stabilization of vaterite at 10 °C has not been observed.

3.2.2.4 Effect of pH

The *in vitro* biomineralization of CaCO₃ in the presence of whey protein was performed at three different pH values to check the influence of pH on the formation of the different polymorphs. At pH 7, the percentage formation of vaterite was 90.03%, Fig. A3.1(B). The FT-IR spectra showed the characteristic peaks of vaterite at 745 cm⁻¹ and 1085 cm⁻¹ with high intensity and much weaker for calcite at 712 cm⁻¹, Fig A3.5(B). The PXRD pattern indicated the formation of vaterite specifically with high-intensity peaks and the characteristic peaks of calcite relatively weaker (ICSD 00-060-0483 and 00-047-1743 vaterite and calcite respectively). The morphology of the particles obtained from FESEM, Fig. 3.6(D), (E) and (F) were spherical as that of vaterite. The hydrodynamic diameter and the zeta potential are 1086.5 nm and -13.8 mV respectively, Fig. A3.11(A) and (B). Similarly, for pH 5, the least stable polymorph vaterite was specifically formed, 88.85% with a very small amount of calcite, Fig. A3.1(G). The FT-IR spectra showed the characteristic peaks of vaterite at 745 cm⁻¹ and 1085 cm⁻¹ with high intensity and a very negligible signal for calcite at 712 cm⁻¹. The PXRD pattern too showed the peaks due to vaterite as more intense compared to the calcite peaks (ICSD 00-060-0483 and 00-047-1743 vaterite and calcite respectively). The morphology of the particles as seen from the FESEM images, Fig. 3.6(D), (E) and (F) specified the formation of spherical vaterite in clusters with the rare occurrence of the rhombohedral calcite particles. The hydrodynamic diameter and the zeta potential are 723.9 nm and -18.3 mV respectively, Fig. A3.11(A) and (B). But in the case of pH 4, the formation of vaterite was lowered to 65.3%, and the formation of the most stable polymorph calcite was comparatively much higher, 34.7%, Fig. A3.1(H), as compared to the other two cases. The I.R spectrum gave almost equal signals due to vaterite and calcite particles at 745 cm⁻¹ and 712 cm⁻¹, respectively, Fig. A3.5(B) and the PXRD pattern, Fig. A3.5(A), for the calcite, has a higher intensity peak as compared to the peaks of vaterite (ICSD 00-060-0483 and 00-047-1743 vaterite and calcite respectively). The morphology as can be seen from the FESEM images, Fig. 3.6(A), (B) and (C) showed an almost equal density of the rhombohedral calcite and the spherical vaterite in clusters. The hydrodynamic diameter measured for the particles

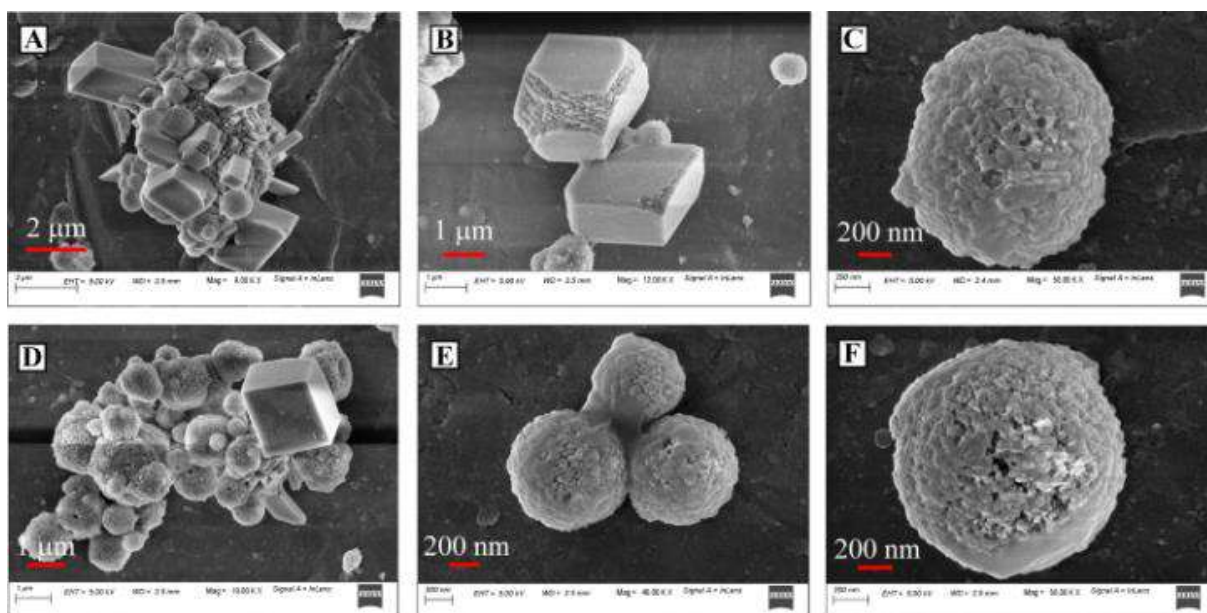


Figure 3.6: FESEM Images (A) (B) and (C) of CaCO_3 at **pH= 4**; (D) (E) and (F) at **pH= 5**.

using DLS was 1748.1 nm and the zeta potential was -21.3 mV, Fig. A3.11(A) and (B).

The explanation for this anomaly in the percentage of the different polymorphs obtained can be drawn from the isoelectric point (pI) of the protein concept. The pI concept is a characteristic of the pH. The pI of whey protein is 4.5.^{3,19} Above and below the pI, whey protein possesses a net charge.^{3,19,3,25} Below the pI, the net charge of the protein is positive which makes it unsuitable for Ca^{2+} binding and above the pI, the net charge of the protein moiety is negative which is a pre-requirement for Ca^{2+} binding. Hence when the *in vitro* biomineralization was carried out at pH 5 and 7 which are higher than the pI of whey protein, the binding of Ca^{2+} ions to the specific regions of the protein took place effectively stabilizing the ions and hence leading to the formation of the least stable polymorph vaterite almost specifically. If the only role of whey protein was to bind to Ca^{2+} ions and influence the precipitation facilitating the vaterite formation, then the 65% vaterite formed at pH 4 cannot be justified. This is because at pH 4, below the pI, the net charge of the protein is negative and hence Ca^{2+} cannot bind to it. But the fact that the protein possesses a net positive charge, hence its solubility increases and its ability to interact with the CaCO_3 pre-clusters via weak interactions to affect the kinetic crystallization pathway exists. Therefore, the role of whey protein in the *in vitro* biomineralization of CaCO_3 at different pH conditions has been justified.

3.2.2.5 Effect of Ionic strength

To observe the influence of the presence of other ions on the formation of CaCO_3 in the presence of whey protein, the *in vitro* biomineralization was performed in two different

conditions. A slight increase in the formation of vaterite was observed in the presence of NaCl. The percentage formation of vaterite in both the cases, in the absence of an electrolyte and in the presence of 100 mM NaCl was 90.03% and 93.10%; Fig. A3.1(B) and Fig. A3.1(I), respectively. In the first case, FT-IR spectra showed high-intensity signals for vaterite at 745 cm^{-1} and 1085 cm^{-1} and a comparatively much weaker signal for calcite at 712 cm^{-1} , Fig. A3.6(B). The PXRD pattern, Fig. A3.6(A) showed the formation of vaterite predominantly over calcite (ICSD 00-060-0483 and 00-047-1743 respectively), and the morphology of the particles obtained using FESEM was spherical as that of vaterite. The hydrodynamic diameter and the zeta potential were 1086.5 nm and -13.8 mV respectively, Fig. A3.12(A) and (B). In the second case, in the presence of 100 mM NaCl, again the phase that was obtained predominantly was vaterite. The formation of vaterite was slightly more than that in the first case. The FT-IR spectrum gave strong signals at 745 cm^{-1} and 1085 cm^{-1} and a very faint signal at 712 cm^{-1} due to calcite, Fig. A3.6(B). Similarly, the PXRD pattern, Fig. A3.6(A), supported the formation of vaterite predominantly over calcite with stronger signals due to vaterite as compared to the signals due to calcite (ICSD 00-060-0483 and 00-047-1743 respectively). The FESEM images, Fig. 3.3(D), (E), (F) and Fig. 3.7(A), (B), (C), showed the formation of spherical vaterite particles both in clusters and also individually for the 0 mM and 100 mM NaCl solutions, respectively. The DLS experiments for the particles obtained from the 100 mM NaCl solution gave the hydrodynamic diameter and the zeta potential as 612.4 nm and -15.6 mV, respectively, Fig. A3.12(A) and (B).

It is already known that the increase in the strength of the ionic solution influences the formation of the least stable phase vaterite.^{3,26} The presence of an electrolyte along the whey protein shows a more prominent influence on the stabilization of the metastable vaterite. During the precipitation of CaCO_3 the dissociated ions of the electrolyte and the protein influence the kinetic crystallization pathway. The ions that are present in the medium would interact with the pre-cluster and hence prevent the conversion of the vaterite phase to the stable calcite phase.

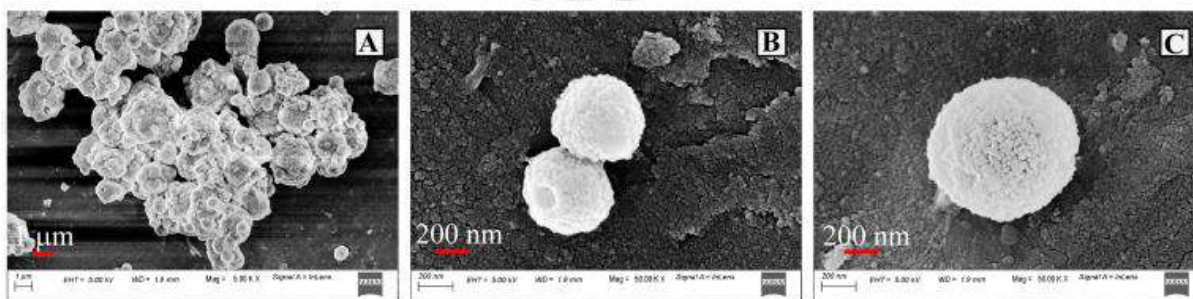
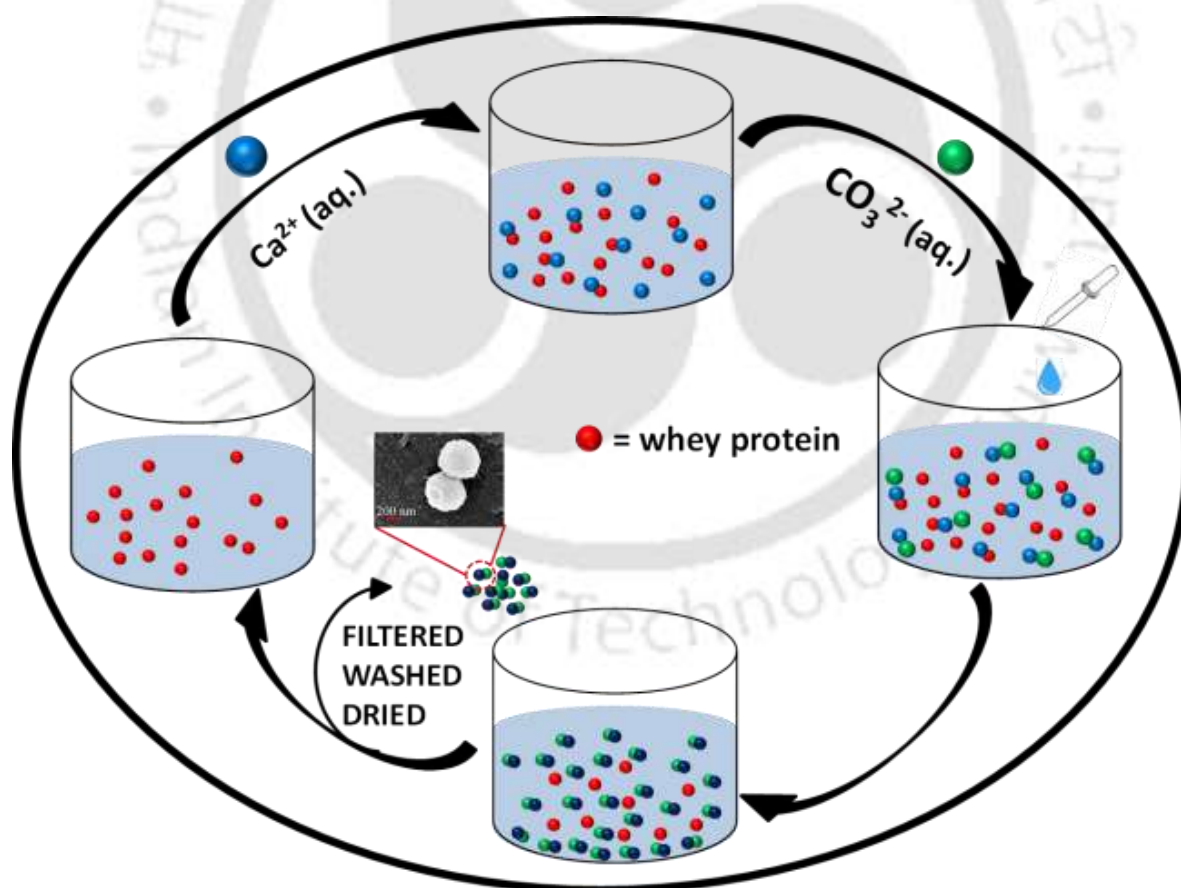


Figure 3.7: FESEM Images (A) (B) and (C) of CaCO_3 in the presence of 100 mM NaCl.

This is the reason why the percentage of the vaterite phase has gone up on increasing the ionic strength of the solution.

3.3 Conclusion

A schematic representation of the whole process representing the proposed plausible mechanism has been depicted in **Scheme 3.1**. To summarise, vaterite particles have been synthesized highly selectively in the presence of whey protein. The recovery and reusability of whey protein render the entire process a very cost-effective one. Subsequent studies by changing various parameters suggested that the presence of whey protein directed the selective formation of vaterite either by selective binding of the Ca^{2+} before the precipitation of CaCO_3 or by adsorption on to the CaCO_3 pre-clusters via weak interactions influencing the kinetic crystallization pathway. Whey protein possesses a net charge above and below its isoelectric point (pI) which facilitates these interactions, hence stabilizing the metastable vaterite phase. Therefore, we have developed an effective method to stabilize the metastable vaterite phase by the assistance of whey protein.



Scheme 3.1: Schematic representation of the proposed plausible mechanism of the whey protein assisted *in vitro* biomineralization of vaterite.

References

- 3.1. M. Moore, On the shape of dissolved crystals, *Mineral. Mag.*, 1986, **50**, 331-332.
- 3.2. Y. Svenskaya, B. Parakhonskiy, A. Haase, V. Atkin, E. Lukyanets, D. Gorin and R. Antolini, Anticancer drug delivery system based on calcium carbonate particles loaded with a photosensitizer, *Biophys. Chem.*, 2013, **182**, 11-15.
- 3.3. H. Yang, Y. Wang, T. Liang, Y. Deng, X. Qi, H. Jiang, Y. Wu and H. Gao, Hierarchical porous calcium carbonate microspheres as drug delivery vector, *Prog. Nat. Sci-Mater.*, 2017, **27**, 674-677.
- 3.4. D. B. Trushina, T. V. Bukreeva, M. V. Kovalchuk and M. N. Antipina, CaCO₃ vaterite microparticles for biomedical and personal care applications, *Mater. Sci. Eng. C*, 2014, **45**, 644-658.
- 3.5. R. Vogel, M. Persson, C. Feng, S. J. Parkin, T. A. Nieminen, B. Wood, N. R. Heckenberg and H. R. Dunlop, Synthesis and Surface Modification of Birefringent Vaterite Microspheres, *Langmuir*, 2009, **25**, 11672-11679.
- 3.6. S.J. Parkin, R. Vogel, M. Persson, M. Funk, V.L.Y. Loke, T.A. Nieminen, N.R. Heckenberg and H.R. Dunlop, Highly birefringent vaterite microspheres: production, characterization and applications for optical micromanipulation, *Opt. Express*, 2009, **17**, 21944-21955.
- 3.7. F. Tao, Q. Han, K. Lu and P. Yang, Tuning Crystallization Pathways through the Mesoscale Assembly of Biomacromolecular Nanocrystals, *Angew. Chem. Int. Ed.*, 2017, **56**, 13440-13444.
- 3.8. F. Tao, Q. Han and P. Yang, Developing Biopolymer Mesocrystals by Crystallization of Secondary Structures, *Langmuir*, 2019, **35**, 183-193.
- 3.9. J. J. J. M. Donners, R. J. J. Nolte and N. A. J. M. Sommerdijk, A Shape-Persistent Polymeric Crystallization Template for CaCO₃, *J. Am. Chem. Soc.*, 2002, **124**, **33**, 9700-9701.
- 3.10. N. Hosada, A. Sugawara, T. Kato, Template Effect of Crystalline Poly(vinyl alcohol) for Selective Formation of Aragonite and Vaterite CaCO₃ Thin Films, *Macromolecules*, 2003, **36**, 6449-6452.
- 3.11. E. A. Foegeding, P. Luck and B. Vardhanabhuti, Whey Protein Characteristics, *Encyclopedia of Dairy Sciences*, ed. 2nd, Elsevier Ltd, Whey Protein Products 2011, **ch. 2**.
- 3.12. K. Sawada, The mechanisms of crystallization and transformation of calcium carbonates, *Pure and Appl. Chem.*, 1997, **69**, 921-928.

- 3.13. H. Tong, W. Ma, L. Wang, P. Wan, J. Hu and L. Cao, Control over the crystal phase, shape, size and aggregation of calcium carbonate via a l-aspartic acid inducing process, *Biomaterials*, 2004, **25**, 3923-3929.
- 3.14. S. Kirboga and M. Oner, Effect of the Experimental Parameters on Calcium Carbonate Precipitation, *Chem. Eng. Trans.*, 2013, **32**, 2119-2123.
- 3.15. D. Ren, Q. Feng and X. Bourrat, Effects of Additives and Templates on Calcium Carbonate Mineralization in vitro, *Micron*, 2011, **42(3)**, 228-245.
- 3.16. W. Hou and Q. Feng, Morphology and formation mechanism of vaterite particles grown in glycine-containing aqueous solutions, *Mater. Sci. Eng. C*, 2006, **26**, 644-647.
- 3.17. M. Tomczyńska-Mleko, E. Kamysz, E. Sikorska, C. Puchalski, S. Mleko, L. Ozimek, G. Kowaluk, W. Gustaw, W. Wesołowska-Trojanowska, Changes of secondary structure and surface tension of whey protein isolate dispersions upon pH and temperature, *Czech J. Food Sci.*, 2014, **32**, 82-89.
- 3.18. H. Y. Celebioglu, M. Gudjonsdottir, S. Meier, J. Duss, S. Lee, I. S. Chronakis, Spectroscopic studies of the interactions between β -lactoglobulin and bovine submaxillary mucin, *Food Hydrocoll.*, 2015, **50**, 203-210.
- 3.19. D. H. G. Pelegrine and C. A. Gasparetto, Whey proteins solubility as function of temperature and pH, *Lebensm.-Wiss. Technol.*, 2005, **38**, 77-80.
- 3.20. E. A. Permyakov and L. J. Berliner, α -Lactalbumin: Structure and Function, *FEBS Lett.*, 2000, **473**, 269.
- 3.21. S. L. Maux, S. Bouhallab, L. Giblin, A. Brodkorb and T. Croguennec, Bovine β -lactoglobulin/fatty acid complexes: binding, structural, and biological properties, *Dairy Sci. and Technol.*, 2014, **94**, 409-426.
- 3.22. N. Sharma, R. Sharma, Y. S. Rajput and B. Mann, Chemical and functional properties of glycomacropeptide (GMP) and its role in the detection of cheese whey adulteration in milk: a review, *Dairy Sci. and Technol.*, 2013, **93**, 21-43.
- 3.23. C. A. Weiss Jr., K. T. Cancel, R. D. Moser, P. G. Allison, E. R. Gore, M. Q. Chandler and P. G. Malone, Influence of Temperature on Calcium Carbonate Polymorph formed from Ammonium Carbonate and Calcium Acetate, *J. Nanotech. Smart Mater.*, 2013, **1**, 1-6.
- 3.24. K. Y. Chong, C. H. Chia and S. Zakaria, Polymorphs calcium carbonate on temperature reaction, *AIP Conf. Proc.*, 2014, **1614**, 52-56.
- 3.25. D. H. G. Pelegrine and M. T. M. S. Gomes, Whey protein solubility curves at several temperature values, *Ciencia e Natura, UFSM*, 2008, **30**, 17-25.

- 3.26. C. Y. Tai and F. -B. Chen, Polymorphism of CaCO_3 , Precipitated in a Constant-Composition Environment, *AIChE J.*, 1998, **44**, 1790-1798.



Annexure-Chapter 3

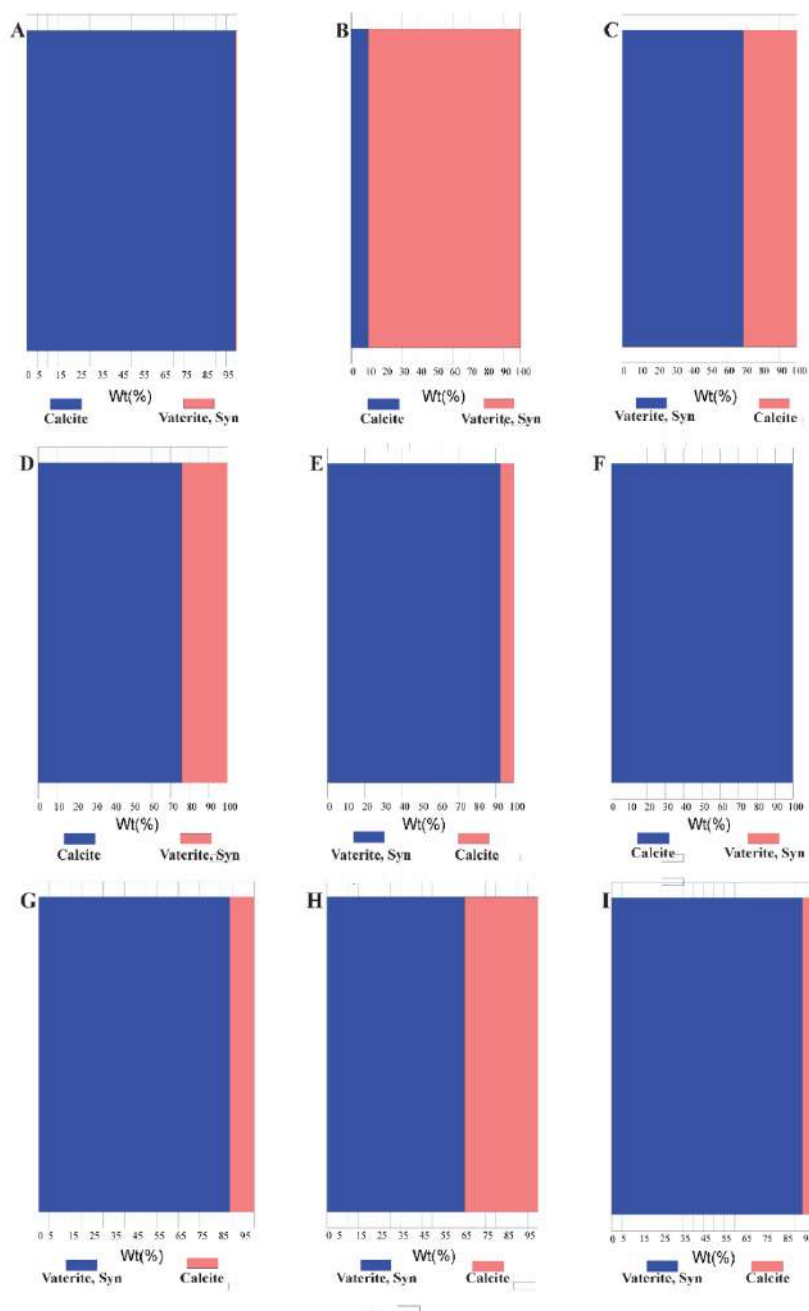


Fig. A3.1: Quantitative analysis result data for the CaCO_3 minerals obtained:(A) under controlled conditions; (B) in presence of 50 mg of whey protein; (C) in presence of 30 mg of whey protein; (D) under reverse sequence of addition; (E) at 60 °C; (F) at 10 °C; (G) at pH=5; (H) at pH=4; (I) in presence of electrolyte (NaCl) of concentration 100 mM.

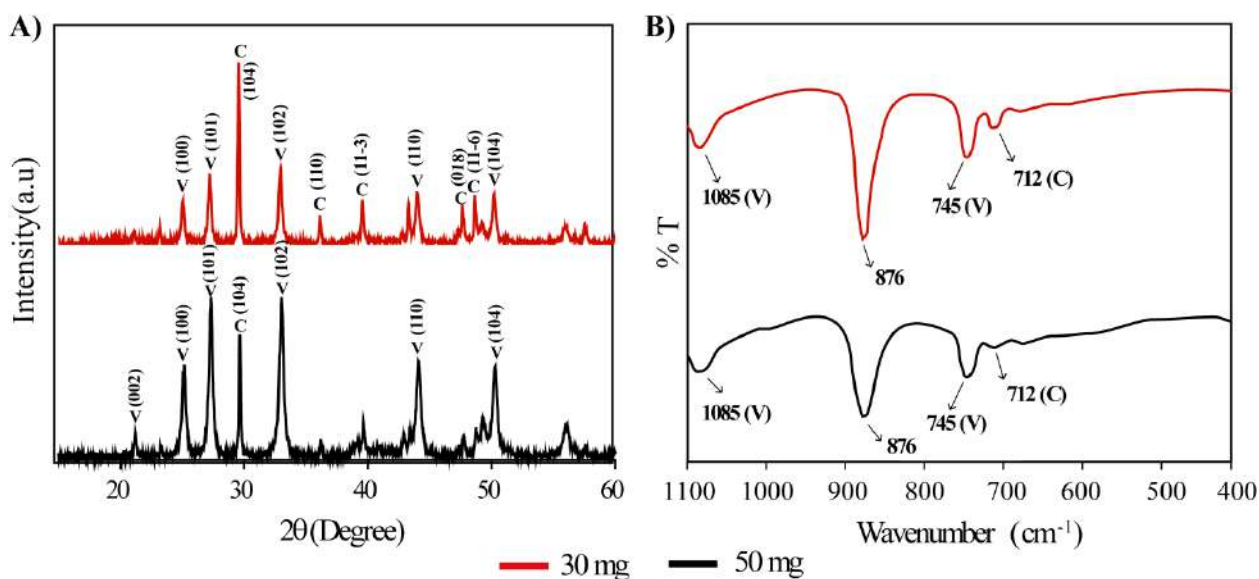


Fig. A3.2: A) PXRD pattern and B) FT-IR spectra of CaCO_3 particles at **different concentrations** of the template.

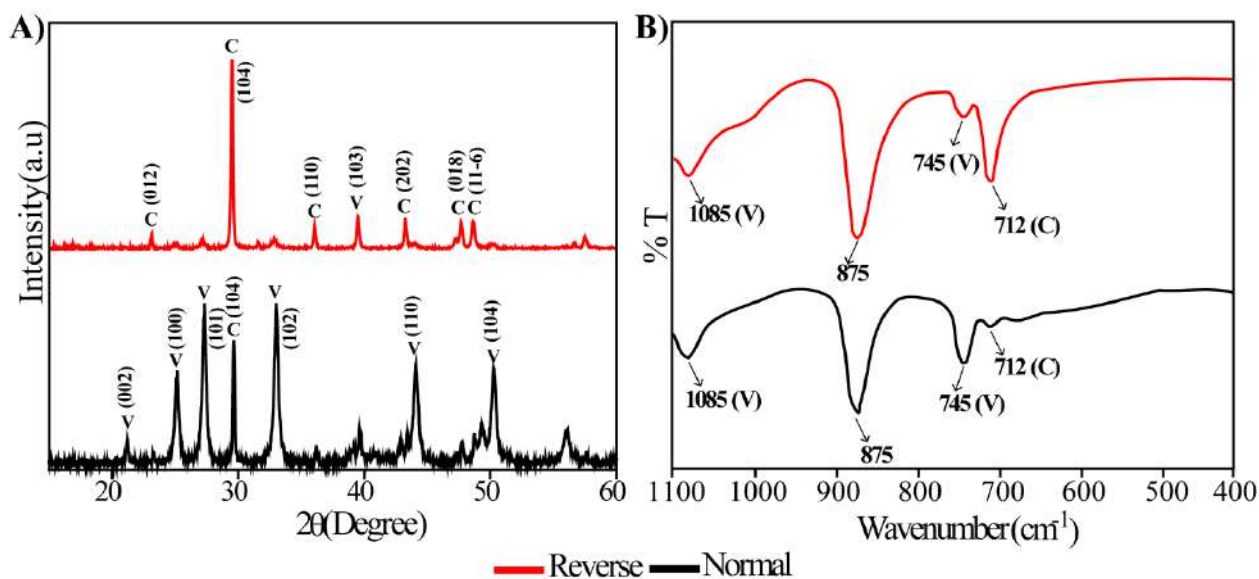


Fig. A3.3: A) PXRD pattern; B) FT-I.R. spectra of CaCO_3 minerals on varying the **sequence of addition**.

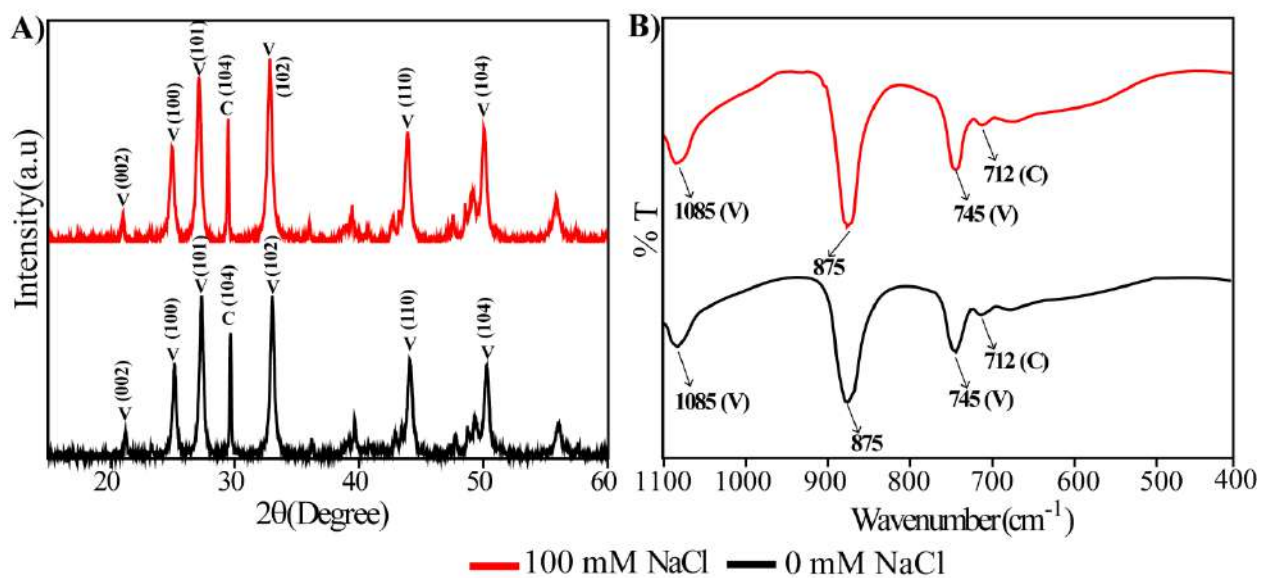


Fig. A3.6: A) PXRD pattern; B) FT-I.R. spectra of CaCO_3 minerals at different ionic strengths of the solution.

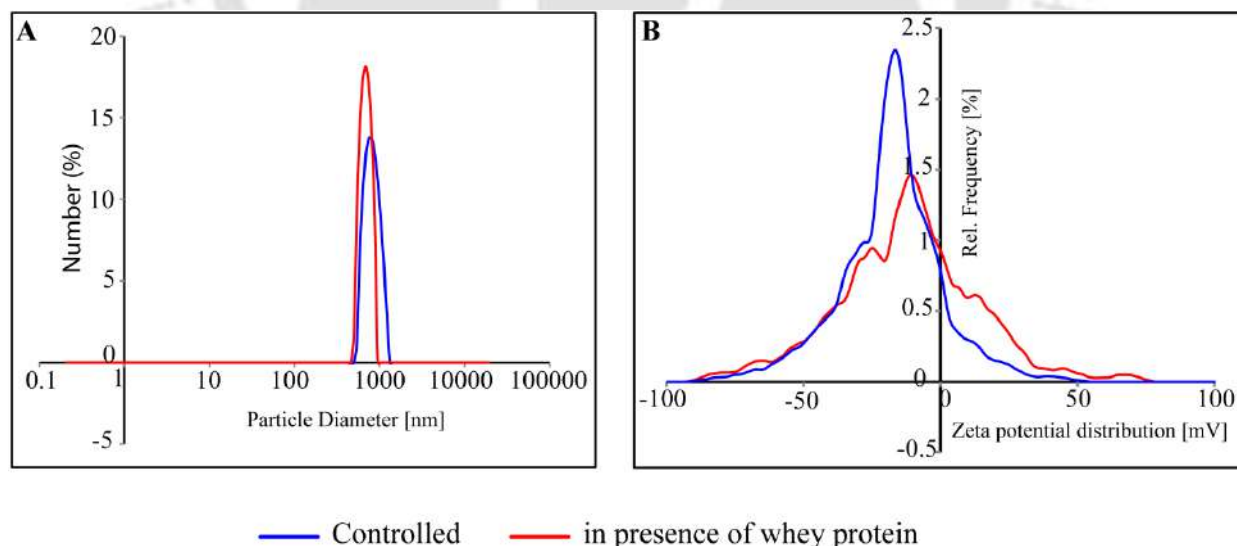


Fig. A3.7: A) DLS based particle size analysis; B) Zeta Potential of CaCO_3 minerals in the presence and in the absence of the template whey protein.

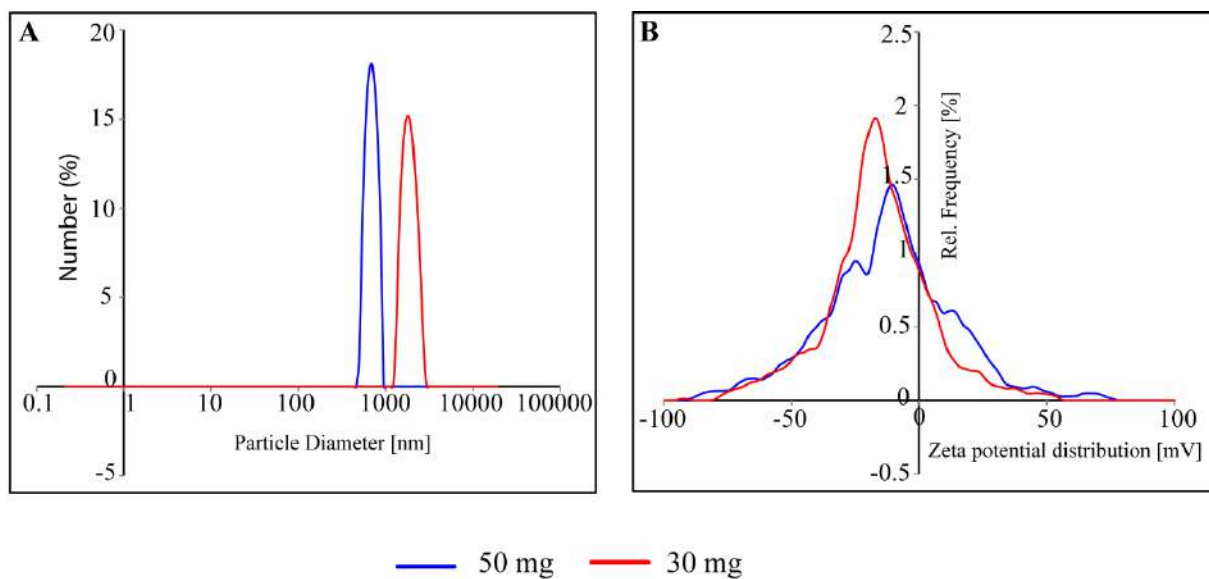


Fig. A3.8: A) DLS based particle size analysis; B) Zeta Potential of CaCO_3 minerals at different concentrations of the template.

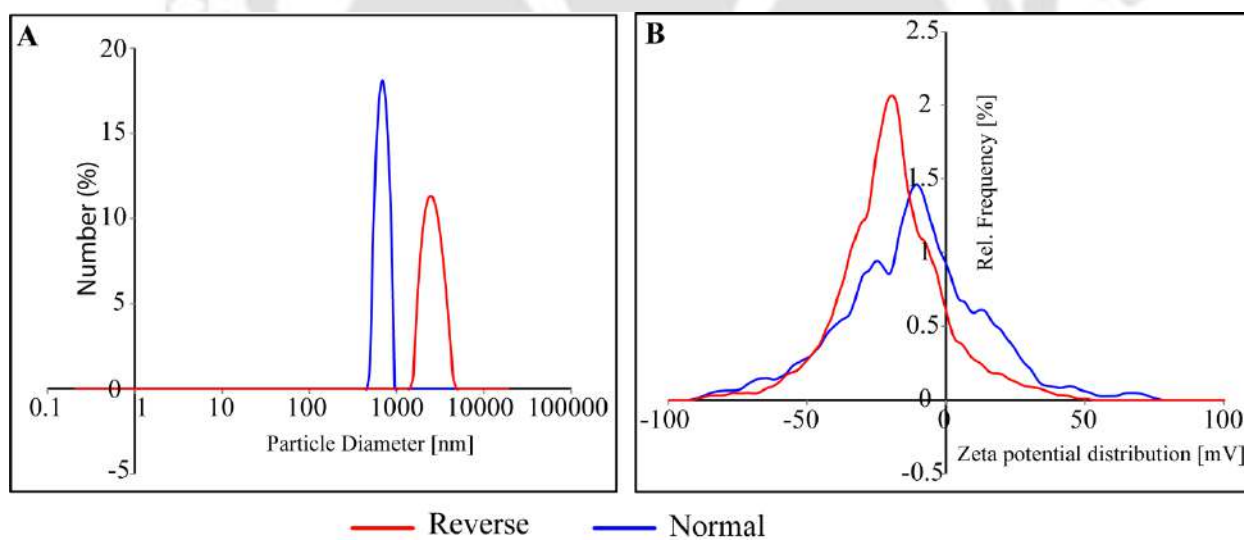


Fig. A3.9: A) DLS based particle size analysis; B) Zeta Potential of CaCO_3 mineral on varying the sequence of addition.

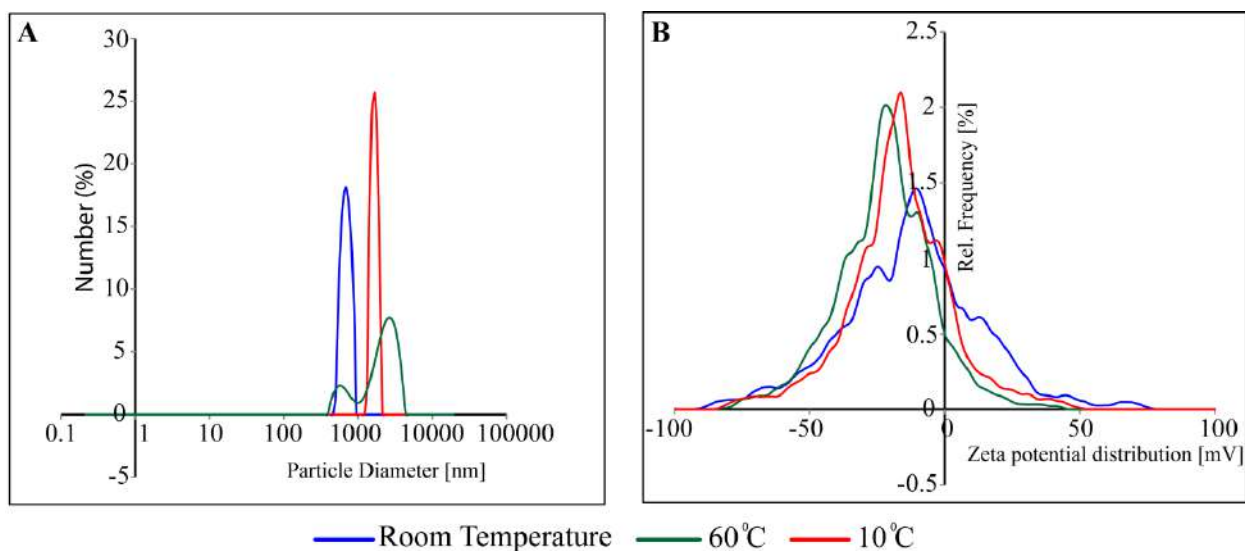


Fig. A3.10: A) DLS based particle size analysis; B) Zeta Potential of CaCO_3 minerals at different temperature conditions.

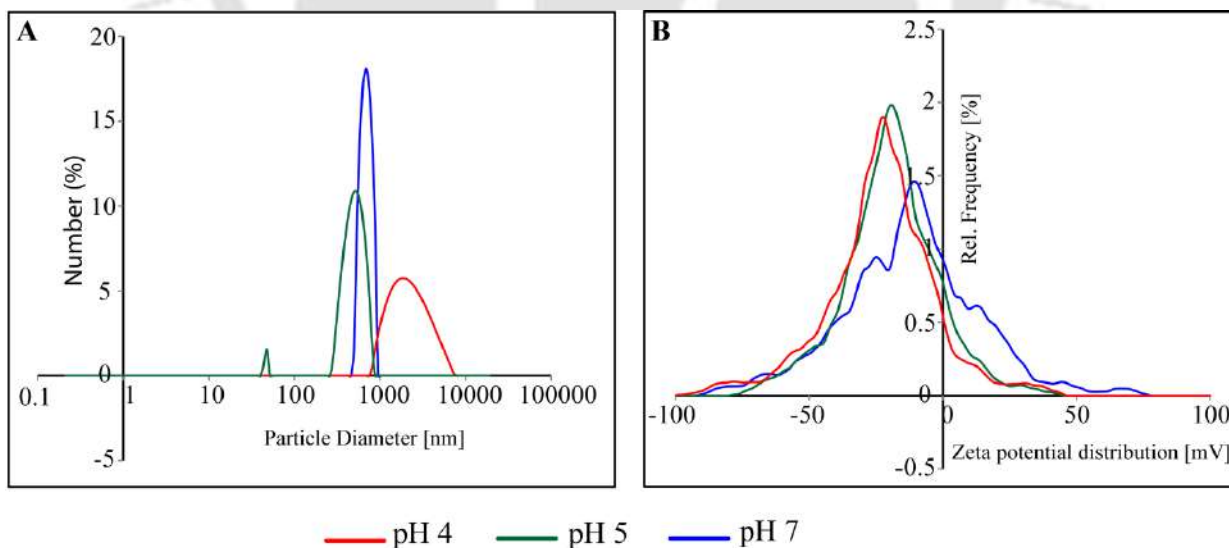


Fig. A3.11: A) DLS based particle size analysis; B) Zeta Potential of CaCO_3 minerals at different pH conditions.

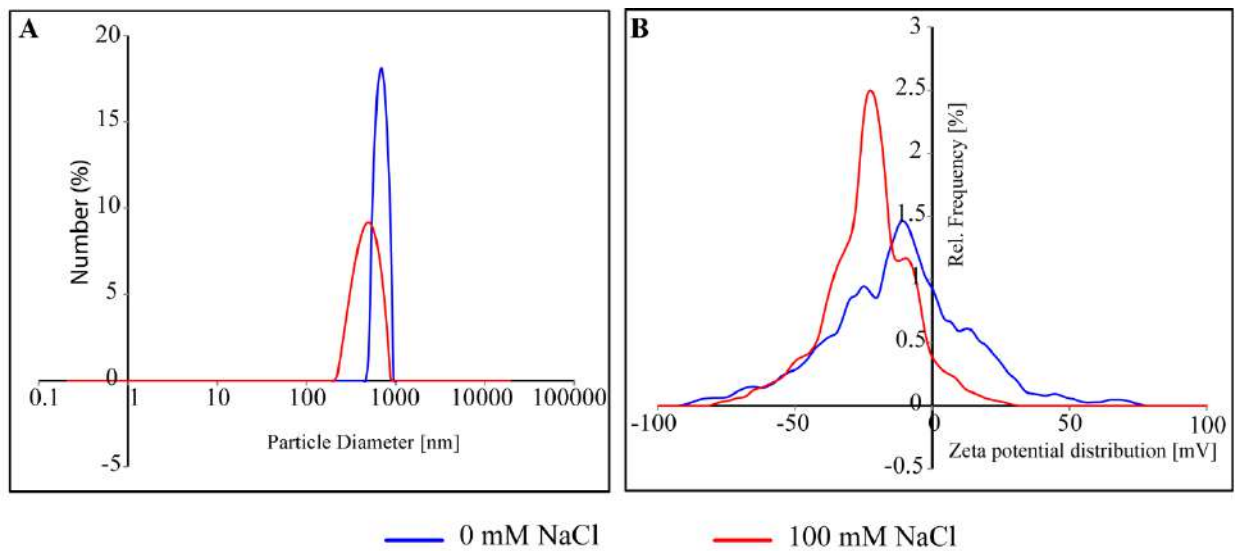


Fig. A3.12: A) DLS based particle size analysis; B) Zeta Potential of CaCO₃ minerals at different ionic strength of the solution.

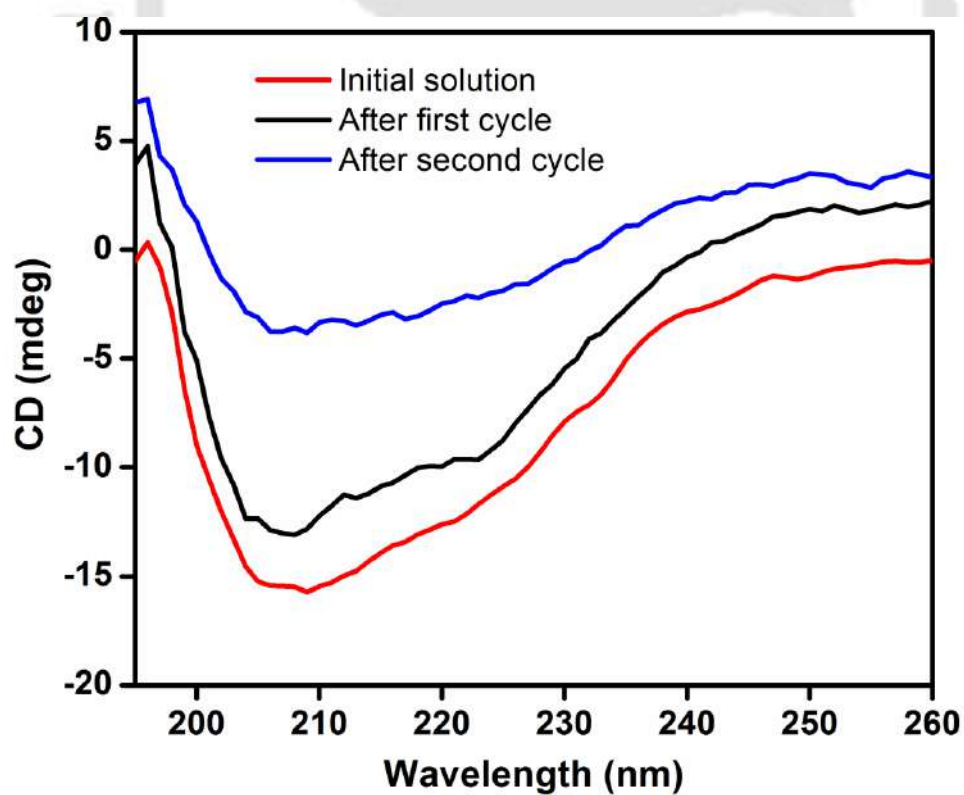


Fig. A3.13: Circular Dichroism Spectra of whey protein from the initial solution and the filtrates after the first and the second cycle.

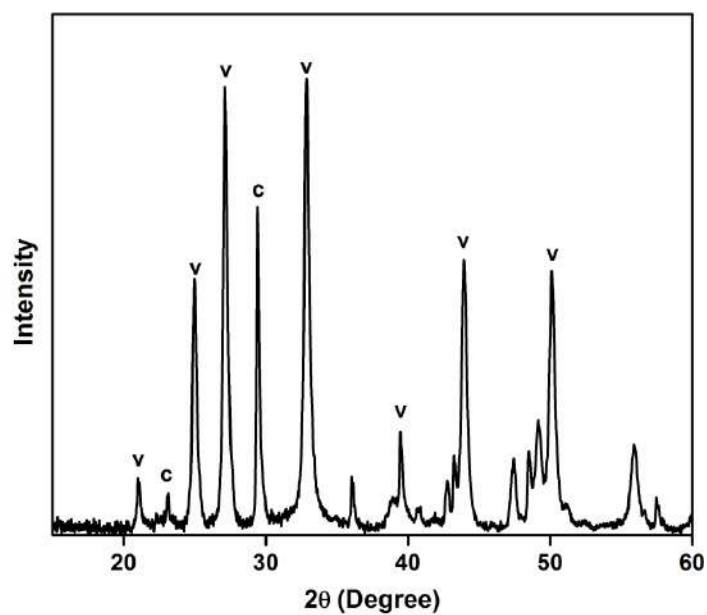


Fig. A3.14: Pxr pattern of the CaCO_3 particles precipitated by reusing the template whey protein recovered after the first cycle.

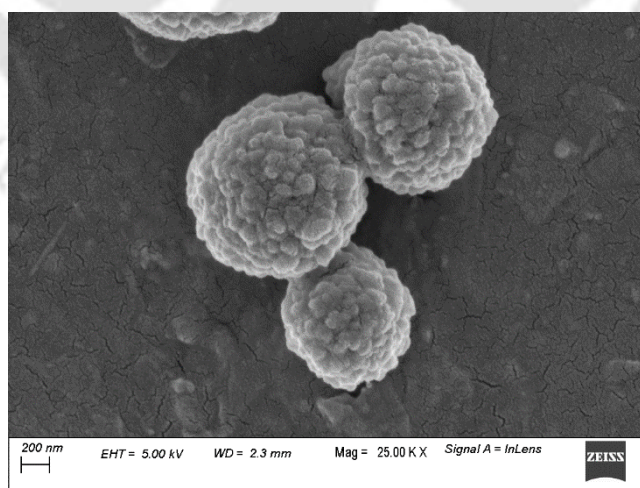


Fig. A3.15: FESEM image of the CaCO_3 particles precipitated by reusing the template whey protein recovered after the first cycle

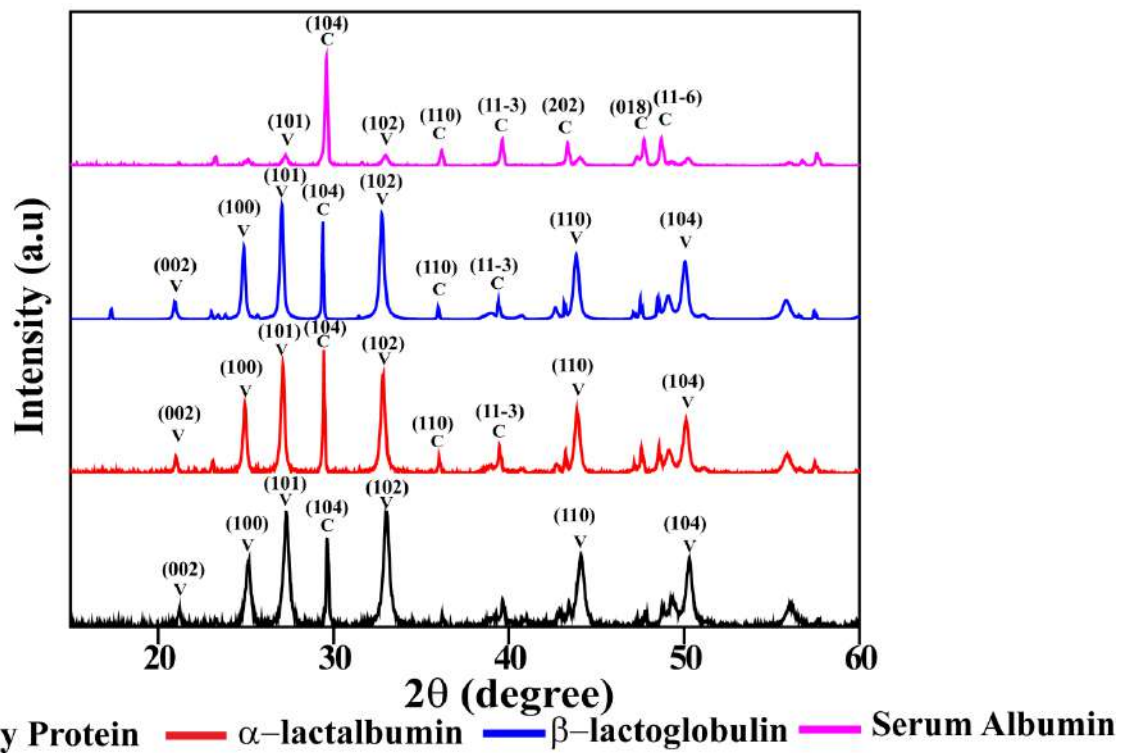


Fig. A3.16: PXRD pattern of CaCO_3 prepared using Whey Protein and its components.

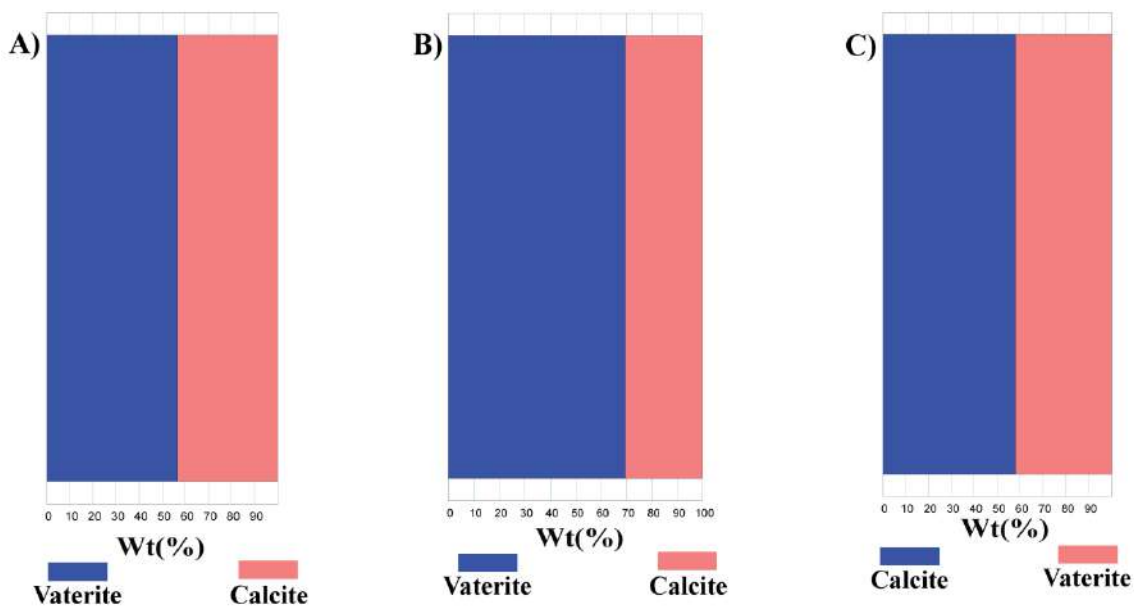
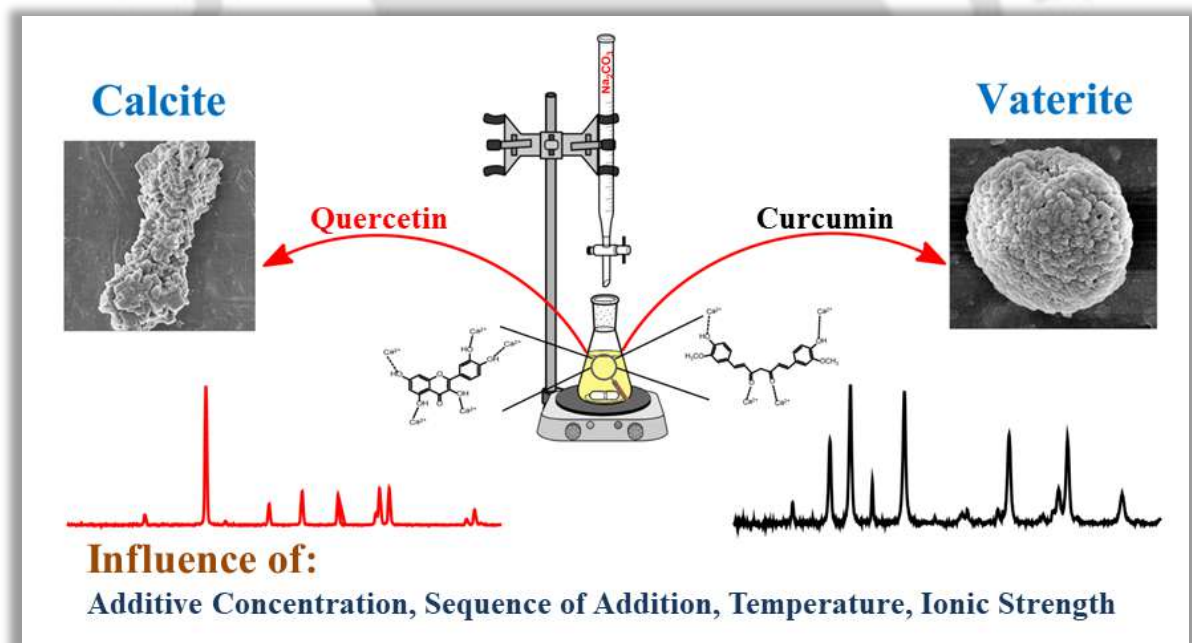


Fig. A3.17: Quantitative analysis result data for the CaCO_3 minerals obtained using (A) α -lactalbumin; (B) β -lactoglobulin and (C) serum albumin.

Role of curcumin and quercetin as additives in the *in vitro* biomineralization of CaCO_3 : A comparative study on phase modulation



4.1 Introduction

Biomaterials based on CaCO_3 constitute a large part of the biomaterial world. Almost all organisms use CaCO_3 as a constituent of their skeleton and protective shells. Fundamentally, there are two modes of biomaterialization; biologically induced mineralization and boundary-organized biomaterialization. The latter is of interest to us as the inorganic materials are grown within or on some organic matrix produced by organisms. These organic matrices behave as templates and dictate the process of biomaterialization.^{4.1-4.3} Biomaterials based on calcium grow on organic molecules containing oxygen and nitrogen atoms. Ca^{2+} prefers oxygen-containing donor ligands; attributed to the hard acid-hard base interactions.^{4.4} The additive changes the activation energy of nucleation which facilitates the formation of unstable phases.^{4.5}

In our continuing efforts to understand the bioinspired synthesis of CaCO_3 in the previous work,^{4.6} we used the complex biopolymer whey protein, which led to the selective formation of the vaterite phase. But the vaterite particles that had formed were not stable in solution for more than twelve hours. Therefore, to address the issue of stability, we decided to assign an organic molecule with comparatively lower molecular weight and simpler structure compared to whey protein. Curcumin, a diarylheptanoid, consisting of two aromatic rings is the primary natural polyphenol found in the rhizome of *Curcuma longa* (turmeric) and in other *Curcuma* species.^{4.7,4.8} The presence of two phenolic groups and two ketonic groups as substituents makes curcumin an excellent candidate to bind to Ca^{2+} . Curcumin has a large number of health benefits,^{4.9} such as aiding in the management of oxidative and inflammatory conditions,^{4.10,4.11} arthritis,^{4.12} metabolic syndrome^{4.13} and anxiety. It is known to show potential anti-cancer activities as well as beneficial for the kidneys^{4.7,4.14} and it also helps manage inflammation and muscle soreness acquired during sports and exercise sessions, thus enhancing recovery and performance in athletes. Additionally, a regular intake of relatively low dose of the complex can improve the overall health of people even though they may not have a diagnosed health condition. Most of the health benefits of curcumin can be attributed to its antioxidant and anti-inflammatory effects.^{4.9,4.11} Surprisingly, in spite of all these benefits, the *wonder* molecule curcumin has never been studied in the field of biomaterialization, as a component in research dealing with calcium-based minerals such as bones. So in this work, we tried to bring curcumin into focus by subjecting it as an additive for *in vitro* Ca biomaterialization. Also, its easy availability makes curcumin a suitable organic molecule for our study. Additionally, a comparative analysis was performed using another similar molecule, *quercetin*, a flavonoid, also a polyphenol, a bio-friendly compound used as a natural flavor in various foods and

beverages.^{4.15} The modification of CaCO_3 morphology especially that of calcite, regulated by templates, additives and operating conditions, has also been a focus of biomimetic research.^{4.16-}
^{4.21} We also studied the role of various external parameters on the morphology of the calcite particles obtained using quercetin. Similar studies were performed to understand the role of external parameters on the phase, morphology and sizes of the CaCO_3 particles during curcumin-directed biomineralization. The maturation of phase in solution with time was also studied to determine the effectiveness of curcumin in stabilizing the unstable vaterite in water.

4.2 Results and Discussions

The effect of the additives and various parameters on the phase transformation, morphology and phase maturation of CaCO_3 has been explained.

4.2.1 Influence of Curcumin and Quercetin in CaCO_3 biomineralization

The curcumin directed *in vitro* biomineralization of CaCO_3 led to the highly selective formation of vaterite, the least stable among the three crystalline phases of CaCO_3 with a very small amount of calcite. The FT-IR spectrum, Fig. 4.1(B), of the particles, showed high-intensity signals at 745 cm^{-1} , 875 cm^{-1} and 1085 cm^{-1} characteristic of the vaterite phase with the presence of a very weak signal at 712 cm^{-1} suggested the small amount of calcite that was formed. The PXRD pattern, Fig. 4.1(A), showed the formation of vaterite selectively over calcite as high-intensity peaks at 2θ values equal to 21.07, 25.59, 27.29, 33.11, 43.98 and 50.41 identical to vaterite can be seen as compared to the much weaker calcite peaks at 2θ values equal to 29.62 and 49.22. These peaks match well with the standard PDF data for the vaterite and the calcite phase of CaCO_3 (ICSD 00-060-0483 and 00-047-1743 respectively). From the quantitative analysis, Fig. A4.1(A), it was found that the percentage of vaterite formed was 90%. Fig. 4.1(C) shows the spherical vaterite particles in bulk and Fig. 4.1(D) shows a high-resolution FESEM image of a single particle. The hydrodynamic diameter and the zeta potential of the particles obtained from the DLS experiments were 1532.1 nm and -16.8 mV, respectively, Fig. A4.2(A) and (B). When the precipitation was done in the presence of quercetin, the most stable calcite phase had formed to 100%, Fig. A4.1(B), analogous to the case where no additive was used. But in this case, the morphology of the particles was different. Unlike the usual rhombohedral calcite particles, the particles formed were of dumbbell shape, as shown in the FESEM images. Fig. 4.1(E) shows the particles in numbers and Fig. 4.1(F) shows a high-resolution image focusing on one particular dumbbell-shaped entity.

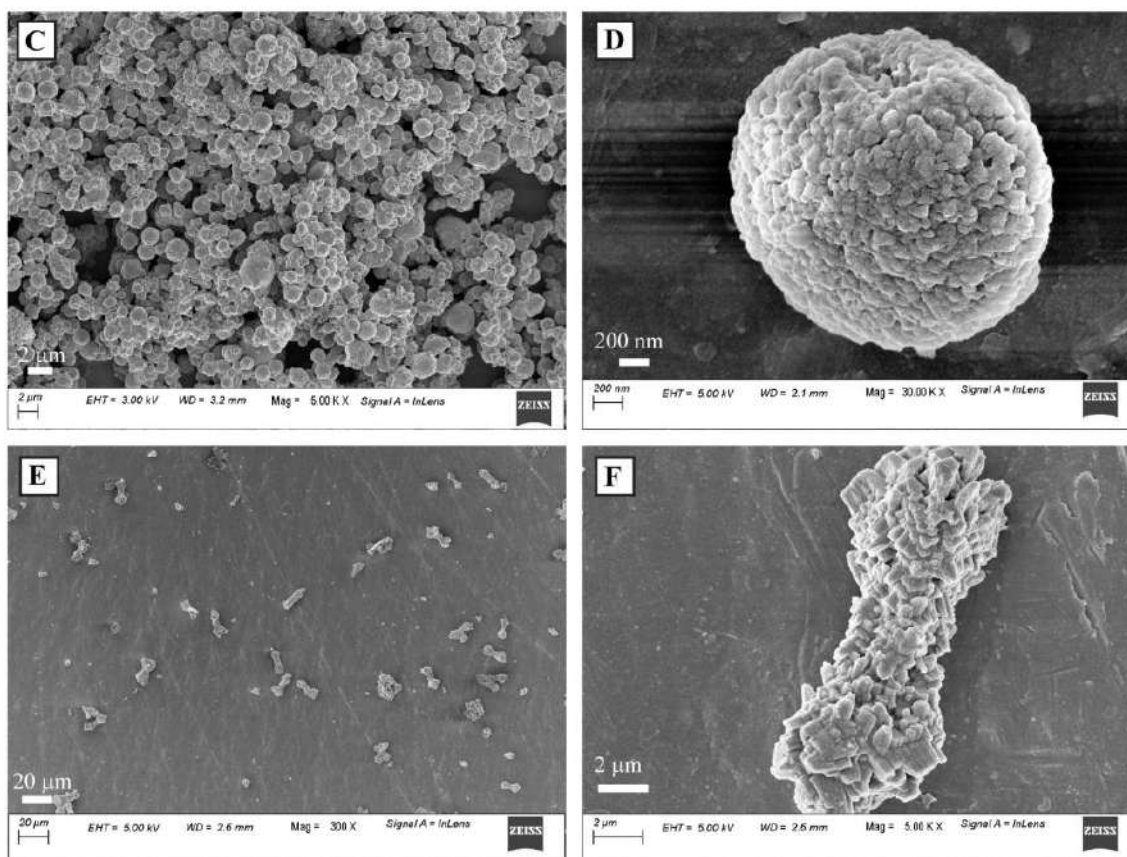
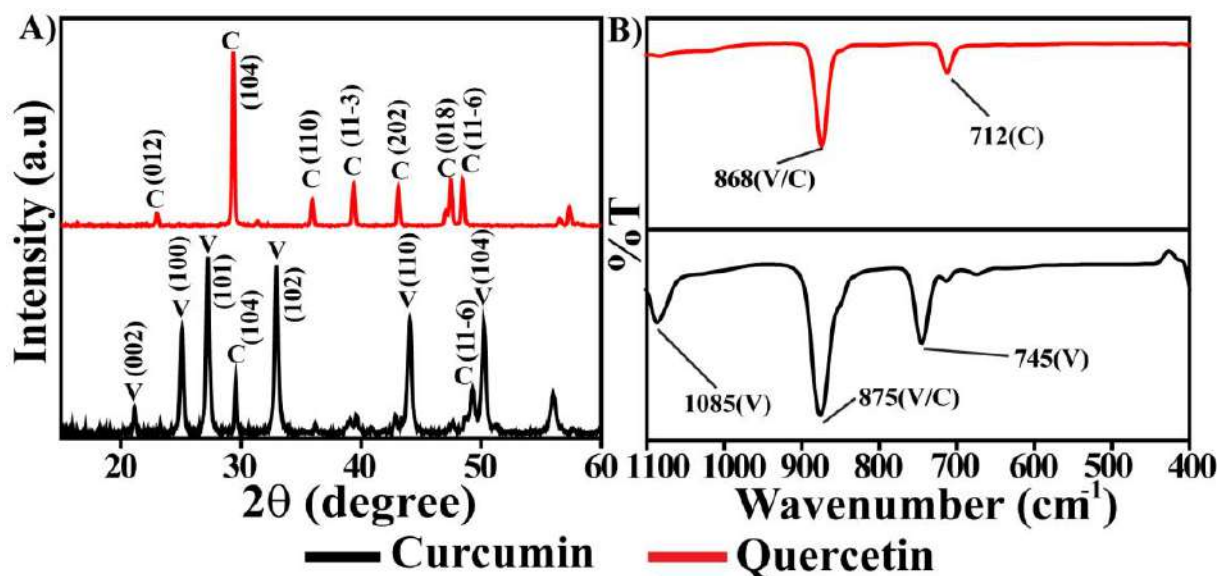
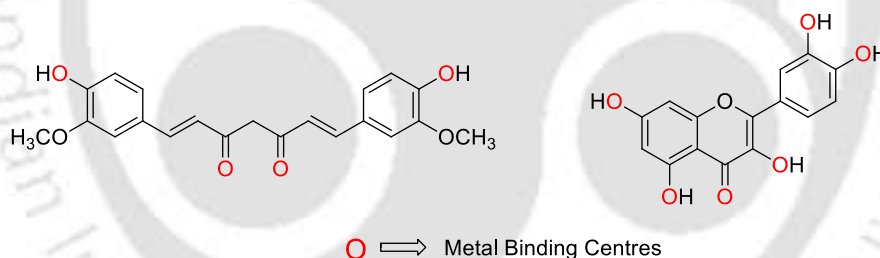


Figure 4.1: (A) PXRD pattern; (B) FT-IR spectra of CaCO_3 particles in the presence of curcumin and quercetin; (C) and (D) FESEM Images of CaCO_3 in the presence of curcumin and (E) and (F) FESEM Images of CaCO_3 in the presence of quercetin.

The FT-IR spectrum, Fig 4.1(B), with peaks at 712 cm^{-1} and 875 cm^{-1} suggested the specific formation of calcite. In the PXRD pattern, Fig. 4.1(A) peaks at 2θ values equal to 23.01, 29.39, 35.84, 39.30, 43.18, 47.44 and 48.50 identical to the standard PDF data for calcite (ICSD 00-047-1743) suggested the presence of only the calcite phase without the trace of any

other phase. The hydrodynamic diameter of these particles obtained was 2391.4 nm and the zeta potential was found to be -17.8 mV, Fig. A4.2(A) and (B).

It was intriguing to see that although both the additives possess structural similarity as they both contain phenolic groups, therefore, a number of –OH groups, yet only curcumin was able to stabilize the least stable vaterite. The affinity of both curcumin and quercetin towards Ca^{2+} binding may be attributed to the negative centres due to the –OX groups. The additive-ion binding between curcumin and quercetin and Ca^{2+} has been illustrated in **Scheme 4.1**. This additive-ion binding is responsible for the mechanism of the biomineralization process. From the observations in terms of the phase obtained, curcumin raises the free energy of nucleation, ΔG_n of calcite to a higher value than that of vaterite leading to the precipitation of the vaterite phase before the calcite phase.^{4,5} Quercetin was not quite able to stabilize the vaterite phase but the observations in terms of morphology tell us that the presence of quercetin did not allow the calcite phase to attain the usual and very stable rhombohedral crystal morphology. Rather, we acquired a dumbbell-shaped morphology of the calcite particles which was another fascinating observation in terms of the CaCO_3 morphology being regulated by an additive.^{4.17-4.21}



Scheme 4.1: Metal binding centres of A) Curcumin and B) Quercetin.

The molecules curcumin and quercetin were used only as additives for the biomineralization process. That is why their concentration taken was considerably low and the precipitation process was performed in a very steady manner with continuous stirring such that the homogeneity is maintained throughout the reaction. The simultaneous or subsequent loading of curcumin and quercetin on the biomineralized CaCO_3 was not considered. So after the mineralization process, any excess of these organic molecules were washed away with acetone. The FT-IR spectra, Fig. A4.3(A) and (B), wherein a comparison between the mineralized CaCO_3 with that of curcumin and quercetin can be drawn. It gives us clear evidence that no excess amount of curcumin and quercetin were present in the respective mineralized CaCO_3 suggesting that only a very

minute amount of the molecules were involved in the additive role and most probably by their incorporation into the CaCO_3 single-crystal. In Fig. A4.3(A), we see the characteristic peaks for curcumin at 1133 cm^{-1} due to C-O-C stretching, 1512 cm^{-1} due to aromatic C=C bending and the peaks at 1580 cm^{-1} and 1625 cm^{-1} due to C=O symmetric and asymmetric stretching. These peaks are not present in the spectrum of the mineralized vaterite. Similarly, in Fig. A4.3(B), the characteristic peaks of quercetin at 1163 cm^{-1} due to C-O-C stretching, 1515 cm^{-1} due to aromatic C=C bending and the peaks at 1605 cm^{-1} and 1654 cm^{-1} due to C=O symmetric and asymmetric stretching are not present in the spectrum of the mineralized calcite.

The ratio of the concentration of the additive used to the concentration of the Ca^{2+} and CO_3^{2-} in each experiment was approximately 1:100. Considering this, the efficiency of the additive in terms of the amount of CaCO_3 obtained was significantly high. Quantitative precipitation of CaCO_3 was attained in all cases.

4.2.1.1 CaCO_3 Phase Maturation

The CaCO_3 crystals formed in the *in vitro* biomineralization using curcumin and quercetin were studied for phase maturation over a period of time in order to observe any change in phase or morphology that may arise. The spherical vaterite particles that were synthesized using curcumin were allowed to remain in solution for several hours to observe the stability and the eventual maturation of the crystals. The usual procedure of precipitation by the dropwise addition of CO_3^{2-} took 3 hours, following which the precipitate was filtered. Here we obtained 90% of vaterite phase, Fig. A4.1(A), with spherical morphology, Fig. 4.3(A). Three different syntheses were carried out simultaneously and the resulting precipitate in each case was allowed to remain in solution for 12 hours, 18 hours and 24 hours. The precipitate was then filtered, washed and dried according to the procedure already mentioned and subjected to the characterization analyses. From the FT-IR spectrum, Fig. 4.2(B) it was observed that after 12 hours, the vaterite phase dominated the product as high-intensity peaks at 745 cm^{-1} , 875 cm^{-1} and 1085 cm^{-1} characteristic of vaterite were observed. Also, a faint signal at 712 cm^{-1} was observed suggesting the formation of a small amount of calcite. The PXRD pattern, Fig. 4.2(A), suggested that the vaterite phase dominated the product as high-intensity peaks due to vaterite could be seen. The quantitative analysis result, Fig. A4.1(C), showed that the product formed contained 83% vaterite and 17% calcite.

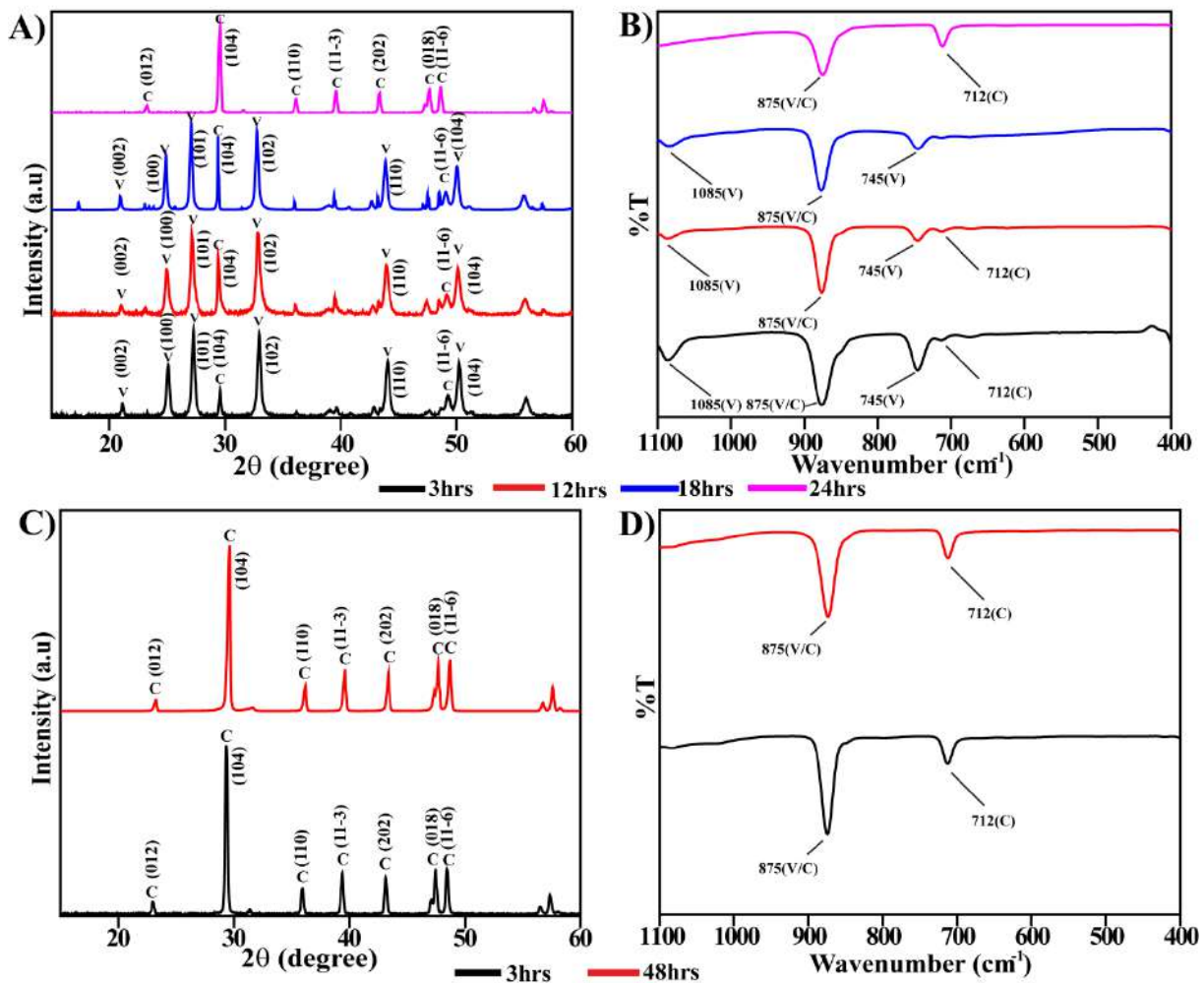


Figure 4.2: (A) PXR D pattern and (B) FT-IR spectra of CaCO₃ particles in the presence of curcumin at different time intervals; (C) PXR D pattern; (D) FT-IR spectra of CaCO₃ particles in the presence of quercetin at different time intervals.

The FESEM images, Fig. 4.3(B), A4.10(C) and (D) show particles with spherical morphology. Hence the CaCO₃ particles prepared using curcumin remained stable in solution for 12 hours without any significant change in phase or morphology. After 18 hours, it was observed that the percentage of vaterite was 70% and that due to calcite was 30%, Fig. A4.1(D). The FT-IR spectrum, Fig. 4.2(B), showed the presence of both the phases, peaks at 745 cm⁻¹ and 1085 cm⁻¹ due to vaterite and the peak at 712 cm⁻¹ due to calcite. The PXR D pattern, Fig. 4.2(A), suggested the formation of both the phases, the least stable vaterite phase dominant over the calcite phase. From the FESEM images, Fig. 4.3(C), A4.10(E) and (F), we can see the presence of the rhombohedral calcite crystals along with the spherical vaterite particles. Therefore, even after 18 hours of incubation of the CaCO₃ precipitate in the solution, the least stable vaterite phase was obtained highly selectively suggesting the

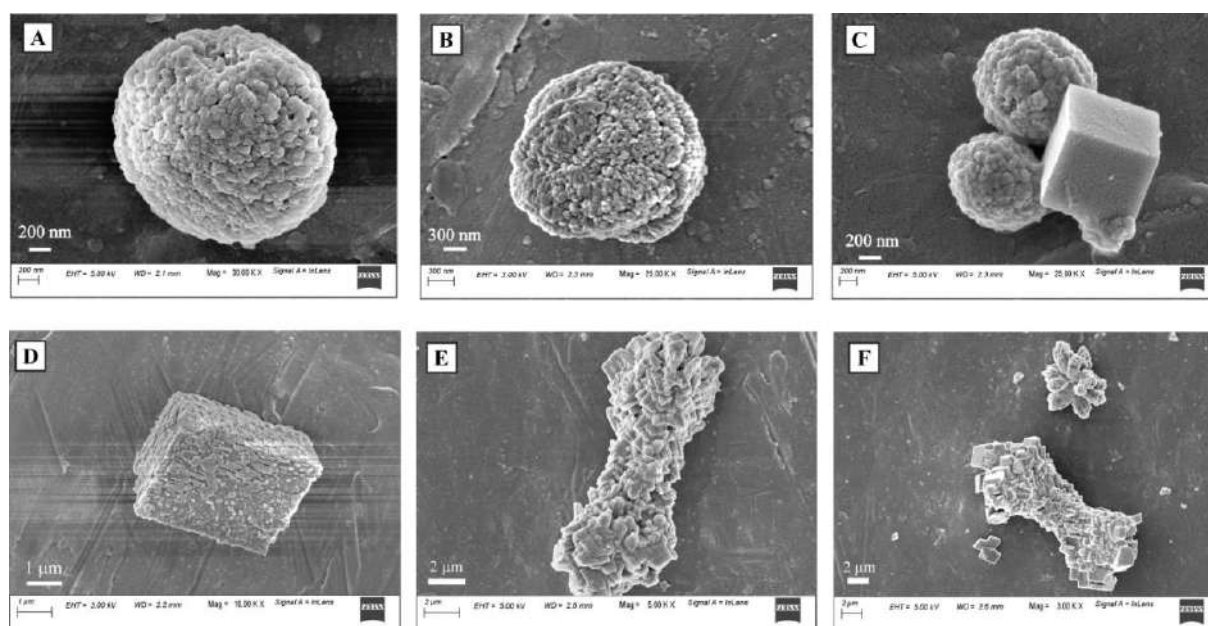


Figure 4.3: FESEM Images of CaCO_3 (A) in the presence of curcumin after 3 hours; (B) in the presence of curcumin after 12 hours; (C) in the presence of curcumin after 18 hours; (D) in the presence of curcumin after 24 hours; (E) in the presence of quercetin after 3 hours; (F) in the presence of quercetin after 48 hours.

efficient role played by curcumin in the *in vitro* biomineralization.

On characterization of the particles obtained after 24 hours of incubation, it was observed that the vaterite phase was no longer present and only the calcite phase had formed. The maturation of the phase from the least stable to the most stable was completed after 24 hours of incubation in solution. This was proved by both FT-IR spectroscopy and the PXRD pattern. In the FT-IR spectrum, Fig. 4.2(B) only the characteristic signals due to calcite at 712 cm^{-1} and 875 cm^{-1} were observed with no trace of the vaterite signals. Similarly, in the PXRD pattern, Fig. 4.2(A) only the calcite peaks were obtained. The morphology of the particles obtained was analogous to that of matured calcite crystals, Fig. 4.3(D), and A4.10(G) and (H). Thus, after studying the phase maturation with time, it was observed that the metastable vaterite phase mineralized using curcumin showed aqueous stability of more than 18 hours.

Although quercetin resulted in the formation of the stable calcite phase, a similar study was carried out to observe any change in morphology and size of the particles that may arise with time. It was observed that even after 48 hours of incubation in solution, the morphology of the particles had not changed and was similar to the ones obtained immediately after the precipitation. As can be seen from the FESEM images, Fig. 4.3(E), 4.3(F), A4.11(C) and A4.11(D), CaCO_3 particles that were obtained had a dumbbell-shaped morphology. Also, from the FT-IR spectrum and the PXRD pattern, Fig. 4.2(C) and 4.2(D), no change was observed.

4.2.2 Effect of Variation in Parameters

4.2.2.1 Effect of additive concentration

The *in vitro* mineralization process was carried out by doubling the concentration of both curcumin and quercetin to that of the usual concentration. It was observed that on increasing the concentration of curcumin, the percentage of vaterite had gone up to ~93%, Fig. A4.1(F). The FT-IR spectrum, Fig. A4.3(B) gave signals at 745 cm^{-1} , 875 cm^{-1} and 1085 cm^{-1} characteristic of the vaterite phase and in the PXRD pattern, Fig. A4.4(A) high-intensity vaterite peaks had occurred whereas the calcite peaks were almost absent. The FESEM images, Fig. 4.4(B), A4.12(C) and (D) showed the formation of spherical vaterite particles, Fig. 4.4(A), A4.12(A) and (B). Hence, the role of curcumin in the nucleation of the unstable vaterite particles is further justified as on increasing its concentration, the percentage of the vaterite phase had increased. With quercetin, no change was observed on increasing the concentration. The calcite phase was obtained in both low as well as high concentration, Fig. A4.4(C) and (D) and the morphology of the particles were also the same, Fig. 4.4(C) and 4.4(D).

In another experiment, both curcumin and quercetin were added in the ratio 1:1 to specifically observe the role played by them in the mixture. From the FT-IR spectrum, Fig. A4.5(B), and the PXRD pattern, Fig. A4.5(A), it was clear that the calcite phase was specifically obtained, 100%, Fig. A4.1(G). The peaks at 712 cm^{-1} and 875 cm^{-1} in the FT-IR spectrum and the high-intensity

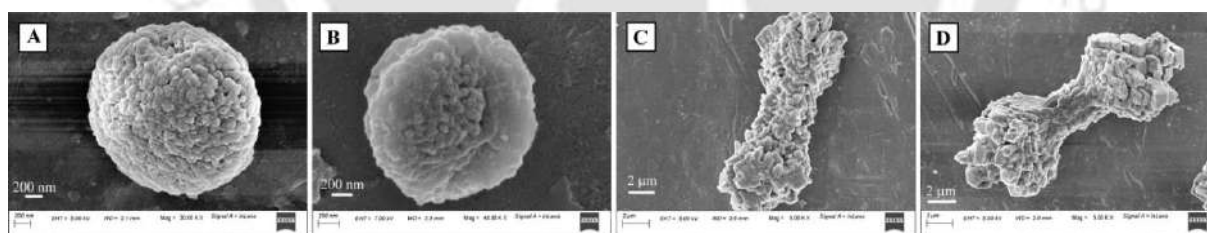


Figure 4.4: FESEM Images of CaCO_3 (A) at low concentration of curcumin; (B) at high concentration of curcumin; (C) at low concentration of quercetin; (D) at high concentration of quercetin.

calcite peaks with no vaterite peaks in the PXRD pattern justified the dominance of quercetin over curcumin during the precipitation when a mixture of both the compounds was used. The FESEM images, Fig. 4.5(A), (B) and (C), further justified this as the morphology of the particles obtained were of dumbbell shape, exactly similar to the ones that were obtained using quercetin. This may be attributed to the tendency of the CaCO_3 particles to attain the stable calcite phase. Although curcumin stabilizes the vaterite phase, the presence of quercetin and the tendency of the CaCO_3 to attain the stable state have facilitated the formation of the calcite phase.

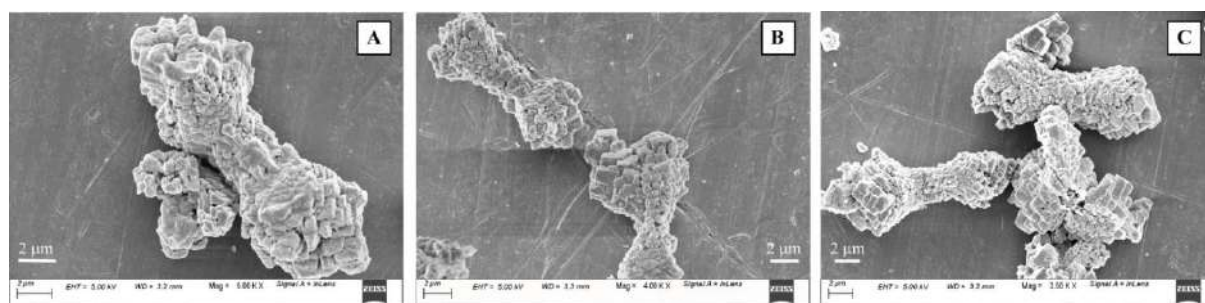


Figure 4.5: FESEM Images (A), (B) and (C) of CaCO_3 particles prepared in the presence of a mixture of curcumin and quercetin.

4.2.2.2 Effect of Sequence of addition

In this study, the sequence of addition of the ions was reversed. Initially, the anions CO_3^{2-} were allowed to interact with the additive followed by the dropwise controlled addition of the Ca^{2+} ions. In the case of curcumin, it was observed from the FT-IR spectrum, Fig. A4.6(B) that only the signals for the calcite phase at 712 cm^{-1} and 875 cm^{-1} were present and in the PXRD pattern, Fig. A4.6(A), the calcite peaks dominated with very low-intensity vaterite peaks. A needle-shaped morphology of the particles was seen from the FESEM images, Fig. 4.6(B), A4.13(C) and (D) which was different from the spherical morphology that was obtained in case of the usual

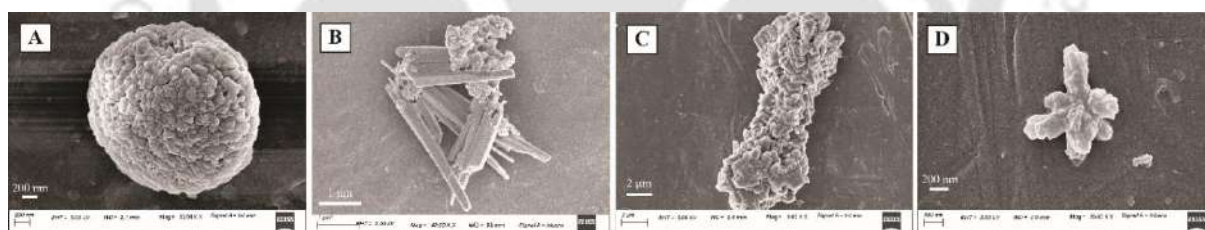


Figure 4.6: FESEM Images of CaCO_3 (A) on normal sequence of addition in the presence of curcumin; (B) on reverse sequence of addition in the presence of curcumin; (C) on normal sequence of addition in the presence of quercetin; (D) on reverse sequence of addition in the presence of quercetin.

sequence of addition, Fig 4.6(A), A4.13(A) and (B). These observations suggest that on reversing the sequence of addition, the role of the additive was neglected and rightly so as the oxygen atoms of the curcumin molecule would act as binding sites only for the Ca^{2+} and not so for the CO_3^{2-} . Hence, the mechanism of the role of the organic molecule curcumin in Ca-based biomineralization was further justified. Similarly, for quercetin, its activity was restricted on reversing the sequence of addition. Although the calcite phase formed had similarity to the one formed during the usual sequence of addition as can be seen from the FT-IR spectrum and PXRD data, Fig. A4.6(C) and (D), but the morphology of the particles had changed and we

obtained particles with no definite morphology, Fig. 4.6(D), A4.13(G) and (H) different from the ones obtained in the normal sequence of addition, Fig. 4.6(C), A4.13(E) and (F).

4.2.2.3 Effect of Temperature

The influence of temperature on the *in vitro* biomineralization of CaCO_3 in the presence of the organic molecules curcumin and quercetin were studied at three different temperatures; 10 °C, 25 °C and 80 °C. At 10 °C, in the presence of curcumin, it was observed that only the calcite phase had formed. This was supported by the FT-IR spectrum, Fig. A4.6(B), where only characteristic signals of calcite at 712 cm^{-1} and 875 cm^{-1} were observed and the PXRD pattern, Fig. A4.7(A), showed the presence of the calcite peaks only. The quantitative analysis result suggested ~100% calcite formation, Fig. A4.1(I). From the FESEM images, Fig. 4.7(A), A4.14(A) and (B), we can see the formation of rhombohedral calcite crystals. At 25 °C, the unstable vaterite phase had formed almost specifically to as high as ~90% over the stable calcite phase. The FT-IR spectrum, Fig. A4.7(B), gave high-intensity signals due to vaterite at 745 cm^{-1} , 875 cm^{-1} and 1085 cm^{-1} with a very weak calcite signal at 712 cm^{-1} . Similarly, the PXRD pattern, Fig. A4.7(A), gave strong peaks for vaterite. The morphology of the particles was spherical analogous to that of vaterite, Fig. 4.7(B), A4.14(C) and (D). At 80 °C, the FT-IR spectrum, Fig. A4.7(B), suggested the formation of calcite [76%, Fig. A4.1(J)] with a very small amount of vaterite. This was supported by the peaks at 712 cm^{-1} and 875 cm^{-1} in the FT-IR spectrum and similarly in the PXRD pattern, Fig. A4.7(A), the calcite peaks of high intensity with very low-intensity vaterite peaks were seen. The FESEM images, Fig. 4.7(C), S4.14(E) and (F), obtained showed the formation of rhombohedral calcite crystals along with some spherical vaterite particles. To draw a comparison, when similar experiments were performed for the formation of CaCO_3 at room temperature, 25 °C, i.e., by the precipitation reaction of CaCl_2 and Na_2CO_3 and under stirring conditions without using any additive, calcite was obtained.^{4,22} Similarly, in the presence of polyacrylic acid (PAA), the calcite phase with aggregate particles of regular plate-like shape was obtained.^{4,23} But using curcumin the stabilization of the metastable vaterite phase at room temperature was achieved, **Table A4.1**.

The influence of temperature on the phase and morphology of the CaCO_3 particles was also carried out with quercetin. Here, at all the three different temperatures; 10 °C, 25 °C and 80 °C, the calcite phase had formed which is supported by the peaks at 712 cm^{-1} and 875 cm^{-1} in the FT-IR spectrum, Fig. A4.7(D) and the PXRD pattern, Fig. A4.7(C). But the interesting fact drawn was in the form of morphology of the particles. At 10 °C, the particles formed had an

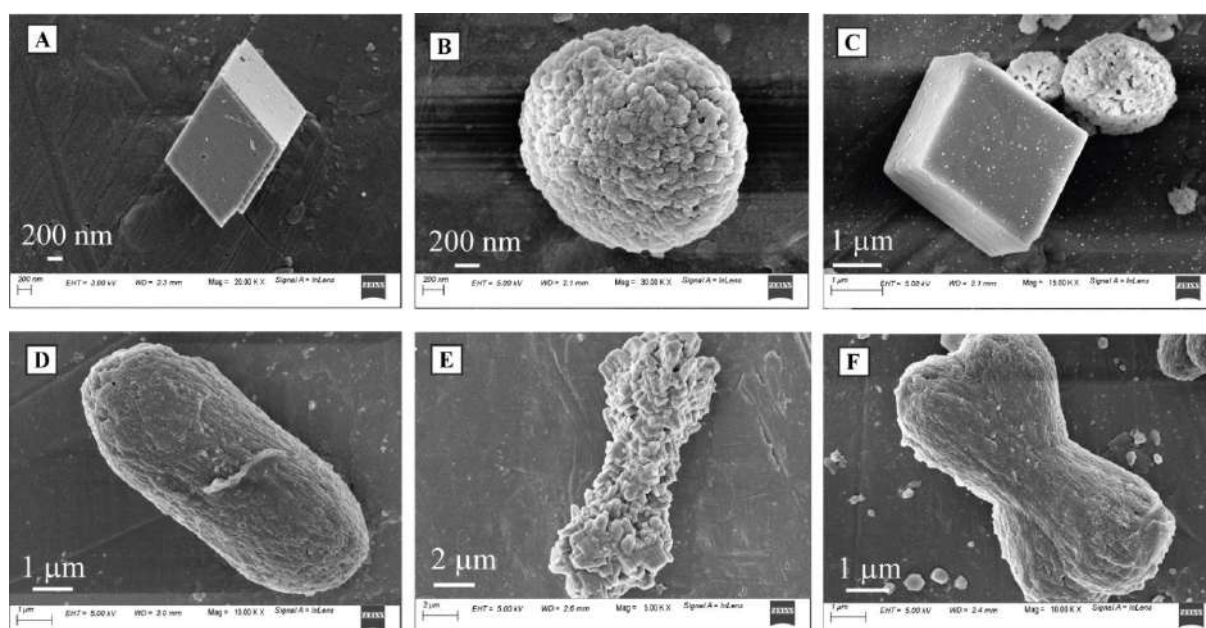


Figure 4.7: FESEM Images of CaCO_3 (A) at 10 °C in the presence of curcumin; (B) at 25 °C in the presence of curcumin; (C) at 80 °C in the presence of curcumin; (D) at 10 °C in the presence of quercetin; (E) at 25 °C in the presence of quercetin; (F) at 80 °C in the presence of quercetin.

elliptical shape, Fig. 4.7(D), A4.14(G) and (H). At 25 °C, Fig. 4.7(E), A4.14(I) and (J), the particles were of dumbbell shape whereas the particles formed at 80 °C were slightly different from those obtained at 10 °C as though the ellipsoids had narrowed towards the centre, giving it a dumbbell shape morphology, Fig. 4.7(F), A4.14(K) and (L), similar to the ones obtained at 25 °C but with a smoother surface. Hence, in the presence of quercetin, although the formation of the calcite phase had taken place, the tuning in morphology of the particles with changes in temperature was observed.

4.2.2.4 Effect of Ionic strength

The presence of an electrolyte during the precipitation of CaCO_3 tends to increase the solubility of CaCO_3 , hence promoting the transformation of the metastable vaterite to the most stable calcite phase. In this process, 100 mM NaCl was used to determine its influence on the *in vitro* biomineralization of CaCO_3 in the presence of the organic molecules. Two different experiments were carried with curcumin, one in the absence of NaCl and the other in the presence of NaCl (100 mM). It was observed that the percentage of vaterite formed in both cases were 90% and 98%, respectively, Figure A4.1(A) and (K). This was supported by the FT-IR spectrum, Fig. A4.7(B), and the PXRD pattern, Fig. A4.8(A), where only the vaterite peaks were observed. Similarly, the FESEM images, Fig. 4.8(A), 4.8(B), A4.15(A), (B), (C) and (D), further justified

the nucleation of the vaterite phase due to the spherical morphology as that of the vaterite particles.

With quercetin in the presence of the electrolytic solution, 100 mM NaCl, there was no change in phase. The calcite phase was obtained both in the absence and in the presence of NaCl, as can be seen from the FT-IR, Fig. A4.7(D), and the PXRD pattern, Fig. A4.7(C), but the morphology of the particles, Fig. 4.8(C), 4.8(D), A4.15(E), (F), (G) and (H), obtained were different. A dumbbell-shaped morphology was observed in both cases. In the presence of the electrolyte, we obtained particles with a smoother surface as compared to particles with a coarse texture in the absence of the electrolyte. The morphology of the calcite particles obtained in the presence of the electrolyte was analogous to those obtained at 80 °C with quercetin.

The presence of NaCl increases the solubility of CaCO₃ and this promotes the transformation of the metastable vaterite phase to the stabilized calcite phase.^{4,24} The resulting high concentration of CaCO₃ in solution promotes crystal growth. In this study, with the use of curcumin we were able to

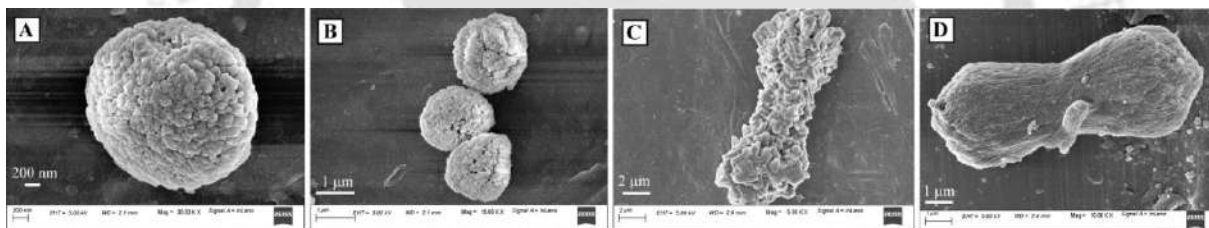


Figure 4.8: FESEM Images of CaCO₃ particles (A) with curcumin in the absence of an electrolyte; (B) with curcumin in the presence of 100 mM NaCl; (C) with quercetin in the absence of an electrolyte; (D) with quercetin in the presence of 100 mM NaCl.

obtain the metastable vaterite particles even in the presence of NaCl. The presence of curcumin in the medium had controlled the otherwise increase in solubility of the CaCO₃ particles in the presence of NaCl, **Table A4.2**. With quercetin, the calcite phase had formed, but the morphology of the particles was different from the usual rhombohedral morphology of the calcite crystals.

4.3 Conclusion

For the first time, the natural polyphenol *curcumin* with multiple health benefits was used to study its influence on Ca-based biomineralization. CaCO₃ particles were mineralized by an additive-directed *in vitro* biomineralization process wherein curcumin dictated the highly selective formation of the least stable crystalline phase vaterite to 90%. The vaterite particles

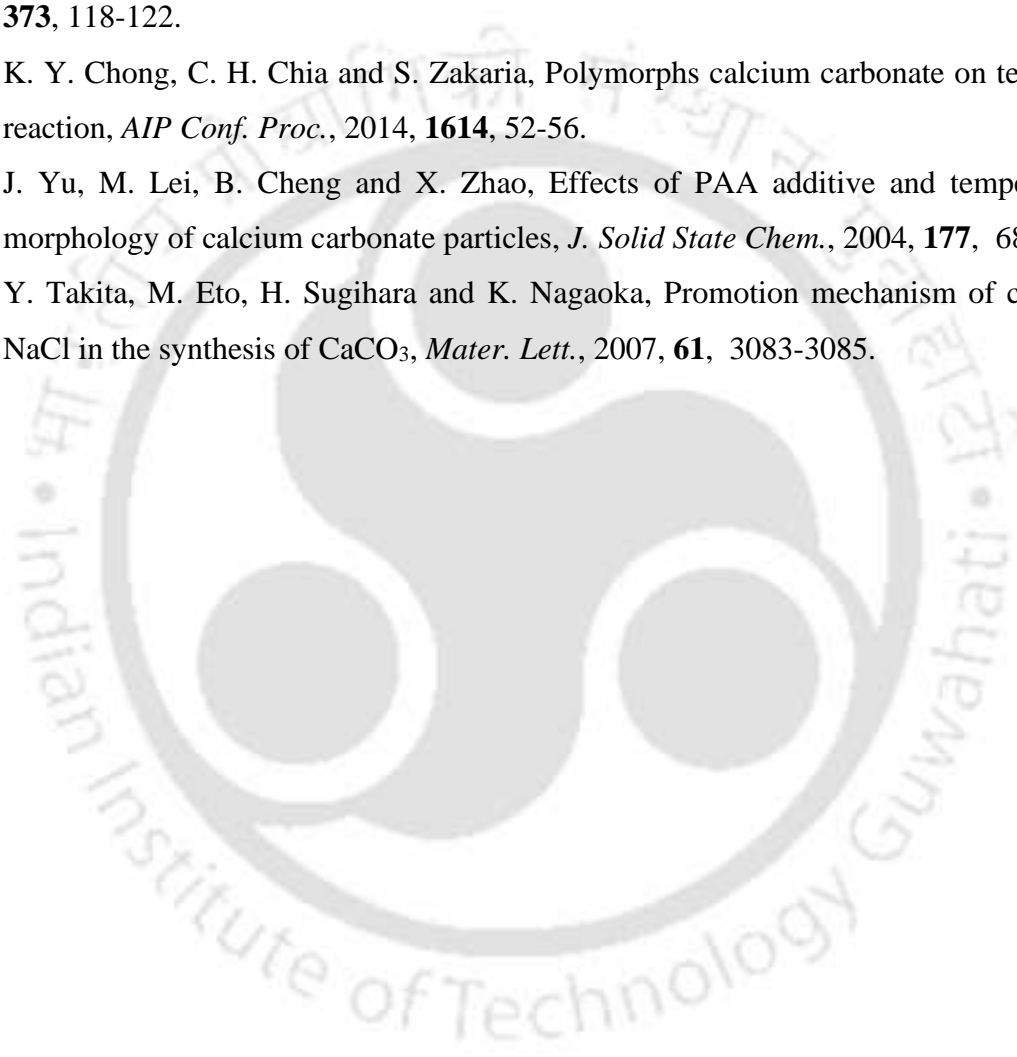
formed were stable in solution for more than 18 hours. A comparative study with *quercetin* was made due to its structural similarity with curcumin. It was fascinating to see that although quercetin possessed several donor oxygen atoms like curcumin, it could not stabilize the unstable vaterite phase. However, the shape of the calcite particles obtained here was different from the typical rhombohedral morphology; rather, a dumbbell-shaped morphology was obtained. During the *in vitro* CaCO₃ mineralization, the formation of the vaterite phase and the calcite particles with unusual morphology justified the respective role of curcumin and quercetin. The change in phase and morphology of the particles on reversing the sequence of addition further justified the role played by the organic molecules. Additionally, the influence of the change in certain parameters; the concentration of the additive, temperature and ionic strength of the solution on the precipitation process mimicking the biomineralization of CaCO₃ were studied. With the change in parameters, calcite particles of different morphologies were formed with quercetin. Hence, work provides a useful insight into biomimetic mineralization and can be adopted as a simple and convenient process for vaterite synthesis and modification of calcite morphology. Most importantly, with curcumin performing the additive role for a Ca based biomineral, it opens up a future scope for this *wonder* molecule to be a promising prospect if explored further in the field of biomineralization and its applications.

References

- 4.1. J. L. Kirschvink and J. W. Hagadorn, The Biomineralization of Nano- and Micro-Structures, ed. E. Bäuerlein. *Wiley-VCH, Weinheim*, 2000.
- 4.2. M. D. Brasier, O. R. Green, A. P. Jephcoat, A. K. Kleppe, M. J. van Kranendonk, J. F. Lindsay, A. Steele and N. V. Grassineau, Questioning the Evidence of Earth's Oldest Fossils, *Nature*, 2002, **416**, 76-81.
- 4.3. A. W. Xu, Y. Ma, H. Colfen, Biomimetic mineralization, *J. Mater. Chem.*, 2007, **17**, 415-449.
- 4.4. B. M. Borah, B. J. Bhuyan and G. Das, Low-Molecular-Weight Poly-Carboxylate as Crystal Growth Modifier in Biomineralization, *J. Chem. Sci.*, 2006, **118**, 519-524.
- 4.5. W. Hou and Q. Feng, Morphology and formation mechanism of vaterite particles grown in glycine-containing aqueous solutions, *Mater. Sci. Eng. C*, 2006, **26**, 644-647.
- 4.6. D. Paul, S. Halder and G. Das, Whey Protein Directed *in vitro* Vaterite Biomineralization: Influence of External Parameters on Phase Transformation, *Colloid Interfac. Sci. Commun.*, 2020, **36**, 100255.
- 4.7. B. B. Aggarwal, A. Kumar and A. C. Bharti, Anticancer potential of curcumin: Preclinical and clinical studies, *Anticancer Res.*, 2003, **23**, 363-398.

- 4.8. K. I. Priyadarsini, The Chemistry of Curcumin: From Extraction to Therapeutic Agent. *Molecules*, 2014, **19**, 20091-20112.
- 4.9. S. C. Gupta, S. Patchva, B. B. Aggarwal, Therapeutic Roles of Curcumin: Lessons Learned from Clinical Trials, *AAPS J.*, 2013, **15**, 195–218.
- 4.10. A. Sahebkar, M. C. Serbanc, S. Ursoniuc and M. Banach, Effect of curcuminoids on oxidative stress: A systematic review and meta-analysis of randomized controlled trials, *J. Funct. Foods*, 2015, **18**, 898–909.
- 4.11. B. B. Aggarwal and K. B. Harikumar, Potential therapeutic effects of curcumin, the anti-inflammatory agent, against neurodegenerative, cardiovascular, pulmonary, metabolic, autoimmune and neoplastic diseases, *Int. J. Biochem. Cell Biol.*, 2009, **41**, 40–59.
- 4.12. V. Kuptniratsaikul, P. Dajpratham, W. Taechaarpornkul, M. Buntragulpoontawe, P. Lukkanapichonchut, C. Chootip, J. Saengsuwan, K. Tantayakom and S. Laongpech, Efficacy and safety of Curcuma domestica extracts compared with ibuprofen in patients with knee osteoarthritis: A multicenter study, *Clin. Interv. Aging*, 2014, **9**, 451–458.
- 4.13. Y. Panahi, M. S. Hosseini, N. Khalili, E. Naimi, L. E. Simental-Mendia, M. Majeed and A. Sahebkar, Effects of curcumin on serum cytokine concentrations in subjects with metabolic syndrome: A post-hoc analysis of a randomized controlled trial, *Biomed. Pharmacother.*, 2016, **82**, 578–582.
- 4.14. J. Trujillo, Y. I. Chirino, E. Molina-Jijón, A. C. Andérica-Romero, E. Tapia and J. Pedraza-Chaverri, Renoprotective effect of the antioxidant curcumin: Recent findings, *Redox Biol.*, 2013, **1**, 448–456.
- 4.15. A. Sharma and H. Gupta, Quercetin- A flavonoid, *Chron. Young Sci.*, 2010, **1**, 1-6.
- 4.16. M. M. Nassar, T. E. Farrag, M. S. Mahmoud, S. Abdelmonem, K. A. Khalil and N. A. M. Barakat, Influence of the operating conditions on the morphology of CaCO₃ nanoparticles prepared by modified co-precipitation with pulse mode feeding, *Adv. Powder Technol.*, 2015, **26**, 914-919.
- 4.17. H. Y. Kim, T. Yang, W. Huh, Y. J. Kwaek, Y. Lee and W. Kim, The Combined Effects of Sr(II) and Poly (Acrylic Acid) on the Morphology of Calcite, *Materials*, 2019, **12**, 3339-3346.
- 4.18. X. Lin, K. Li, C. Wu, Z. Li, B. Wu, X. Duan, Y. Zhou and C. Pei, Influence of copper (II) on biomineralization of CaCO₃ and preparation of micron pearl-like biomimetic CaCO₃, *Ceram. Int.*, 2019, **45**, 14354-14359.
- 4.19. L. Pastero, E. Costa, M. Bruno, M. Rubbo, G. Sgualdino and D. Aguilano, Morphology of Calcite (CaCO₃) Crystals Growing from Aqueous Solutions in the Presence of

- Li⁺ Ions. Surface Behavior of the {0001} Form, *Crystal Growth & Design*, 2004, **4**, 485-490.
- 4.20. B. Kanoje, D. Patel and K. Kuperkar, Morphology modification in freshly precipitated calcium carbonate particles using surfactant-polymer template, *Mater. Lett.*, 2017, **187**, 44-48.
- 4.21. N. S. Sambudi, S. B. Park and S. W. Lee, CaCO₃ crystallization and morphology control by using purified soluble protein related to shell regeneration, *J. Cryst. Growth*, 2013, **373**, 118-122.
- 4.22. K. Y. Chong, C. H. Chia and S. Zakaria, Polymorphs calcium carbonate on temperature reaction, *AIP Conf. Proc.*, 2014, **1614**, 52-56.
- 4.23. J. Yu, M. Lei, B. Cheng and X. Zhao, Effects of PAA additive and temperature on morphology of calcium carbonate particles, *J. Solid State Chem.*, 2004, **177**, 681-689.
- 4.24. Y. Takita, M. Eto, H. Sugihara and K. Nagaoka, Promotion mechanism of co-existing NaCl in the synthesis of CaCO₃, *Mater. Lett.*, 2007, **61**, 3083-3085.



Annexure-Chapter 4

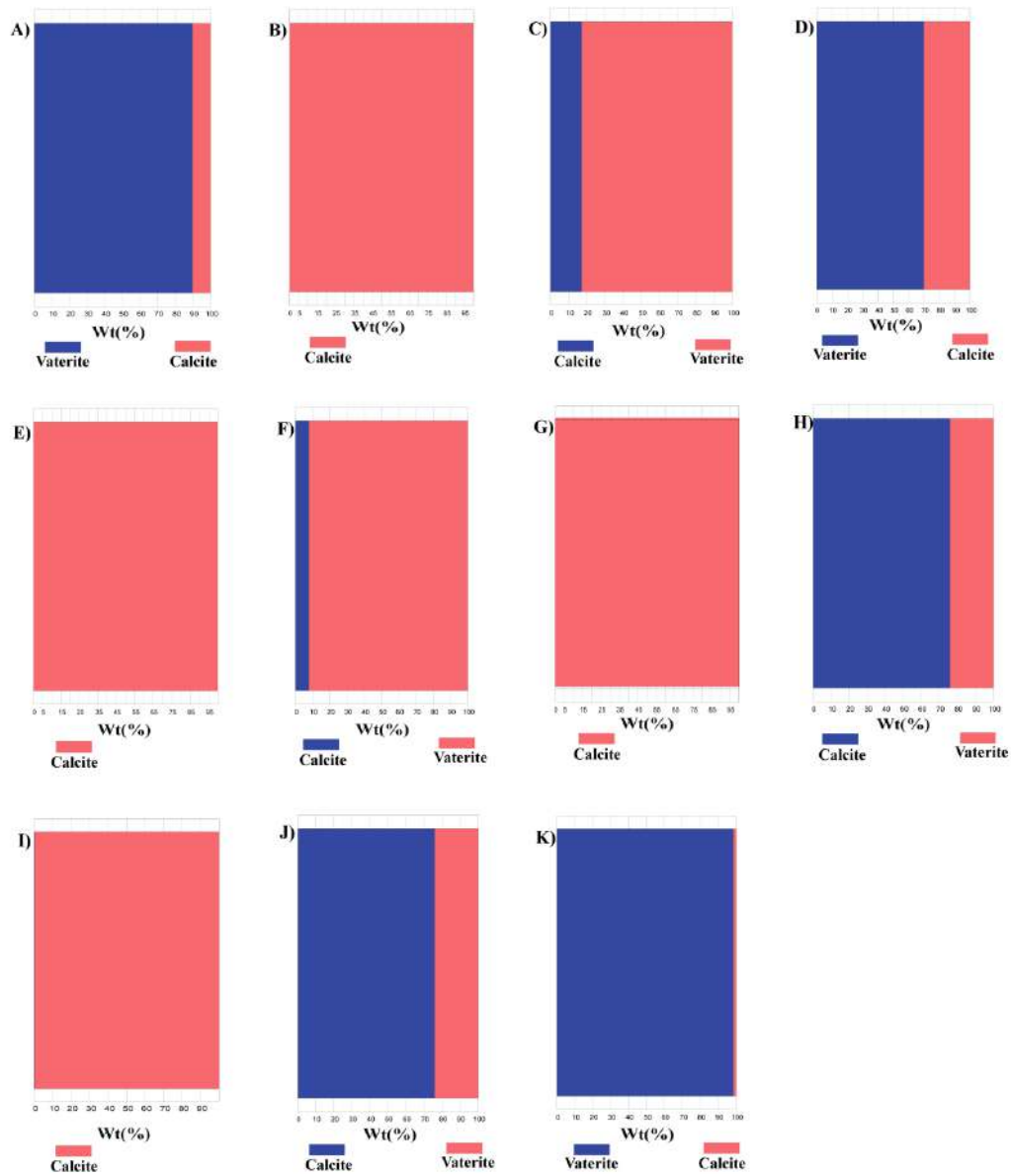


Figure A4.1: Quantitative analysis result data for the CaCO_3 minerals obtained:(A) using curcumin; (B) using quercetin; (C) after 12 hours in solution; (D) after 18 hours in solution; (E) after 24 hours in solution; (F) on doubling the concentration of curcumin; (G) 1:1 ratio of Curcumin/Quercetin; (H) on reversing the sequence of addition; (I) at 10°C ; (J) at 80°C ; (K) in presence of electrolyte (NaCl) of concentration 100 mM.

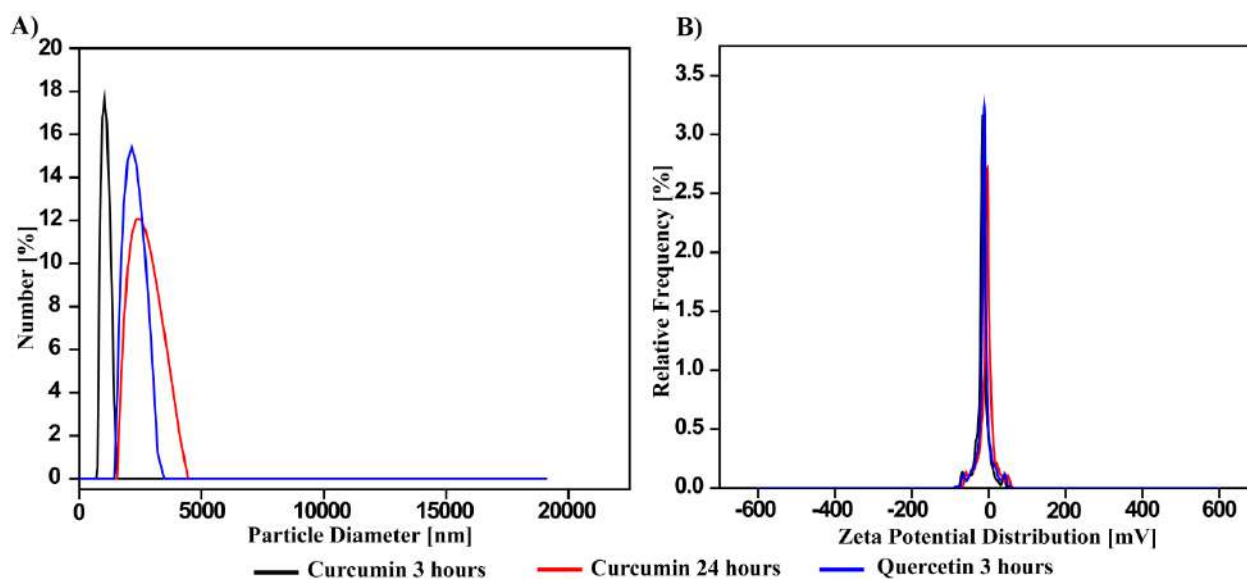


Figure A4.2: A) DLS based particle size analysis; B) Zeta Potential of CaCO_3 particles in the presence of curcumin and quercetin.

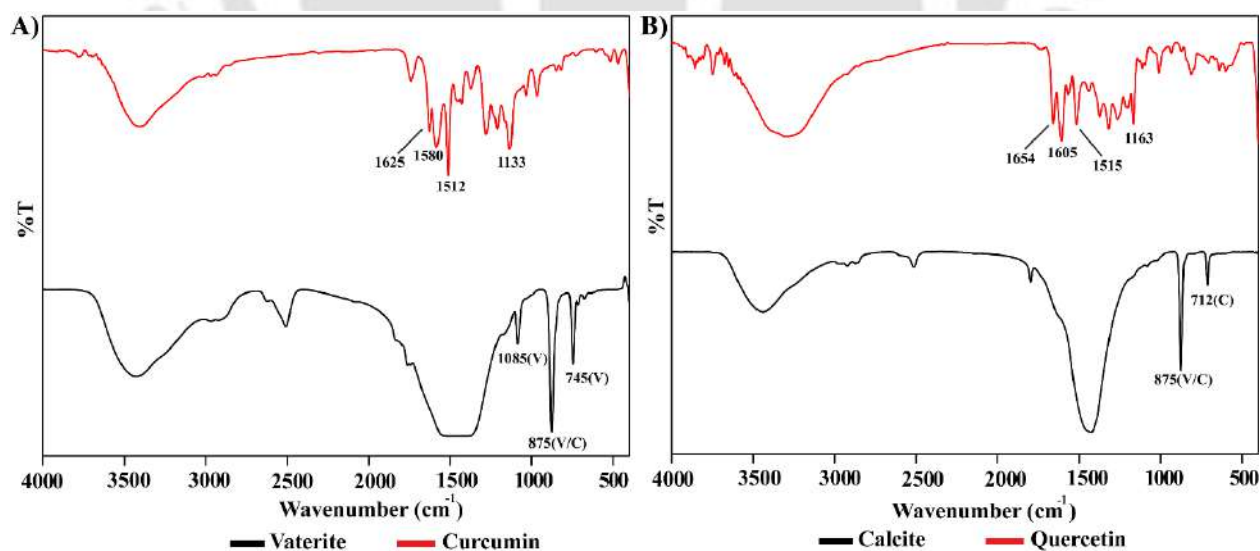


Figure A4.3: A) FT-IR spectra of CaCO_3 (Vaterite) and Curcumin; B) FT-IR spectra of CaCO_3 (Calcite) and Quercetin.

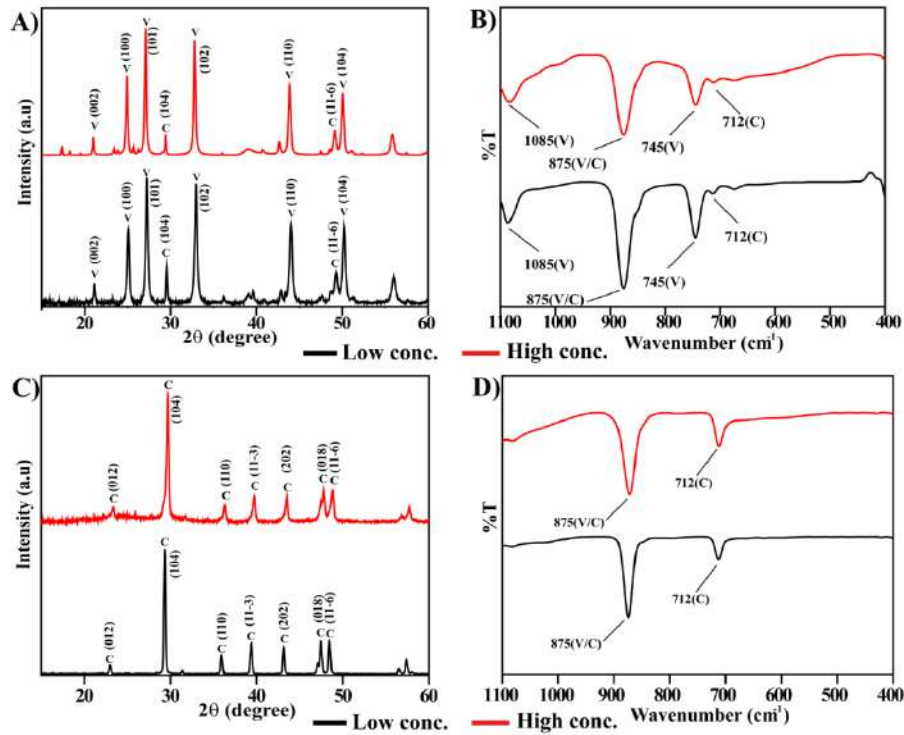


Figure A4.4: A) PXRD pattern; B) FT-IR spectra of CaCO₃ particles at **different concentrations** of curcumin; C) PXRD pattern and D) FT-IR spectra of CaCO₃ particles at **different concentrations** of quercetin.

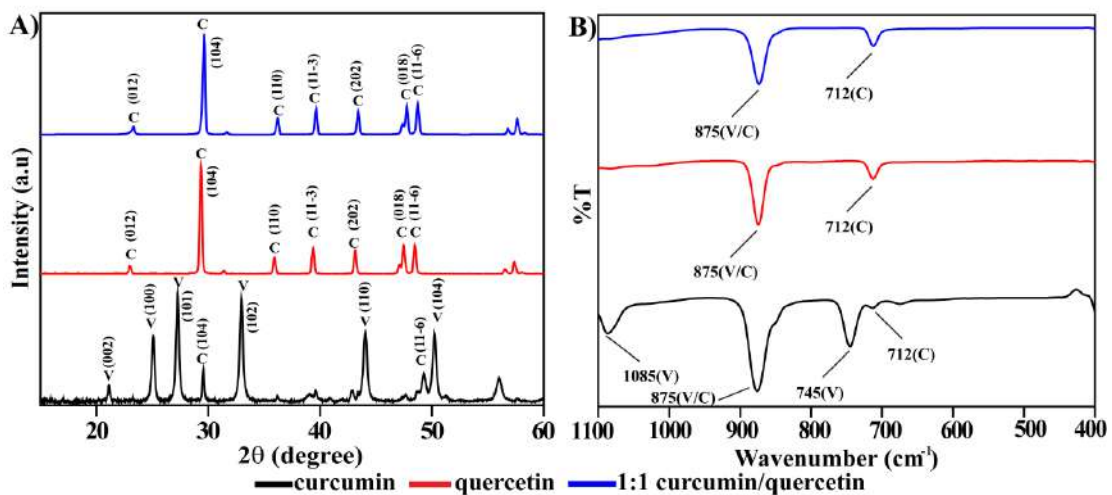


Figure A4.5: A) PXRD pattern; B) FT-IR spectra of CaCO₃ particles in the presence of curcumin, quercetin and **mixture of both**.

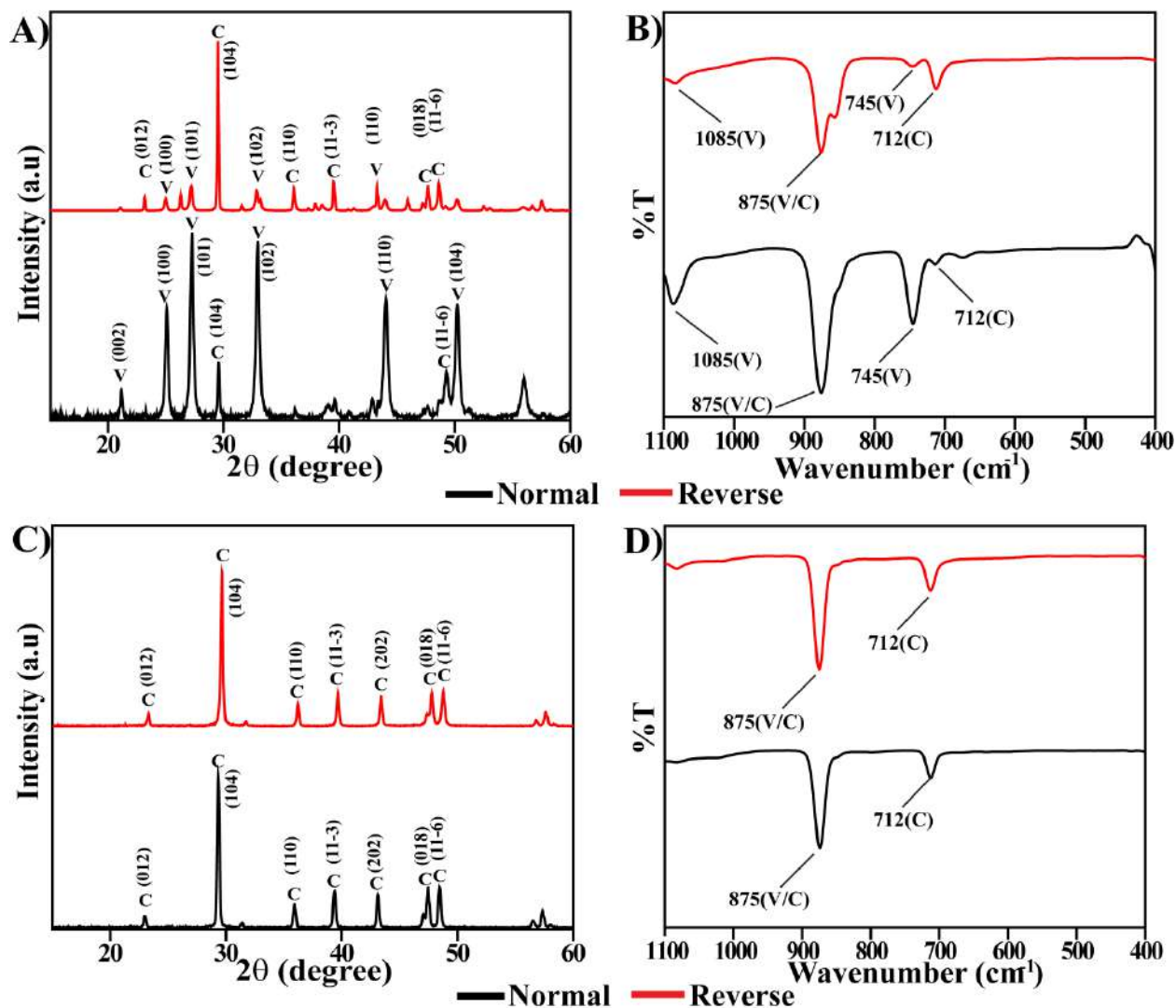


Figure A4.6: A) PXRD pattern; B) FT-IR spectra of CaCO₃ particles with curcumin on **varying the sequence of addition**; C) PXRD pattern and D) FT-IR spectra of CaCO₃ particles with quercetin on **varying the sequence of addition**.

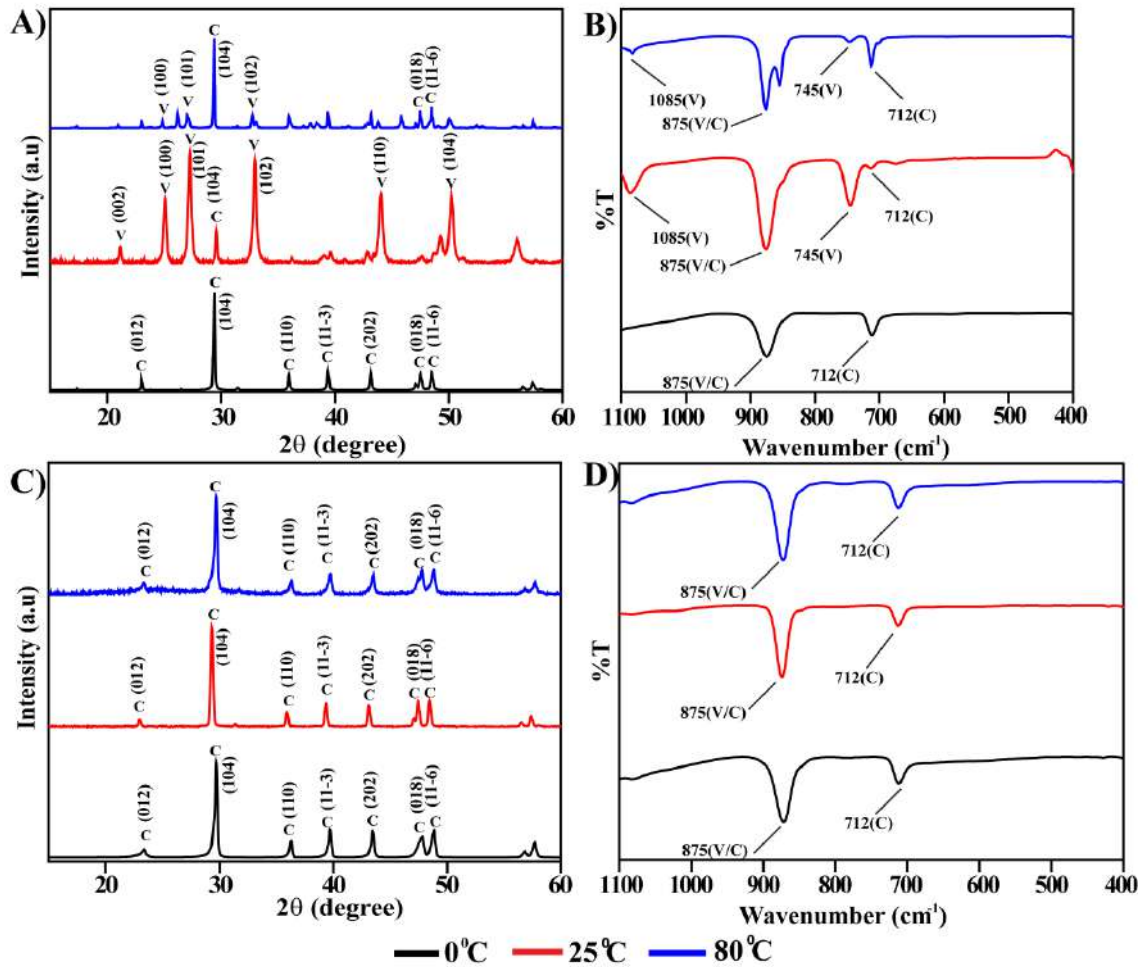


Figure A4.7: A) PXRD pattern and B) FT-IR spectra of CaCO₃ particles at **different temperatures** with curcumin; C) PXRD pattern and D) FT-IR spectra of CaCO₃ particles at **different temperatures** with quercetin.

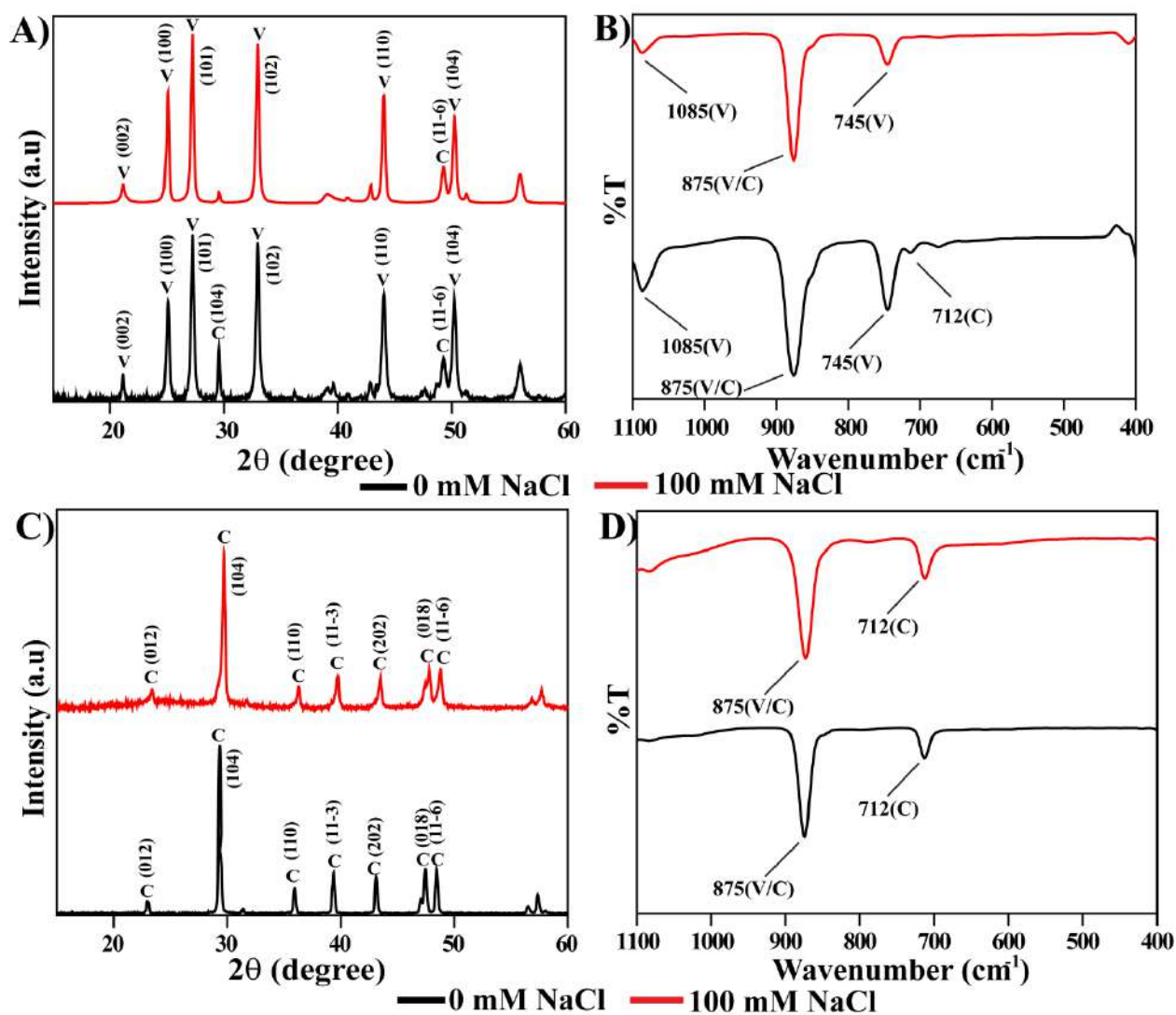


Figure A4.8: A) XRD pattern and B) FT-IR spectra of CaCO_3 minerals at different ionic strengths of the solution with curcumin; C) XRD pattern and D) IR spectra of CaCO_3 minerals at different ionic strengths of the solution with quercetin.

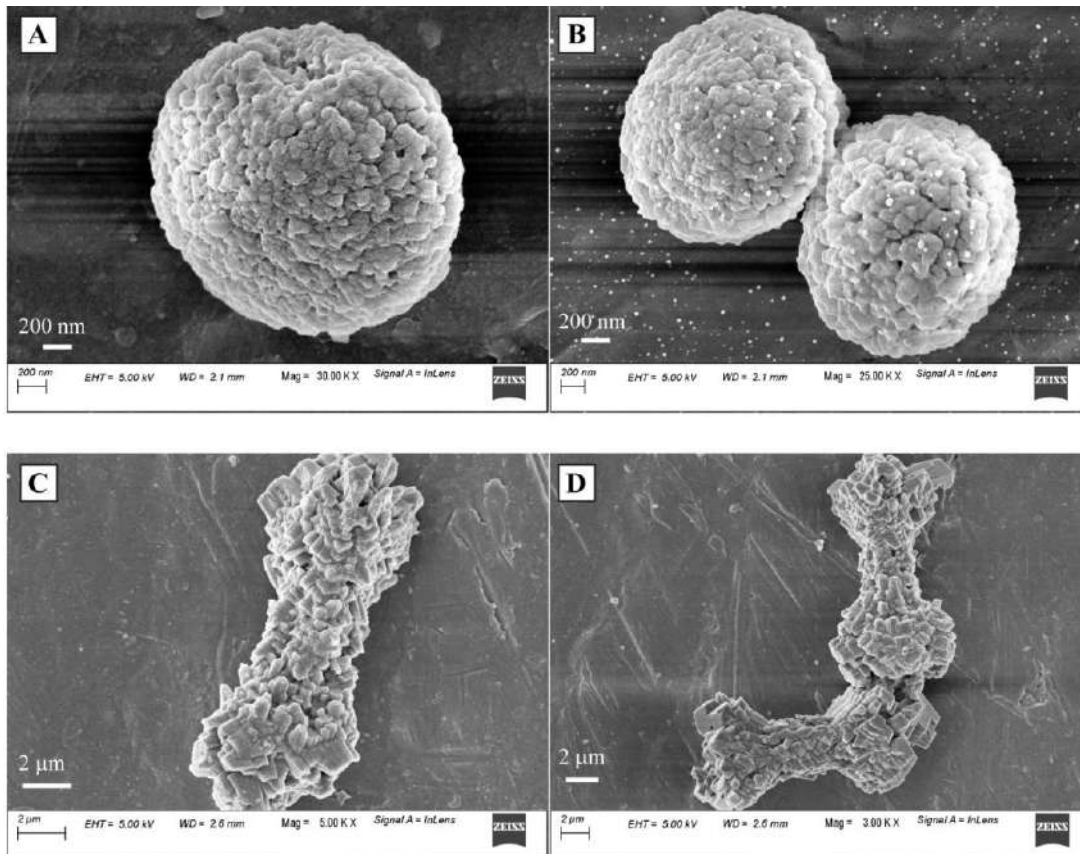


Figure A4.9: FESEM Images of CaCO_3 (A) and (B) in the presence of curcumin; (C) and (D) in the presence of quercetin.

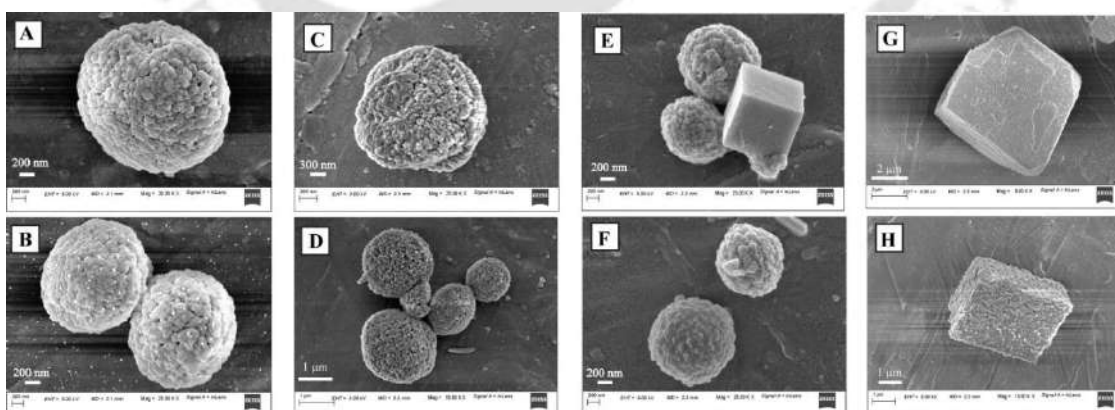


Figure A4.10: FESEM Images of CaCO_3 (A) and (B) in the presence of curcumin after 3 hours; (C) and (D) in the presence of curcumin after 12 hours; (E) and (F) in the presence of curcumin after 18 hours; (G) and (H) in the presence of curcumin after 24 hours.

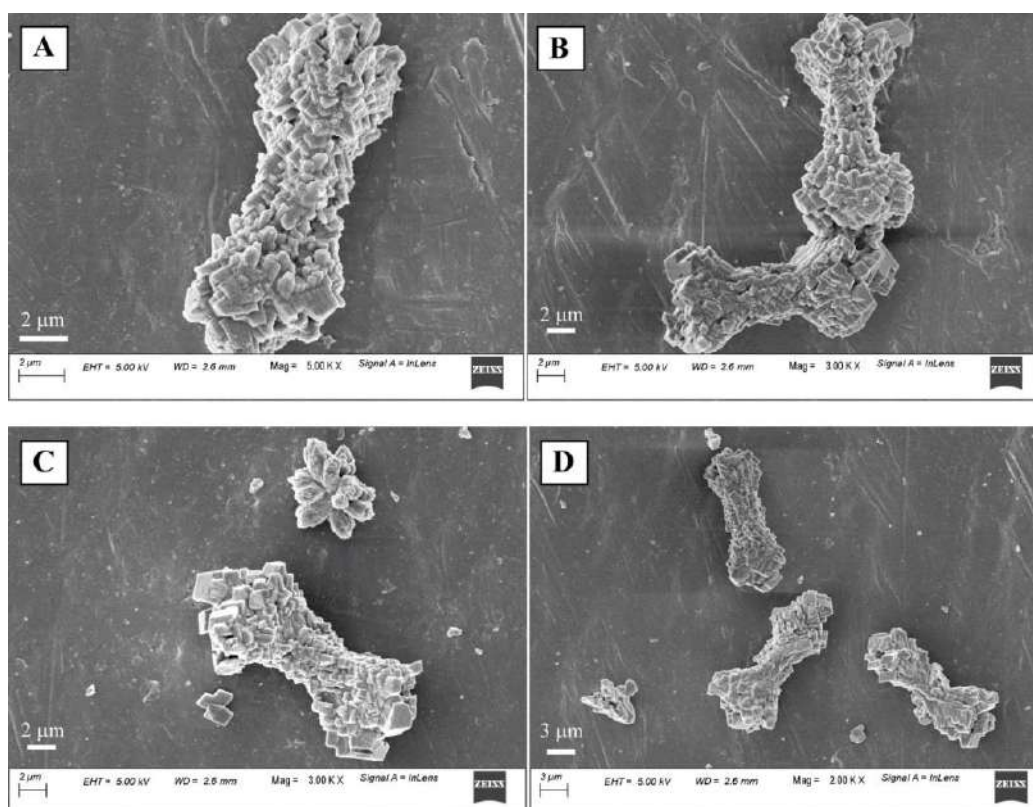


Figure A4.11: FESEM Images (A) and (B) of CaCO₃ in the presence of quercetin after 3 hours; (C) and (D) of CaCO₃ in the presence of quercetin after 48 hours.

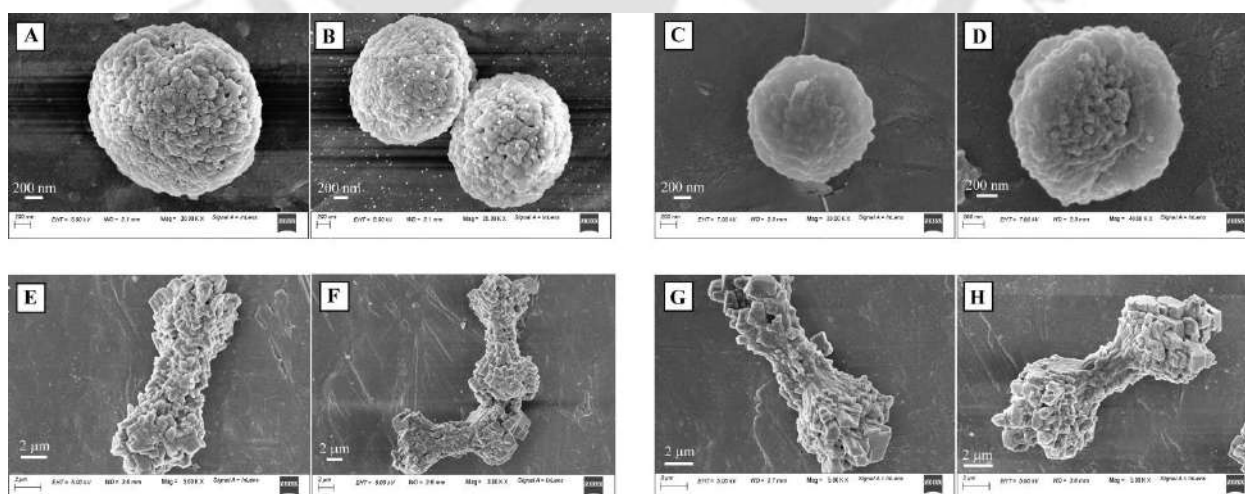


Figure A4.12: FESEM Images of CaCO₃ (A) and (B) at low concentration of curcumin; (C) and (D) at high concentration of curcumin; (E) and (F) at low concentration of quercetin; (G) and (H) at high concentration of quercetin.

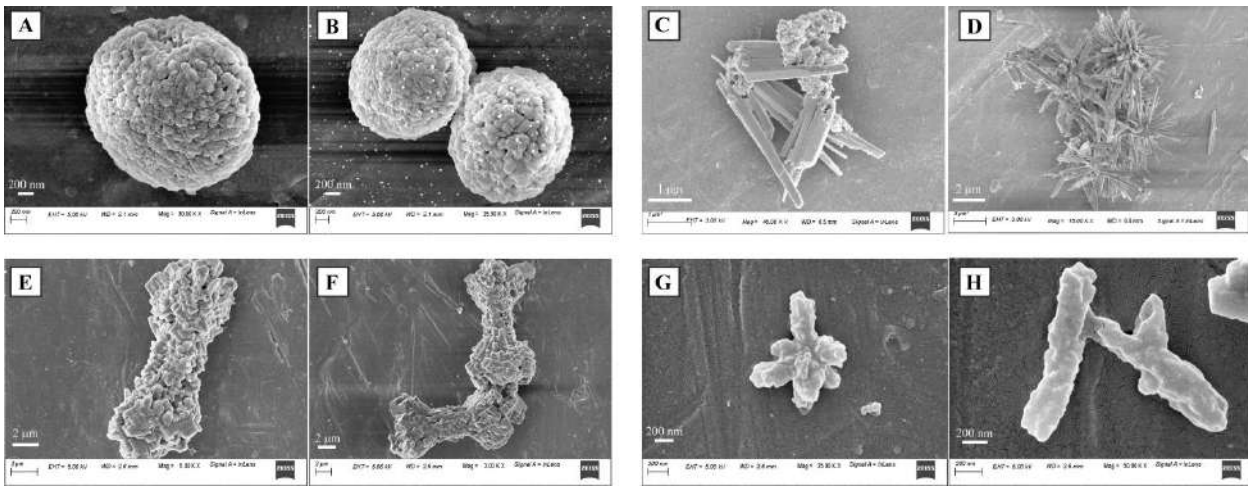


Figure A4.13: FESEM Images of CaCO_3 (A) and (B) under normal sequence of addition in the presence of curcumin; (C) and (D) under reverse sequence of addition in the presence of curcumin; (E) and (F) under normal sequence of addition in the presence of quercetin; (G) and (H) under reverse sequence of addition in the presence of quercetin.

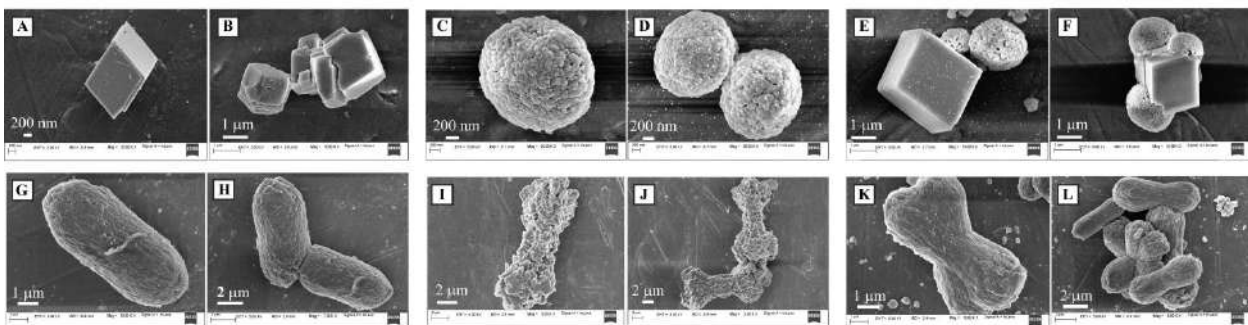


Figure A4.14: FESEM Images of CaCO_3 (A) and (B) at $10\text{ }^\circ\text{C}$ in the presence of curcumin; (C) and (D) at $25\text{ }^\circ\text{C}$ in the presence of curcumin; (E) and (F) at $80\text{ }^\circ\text{C}$ in the presence of curcumin; (G) and (H) at $10\text{ }^\circ\text{C}$ in the presence of quercetin; (I) and (J) at $25\text{ }^\circ\text{C}$ in the presence of quercetin; (K) and (L) at $80\text{ }^\circ\text{C}$ in the presence of quercetin.

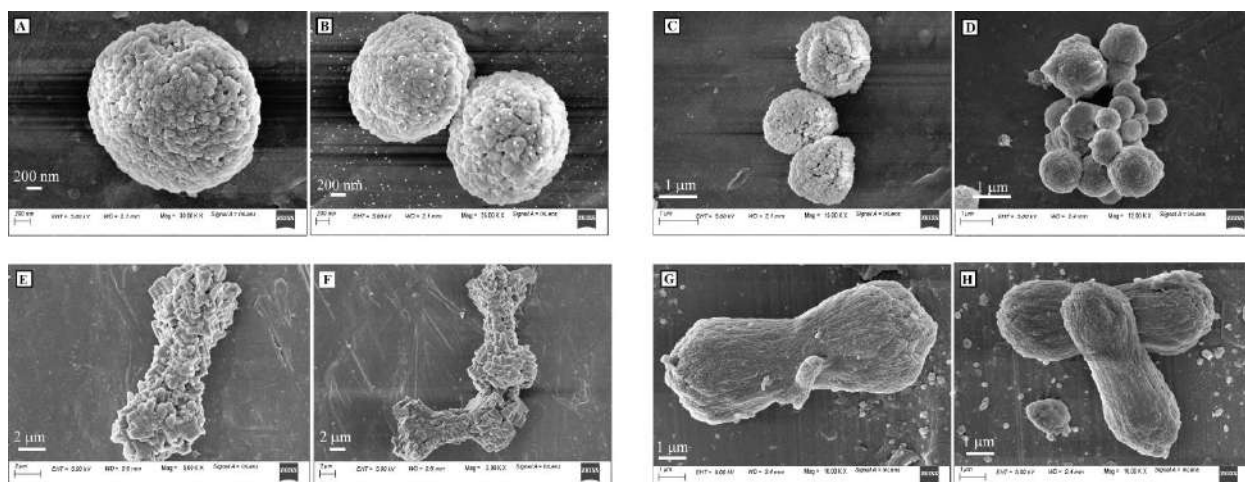


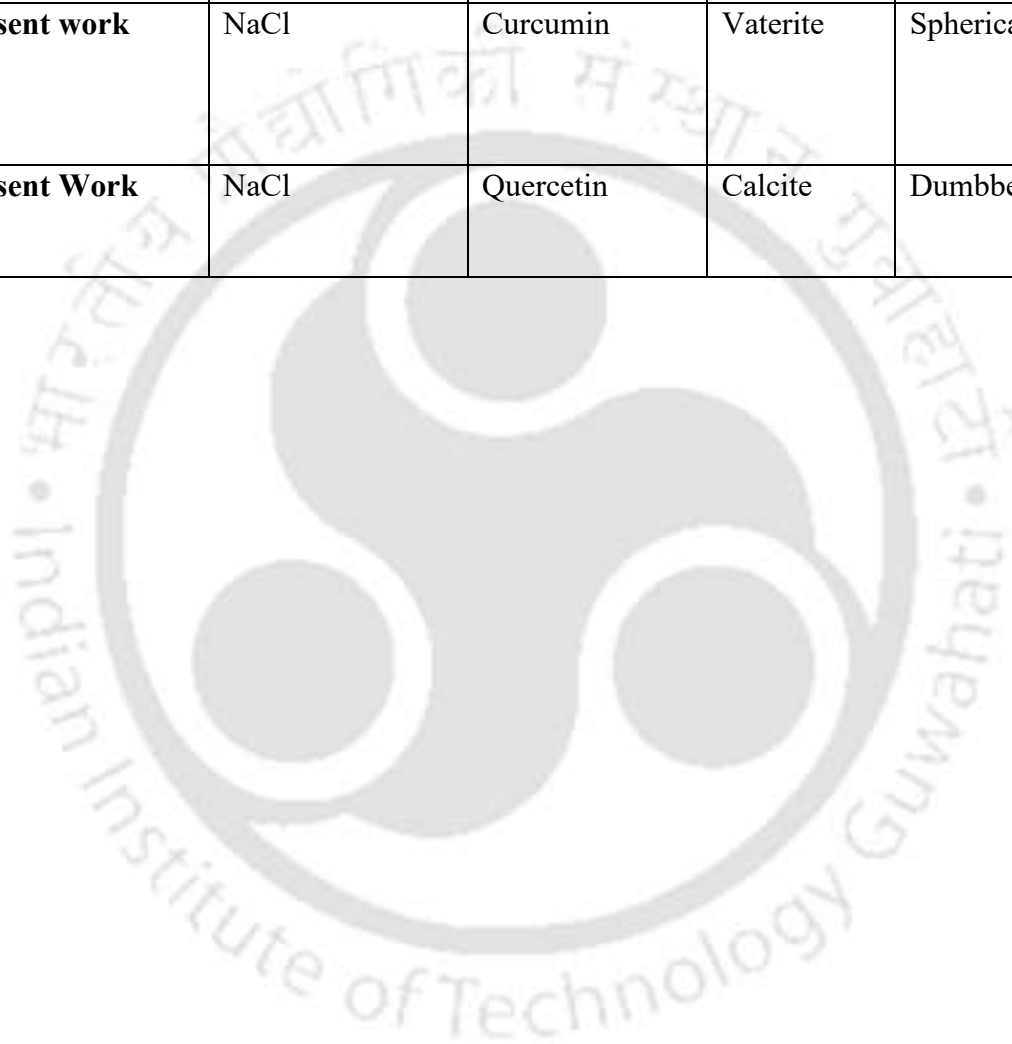
Figure A4.15: FESEM Images of CaCO_3 particles (A) and (B) with curcumin in the absence of an electrolyte; (C) and (D) with curcumin in the presence of 100 mM NaCl; (E) and (F) with quercetin in the absence of an electrolyte; (G) and (H) with quercetin in the presence of 100 mM NaCl.

Table A4.1: Effect of Temperature on CaCO_3 mineralization, a comparative study

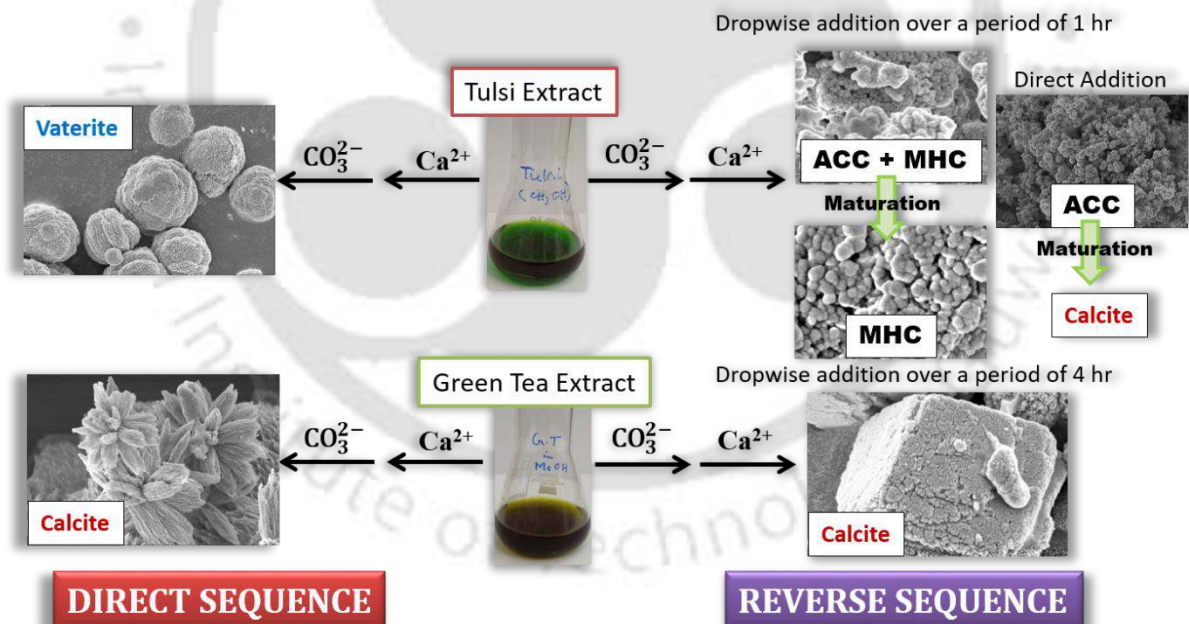
Sl. No.	Reference	Temperature	Additive used	Phase obtained	Morphology
1.	<i>AIP Conf. Proc.</i> 1614, 2014, 52-56	20 °C 80 °C	Without additive	Calcite Aragonite	Rhombohedral Needle Shape
2.	<i>J. Solid State Chem.</i> 177, 2004, 681-689	25 °C 80 °C	Polyacrylic acid (PAA)	Calcite Calcite	Plate like Rhombohedral
3.	Present work	10 °C 25 °C 80 °C	Curcumin	Calcite Vaterite Calcite & Vaterite	Rhombohedral Spherical Spherical
4.	Present Work	10 °C 25 °C 80 °C	Quercetin	Calcite Calcite Calcite	Elliptical Dumbbell Dumbbell

Table A4.2: Effect of Ionic Strength on CaCO₃ mineralization, a comparative study

Sl. No.	Reference	Electrolyte	Additive used	Phase obtained	Morphology
1.	<i>Mater. Lett.</i> 61, 2007, 3083–3085	NaCl	Without additive	Calcite	Rhombohedral
2.	Present work	NaCl	Curcumin	Vaterite	Spherical
3.	Present Work	NaCl	Quercetin	Calcite	Dumbbell



Tuning of CaCO_3 phase and morphology directed by plant-based *in vitro* model systems: A thorough insight into the formation of monohydrocalcite



5.1 Introduction:

In the world of biomineralization, minerals based on CaCO_3 are the most abundant and widespread. Since its very introduction, the biomimetic synthesis of CaCO_3 , owing to its polyphasic and polymorphic characteristics, has been a very intriguing topic. In addition to the anhydrous phases, calcite, aragonite, and vaterite; CaCO_3 exists in two hydrated crystal phases; monohydrocalcite ($\text{CaCO}_3 \cdot \text{H}_2\text{O}$) and ikaite ($\text{CaCO}_3 \cdot 6\text{H}_2\text{O}$). Monohydrocalcite (MHC) was first observed during the dehydration of ikaite and eventually observed in marine organisms.^{5.1,5.2} It is metastable compared to the anhydrous phases and readily gets converted to these phases upon dehydration at high temperatures. Owing to its, hydrous nature MHC requires certain special conditions for its formation and occurrence.^{5.3,5.4} Therefore, compared to other phases of CaCO_3 , research on MHC, especially the *in vitro* synthesis, has been limited. For the formation of MHC, it is a prerequisite that the medium possesses magnesium which facilitates the stabilization of this metastable phase via the amorphous precursor.^{5.5} The formation of all the stable polymorphs during the crystallization of CaCO_3 takes place through an amorphous intermediate, popularly known as amorphous calcium carbonate (ACC).^{5.6,5.7} ACC has been recognized as the intermediate between pre-nucleation clusters and the crystalline phases. In recent years, an extensive study on the role of ACC in forming biologically relevant functional materials has led to an increase in interest in its synthesis. However, due to its instability, the synthesis of ACC still stands as a challenge. The additives such as magnesium, phosphate or sulphate ions, organic templates, and the reaction conditions along with the amount of water determine the formation and the stability of ACC.^{5.8,5.9}

Biominerals based on Ca grow on organic templates bearing oxygen as Ca^{2+} prefer oxygen-containing donor ligands due to the hard acid-hard base interactions. The role of a template is to lower the activation energy of nucleation of the unstable phases, which facilitates their formation over the otherwise stable phase (rhombohedral calcite).^{5.10} In the previous chapters, we discussed the isolation of the metastable vaterite phase and the formation of calcite phase with unusual and beautiful morphologies by using templates such as the complex biopolymer whey protein and the polyphenolic organic molecules curcumin and quercetin. In the natural biomineralization process, an organism can tune between the different polymorphs according to the requirements. The ability of the tiniest of organisms to control the formation of biominerals, especially to adapt to environmental conditions, is captivating. Therefore, in our quest to understand and isolate the different polymorphs, both hydrated and anhydrous irrespective of their unstable nature, we have used Tulsi (*Ocimum sanctum*) extracts in this work as templates

during the *in vitro* CaCO₃ crystallization. Tulsi, also known as Holy Basil, grows in several parts of India and is popularly used in Ayurveda to cure various diseases like asthma, bronchitis, dysentery, skin diseases, etc., for maintaining general wellness and boosting natural immunity. The antioxidant, antimicrobial, antispasmodic, antifungal and anticancer properties of *Ocimum sanctum* have been reported due to various phytochemical constituents eugenol, ursolic acid, rosmarinic acid, oleanolic acid, etc.^{5.11-5.15} Considering the widespread availability and noble chemical composition of tulsi, apart from its utilization as a boon for maintaining a healthy body and overall wellness, tulsi has been used in other fields of research, such as in the synthesis and stabilization of metal nanoparticles.^{5.16-5.18} But surprisingly, to date, there has been no report on the direct application of tulsi in the crystallization of Ca-based minerals. Therefore, in this work, we intend to provide a useful insight by studying the *in vitro* crystallization of CaCO₃, whereby a successful approach would generate a vast scope to be explored in the field of biomineralization. Additionally, in the first part of this work, we drew a comparison by performing the crystallization process in the presence of green tea extracts due to their similarity with tulsi in terms of chemical composition. Green tea, *Camellia sinensis*, used as a beverage globally, shows several health benefits due to its antioxidant, antidiabetic, antimicrobial, and anti-mutagenic activities.^{5.19-5.21} The methanol and water extracts of both tulsi and green tea were subjected as templates for CaCO₃ crystallization and the change of phase and morphology of the particles on tuning the experimental conditions were studied. The second part of this work discusses the formation of a hydrated phase, MHC, with an insight into its transformation via the unstable amorphous precursor. The ability of the tulsi extract to stabilize the amorphous phase in an aqueous solution was also studied. We intended to arrest all the three stages, the amorphous precursor, the matured MHC, and the stage where both the phases co-existed and eventually study the transformation to the thermodynamically stable calcite phase, therefore, providing a convenient and straightforward method for their synthesis.

5.2 Results and Discussions:

The first part of this work deals with a comparative study between the methanol and the water extracts of tulsi and green tea in their roles as templates during the *in vitro* crystallization of CaCO₃. In the second part, we study the formation of monohydrocalcite via the amorphous precursor intermediate and their subsequent transition to the stable calcite phase.

5.2.1 Normal sequence of addition

5.2.1.1 Crystallization of CaCO_3 in the presence of tulsi and green tea extracts in methanol

The *in vitro* crystallization of CaCO_3 in the presence of tulsi extract in methanol as template-directed the formation of the least stable crystalline phase, vaterite. For preliminary characterization, the particles were subjected to FT-IR spectroscopy. In the spectra, Fig. 5.1(A), we could observe high-intensity signals at 746 cm^{-1} , 875 cm^{-1} , and 1087 cm^{-1} which are characteristic of the vaterite phase. Followed by the PXRD analysis, Fig. 5.1(B), where again the characteristic peaks for vaterite at 2θ values equal to 20.91 , 25.10 , 27.03 , 32.81 , 43.72 , and 50.11 were observed, and these peaks are identical to the standard PDF data for the vaterite phase (ICSD 00-060-0483), confirming the specific formation of the vaterite phase.

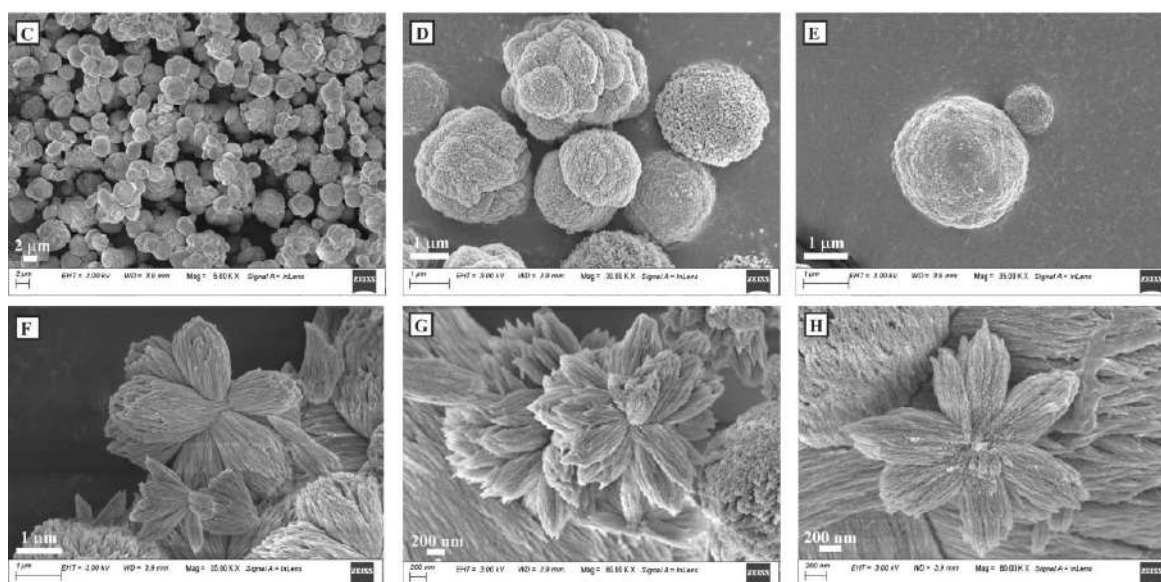
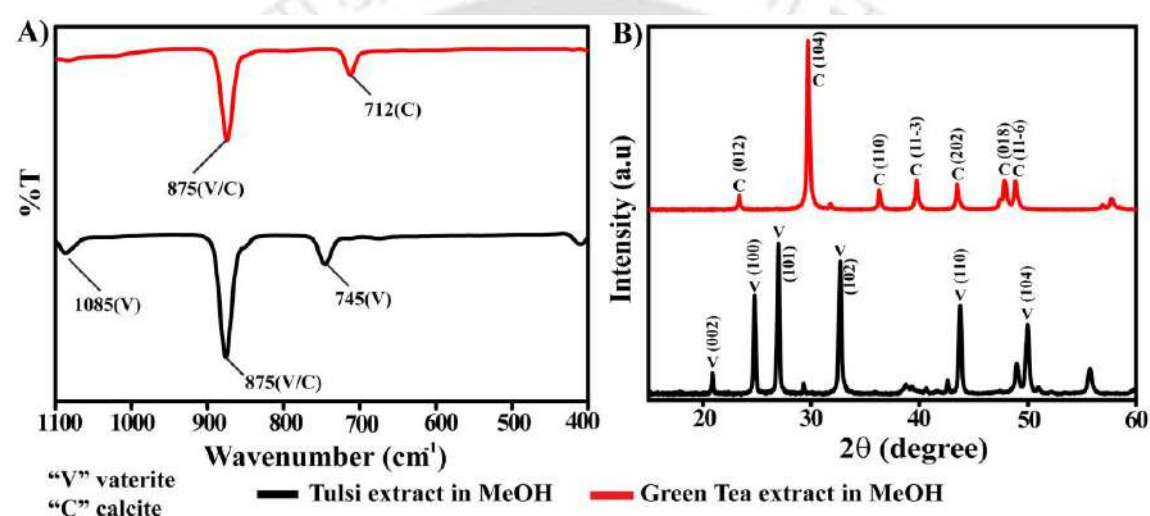


Figure 5.1: (A) FT-IR spectra; (B) PXRD pattern of CaCO_3 particles precipitated in the presence of Tulsi and Green tea extract in methanol; (C), (D), and (E) FESEM images of CaCO_3 particles precipitated in the presence of Tulsi extract in methanol; (F), (G) and (H) FESEM images of CaCO_3 particles precipitated in the presence of Green tea extract in methanol.

The morphology of the particles can be observed from the FESEM images, where Fig. 5.1(C), shows the vaterite particles in bulk, and in Fig. 5.1(D) and (E), we see high-resolution images of the spherical vaterite particles. From the DLS experiments, Fig. A5.1(A) and (B), we obtained the hydrodynamic diameter and the zeta potential of the particles as 843.2 nm and -31.85 mV, respectively. With the green tea extract in methanol, the *in vitro* crystallization of CaCO_3 yielded the calcite phase. In the FT-IR spectra, Fig. 5.1(A), we obtained signals at 712 cm^{-1} and 875 cm^{-1} which are characteristic of the calcite phase, and from the PXRD analysis, Fig. 5.1(B), the peaks at 2θ values equal to 23.31, 29.72, 35.94, 39.70, 43.38, 47.84 and 48.61 matches well with the PDF data for calcite (ICSD 00-047-1743). As already known, usually, the calcite phase being the most stable phase as such requires no special conditions for its formation. But the most intriguing point about calcite is its ability to exhibit variations in morphology, and in this particular case, with the use of green tea extract in methanol, we obtained a very captivating and unusual morphology of the calcite particles. As can be seen in Fig. 5.1(F), (G), and (H), the calcite particles with a beautiful floral pattern, daffodil-like, were obtained. Further, from the DLS experiments, it was observed that the particles exhibit a hydrodynamic diameter of 867.3 nm and zeta potential of -14.5 mV, Fig. A5.1(A) and (B).

5.2.1.2 Crystallization of CaCO_3 in the presence of tulsi and green tea extracts in water

The use of the tulsi extract in water, unlike the methanol extract, was not able to stabilize the metastable vaterite phase. In this case, we obtained the calcite phase as seen from the FT-IR spectra, Fig. 5.2(A) with signals at 713 cm^{-1} and 874 cm^{-1} and accordingly from the PXRD pattern, Fig. 5.2(B) the peaks at 23.22, 29.48, 36.15, 39.58, 43.36, 47.63 and 48.60 identical to that of the calcite phase (ICSD 00-047-1743) were obtained. The highlight, in this case, was the morphology of the calcite particles, Fig. 5.2(C) and (D), at low-resolution, in large numbers the particles are analogous to the spherical vaterite, but under high-resolution, we could observe an elegant rose-like calcite particle. The hydrodynamic diameter and zeta potential of the particles was 2984.7 nm and -29.61 mV, respectively, Fig. A5.2(A) and (B). Similarly, with the green tea extract in the water, we obtained the calcite phase, but with morphology different from the usual rhombohedral morphology, Fig. 5.2(E) and (F), the particles exhibited a spherical morphology which is usually associated with the vaterite phase. The FT-IR spectra, Fig. 5.2(A) with signals at 712 cm^{-1} and 873 cm^{-1} and the PXRD pattern, Fig. 5.2(B) exhibiting peaks at 23.09, 29.36, 36.04, 39.60, 43.28, 47.64, and 48.56, all of which are identical to the calcite phase (ICSD 00-047-1743). In this case, the hydrodynamic diameter of the particles was 3926.8 nm, and the zeta potential -21.85 mV, Fig. A5.2(A) and (B).

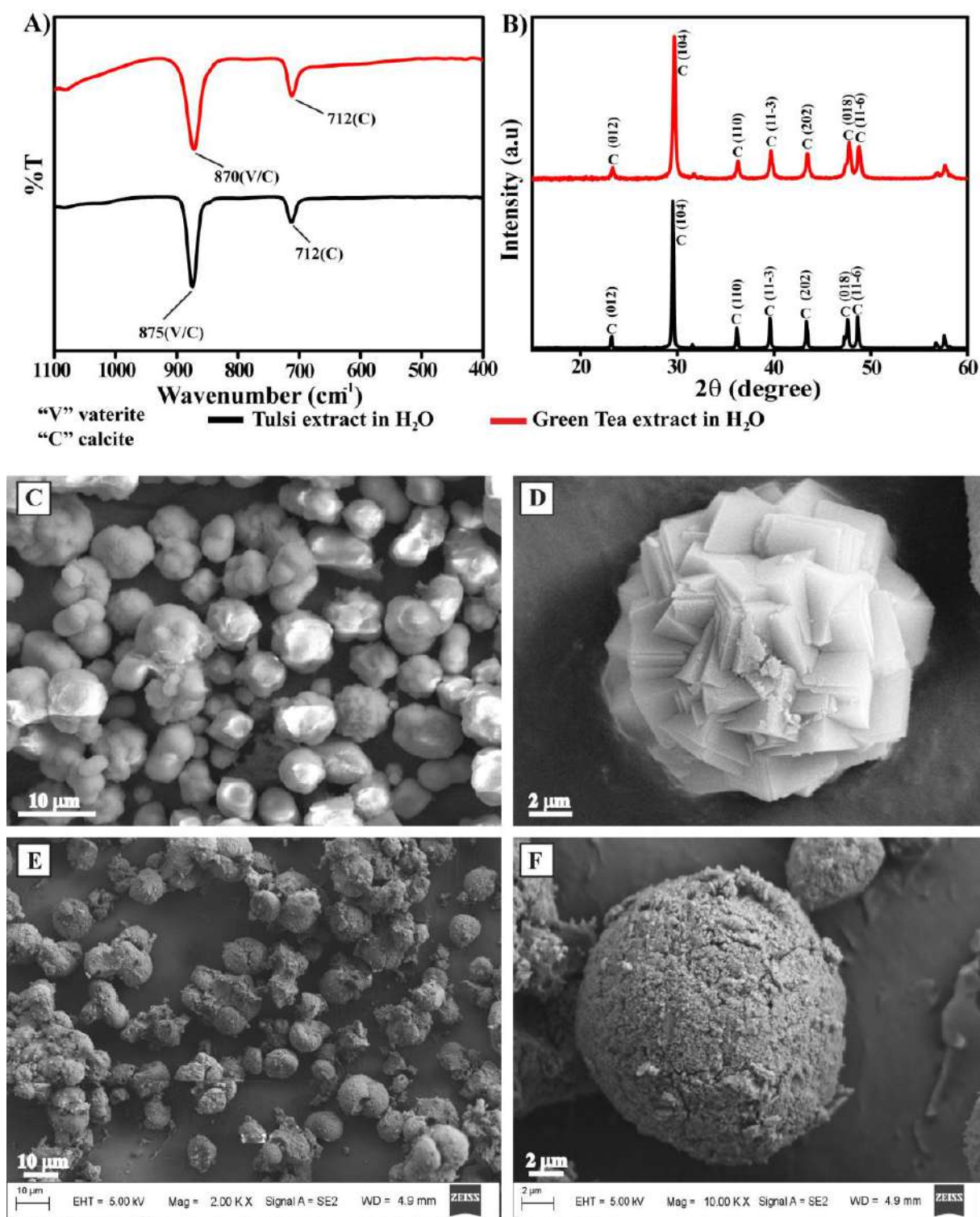


Figure 5.2: (A) FT-IR spectra; (B) PXRD pattern of CaCO_3 particles precipitated in the presence of Tulsi and Green tea extract in water; (C) and (D) FESEM Images of CaCO_3 particles precipitated in the presence of Tulsi extract in water; (E) and (F) FESEM Images of CaCO_3 particles precipitated in the presence of Green tea extract in water.

From the above experiments, we have observed that only the tulsi extract in methanol stabilized the unstable vaterite phase, but the other three extracts were unable to do so. However, in

addition to obtaining the vaterite phase, the other fascinating observations were in terms of the morphology of the calcite phase. In the other three syntheses, the morphology exhibited by the calcite particles was different from the typical rhombohedral calcite morphology. These observations suggest that the various extracts used as templates during the crystallization process-induced different roles owing to the difference in composition. Both tulsi and green tea are complex mixtures of compounds such as polyphenols, flavonoids, etc. The phytochemical constituents present in tulsi and green tea have been listed in **Table A5.1**.^{5.22-5.25} It can be seen that apart from the common components present in both, tulsi possesses additional compounds such as acids, essential oils and fatty acids. The extraction of tulsi in different solvents, both polar such as methanol, ethanol, water and non-polar such as hexane and chloroform, leads to the separation of various components. Since the *in vitro* crystallization is performed in water, the extractions in polar solvents were considered. Hence, we have used the methanol and water extracts of both tulsi and green tea in our study. Literature suggests that the extraction of tulsi in methanol yields the highest percentage of the chemical constituents, 8%, whereas water yields about 5% of the components; all the constituents have been presented in **Table A5.2**.^{5.13,5.22} **Table A5.3** gives the percentage concentration of the major phytochemical constituents in the methanol extract of tulsi.^{5.24} Among all these, the constituents that were under consideration were the ones with a molecular structure that would influence the precipitation process. As already mentioned, it is the oxygen-containing groups that bind to Ca^{2+} through hard acid-hard base interactions and dictates the process of mineralization. The constituents of tulsi that are primarily responsible for such interactions are polyphenols, flavonoids, and acids. Most of them are majorly found in the methanol extract rather than in the water extract; namely, the major acid groups found in the methanol extract are Oleanolic acid, Ursolic acid, Rosmarinic acid, Tuberonic acid, etc. The leaves of tulsi contain 0.7% essential oil, all of which are extracted in methanol and out of it 71% comprising of Eugenol and 20% Methyl eugenol. The complete list of acid and essential oil present in the methanol extract has been presented in **Table A5.4**.^{5.22,5.24} This difference in composition of the methanol and water extracts justifies the specific formation of the least stable vaterite phase with the methanol extract of tulsi. The templates, such as acids and polyphenols facilitate the stabilization by lowering the free energy of nucleation, ΔG_n of the vaterite phase, compared to that of the calcite phase.^{5.10} With the water extract, however, the isolation of the vaterite phase was not observed, but the presence of polyphenols and flavonoids regulated the morphology of the calcite phase. The green tea extracts in both methanol and water were not able to stabilize the vaterite phase. However, the presence of phenolic compounds and the flavonoid catechin influenced the modification of morphology, resulting in a beautiful floral

pattern of calcite and an unusual vaterite-like spherical-shaped calcite. The role of polyphenols and flavonoids in the crystallization of CaCO_3 is supported by one of our recent work, where we reported how the polyphenol curcumin and the flavonoid quercetin influenced the phase and morphology of CaCO_3 during the *in vitro* crystallization process. Therefore, to summarize this part, since the extraction efficiency of methanol has been reported to be higher than that of water in the case of tulsi and in comparison between the extracts of tulsi and green tea in methanol, the fact that tulsi resulted in the formation of the vaterite phase, the additional presence of acids and essential oils in the methanol extract of tulsi is responsible for this stabilization. However, although their modes of action were different, the modulation of phase and morphology justifies the influence of both tulsi and green tea as templates in CaCO_3 crystallization.

5.2.1.3 Reusability of tulsi extract in methanol and the effectiveness of the mixture of tulsi and green tea extracts in methanol

The protein and organic molecules responsible as templates in the natural biomineralization process can retain their role over multiple cycles; an *in vitro* crystallization template needs to maintain its ability to behave as a template over several cycles. In this work, since the tulsi extract in methanol gave us the vaterite phase, we extended our study to investigate its ability to retain its templating role. It was observed that the selective formation of vaterite had taken place at least for three consecutive cycles, Fig. A5.3, justifying the fact that the role played by the tulsi extract is comparable in this respect to the organic molecules involved in natural crystallization.

Additionally, both the tulsi and the green tea extracts in methanol were mixed in a 1:1 ratio to study the combined effect individually. The two gave us vaterite and calcite, respectively. In this case, we observed that the stable calcite phase had formed, which may easily be attributed to the natural tendency of the CaCO_3 particles to attain the stable calcite phase, Fig. A5.4. However, the presence of green tea extract would hasten the maturation of calcite, so even in the presence of the vaterite-directing tulsi extract, the stabilization of vaterite did not take place.

5.2.2 Reverse sequence of addition

The CO_3^{2-} ions were first allowed to interact with the methanol extract of tulsi. As such, the oxygen-containing groups such as polyphenols, flavonoids, fatty acids, etc., would not interact with CO_3^{2-} . Hence, the templating role provided by these groups is not applicable in the reverse process; this was previously shown by us when we used polyphenols curcumin and quercetin. In this part of the study, five different experiments were performed by varying the time taken to add the Ca^{2+} ions into the medium containing the CO_3^{2-} ions and the methanol extract of tulsi.

Among the five variations, one of them involved the direct addition of the Ca^{2+} ions; this was followed by the dropwise additions whereby the frequency of drops was maintained in such a manner that the time taken for complete addition were 30 mins, 1 hour, 2 hours and 4 hours, respectively. In the first case, i.e., the direct addition under the influence of the tulsi extract, followed by immediate filtration, allowed the isolation of the highly unstable ACC phase. The particles were characterized initially by the FT-IR measurements where we obtained a split signal at 1475 cm^{-1} and 1415 cm^{-1} and a signal at 864 cm^{-1} , which are characteristics of the ACC phase, Fig. 5.3(A)(a). In the PXRD analysis, a pattern with a broad hump at 2θ equal to 32° , without any sharp peak, was observed, which justified the formation of ACC, Fig. 5.3(B)(a). In FESEM images, we can see that the ACC particles appear as tiny nanospheres, mostly in the range of 30-50 nm, Fig. 5.4(A). In the next experiment, the Ca^{2+} ions were added dropwise for 30 mins. Here too, the CaCO_3 that had formed was amorphous and was characterized by the FT-IR analysis, where a split signal at 1475 cm^{-1} and 1412 cm^{-1} and a signal at 864 cm^{-1} were observed, Fig. 5.3(A)(b), the PXRD pattern obtained was a broad hump at 2θ equal to 32° , Fig. 5.3(B)(b), and the FESEM analysis confirmed the formation of tiny ACC nanospheres, Fig. 5.4(B). In the third process, the dropwise addition was performed over a time of 1 hour. The observation, in this case, was intriguing; we obtained a mixed-phase where in addition to the unstable ACC phase, the hydrated MHC phase was obtained. The initial characterization performed was the FT-IR analysis, Fig. 5.3(A)(c), where the split signal at 1477 cm^{-1} and 1400 cm^{-1} was observed, now the splitting was more prominent, and an additional signal, although very faint, could be seen at 700 cm^{-1} and the signal similar to the one observed at 864 cm^{-1} for

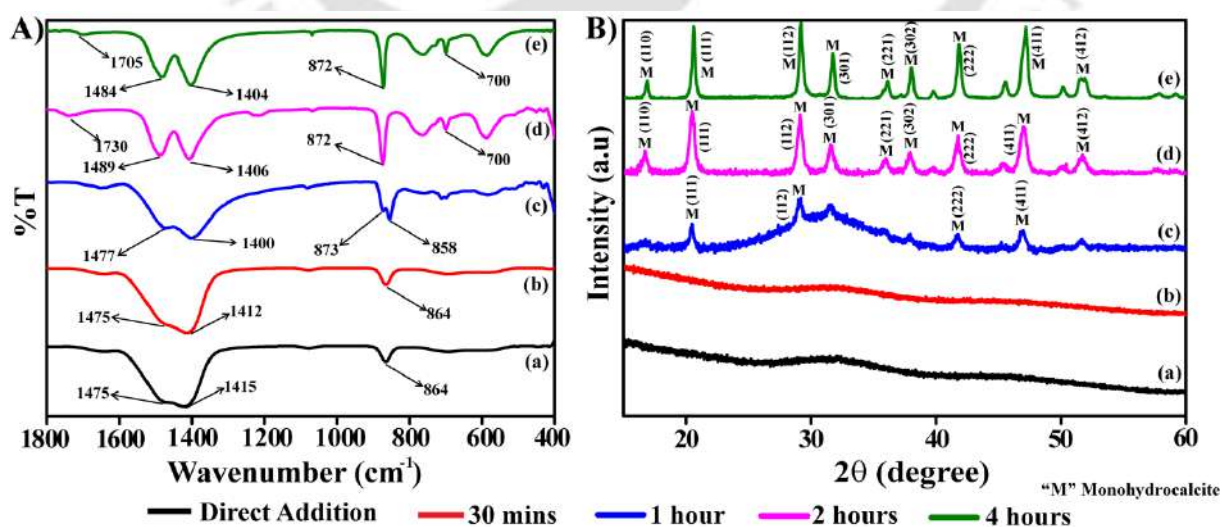


Figure 5.3: (A) FT-IR spectra; (B) PXRD pattern of CaCO_3 particles precipitated by reverse sequence of addition (a) by direct addition, (b) in 30 mins; (c) in 1 hour; (d) in 2 hours; (e) in 4 hours.

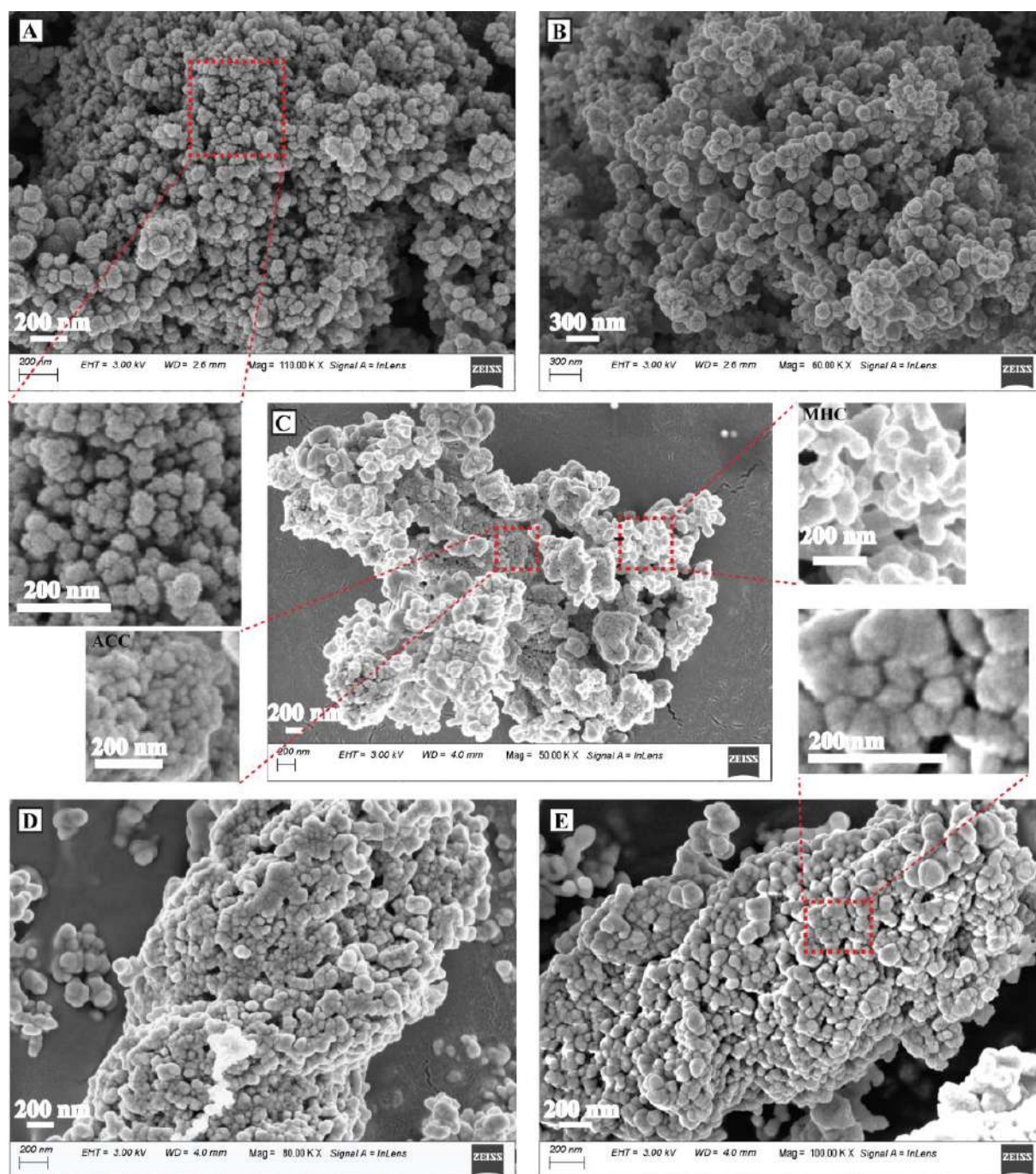


Figure 5.4: FESEM Images of CaCO₃ particles precipitated by the reverse sequence of addition in the presence of tulsi extract in methanol (A) by direct addition, (B) in 30 mins; (C) in 1 hour; (D) in 2 hours; (E) in 4 hours.

ACC was seen as a split signal at 873 cm^{-1} and 858 cm^{-1} , these observations suggested the co-existence of both the phases, ACC and MHC.^{5,26} In the PXRD pattern, Fig. 5.3(B)(c), the peaks at 2θ equal to 20.41, 29.11, 41.58, and 47.01 due to MHC could be observed, but the intensity was low. Additionally, a broad peak at 2θ equal to 32, attributed to the ACC phase, was observed, indicating the co-existence between both the phases. In the FESEM image, Fig. 5.4(C), the co-existence of both the phases can be seen, and the ACC particles can be identified

as tiny nanospheres (magnified), whereas the MHC particles (magnified) can be differentiated from them as they appear to be agglomerated. In another experiment, the time for dropwise addition was maintained at 2 hours. When the particles obtained were characterized, in the FT-IR spectrum, Fig. 5.3(A)(d), we could see a signal at 1730 cm^{-1} , a prominent split signal at 1489 cm^{-1} and 1406 cm^{-1} and two signals at 872 cm^{-1} and 700 cm^{-1} , accordingly, in the PXRD pattern, we obtained peaks at 2θ equal to 16.66, 20.51, 29.09, 31.56, 35.91, 37.93, 41.78, 47.11 and 51.72, Fig. 5.3(A)(d), identical to the PDF data for MHC (ICSD 00-029-0306). In the FESEM image, Fig. 5.4(D), we could see the particles as tiny nanospheres which are agglomerated. In the final experiment, the time of addition was extended to 4 hours; here too, the MHC phase had formed. This was confirmed by the FT-IR spectrum, Fig. 5.3(A)(e), where we could see a signal at 1705 cm^{-1} , a prominent split signal at 1484 cm^{-1} and 1404 cm^{-1} and two signals at 872 cm^{-1} and 700 cm^{-1} , all the signals being characteristics of the MHC phase. Accordingly, in the PXRD pattern, Fig. 5.3(B)(e), we obtained peaks at 2θ equal to 16.86, 20.61, 29.21, 31.76, 36.15, 37.98, 41.78, 47.22, and 51.79, identical to the PDF data for MHC (ICSD 00-029-0306). The morphology, Fig. 5.4(E), was exactly like that of the MHC particles obtained in the previous case, as we could see tiny agglomerated nanospheres.

After performing the above set of experiments based on the time-dependent addition of Ca^{2+} , the solution in each case containing the precipitated CaCO_3 in the presence of methanol extract of tulsi were divided into two parts in addition to a part being filtered and dried such that the particles obtained were subjected to various characterizations. Out of the two parts that were separated, one of them was used to study the maturation of the CaCO_3 particles in the aqueous solution for 3 hours. The second part was subjected to heating at $80\text{ }^\circ\text{C}$ for 1 hour to observe the thermodynamic stability of the phases compared to the maturation in solution at room temperature. This extended study was performed because, in all the five cases, the phases obtained were all unstable, hence, on maturation or heat treatment, interesting observations regarding the change in phase and morphology would lead to an insightful understanding of the intriguing CaCO_3 polymorphism. When the ACC particles synthesized by the direct addition were allowed to mature in solution for 3 hours, the amorphous phase was transformed into the stable calcite phase. In the FT-IR spectrum, Fig. A5.5(A)(a), a broad signal at 1390 cm^{-1} and signals at 712 cm^{-1} and 872 cm^{-1} suggested the specific formation of calcite. In the PXRD pattern, Fig. 5.5(A)(a) peaks at 2θ values identical to the standard PDF data for calcite (ICSD 00-047-1743), suggested the complete transformation to the calcite phase. The morphology of the particles, Fig. 5.6(A), was rhombohedral as that of the calcite phase. Also, when the second

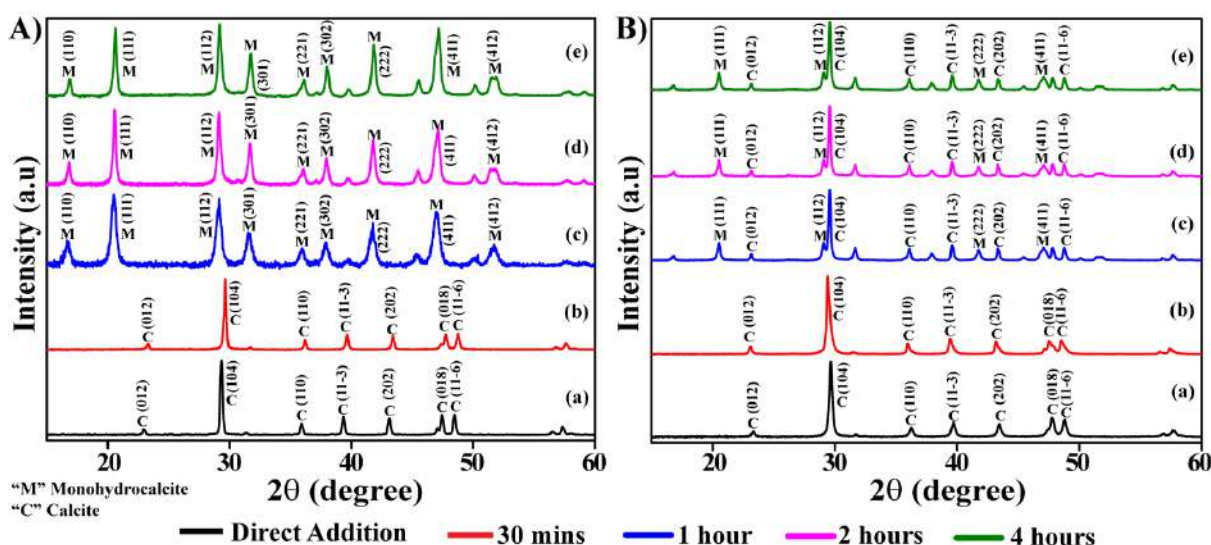


Figure 5.5: PXRD pattern of CaCO_3 particles precipitated by reverse sequence of addition at different addition rates in the presence of tulsi extract in methanol followed by (A) Maturation of the particles in solution at room temperature, (B) Heating the particles in solution at 80°C .

part of the precipitated solution was heated for 1 hour, the unstable amorphous phase had converted into the stable calcite phase. This conversion was supported initially by the FT-IR spectrum, Fig. A5.5(B)(a), as we could see the signals due to calcite at 711 cm^{-1} and 874 cm^{-1} , followed by the PXRD analysis, Fig. A5.5(B)(a), in which the peaks obtained are identical to the standard PDF data for calcite (ICSD 00-047-1743). From the FESEM image, Fig. 5.7(A), we can see the formation of rhombohedral calcite particles. Again, when the ACC particles formed in the second type of addition (30 mins) were respectively allowed to mature and heated, the complete transformation to the stable calcite phase had taken place in both the cases. In the first case, two signals at 713 cm^{-1} and 872 cm^{-1} , Fig A5.5(A)(b), and in the second case, signals at 712 cm^{-1} were observed in the FT-IR spectrum. In the PXRD pattern, Fig. 5.5(A)(b) and Fig. (b), respectively for both the cases, peaks at 2θ values identical to the calcite phase were obtained, and a rhombohedral morphology of calcite was observed in both the cases, Fig. 5.6(B) and Fig. 5.7(B). The mixed-phase particles (MHC and ACC) obtained in the third case, when allowed to mature in solution at room temperature for 3 hours, it was observed that the complete transformation to the MHC phase had taken place. In the FT-IR spectrum, Fig. A5.5(A)(c), a new signal was observed at 1703 cm^{-1} , the split signal was observed at 1481 cm^{-1} and 1401 cm^{-1} , here the splitting was so prominent that it led to the bifurcation of the signals, the peak at 864 cm^{-1} had now transformed into a peak at 873 cm^{-1} , and a prominent peak at 700 cm^{-1} , the characteristic peak for the MHC phase could be seen. In the PXRD pattern, the peaks obtained support the complete conversion to MHC with 2θ equal to 16.86, 20.66, 29.15, 31.76, 36.13,

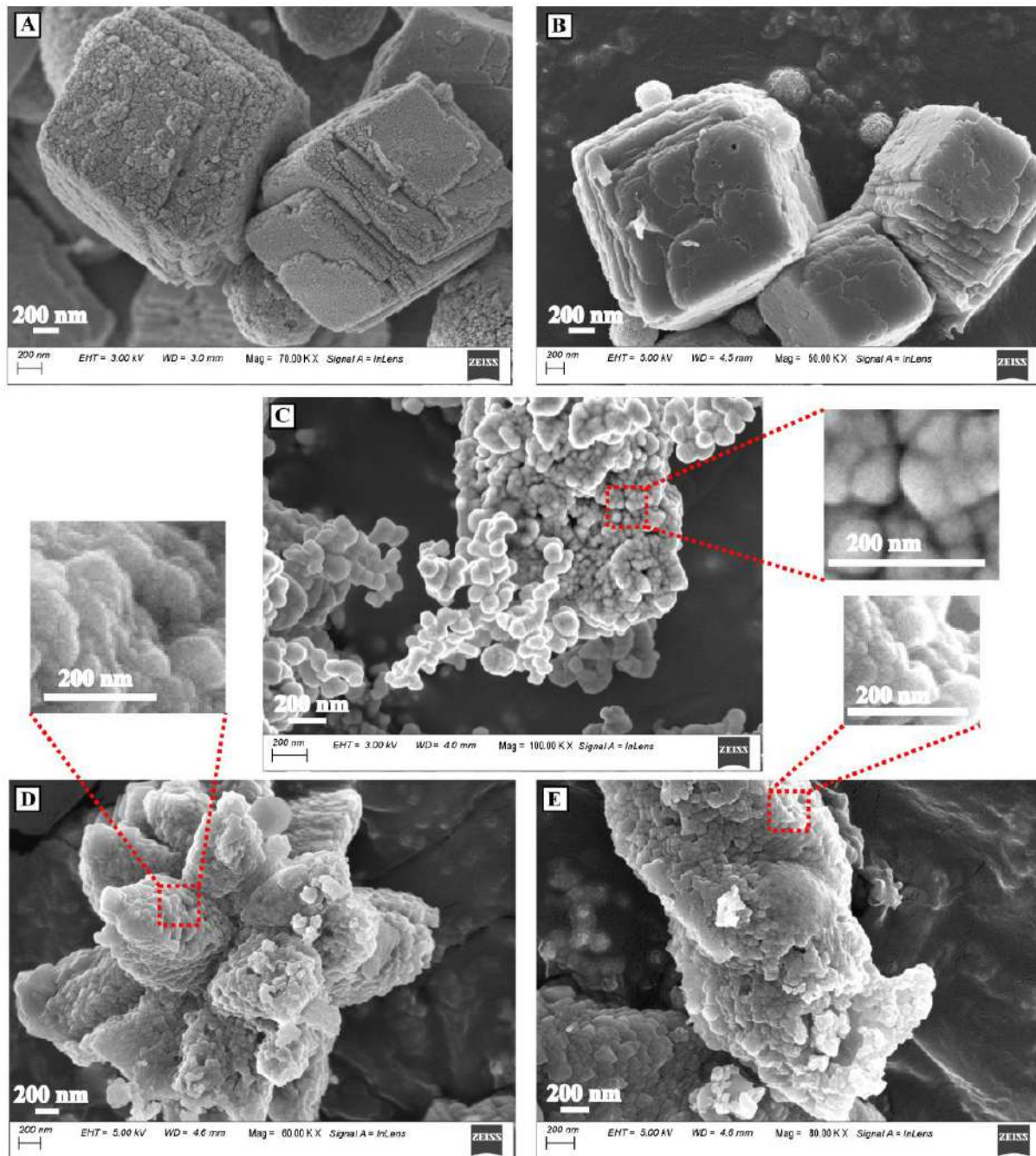


Figure 5.6: FESEM Images of CaCO_3 particles precipitated by the reverse sequence of addition in the presence of tulsi extract in methanol (A) by direct addition, (B) in 30 mins; (C) in 1 hour; (D) in 2 hours; (E) in 4 hours followed by maturation in solution at room temperature.

37.88, 41.86, 47.21, and 51.77, Fig. 5.5(A)(c), identical to the PDF data for MHC (ICSD 00-029-0306). The MHC particles appear as agglomerated near-spherical nanoparticles, as shown in Fig. 5.6(C), obtained from the FESEM imaging technique. When the mixed-phase particles were subjected to heating, it was observed that the particles were transforming into the stable crystalline calcite phase; here, another mixed phase, at this time, MHC and calcite, was observed. On characterizations, we could observe the co-existence of the MHC and the

calcite phases. In the FT-IR analysis, Fig. A5.5(B)(c), the split signal at 1500-1400 cm^{-1} had converted to a single peak 1450 cm^{-1} , two peaks were observed, one at 875 cm^{-1} and the other at 701 cm^{-1} due to the MHC phase and similarly, two other peaks at 854 cm^{-1} and 712 cm^{-1} , characteristic of the calcite phase were observed. In the PXRD pattern, Fig. 5.5(B)(c), along with the peaks at 2θ equal to 20.58, 29.12, 31.70, 41.77, and 46.99 due to the MHC phase, we could also observe peaks at 23.23, 29.51, 36.09, 39.52, 43.37, 48.82 which correspond to the calcite phase. In the FESEM image, Fig. 5.7(C), we could see the co-existence of the two phases. Along with the MHC nanoparticles, a significant number of rhombohedral crystals of diameter ~ 300 nm (magnified) could be seen, suggesting the transformation into the matured calcite phase. The MHC particles obtained by the addition in 2 hours, when subjected to maturation in solution for 3 hours, did not result in any phase or morphology change and remained as such, suggesting the stability of the MHC particles obtained using the tulsi extract. This was justified by the FT-IR and PXRD analysis, whereby the signals, Fig. A5.5(A)(d), and peaks (2θ), Fig. 5.5(A)(d), remained similar to the ones corresponding to the particles isolated immediately after the addition. From the FESEM imaging technique, we can see the MHC particles appear as agglomerated near-spherical nanoparticles, Fig. 5.6(D), obtained. But, when the MHC particles were subjected to the heating condition, as in the previous case, it was observed that the particles were transforming into the crystalline calcite phase. This was justified by the different characterizations, where we could observe the co-existence of the MHC and the calcite phases. In the FT-IR analysis, Fig. A5.5(B)(d), the split signal at 1500-1400 cm^{-1} had converted to a single peak 1465 cm^{-1} , two peaks were observed, one at 873 cm^{-1} and the other at 700 cm^{-1} due to the MHC phase and similarly, two other peaks at 855 cm^{-1} and 713 cm^{-1} characteristic of the calcite phase were observed. In the PXRD pattern, Fig. 5.5(B)(d), along with the peaks at 2θ equal to 20.45, 29.07, 31.72, 41.77, and 47.07 due to the MHC phase, we could also observe peaks at 23.23, 29.54, 36.06, 39.58, 43.37, 48.85 which correspond to the calcite phase. In the FESEM image, Fig. 5.7(D), the co-existence of the two phases is clearly visible where, along with the MHC particles, a significant number of rhombohedral crystals could be seen. The MHC particles obtained in the final case (4 hours) were also subjected to maturation and heating. In both the cases, the results obtained were similar to the previous case, as on maturation in solution, there was no change in phase and morphology of the MHC particles as can be seen from the FT-IR and PXRD analysis, Fig. A5.5(A)(e) and Fig. 5.5(A)(e), where the signal and peak positions correspond to the MHC phase and the FESEM image in Fig. 5.6(E) shows agglomerated near-spherical nanoparticles. The MHC particles, when subjected to heating, the co-existence of the MHC and the calcite phase were confirmed, initially, by the FT-

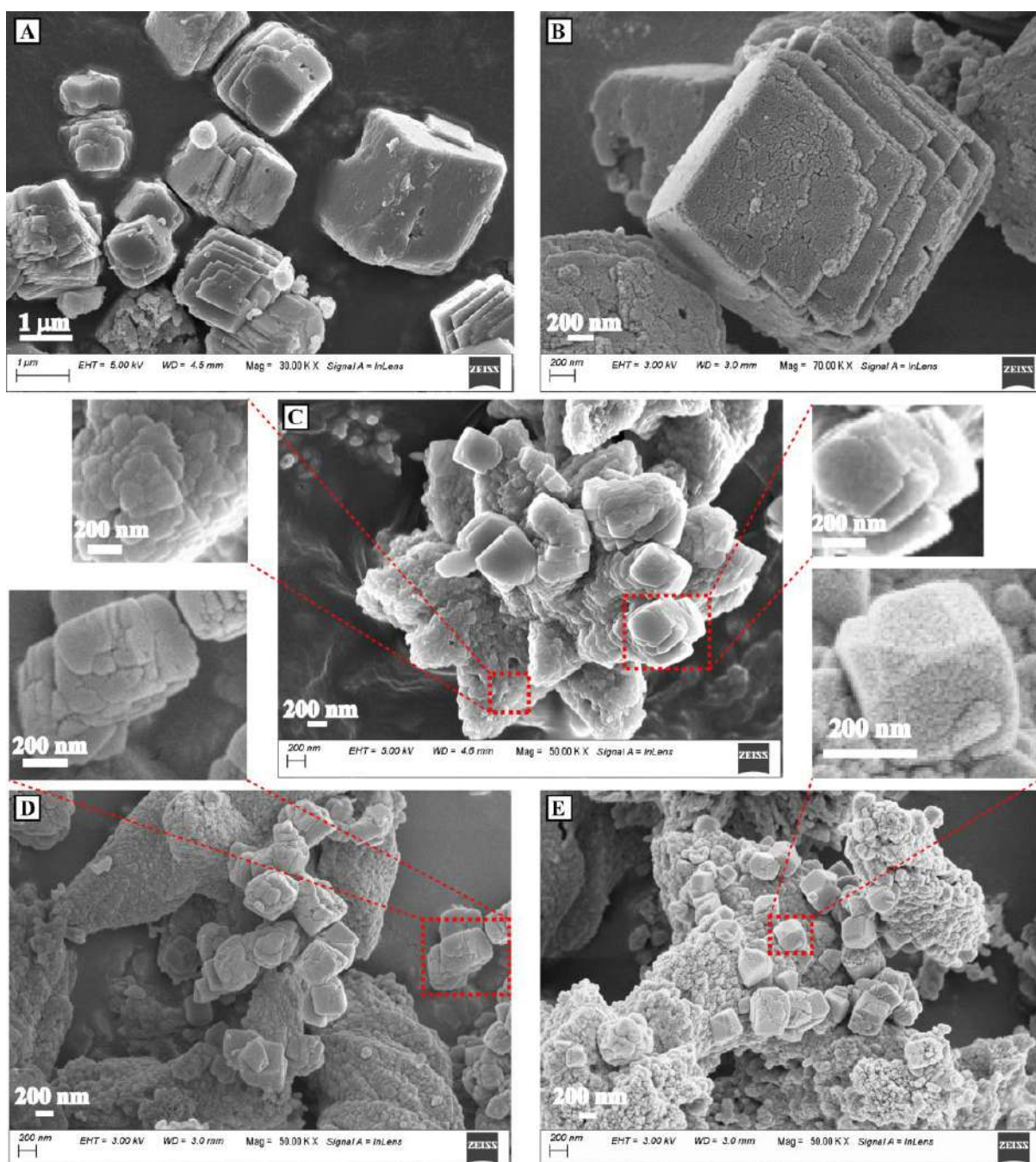


Figure 5.7: FESEM Images of CaCO_3 particles precipitated by the reverse sequence of addition in the presence of tulsi extract in methanol (A) by direct addition, (B) in 30 mins; (C) in 1 hour; (D) in 2 hours; (E) in 4 hours followed by heating at 80°C .

FT-IR analysis, Fig. A5.5(B)(e), followed by the PXRD pattern, Fig. 5.5(B)(e), where along with the peaks due to the MHC phase we could also observe peaks which correspond to the calcite phase. Again, the co-existence of the two phases could clearly be seen in the FESEM image, Fig. 5.7(E), where along with the MHC nanoparticles we can see a good number of rhombohedral crystals, suggesting the transformation to the calcite phase on heating. The results obtained on performing the reverse sequence of addition followed by the maturation and

heating studies have been comprehended in **Table A5.5**.

In addition to exhibiting polymorphism, CaCO_3 possesses another fascinating characteristic of existing in both the hydrated and anhydrous forms. On performing the above set of experiments, we obtained both the hydrated and the anhydrous phases of CaCO_3 . This could best be understood by the TG/DTG analysis of the particles obtained in the first case (ACC), the third case (pure MHC) and the calcite particles obtained from the maturation of the ACC. Both ACC and MHC are known to contain structure water molecules,^{5,27} whereas the calcite phase is known to be free of it. In the TG/DTG analysis of ACC, Fig. 5.8(A), four different mass losses were observed in the TGA curve. The first loss observed was 2%, due to the physically adsorbed water up to 100 °C, the second loss of 15% was observed in the temperature range of 100-220 °C attributed to the structure water responsible for rendering the phase a hydrated one, the third loss of 10% at 350-500 °C is due to the loss of organic groups from the template and finally, the loss at 620-740 °C, 25%, is due to the loss of CO_2 . Correspondingly, in the DTG curve, Fig. 5.8(A), 3 major peaks were observed at 130 °C, 360 °C and 730 °C attributed to the dehydration, decarboxylation and decarbonization processes, respectively. The TG/DTG analysis for MHC phase validated the formation of the hydrated calcite phase. In the TGA curve, Fig. 5.8(B), we could see three different mass losses, the first one in the range of 60-150 °C, 5%, due to the physically adsorbed water. The second mass loss, the most important one, is due to the loss of the structure water, a characteristic of the hydrated phase and this was observed in the range of 170-230 °C and accounting for 12% of mass loss; this was followed by a smooth line, which happens due to the corresponding transformation of the MHC to the anhydrous phase and finally, the loss of CO_2 from calcite was observed at 650-770 °C and this accounted for 35% of the mass loss. The corresponding DTG curve, Fig. 5.8(B), showed three different peaks at 120 °C, 170 °C, and 750 °C, the first and the second peak are due to the dehydration of the physically and chemically adsorbed water. The third peak is due to the decarbonization of CaCO_3 .



Figure 5.8: TGA/DTG curve of (A) ACC nanoparticles; (B) MHC phase; (C) Calcite phase in the temperature range of 25-800 °C.

However, for the anhydrous calcite phase, the TGA curve, Fig. 5.8(C), showed two different mass losses, ~3% due to the loss of the physically absorbed water at around 100 °C and ~40% loss due to decarbonization in the range of 650-770 °C. Similarly, in the DTG curve, Fig. 5.8(C), we obtained two different peaks at 135 °C and 750 °C due to dehydration and decarbonization, respectively. Hence, from the TG/DTA analysis, the formation and the distinction between the hydrated and the anhydrous phases were established.

The formation of the various phases of CaCO_3 takes place via the amorphous precursor (ACC). On performing the different sets of experiments under the reverse sequence of addition and characterizing the synthesized particles, we were able to understand the formation of the MHC phase via the ACC precursor, **Scheme A5.1**, followed by the subsequent conversion of MHC to calcite at high temperatures. It was observed that up to 30 mins of dropwise addition, we were able to obtain and isolate the ACC particles suggesting that the tulsi extract in methanol was a promising template for synthesizing this unstable phase. Therefore, this work was also extended in order to study the ACC phase w.r.t. the stabilization in aqueous solution and also the isolated particles. The precipitated ACC particles were allowed to remain in solution and the phase was monitored every hour by isolating a certain portion of it by vacuum filtering and then subjecting the particles to FT-IR analysis, Fig. A5.6. It was observed that the particles in the solution were stable for at least two hours. The FT-IR spectrum of the particles isolated at the end of 3 hours suggested the conversion to the crystalline calcite phase. The isolated ACC particles remained stable even after 7 days under ambient conditions suggesting the high stability of the ACC particles synthesized in the presence of the tulsi extract. This has been proved by obtaining the PXRD pattern, Fig. A5.7(A) and the FESEM images, Fig. A5.7(B), (C), (D) of the particles after days 1, 4 and 7.

The stability of the ACC particles in solution was studied by obtaining the FT-IR spectrum, Fig. A5.7, of the particles by isolating them every hour by vacuum filtration. On isolation immediately after the precipitation, it was observed that a split signal at 1475 cm^{-1} and 1415 cm^{-1} and a signal at 864 cm^{-1} , which are characteristics of the ACC phase, were present. The particles isolated after hour 1 and 2 also showed similar patterns with split signals at 1481 cm^{-1} and 1418 cm^{-1} and at 1473 cm^{-1} and 1420 cm^{-1} , respectively, and the signal at 864 cm^{-1} being common in both the cases. These being the characteristics of the ACC phase, suggested the stabilization of the unstable phase in aqueous solution at least for 2 hours. The particles isolated after 3 hours showed characteristic of the calcite phase with signals at 1440 cm^{-1} , 872 cm^{-1} and 713 cm^{-1} , suggesting the conversion of the amorphous precursor to the stable crystalline phase.

However, the isolated particles showed great stability even when stored under ambient conditions. The particles were subjected to PXRD analysis, after days 1, 4 and 7, where in each case a similar pattern with no sharp peaks but a pattern with a broad hump at 2θ equal to 32, Fig. A5.8(A) characteristic of the amorphous phase suggested the stability of the ACC phase. The FESEM images, Fig. A5.8(B), (C) and (D), of the particles were also obtained and it could be seen that the particles remained as stable nanospheres with no change in morphology even after 7 days.

The conversion of the amorphous precursor to crystalline calcite takes place by dissolution followed by recrystallization. This two-step process takes place so quickly within a few milliseconds that the isolation of ACC stands as a challenge. However, the stabilization of the amorphous phase can be achieved by controlling the size of the particles below the critical size necessary for the evolution to crystalline polymorphs or by preventing its dehydration or shielding it from the aqueous phase.⁴⁵ The use of inorganic ions such as Mg^{2+} and additives such as polycarboxylates or alcohols have allowed the extended stability of this very unstable phase.^{5.28,5.29} The tulsi extract of methanol containing Mg^{2+} ,^{5.24} phenolic compounds and acids such as Oleanolic acid, Ursolic acid, Rosmarinic acid,^{5.22} among others, are responsible for the stabilization of ACC. Usually, when a particular additive is used to prevent the crystallization, a significant amount of it, w.r.t. the amount of ACC, is used. The additives such as polycarboxylates induce stabilization by surface adsorption, whereas the ions such as Mg^{2+} perform via bulk incorporation.^{5.30} In this case, these ions and compounds are either present in trace amounts or in very small concentrations. Hence, we propose a plausible mechanism where a combined effect of the Mg^{2+} ions and the other compounds stabilize the ACC phase by incorporation and surface adsorption, respectively.

The conversion of ACC to calcite took place in solution both at room temperature and on heating, and in both these cases, the morphology of the calcite particles was found to be the hour, we were able to trap the stage where both the precursor ACC and the MHC phase co-existed, and when these biphasic particles were allowed to mature in solution, the complete conversion to the MHC phase took place. We could understand that the control in terms of the addition of Ca^{2+} leading to the precipitation of $CaCO_3$ plays the most crucial part here, along with the tulsi extract in directing the phase. To justify this transformation, the synthesis was performed by increasing the time of addition to 2 hours and 4 hours, and in both these cases, we obtained the MHC phase. It was also observed that the MHC particles on further maturation in solution at room temperature did not undergo any phase transformation. However, on subjecting

to heat, we were again able to trap a phase whereby the transition from the hydrated phase to the thermodynamically stable anhydrous calcite phase was taking place. This transformation suggested that the higher temperature is not favourable for MHC.

As already mentioned, Mg plays a vital role in the formation of both ACC and MHC, especially in the case of MHC, where the medium is pre-requisitely supposed to contain an excess of Mg ions. It can be understood that the Mg ions present in the methanol extract of tulsi played a key role, the EDX analysis confirmed the presence of Mg in MHC, Fig. 5.9(F), where we could see the presence of ~1.5% of Mg along with the other elements of CaCO_3 . The EDX mapping images, Fig. 5.9(A), (B), (C), (D) and (E), gave us a clear picture of how this small amount of Mg is distributed evenly around the CaCO_3 . In this case, we see how a minimal amount of Mg can prevent the MHC from dehydrating to the anhydrous calcite phase. Hence, we can infer that the polyphenols and acids present in the tulsi extract in methanol perform the supporting role to boost the Mg^{2+} ions in stabilizing this hydrated phase by preventing dehydration.

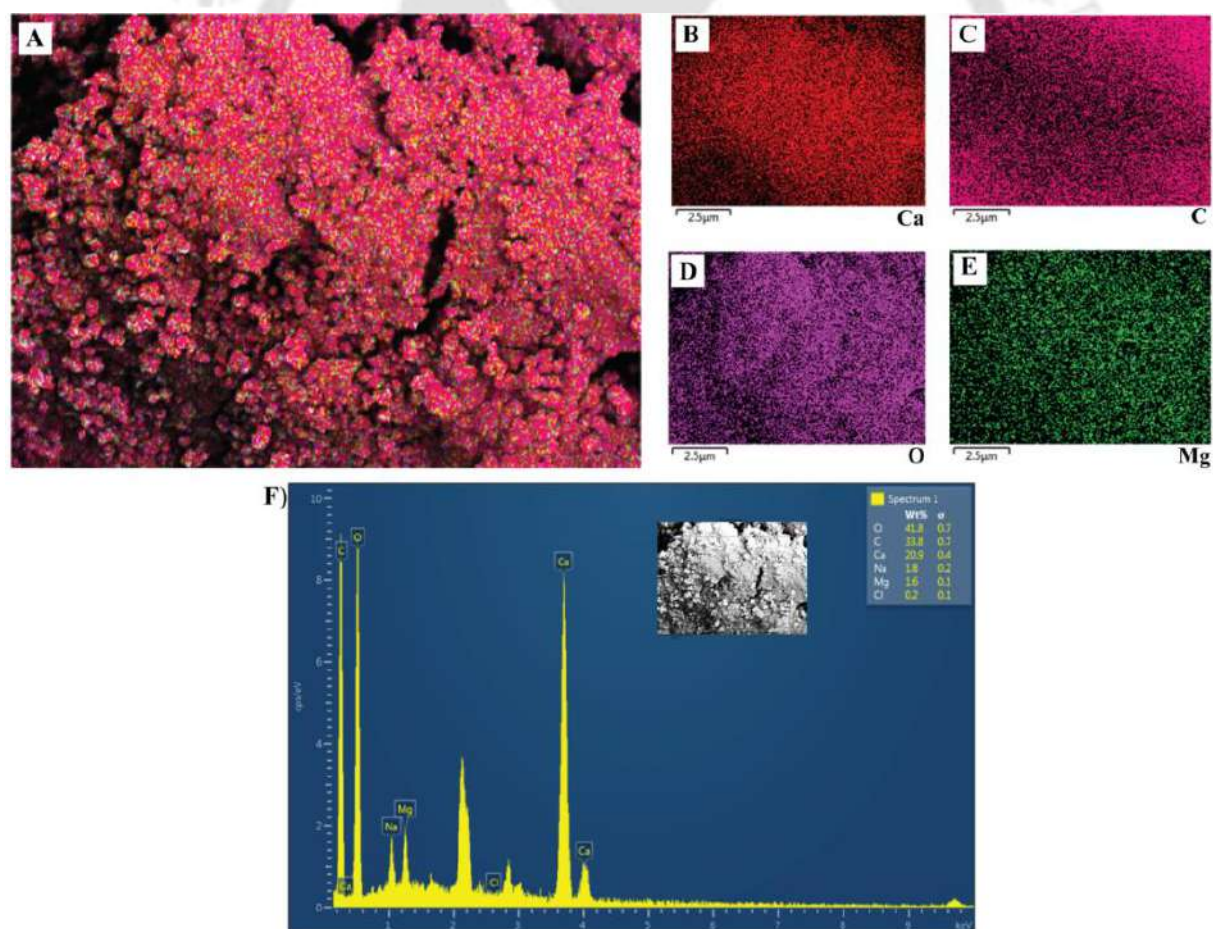


Figure 5.9: (A) EDX mapping of MHC particles highlighting all the elements; (B), (C), (D), (E) highlighting the individual elements Ca, C, O, Mg, respectively; (F) EDX elemental analysis of MHC.

To justify our findings, we performed the control experiments with the methanol extracts of mango and guava leaves, maintaining all other conditions the same. In both these cases, the calcite phase, Fig. A5.8, was obtained irrespective of the presence of Mg ions in the extracts. Since the extracts were used in small amounts to act as templates hence, solely the very low concentration of Mg ions in them would not be able to direct the formation of the hydrated phase. With the methanol extract of green tea, the reverse sequence synthesis performed by the dropwise addition of Ca^{2+} yielded the rhombohedral calcite, Fig. A5.9. The formation of the matured calcite crystals suggested that on reversing the sequence of addition, there was no definite role played by the template.

5.3 Conclusion

For the very first time, the role of tulsi and green tea in the *in vitro* crystallization of a Ca-based mineral was studied. We were able to synthesize the metastable vaterite phase, and also, interestingly, three different and mesmerizing morphologies of the calcite phase were discovered. Although both tulsi and green tea possess similar chemical compositions, their difference in the phase and morphology modulation was highlighted. In the second part of the work, we presented a straightforward and convenient method to synthesize the highly unstable ACC nanoparticles and the hydrated MHC phase using the tulsi extract in methanol. Additionally, the formation of MHC was obtained by controlling the addition of the Ca^{2+} ions, and the subsequent transformation of the MHC particles to the thermodynamically stable calcite phase at high temperature was studied. The role played by the trace amount of Mg in tandem with the diverse chemical composition of the tulsi extract in methanol in preventing the dehydration of MHC to anhydrous calcite was observed. To summarize, by tuning the sequence of addition of the precursor ions in the presence of the tulsi extract, changes in both phase and morphology were observed, whereas, with the green tea extract, only the morphology change was observed. The successful utilization of tulsi due to its wide availability worldwide and effectively zero cost of production makes it a genuinely important research prospect, widening the scope for exploring the possibilities in the field of Ca-based mineral research.

References

- 5.1. N. Neumann and M. Epple, Monohydrocalcite and Its Relationship to Hydrated Amorphous Calcium Carbonate in Biominerals, **Eur. J. Inorg. Chem.**, 2007, 1953-1957.

- 5.2. E. E. Coleyshaw, G. Crump and W. P. Griffith, Vibrational spectra of the hydrated carbonate minerals ikaite, monohydrocalcite, lansfordite and nesquehonite, *Spectrochimica Acta*, 2003, **59**, 2231-2239.
- 5.3. R. Nishiyama, T. Munemoto, and K. Fukushi, Formation condition of monohydrocalcite from $\text{CaCl}_2\text{-MgCl}_2\text{-Na}_2\text{CO}_3$ solutions, *Geochimica et Cosmochimica Acta*, 2013, **100**, 217-231.
- 5.4. B. Purgstaller, V. Mavromatis, K. E. Goetschl, F. R. Steindla and M. Dietzela, Effect of temperature on the transformation of amorphous calcium magnesium carbonate with near-dolomite stoichiometry into high Mg-calcite, *CrystEngComm*, 2021, **23**, 1969-1981.
- 5.5. J. D. Rodriguez-Blanco, S. Shaw, P. Bots, T. Roncal-Herrero and L. G. Benning, The role of Mg in the crystallization of monohydrocalcite, *Geochimica et Cosmochimica Acta*, 2014, **127**, 204–220.
- 5.6. K. Nobuyoshi, Y. Nakagoe and H. Tanaka, Crystallization of amorphous calcium carbonate, *Thermochimica Acta*, 1998, **318**, 239-244.
- 5.7. F. Konrad, F. Gallien, D. E. Gerard and M. Dietzel, Transformation of Amorphous Calcium Carbonate in Air, *Cryst. Growth Des.*, 2016, **16**, 6310-6317.
- 5.8. J. M. Xto, C. N. Borca, J. A. Bokhoven and T. Huthwelke, Aerosol-based synthesis of pure and stable amorphous calcium carbonate, *Chem. Commun.*, 2019, **55**, 10725-10728.
- 5.9. S. Chen, H. Colfen, M. Antonietti and S. Yu, Ethanol assisted synthesis of pure and stable amorphous calcium carbonate nanoparticles, *Chem. Commun.*, 2013, **49**, 9564-9566.
- 5.10. W. Hou and Q. Feng, Morphology and formation mechanism of vaterite particles grown in glycine-containing aqueous solutions, *Mater. Sci. Eng. C*, 2006, **26**, 644-647.
- 5.11. S. Maurya, Phytochemical efficiency of *Ocimum sanctum* (Tulsi) in health enhancement and disease prevention: A review, *IJARESM*, 2021, **9**, 1346-1351.
- 5.12. P. Prakash and N. Gupta, Therapeutic uses of *Ocimum sanctum* linn (tulsi) with a note on eugenol and its pharmacological actions: a short review, *Indian J. Physiol. Pharmacol.*, 2005, **49**, 125-131.
- 5.13. R. Borah and S. P. Biswas, Tulsi (*Ocimum sanctum*), excellent source of phytochemicals, *IJEAB*, 2018, **3**, 1732-1738.
- 5.14. A. A. Khalil, U. Rahman, M. R. Khan, A. Sahar, T. Mehmood and T. Khan, Essential oil eugenol: sources, extraction techniques and nutraceutical perspectives, *RSC Adv.*, 2017, **7**, 32669-32681.

- 5.15. R. C. Padalia and R. S. Verma, Comparative volatile oil composition of four *Ocimum* species from northern India, *Nat. Prod. Res.*, 2011, **25**, 569-575.
- 5.16. J. Singh, A. Mehta, M. Rawat and S. Basu, Green synthesis of silver nanoparticles using sun dried tulsi leaves and its catalytic application for 4-Nitrophenol reduction, *J. Environ. Chem. Eng.*, 2018, **6**, 1468-1474.
- 5.17. K. V. Alex, T. P. Pavai, R. Rugmini, M. S. Prasad, K. Kamakshi and K. C. Sekhar, Green Synthesized Ag Nanoparticles for Bio-Sensing and Photocatalytic Applications, *ACS Omega*, 2020, **5**, 13123-13129.
- 5.18. S. Iravani, Green synthesis of metal nanoparticles using plants, *Green Chem.*, 2011, **13**, 2638-2650.
- 5.19. S. Pastoriza, M. Mesias, C. Cabrera and J. A. Rufián-Henares, Healthy properties of green and white teas: an update, *Food Funct.*, 2017, **8**, 2650-2662.
- 5.20. E. W. C. Chan, Y. Y. Lim and Y. L. Chew, Antioxidant activity of *Camellia sinensis* leaves and tea from a lowland plantation in Malaysia, *Food Chemistry*, 2007, **102**, 1214-1222.
- 5.21. H. Vishnoi, R. B. Bodla and R. Kant, Green tea (*Camellia sinensis*) and its antioxidant property: a review, *IJPSR*, 2018, **9**, 1723-1736.
- 5.22. D. J. Jain and S. K. Rajurkar, Chemical Composition of Methanolic Extract of Tulsi Leaves (*Ocimum sanctum* L.), *IJRSI*, 2019, **6**, 113-114.
- 5.23. C. G. Bihari, B. Manaswini, P. S. Keshari and T. S. Kumar, Phytochemical investigation & evaluation for antidiabetic activity of leafy extracts of various *Ocimum* (Tulsi) species by alloxan induced diabetic model, *J Pharm Res.*, 2011, **4(1)**, 28-29.
- 5.24. S. I. Vidhani, V. G. Vyas, H. J. Parmar, V. M. Bhalani, M. M. Hassan, A. Gaber and B. A. Golakiya, Evaluation of Some Chemical Composition, Minerals Fatty Acid Profiles, antioxidant and Antimicrobial Activities of Tulsi (*Ocimum sanctum*) from India, *Am. J. Food Technol.*, 2016, **4**, 52-57.
- 5.25. S. M. Chacko, P. T. Thambi, R. Kuttan and I. Nishigaki, Beneficial effects of green tea: A literature review, *Chin. Med.*, 2010, **5**, 1-9.
- 5.26. R. Liu, F. Liu, S. Zhao, Y. Su, D. Wang and Q. Shen, Crystallization and oriented attachment of monohydrocalcite and its crystalline phase transformation. *CrystEngComm*, 2013, **15**, 509-515.
- 5.27. Y. Wang, Q. Yao, G. Zhou and S. Fu, Transformation of amorphous calcium carbonate into monohydrocalcite in aqueous solution: a biomimetic mineralization study, *Eur. J. Mineral.*, 2015, **27**, 717-729.

- 5.28. N. A. J. M. Sommerdijk and G. de With, Biomimetic CaCO₃ Mineralization using Designer Molecules and Interfaces, *Chem. Rev.*, 2008, **108**, 4499–4550.
- 5.29. X. Xu, J. T. Han, and K. Cho, Formation of Amorphous Calcium Carbonate Thin Films and Their Role in Biomineralization, *Chem. Mater.*, 2004, **16**, 1740-1746.
- 5.30. Z. Zou, X. Yang, M. Albéric, T. Heil, Q. Wang, B. Pokroy, Y. Politi and L. Bertinetti, Additives Control the Stability of Amorphous Calcium Carbonate via Two Different Mechanisms: Surface Adsorption versus Bulk Incorporation, *Adv. Funct. Mater.*, 2020, **30**, 2000003.



Annexure-Chapter 5

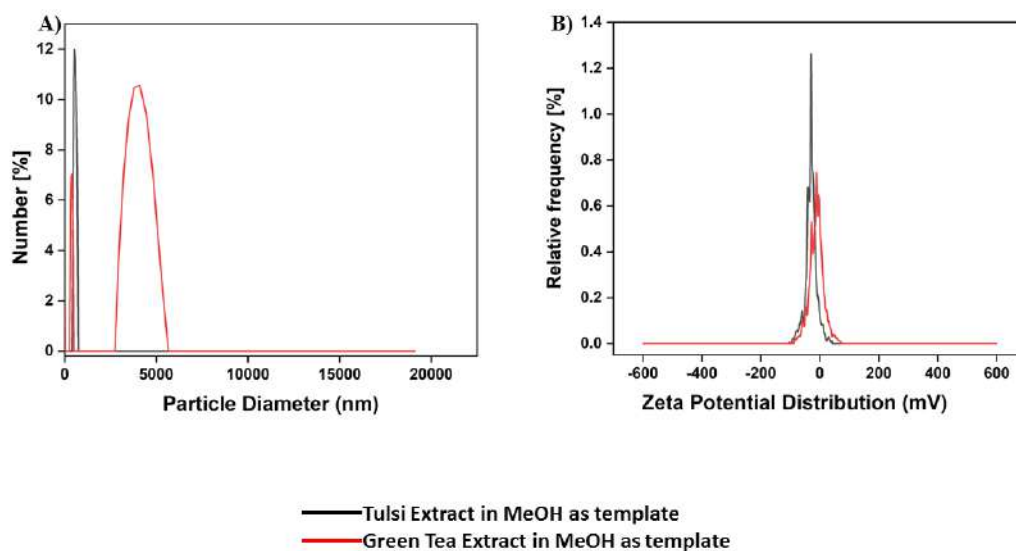


Figure A5.1: A) DLS-based particle size analysis; B) Zeta Potential of CaCO₃ particles synthesized in the presence of the tulsi and green tea extract in methanol.

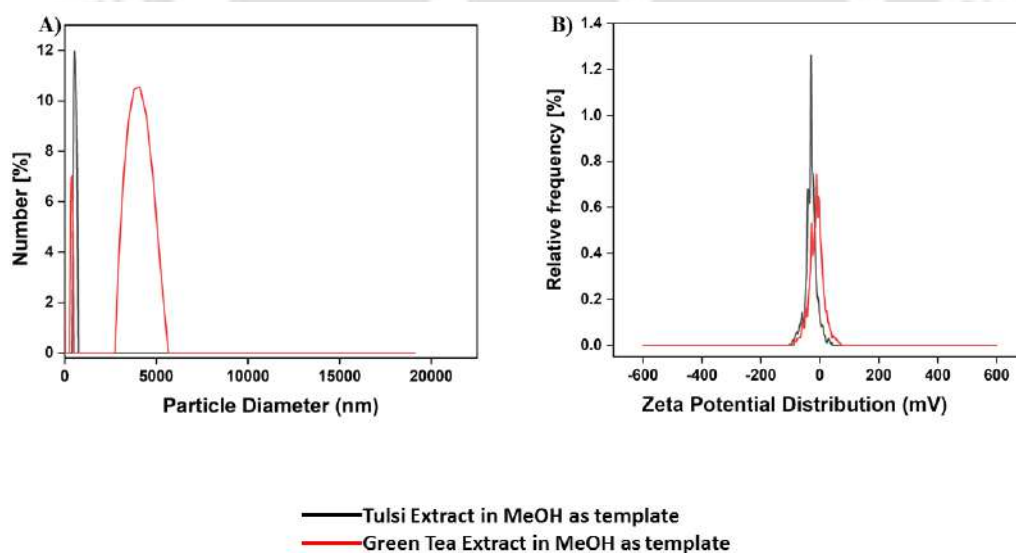


Figure A5.2: A) DLS-based particle size analysis; B) Zeta Potential of CaCO₃ particles synthesized in the presence of the tulsi and green tea extract in water.

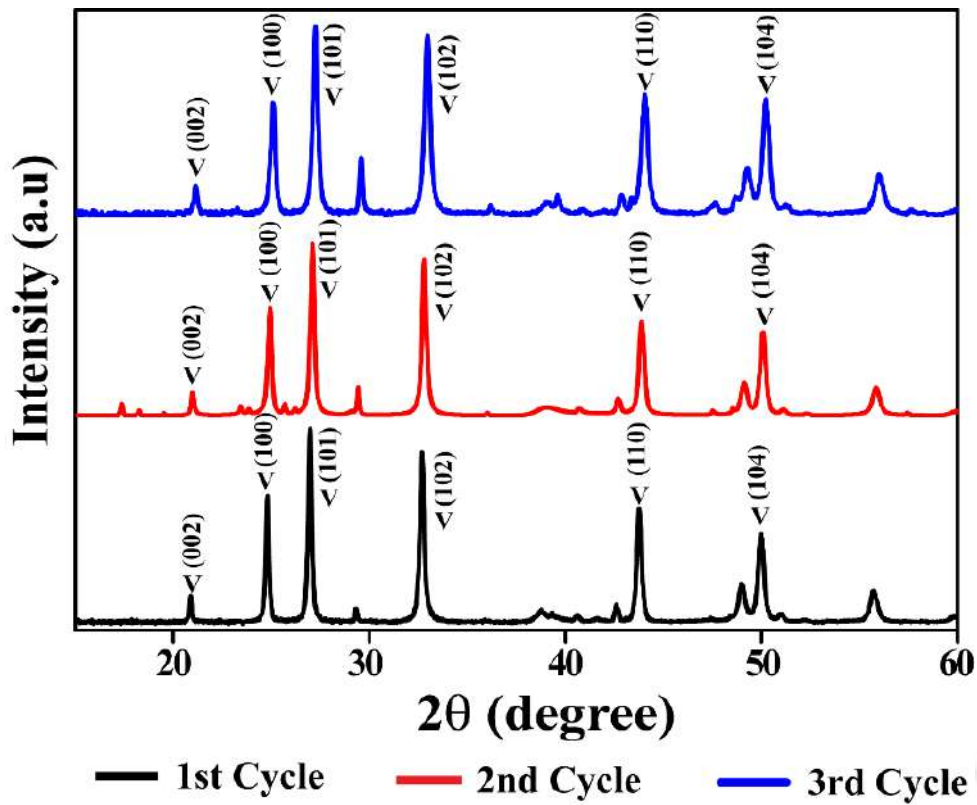


Figure A5.3: PXR D pattern showing the formation of vaterite after using the tulsi extract (in methanol) for three consecutive cycles.

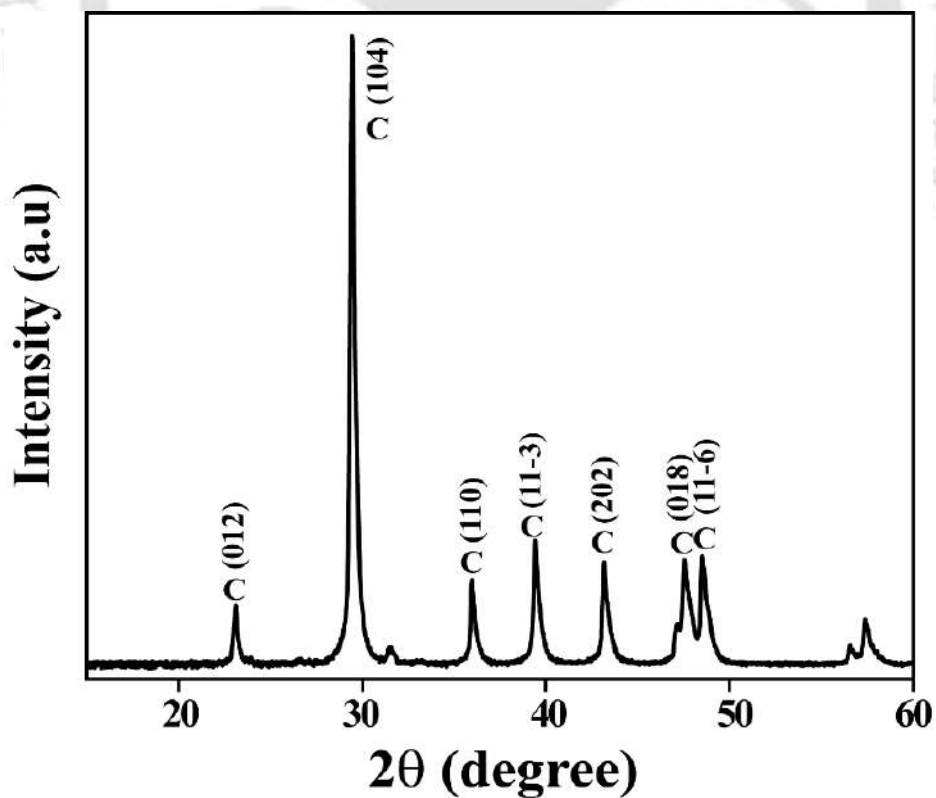


Figure A5.4: PXR D pattern showing the formation of calcite on using both the templates (tulsi and green tea in methanol) in the ratio 1:1.

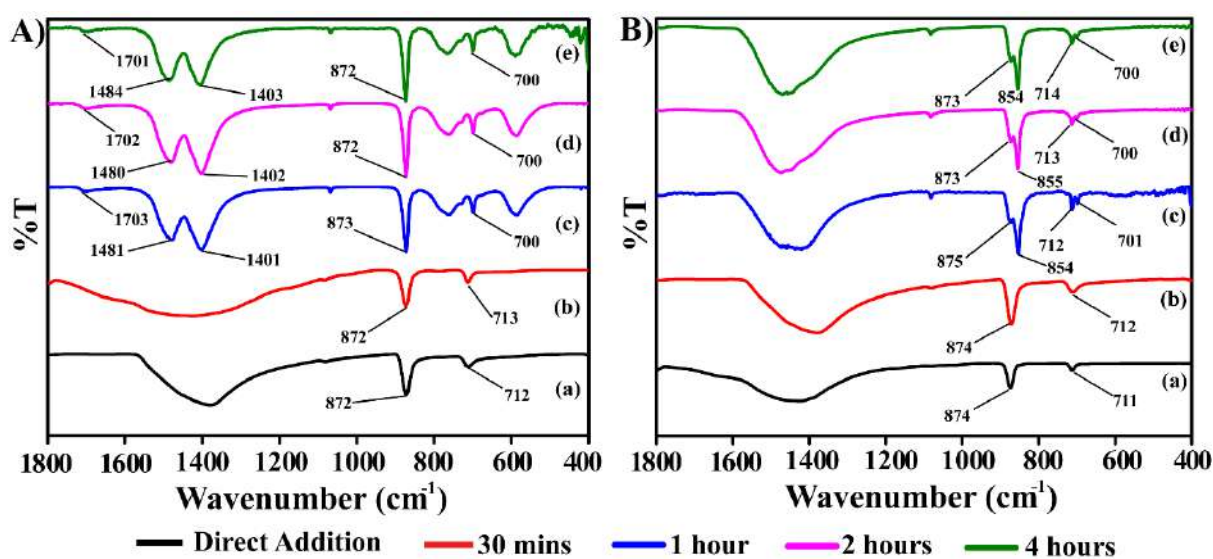


Figure A5.5: FT-IR spectra of CaCO_3 particles precipitated by reverse sequence of addition at different addition rates in presence of tulsi extract in methanol followed by (A) Maturation of the particles in solution at room temperature; (B) Heating the particles in solution at 80°C .

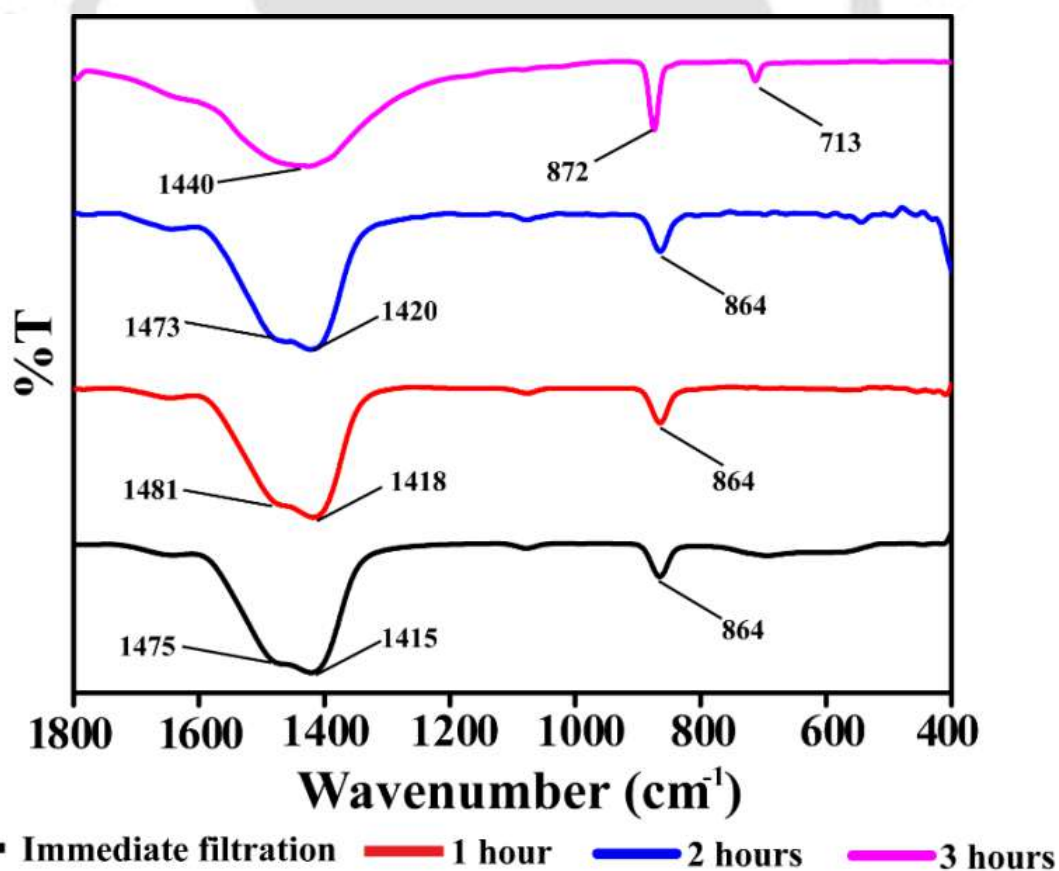


Figure A5.6: FT-IR spectra of the ACC particles isolated at 1 hour interval of time.

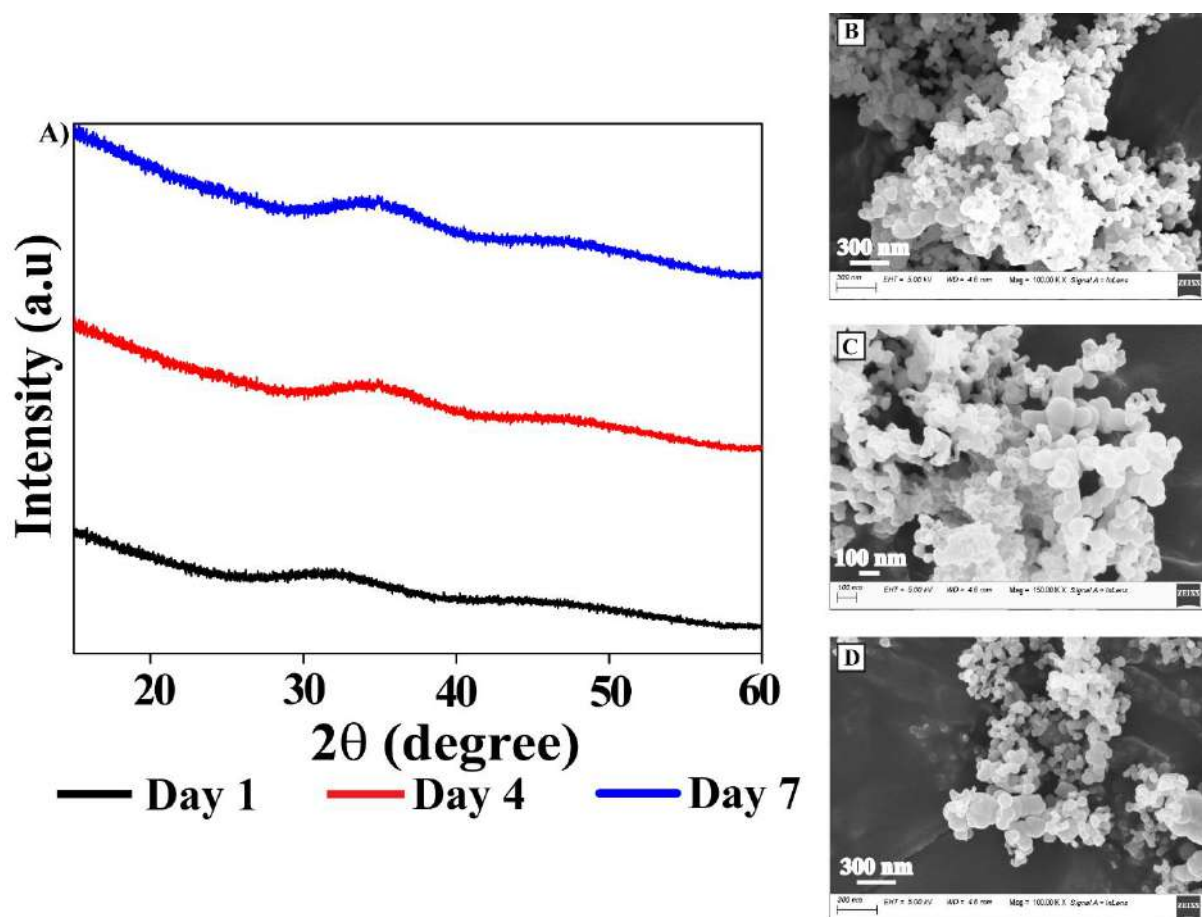


Figure A5.7: (A) PXRD pattern of the ACC particles synthesized by the reverse sequence of addition in the presence of the tulsi extract in methanol after day 1, 4 and 7; FESEM image of the ACC particles after (B) Day 1; (C) Day 4; (D) Day 7.

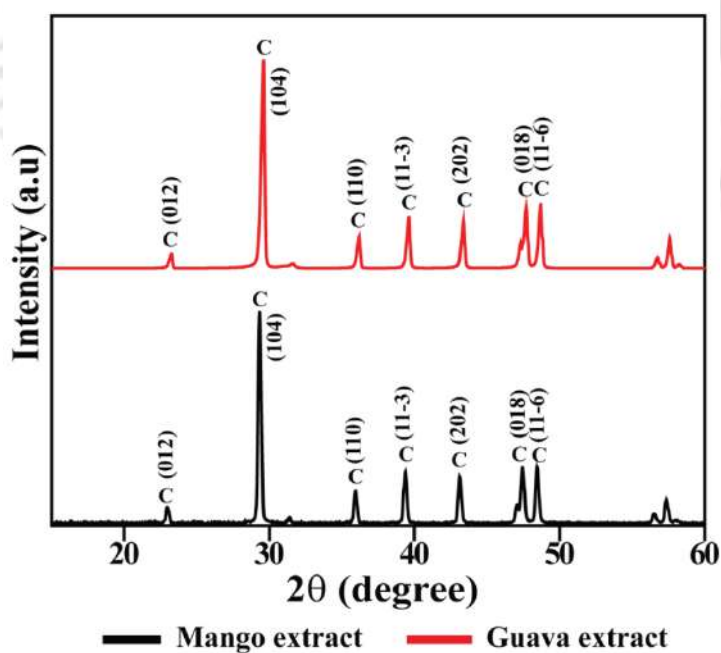


Figure A5.8: PXRD pattern of CaCO_3 particles precipitated in the presence of mango and guava extracts in methanol.

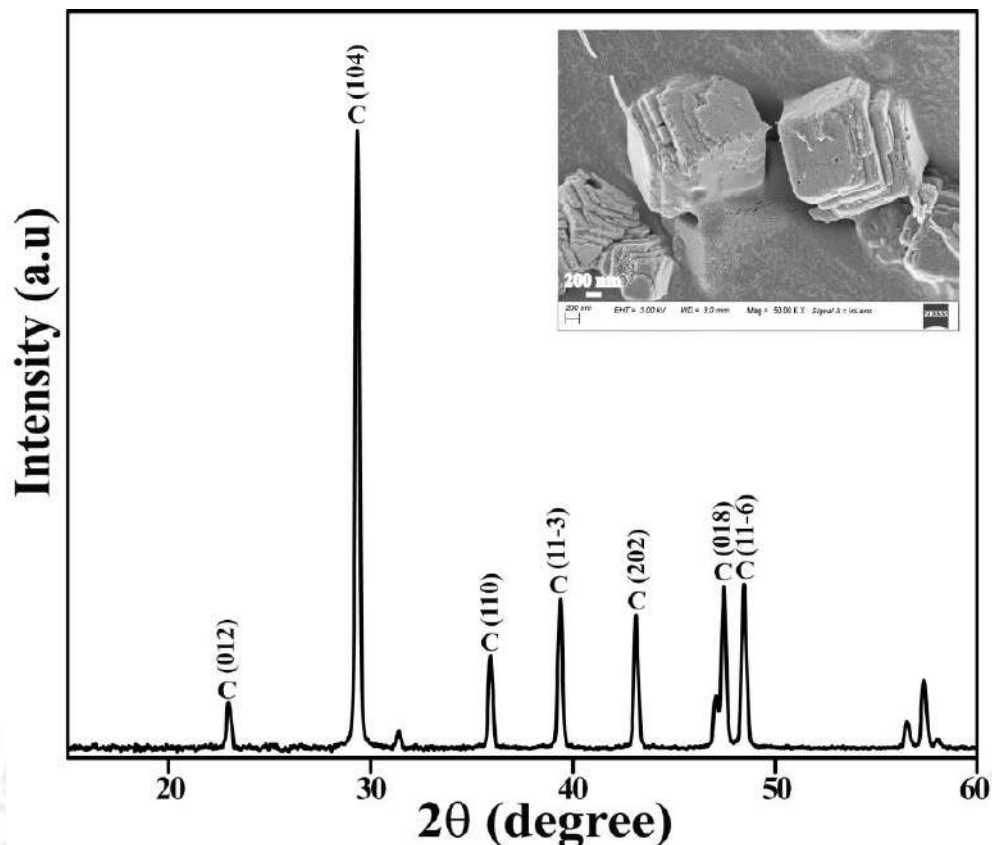
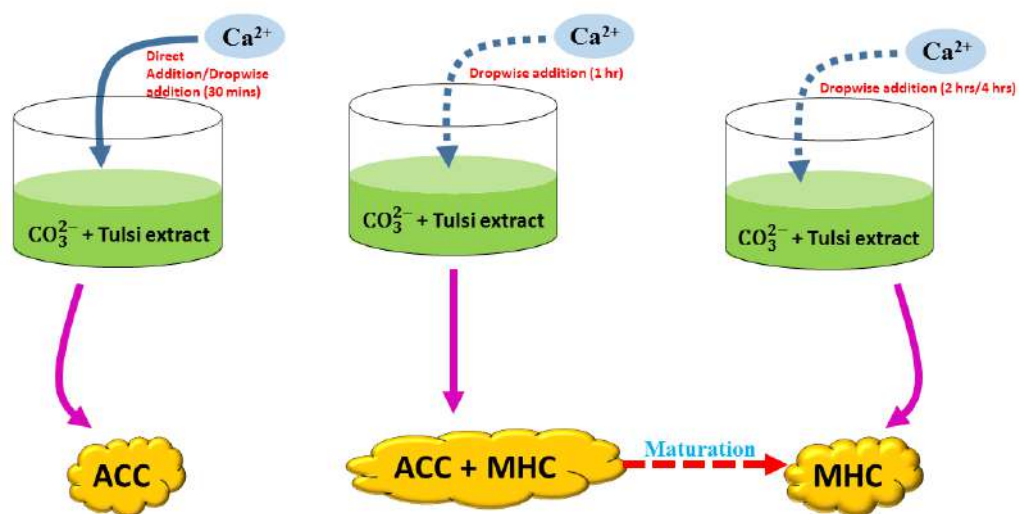


Figure A5.9: PXRD pattern and FESEM image of CaCO_3 particles precipitated by the reverse sequence of addition in the presence of the green tea extract in methanol.



Scheme A5.1: Illustration of the reverse sequence of addition in the presence of tulsi extract (in methanol) to obtain the MHC phase via the amorphous precursor.

Table A5.1: Phytochemical constituents of Tulsi and Green Tea

<i>Tulsi (Ocimum sanctum)</i>	<i>Green Tea (Camellia sinensis)</i>
Proteins	Proteins
Amino acids	Amino acids
Carbohydrates	Carbohydrates
Phenolic compounds	Phenolic compounds
Flavonoids	Flavonoids (Catechin)
Glycosides	Alkaloids (Caffeine)
Tannins	Fibers
Steroids	Vitamins
Sterols	Sterols
Terpenoids	Minerals and Trace elements
Minerals and Trace elements	
Organic acids	
Essential oils and Fatty acids	

Table A5.2: Phytochemical constituents in Methanol and Aqueous extracts of Tulsi

<i>Phytochemicals</i>	<i>Methanol extract</i>	<i>Aqueous extract</i>
Proteins	-	-
Carbohydrates	+	-
Phenols	+	+
Flavonoids	+	+
Tannins	+	-
Glycosides	+	+
Steroids	-	-
Terpenoids	+	-
Essential oils and Fatty acids	+	-

Table A5.3: Percentage concentration of the major phytochemical constituents in Methanol extract of Tulsi

<i>Phytochemicals</i>	<i>Concentration</i>
Proteins	~21%
Carbohydrates	~40%
Phenols (mg/g)	~2 mg/g
Flavonoids (mg/g)	~29 mg/g
Glycosides	~3.50%
Essential oils and Fatty acids	~3.60%

Table A5.4: Acids and Essential oils and Fatty acids present in the methanol extract of Tulsi

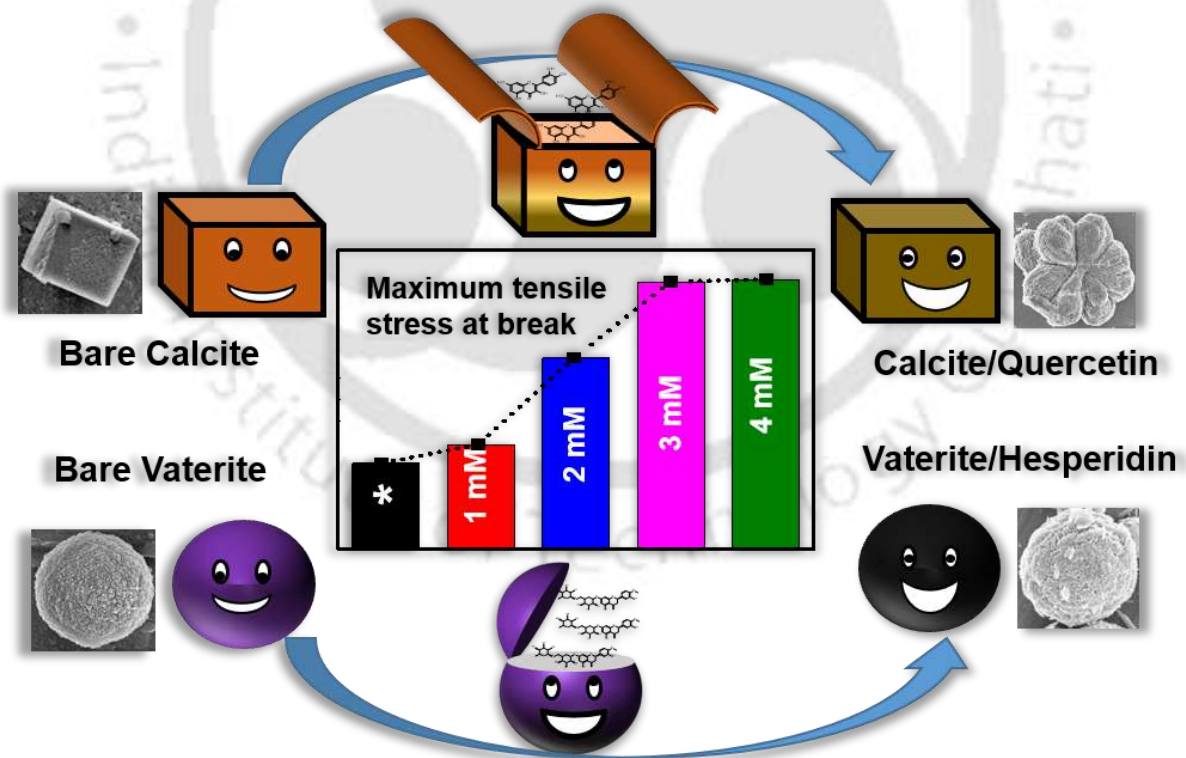
<i>Acids</i>	<i>Essential oils and Fatty acids</i>
Oleanolic acid	Eugenol
Ursolic acid	Methyl Eugenol
Rosmarinic acid	Carvacrol
Tuberonic acid	Lauric acid
4-Hydroxypelargonic acid	Myristic acid
5-Phenylaleric acid	Palmitic acid
Usnic acid	Palmitoleic acid
Pteroyl-D-glutamic acid	Stearic acid
Undecylic acid	Oleic acid
3-Phenoxypropionic acid	Linoleic acid
5-Phenylvaleric acid	Linolenic acid
6-Methyl caprylic acid	

Table A5.5: Phase obtained on performing the reverse sequence of addition with varying time of dropwise addition

Time taken for addition	Initial phase obtained	On maturation (3 hours)	On heating (at 80 °C)
Direct addition	ACC	Calcite	Calcite
30 mins	ACC	Calcite	Calcite
1 hour	MHC + ACC	MHC	MHC + Calcite
2 hours	MHC	MHC	MHC + Calcite
4 hours	MHC	MHC	MHC + Calcite



Incorporation of flavonoids into CaCO_3 and their influence on the phase, morphology and mechanical strength of the composites: A bio-inspired approach



6.1 Introduction

The fascination garnered by the scientists on studying biominerals may be devoted to two of its most alluring characteristics; their intriguing morphologies and the superior properties of these materials.^{6.1-6.3} Strategizing the *in-vitro* synthesis of these biogenic materials by employing an organic matrix to match the strength and toughness of the biological counterparts is a hot topic in biomimetic research.^{6.4,6.5} The bio-inspired synthesis of CaCO_3 with a view to mimic the toughness exhibited by the biogenic counterparts is always in demand and these materials upon synthesis have been exploited for applications across various fields.^{6.6-6.8} The polymorphism exhibited by CaCO_3 makes it highly interesting and the organisms are able to tune among the different phases and exhibit varying morphologies based on their requirements, suggesting that the various phases and morphologies are associated with specific mechanical properties optimized to perform special roles and functions. In the previous chapters, we have reported the use of organic additives in the *in vitro* synthesis of the metastable phases of CaCO_3 and their subsequent role in influencing the morphology of the particles.

The hierarchically structured biominerals are classic examples of composites comprising an organic matrix surrounded by an inorganic mineral phase. This simple biogenic technique can be utilized to synthesize materials with improved strengths and mechanical properties. The hardening of the materials results from the interaction between the organic and the inorganic phases and to clearly understand the hardening mechanism, it is important to determine the relationship between the hardness and the concentration of the occluded species.^{6.9} Although there have been reports on the incorporation of species ranging from nanoparticles to large molecules such as peptides and proteins in CaCO_3 but the determination of the influence of a large number of such species on the mechanical properties of the composite still remains unexplored.^{6.5,6.10-6.15} In this work, we made an attempt to understand the change in mechanical properties of the materials on varying the concentration of the incorporated organic additives.

Herein, we describe CaCO_3 model systems obtained by incorporating the flavonoids, quercetin and hesperidin. The composition of the composites was varied by tuning the concentrations of the organic phase and the resulting composites were initially characterized by powder X-ray diffraction (PXRD) and Fourier Transform Infrared Spectroscopy (FT-IR) to determine the phase of CaCO_3 formed. Subsequently, the morphologies of the composites were obtained from the Field Emission Scanning Electron Microscope (FESEM) imaging technique. Solid-state nuclear magnetic resonance (ssNMR) was performed to show that the flavonoid molecules incorporated within the CaCO_3 crystals are present as individual molecules. The quantification of the occluded organic molecules within the crystals was performed by the Thermogravimetric

analysis (TGA) and the interaction between the inorganic crystal phase (CaCO_3) and the organic matrix was shown by the X-ray Photoelectron Spectroscopy (XPS) studies. Also, the influence of the incorporated organic molecules on the mechanical properties of the resulting CaCO_3 composite materials was determined post their incorporation into gelatin films.

6.2 Results and Discussions

6.2.1 Incorporation of quercetin and hesperidin in CaCO_3 crystals

The composite materials synthesized by the incorporation of the organic additives were initially characterized by FT-IR spectroscopy followed by the PXRD analysis in order to determine the phase of CaCO_3 in the composite. In the FT-IR spectra of the quercetin containing composites, Fig. 6.1(A), we can see that the CaCO_3 synthesized using quercetin (1 mM, 2 mM, 3 mM and 4 mM) showed signals at $712/711\text{ cm}^{-1}$ and 871 cm^{-1} suggesting the formation of the calcite phase in each of the four cases. This was further confirmed by the PXRD analysis, Fig. 6.2(A), where for 1 mM concentration of quercetin, the composite showed a PXRD pattern with peaks at 2θ values equal to 22.97, 29.29, 35.92, 39.30, 43.05, 47.44 and 48.45. These peaks were identified as corresponding to (012), (104), (110), (11-3), (202), (018) and (11-6) planes of calcite, confirmed by matching with the standard PDF data for calcite (ICSD 00-047-1743). For 2 mM concentration of quercetin, the composite showed a PXRD pattern with peaks at 2θ values equal to 22.97, 29.43, 35.85, 39.30, 43.05, 47.44 and 48.37 identified as corresponding to (012), (104), (110), (11-3), (202), (018) and (11-6) planes of calcite and identical to the standard PDF data for calcite (ICSD 00-047-1743). Similarly, for 3 mM concentration of quercetin, the PXRD

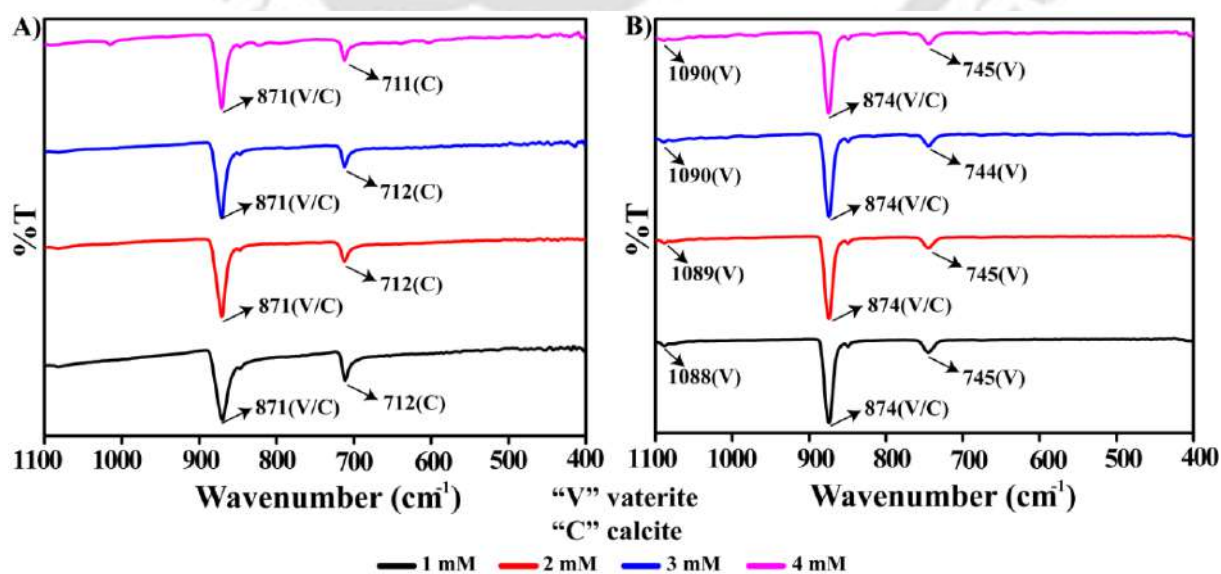


Figure 6.1: FT-IR spectra of (A) CaCO_3 incorporated with Quercetin of different concentrations; (B) CaCO_3 incorporated with Hesperidin of different concentrations.

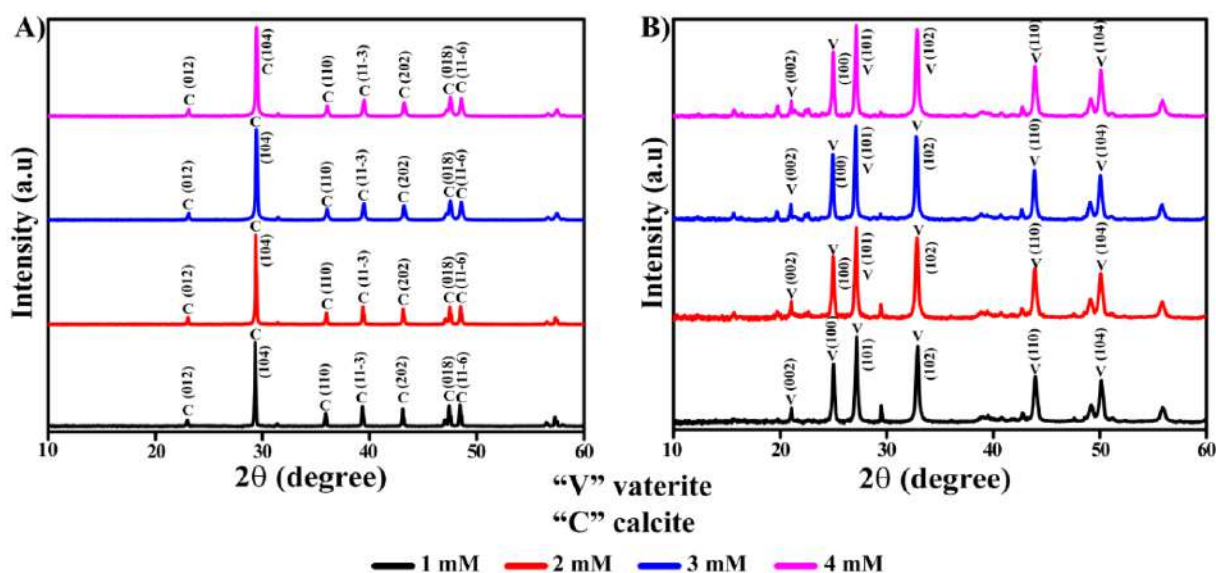


Figure 6.2: PXRD pattern of (A) CaCO_3 incorporated with Quercetin of different concentrations; (B) CaCO_3 incorporated with Hesperidin of different concentrations.

pattern showed peaks at 2θ values equal to 23.03, 29.44, 35.92, 39.45, 43.19, 47.51 and 48.52 identified as corresponding to (012), (104), (110), (11-3), (202), (018) and (11-6) planes of calcite and matching with the standard PDF data for calcite (ICSD 00-047-1743). Also, for 4 mM concentration of quercetin, the PXRD pattern showed peaks at 2θ values equal to 23.10, 29.37, 35.97, 39.45, 43.19, 47.51 and 48.52 identified as corresponding to (012), (104), (110), (11-3), (202), (018) and (11-6) planes of calcite and again, matching well with the standard PDF data for calcite (ICSD 00-047-1743). The composite materials obtained by varying the concentrations of hesperidin (1 mM, 2 mM, 3 mM and 4 mM) were also characterized in the same manner to determine the phase of CaCO_3 , initially by FT-IR, followed by PXRD. In the FT-IR spectra of the hesperidin-based composites, Fig. 6.1(B), all the four composites showed three signals at $744/745\text{ cm}^{-1}$, 874 cm^{-1} and $1088/1089/1090\text{ cm}^{-1}$, suggesting the formation of the vaterite phase in each case. These observations were further confirmed by the PXRD analysis, Fig. 6.2(B), where for 1 mM of hesperidin, the composite showed a PXRD pattern with peaks at 2θ values equal to 21.02, 24.90, 27.14, 32.89, 43.98 and 50.17. These peaks were identified as corresponding to (002), (100), (101), (102), (110) and (104) planes of vaterite, confirmed by matching with the standard PDF data for vaterite (ICSD 00-060-0483). Similarly, for 2 mM of hesperidin, the composite showed a PXRD pattern with peaks at 2θ values equal to 21.01, 24.98, 27.14, 32.76, 43.90 and 50.10, identified as corresponding to (002), (100), (101), (102), (110) and (104) planes of vaterite. This was also confirmed by matching with the standard PDF data for vaterite (ICSD 00-060-0483). For 3 mM of hesperidin, the PXRD pattern showed

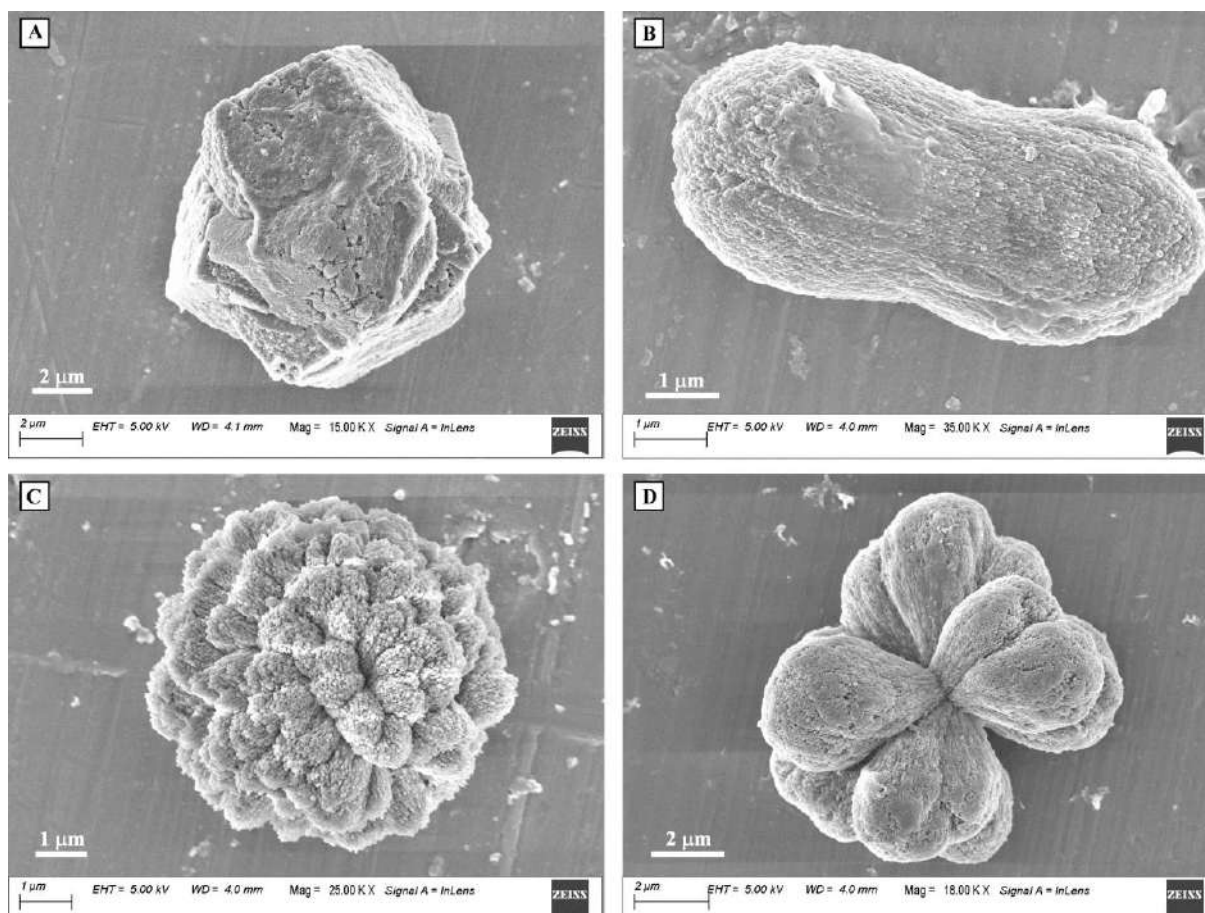


Figure 6.3: Morphology of (A) CaCO_3 /Quercetin (1 mM) composite; (B) CaCO_3 /Quercetin (2 mM) composite; (C) CaCO_3 /Quercetin (3 mM) composite; (D) CaCO_3 /Quercetin (4 mM) composite.

peaks at 2θ values equal to 21.02, 24.98, 27.14, 32.76, 43.91 and 50.10 identical to the (002), (100), (101), (102), (110) and (104) planes of vaterite, also confirmed by matching with the standard PDF data for vaterite (ICSD 00-060-0483). Accordingly, for 4 mM of hesperidin, the PXRD pattern with peaks at 2θ values equal to 20.95, 24.90, 27.07, 32.76, 43.91 and 50.10 identical to the (002), (100), (101), (102), (110) and (104) planes of vaterite were obtained. This was confirmed to be identical with the standard PDF data for vaterite (ICSD 00-060-0483). The PXRD analysis of the CaCO_3 particles synthesized without any additive, as a control, showed PXRD pattern, Fig. A6.1, with peaks at 2θ values equal to 23.07, 29.40, 36.02, 39.43, 43.23, 47.47 and 48.48 identified as corresponding to (012), (104), (110), (11-3), (202), (018) and (11-6) planes of calcite and matched with the standard PDF data for calcite (ICSD 00-047-1743). Hence, confirming that the calcite phase was obtained on performing the control synthesis.

The calcite particles with a perfect rhombohedral morphology as obtained, Fig. A6.2(A) and (B), was a result of the control reaction without any additive. However, interesting results in the form of morphology of the calcite particles synthesized by varying the concentration of the additive

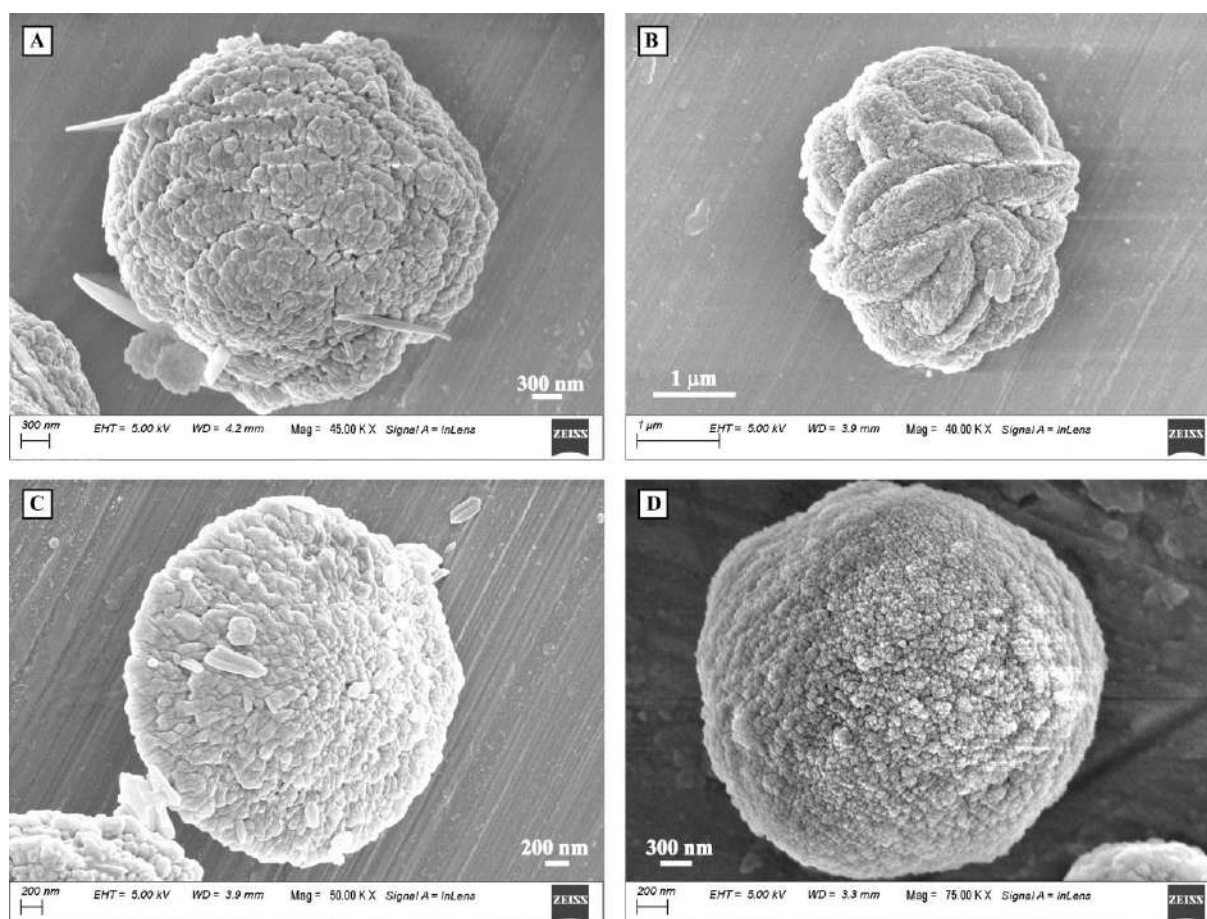


Figure 6.4: Morphology of (A) CaCO₃/Hesperidin (1 mM) composite; (B) CaCO₃/Hesperidin (2 mM) composite; (C) CaCO₃/Hesperidin (3 mM) composite; (D) CaCO₃/Hesperidin (4 mM) composite.

quercetin was obtained. With 1 mM quercetin, although the calcite phase was obtained, the morphology of the composite was different from the usual rhombohedral calcite as can be seen in Fig. 6.3(A). On increasing the concentration, a substantial change in the morphology of the composites was observed where they showed a peanut-shaped morphology for 2 mM, Fig. 6.3(B), and two different flower-like morphologies for 3 mM and 4 mM of quercetin, Fig. 6.3(C) and (D), respectively. The variation from the usual rhombohedral morphology is due to incorporating the quercetin molecules within the CaCO₃ single-crystals. We see that on using low concentration, 1 mM, the morphology obtained had similarity with the usual rhombohedral morphology, but, the particle appears to be elongated and has a rough surface texture, making it different. However, on using higher concentrations, significant changes in morphology were observed clearly suggesting the influence of the incorporated organic molecules on the morphology of the composite. The morphology of all the four different vaterite particles obtained by the incorporation of varying concentrations of hesperidin molecules was spherical, Fig. 6.4(A), (B), (C) and (D). Slight differences could be observed only in terms of the surface texture of the particles with no significant variation in shape.

Solid-state NMR (ssNMR) is one of the most convenient tools to study organic compounds; however, this technique is not used extensively to study the incorporation of organic materials within the crystal. This technique can easily provide structural information and give us an idea about the surrounding environment as well as the interaction among the materials.^{6.16} However, assigning the peaks in ssNMR is difficult owing to paramagnetic and line-broadening effects.^{6.17} The ¹³C ssNMR of two composite materials from each set were performed to evidently prove that organic molecules within the CaCO₃ crystals are intact as individual molecules. In the ¹³C ssNMR of the quercetin (3 mM) incorporated CaCO₃, Fig. A6.3(A), the carbonate carbon (CO₃²⁻) of calcite appeared as a sharp peak at 166.8 ppm,^{6.18} and the characteristic peaks of quercetin were observed as a small hump close to 169.00 ppm which is possibly attributed to the carbonyl carbon and the carbons attached to hydroxyl groups, it should be noted that the low amount of additive as compared to CaCO₃ in the composite and also the weak signal intensity of the carbonyl group of quercetin contribute to the weakening of the signal. The broad peak starting from approximately 58.0 ppm to 134.0 ppm accounted for the aromatic carbon atoms of quercetin. The ¹³C ssNMR of the hesperidin (3 mM) incorporated CaCO₃, Fig. A6.3(B), gave a singlet peak at 16.2 ppm attributed to the sp³ C of the methyl groups, the peaks at 52.5 ppm and 71.0 ppm ascribed to the sp³ carbons directly attached to an oxygen atom, the broad peak ranging from approximately 80.0 ppm to 160.0 ppm accounted for the aromatic carbon atoms and the two peaks which merged at 168.0 ppm and 167.0 ppm are due to the carbonate carbon (CO₃²⁻) of vaterite^{6.18} and the small hump next to these peaks at ~170.0 - 175.0 ppm is attributed to the carbonyl carbon and the aromatic carbon atoms attached to electronegative -O atom of hesperidin. Hence, from these results, we can safely say that the flavonoid molecules, quercetin and hesperidin are perfectly incorporated as individual molecules in the composite.

6.2.2 Quantification of the incorporation of quercetin and hesperidin in CaCO₃ crystals

The TG analysis was used to determine the amount of organic additive occluded in the CaCO₃ crystal systems. It is well established that the TGA curve of bare CaCO₃ (calcite) would show two mass losses, first one at around 100 °C due to the loss of any physically adsorbed water and the second one in the range of 650-750 °C attributed to decarbonization (- CO₂). However, in the case of composites of CaCO₃ based on organic matrices, another mass loss attributed to decarboxylation of the organic compound is observed in the range of 150-600 °C and this region in the TGA curve is of significant importance to us since it is from the mass loss in this region that we are going to determine the amount of organic additive incorporated in CaCO₃. The CaCO₃ particles synthesized as control were first subjected to TG analysis where we observed

two mass losses, one of ~3% at 100-150 °C due to dehydration and the other a ~45% mass loss due to loss of CO₂ (decarbonization), in the range of 600-770 °C, Fig. A6.4. The TGA curves of all the composites synthesized by the occlusion of the organic additives show three different mass losses, the first (~2% at 100-150 °C) and the third (~45% at 600-770 °C) being almost the same in all the cases irrespective of the amount of additive. However, the second mass loss region due to the loss of organic compound, is of concern to us. For the quercetin incorporated composites, the mass loss in this region for the four different concentrations, 1 mM, 2 mM, 3 mM and 4 mM were 6%, 10%, 14% and 18%, respectively, Fig. 6.5(A), indicating that with every 1 mM increase in the concentration of quercetin, a uniform increase in the percentage of the occluded organic compound (~4%) was observed. Similarly, for the composites based on hesperidin, 1 mM, 2 mM, 3 mM and 4 mM the mass loss in the temperature range of 150-600 °C were 10%, 14%, 19% and 23%, respectively, Fig. 6.5(B). In this sequence too, with every 1 mM increase in the concentration of hesperidin, a uniform increase in the percentage of the occluded organic compound (~4%) was observed.

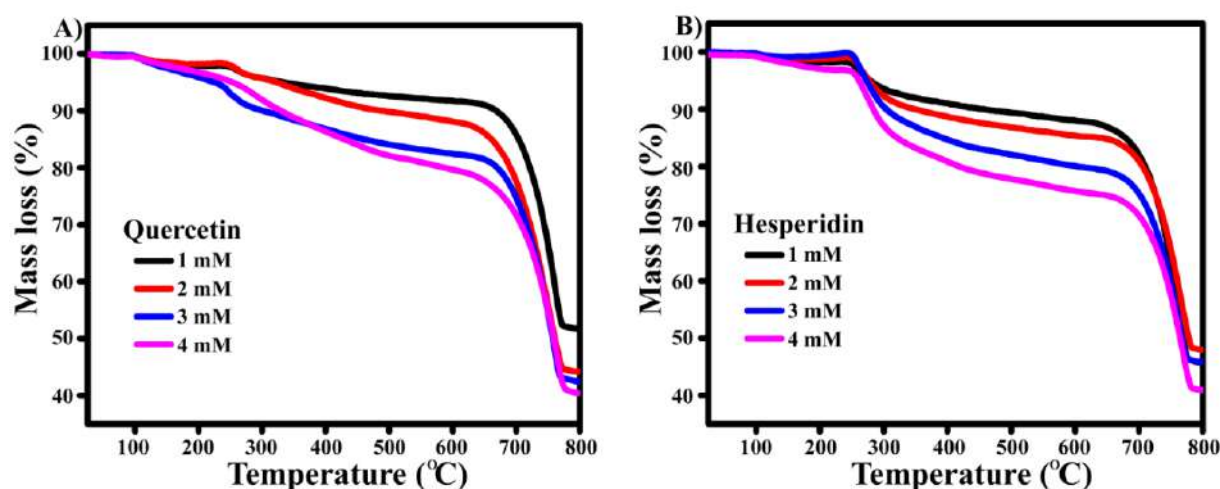


Figure 6.5: TGA curve of (A) CaCO₃ incorporated with Quercetin of different concentrations; (B) CaCO₃ incorporated with Hesperidin of different concentrations.

6.2.3 Effects of incorporated organic compounds on CaCO₃

From the initial characterization using FT-IR and PXRD, we saw that the two different additives led to two distinct phases of CaCO₃, hesperidin due to more number of –OH groups in its structure was able to stabilize the metastable vaterite phase. Due to favorable interaction between Ca and O attributed to the hard acid-hard base interaction, the more number of –OH groups preferably favor the formation of the metastable vaterite. But, with quercetin as an additive, we have seen from the FESEM images how the variation in its concentration led to the formation of composites with different morphologies, clearly suggesting the role of the additive.

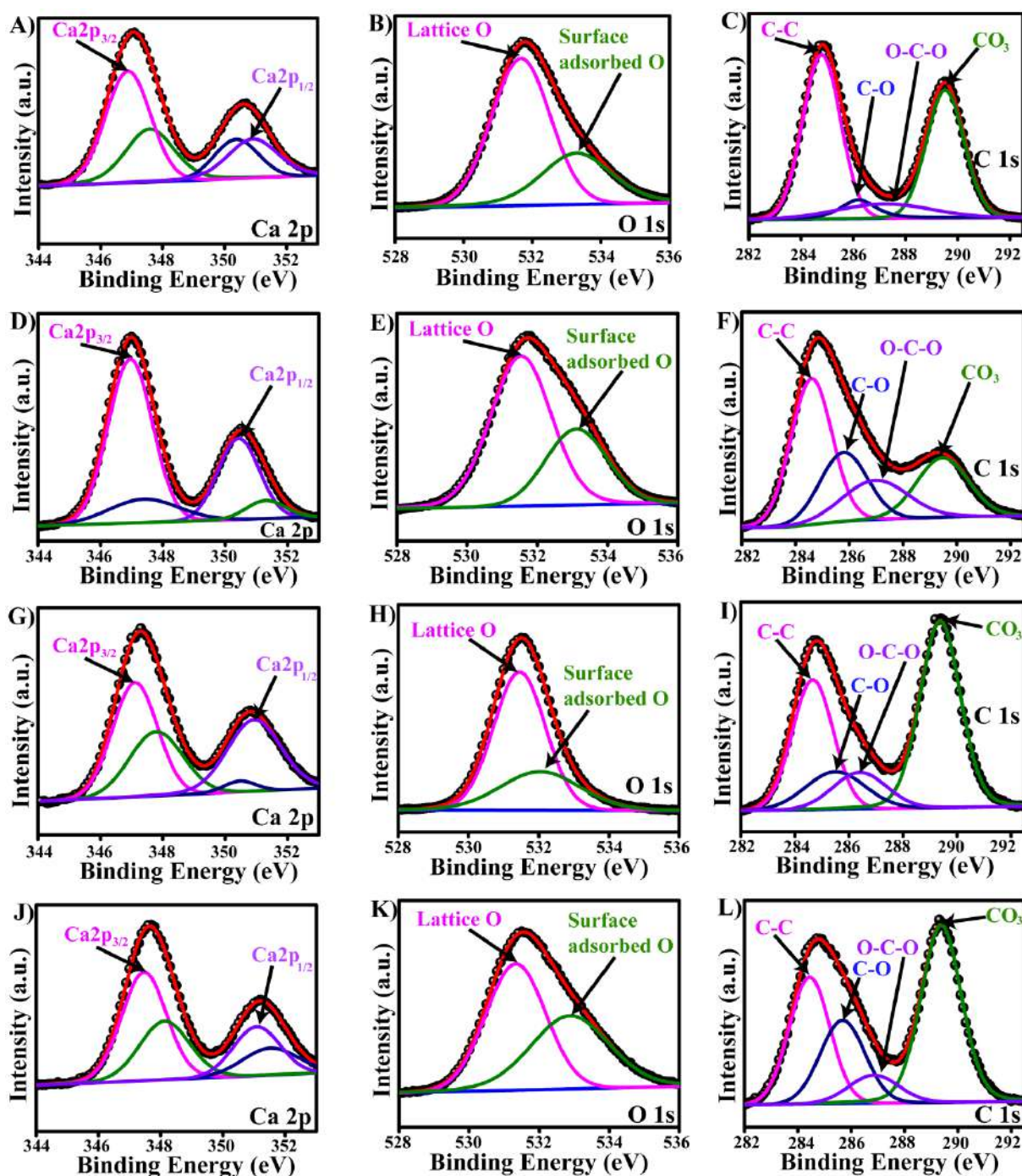


Figure 6.6: XPS analysis of (A) Ca 2p, (B) O 1s, (C) C 1s of CaCO₃/Quercetin (1 mM) composite; (D) Ca 2p, (E) O 1s, (F) C 1s of CaCO₃/Quercetin (2 mM) composite; (G) Ca 2p, (H) O 1s, (I) C 1s of CaCO₃/Quercetin (3 mM) composite; (J) Ca 2p, (K) O 1s, (L) C 1s of CaCO₃/Quercetin (4 mM) composite.

For a better understanding, the influence of incorporated flavonoid molecules of varying concentrations on the resulting composite, the XPS analysis of Ca 2p, O 1s and C 1s of all the composites were performed and compared with the spectra of bare CaCO₃. In all the cases, four different peaks were obtained for Ca 2p, two high-intensity peaks corresponding to Ca 2p_{3/2} and Ca 2p_{1/2} core level electrons and two satellite peaks. Two peaks were obtained for O 1s, one for

the lattice oxygen and the other for the surface adsorbed oxygen. For C 1s, four different peaks were obtained.^{6.19-6.21} All the values corresponding to the various peaks for all the materials have been represented in **Table A6.1**. In the spectrum of Ca 2p of bare CaCO₃ among the four different peaks, the peak at 346.83 eV is due to the Ca 2p_{3/2} core level electrons and the peak at 350.63 eV is due to the Ca 2p_{1/2} core level electrons and the other two being the corresponding satellite peaks at 347.64 eV and 350.49 eV, Fig. A6.5(A). The two peaks in the spectrum of O 1s of bare CaCO₃ were at 532.00 eV and 533.54 eV, Fig. A6.5(B). The four peaks in the spectrum of C 1s of bare CaCO₃ were at 284.64 eV, 289.99 eV, 286.22 eV and 287.53 eV correspond to adventitious C, carbonate C, C-O, O-C-O, respectively, Fig. A6.5(C). In the XPS spectra of Ca 2p of all the quercetin-based CaCO₃ composite of varying concentrations of quercetin, 1 mM, 2 mM, 3 mM and 4 mM, the peak due to Ca 2p_{3/2} were obtained at 346.88 eV, 346.95 eV, 347.11 eV and 347.46 eV, respectively, Fig. 6.6(A), (D), (G) and (J). Here, we see a gradual increase in binding energy and similar observations were made in the case of Ca 2p_{1/2}, the values represented in **Table A6.1**. The binding energy values of the occluded calcite is higher than that of bare calcite and the value is highest for 4 mM of quercetin; this is because with a decrease in electron density, the binding energy becomes low, which is attributed to the interaction of Ca with the electronegative O of the additive. The peak values of the lattice oxygen in the O 1s spectra for all these composites were 531.67 eV, 531.54 eV, 531.45 eV and 531.33 eV, respectively, Fig. 6.6(B), (E), (H) and (K), showing a gradually decreasing trend. Among the four peaks observed, the peak due to C atom of carbonate in the four cases was at 289.52 eV, 289.45 eV, 289.37 eV and 289.36 eV, respectively, Fig. 6.6(C), (F), (I) and (L), the binding energy slightly decreasing with the increasing concentration.

Similarly, for the hesperidin incorporated composites, 1 mM, 2 mM, 3 mM and 4 mM, in the XPS spectra of Ca 2p, the peak due to Ca 2p_{3/2} were obtained at 346.60 eV, 346.78 eV, 346.80 eV and 346.81 eV, respectively, Fig. 6.7(A), (D), (G) and (J). These values are slightly lower than that of bare calcite due to the higher electron density around vaterite and among the four composite, the binding energy value gradually increases with increase in the concentration of hesperidin exactly in the same way as was observed in the case of quercetin. The O 1s spectra of these composites gave the peaks for lattice O at 531.31 eV, 531.30 eV, 531.29 eV and 531.20 eV, respectively, Fig. 6.7(B), (E), (H) and (K); here too we obtained a decreasing trend as in the case of quercetin. For the C 1s spectra, the peak due to C atom of carbonate was obtained at 289.33 eV, 289.16 eV, 289.06 eV and 288.69 eV, respectively, Fig. 6.7(C), (F), (I) and (L), with a decreasing trend. Hence, the deviation in the binding energy values of all the atoms compared to that of bare CaCO₃ justified the role played by the additives upon their incorporation into the

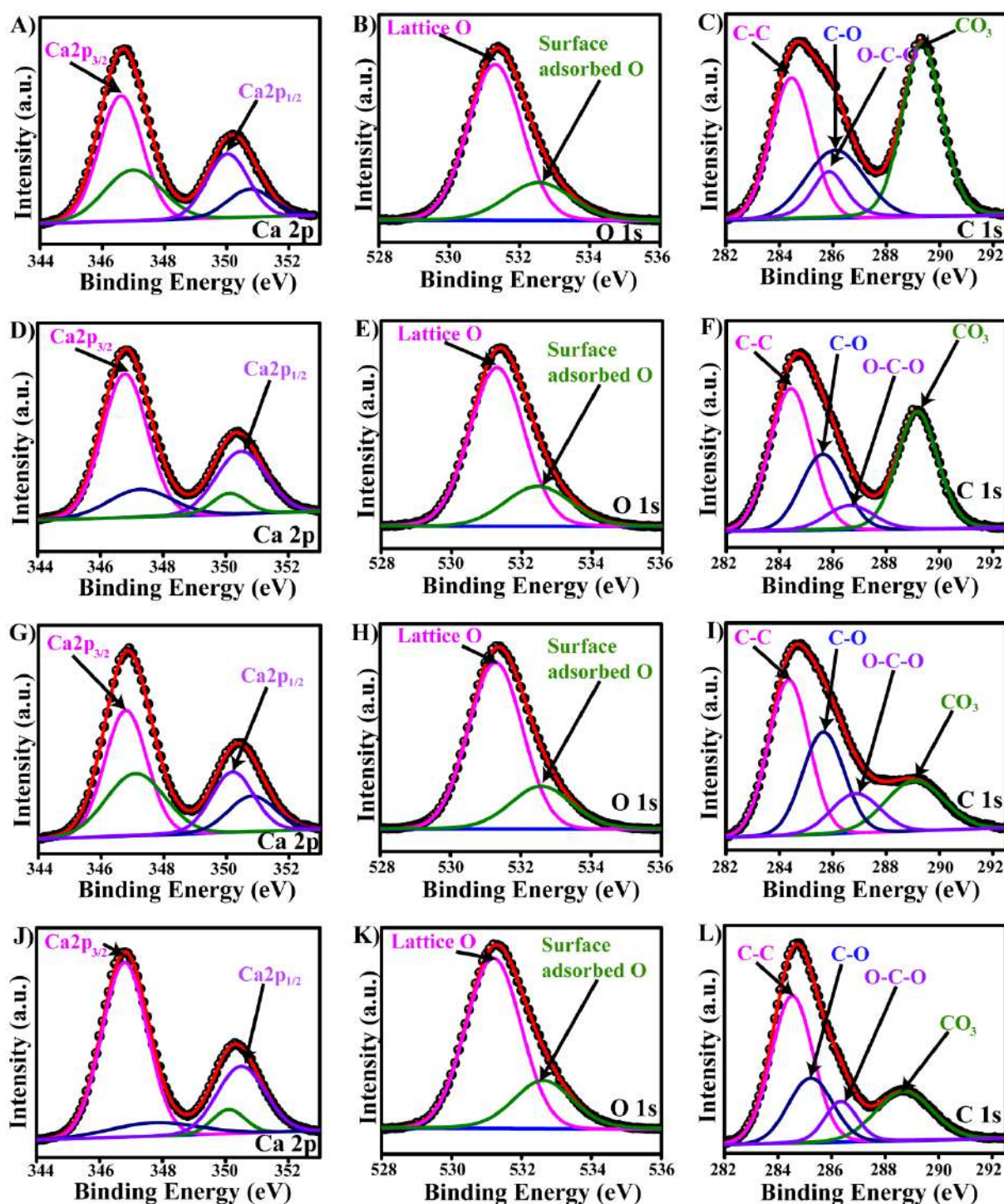


Figure 6.7: XPS analysis of (A) Ca 2p, (B) O 1s, (C) C 1s of CaCO₃/Hesperidin (1 mM) composite; (D) Ca 2p, (E) O 1s, (F) C 1s of CaCO₃/Hesperidin (2 mM) composite; (G) Ca 2p, (H) O 1s, (I) C 1s of CaCO₃/Hesperidin (3 mM) composite; (J) Ca 2p, (K) O 1s, (L) C 1s of CaCO₃/Hesperidin (4 mM) composite.

CaCO₃ crystals. A gradual increasing or decreasing trend in the binding energy values of a particular set of composite confirmed that the concentration of the additives incorporated has a pivotal role in molding the properties of the composite. The XPS spectrum surveys of the materials are represented in Fig. A6.6 (A-I).

6.2.4 Determination of mechanical strength

The mechanical strength of the organic additive incorporated CaCO_3 composites were determined by incorporating them in gelatin films and then comparing the corresponding mechanical strength of the doped films with that of the bare gelatin film. The mechanical strength of the gelatin film doped with bare CaCO_3 was also evaluated to understand the influence of the incorporated organic additives on the mechanical strength of the resulting CaCO_3 composite. The mechanical strength of the films is displayed by their tensile stress-strain curve, Fig. 6.8(A) and (B). On incorporation of the composite, there was a substantial increase in the mechanical strength of the film and most importantly, it should be noted that for both the additives, with an increase in its concentration, the mechanical strength of the resulting film had increased. This is clearly delineated by the area under the corresponding tensile stress-strain curve. The maximum tensile stress (kPa) at break for the bare gelatin film and the gelatin film after incorporating bare CaCO_3 were found to be 1003 ± 6 kPa and 1160 ± 14 kPa, respectively. The mechanical strength of the synthesized CaCO_3 composites was evaluated w.r.t the bare gelatin film. In Fig. 6.8(C), we can see that the maximum tensile stress (kPa) at break for the quercetin-based composite had gradually increased with an increase in its concentration, 1 mM, 2 mM and 3 mM. The values of 1513 ± 19 kPa, 2071 ± 24 kPa and 2667 ± 35 kPa, respectively, were obtained; however, for 4 mM of quercetin, the value obtained, 2728 ± 34 kPa, was slightly more than that obtained using 3 mM. This suggests that probably a limiting value was attained w.r.t the maximum tensile strength influenced by the concentration of quercetin that could be incorporated within the calcite crystals. Similarly, for the hesperidin-derived CaCO_3 too, the maximum tensile stress (kPa) at break, Fig. 6.8(D), had gradually increased with an increase in the concentration, 1 mM, 2 mM and 3 mM w.r.t the bare gelatin film (1003 ± 6 kPa). The values obtained were 1221 ± 32 kPa, 2231 ± 29 kPa and 3122 ± 58 kPa, respectively. Here again, the maximum tensile stress at break for the composite containing 4 mM of hesperidin, 3152 ± 52 kPa, was close to that obtained using 3 mM, suggesting that the approximate limiting value for the maximum tensile strength arising out of the amount of hesperidin that can be incorporated within the vaterite crystals was reached. On analyzing the results obtained in both the set of experiments, with quercetin and hesperidin, it can be easily comprehended that the mechanical strength of CaCO_3 had increased gradually on incorporating the organic additives in comparison to the bare CaCO_3 (1160 ± 14 kPa). It is already known that the presence of incorporated molecules within CaCO_3 changes the mechanical properties of the crystals.^{6.4,6.22} The organic molecules themselves are not likely to exhibit resistance to the applied stress or strain, but their inclusion within the crystal would render toughness to the

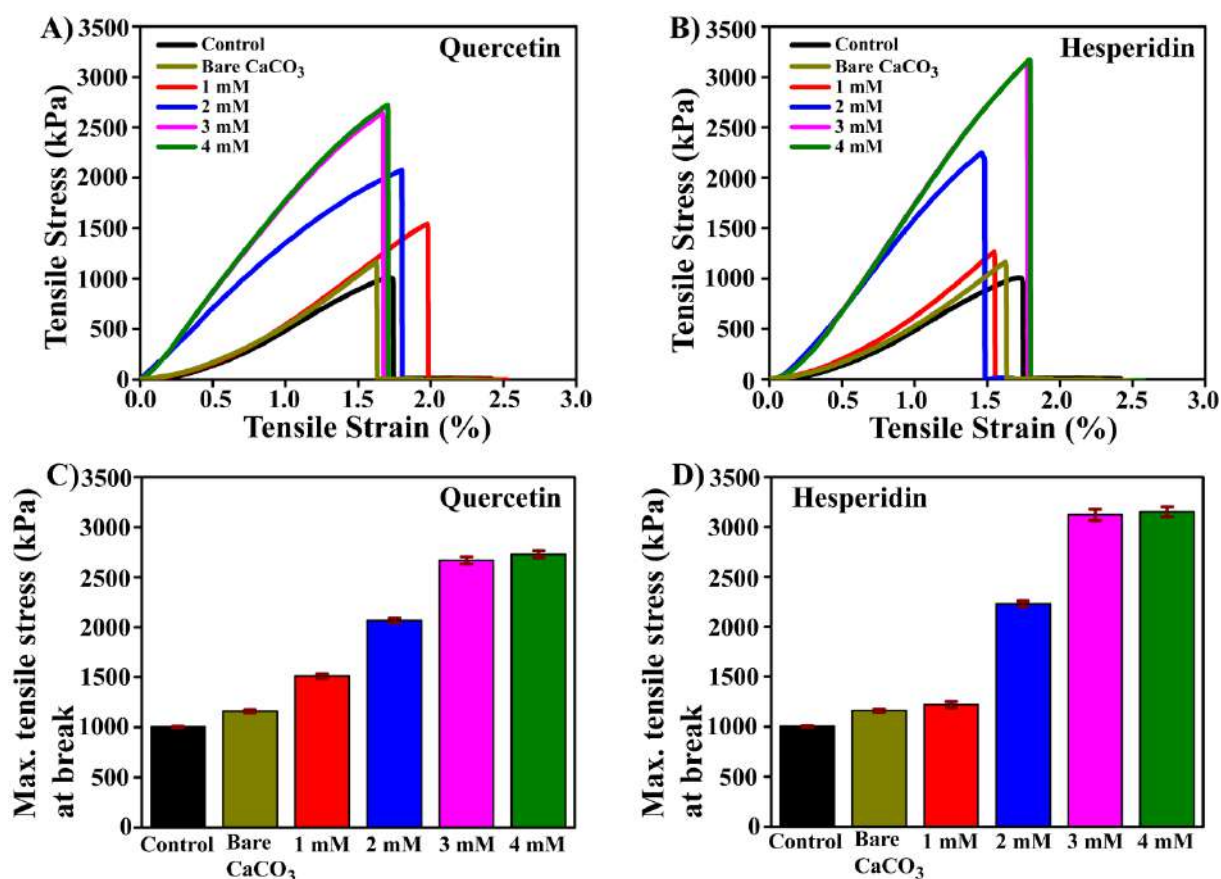


Figure 6.8: (A) Tensile stress-strain curve of gelatin films incorporated with CaCO₃/Quercetin composite of different additive concentrations; (B) Tensile stress-strain curve of gelatin films incorporated with CaCO₃/Hesperidin composite of different additive concentrations; (C) Maximum tensile stress at break for gelatin films incorporated with CaCO₃/Quercetin composites; (D) Maximum tensile stress at break for gelatin films incorporated with CaCO₃/Hesperidin composites.

composite. The organic molecules incorporated are known to impede the dislocation motion within the crystals, which results in improved mechanical strength and this improvement is directly proportional to the organic phase content as was exactly observed in this study with the incorporated flavonoid content.^{6,9} From the XPS spectra of the composites, it was evident that the incorporated organic molecules interacted with CaCO₃ and influenced the properties of the composites, which resulted in the difference in binding energies of the constituent elements. As a result, the gelatin films, when doped with the flavonoid incorporated CaCO₃, showed increased mechanical strength and the magnitude of tensile stress was observed to be increasing gradually with the increase in the concentration of the incorporated molecules. Therefore, the inclusion of the flavonoids, quercetin and hesperidin within CaCO₃ crystals offered a facile method to synthesize composite materials with increased mechanical strength.

6.2.5 Characterization of the films

Post incorporation of the organic additive-based CaCO_3 composites in the gelatin films, the films were subjected to PXRD analysis in order to prove that the composite, as well as the CaCO_3 phases within the film, are intact. All the four different films containing the quercetin-based composites showed two distinct peaks, Fig. A6.7(A), a broad peak at 2θ equal to 21.30, which is the characteristic peak of gelatin and a sharp peak at 2θ equal to 29.30 corresponding to (104) plane of calcite. Similarly, the four different films incorporated with the hesperidin based composites showed four distinct peaks, Fig. A6.7(B), a broad peak at 2θ equal to 21.45, which is the characteristic peak of gelatin and three sharp peaks at 2θ equal to 24.97, 27.09 and 32.66 corresponding to (100), (101) and (102) planes of vaterite. Therefore, from the PXRD analysis, we could say that corresponding phases of CaCO_3 before and after the incorporation into the gelatin films remained intact. Also, in order to see whether the morphology of these composites remained intact or not post their incorporation into the film, the FESEM images of two films, one a quercetin (3mM) based and the other a hesperidin (3mM) based, were taken. From Fig. A6.8(A), we can see that the flower-like morphology of the 3 mM quercetin based calcite, Fig. 6.3(C), remained the same and from Fig. A6.8(B) it is clearly visible that the spherical morphology of the 3 mM hesperidin derived vaterite, Fig. 6.4(C), remained intact. It should also be noted that in both these images (of gelatin films), the composite particles are present as aggregates and not as distinct individual particles as they were before their incorporation into the films. Hence, from the PXRD analysis and the FESEM imaging, we have a clear understanding that the characteristics of the composites remained unchanged on their incorporation into the gelatin films. It was important to perform these characterizations to justify the mechanical strength of the organic additive based composites as any change in the phase and morphology of the composites while fabricating the film would influence its properties and hence the correlation between the specific composite and the results obtained in terms of the maximum tensile stress would be invalid.

6.3 Conclusion

In this work, we have demonstrated new insights in terms of the mechanical strength of flavonoid incorporated CaCO_3 composites. The flavonoids quercetin and hesperidin were used as additives during CaCO_3 precipitation and their inclusion in the crystal system of CaCO_3 resulted in the formation of calcite with different morphologies and the metastable vaterite, respectively. The role of these additives in influencing the toughness of the resulting composites

was studied by varying the concentration of the additives and observing the maximum tensile stress (kPa) at break of the composites. It was observed that in both cases, with an increase in the concentration of occluded organic molecules, the mechanical strength of the composite increases until it reaches a limiting concentration (3-4 mM). Hence, for the very first time, the influence of flavonoids on the mechanical strength of biominerals was described by the use of *in vitro* model systems based on quercetin/hesperidin-CaCO₃ composites.

References

- 6.1. P. Fratzl, H. S. Gupta, F. D. Fischer and O. Kolednik, Hindered Crack Propagation in Materials with Periodically Varying Young's Modulus—Lessons from Biological Materials, *Adv. Mater.*, 2007, **19**, 2657-2661.
- 6.2. K. Tai, M. Dao, S. Suresh, A. Palazoglu and C. Ortiz, Nanoscale heterogeneity promotes energy dissipation in bone, *Nat. Mater.*, 2007, **6**, 454-462.
- 6.3. F. Nudelman and N. A. J. M. Sommerdijk, Biomineralization as an Inspiration for Materials Chemistry, *Angew. Chem., Int. Ed.*, 2012, **51**, 6582-6596.
- 6.4. Y. Y. Kim, L. Ribeiro, F. Maillot, O. Ward, S. J. Eichhorn and F. C. Meldrum, Bio-inspired synthesis and mechanical properties of calcite-polymer particle composites, *Adv. Mater.*, 2010, **22**, 2082-2086.
- 6.5. Y. Y. Kim et al., An artificial biomineral formed by incorporation of copolymer micelles in calcite crystals, *Nature Mater.*, 2011, **10**, 890-896.
- 6.6. D. Paul, D. Sachan and G. Das, Silver nanoparticles embedded on in-vitro biomineralized vaterite: A highly efficient catalyst with enhanced catalytic activity towards 4-Nitrophenol reduction, *Mol. Catal.*, 2021, **504**, 111433.
- 6.7. D. Paul and G. Das, Efficient solid-state synthesis of biomineralized vaterite-derived pure CaMnO₃ Perovskite as an effective photocatalyst, *CrystEngComm*, 2021, **23**, 4050-4058.
- 6.8. D. B. Trushina, T. V. Bukreeva, M. V. Kovalchuk and M. N. Antipina, CaCO₃ vaterite microparticles for biomedical and personal care applications, *Mater. Sci. Eng. C.*, 2014, **45**, 644-658.
- 6.9. Y. -Y. Kim et al., Tuning hardness in calcite by incorporation of amino acids, *Nature Mater.*, 2016, **15**, 903-910.
- 6.10. Y.-Y. Kim et al., Structure and properties of nanocomposites formed by the occlusion of block copolymer worms and vesicles within calcite crystals, *Adv. Funct. Mater.*, 2016, **26**, 1382-1392.

- 6.11. S. Borukhin et al., Screening the incorporation of amino acids into an inorganic crystalline host: the case of calcite, *Adv. Funct. Mater.*, 2012, **22**, 4216-4224.
- 6.12. A. N. Kulak et al., One-pot synthesis of an inorganic heterostructure: uniform occlusion of magnetite nanoparticles within calcite single crystals, *Chem. Sci.*, 2014, **5**, 738-743.
- 6.13. A. N. Kulak, P. C. Yang, Y. Y. Kim, S. P. Armes and F. C. Meldrum, Colouring crystals with inorganic nanoparticles, *Chem. Commun.*, 2014, **50**, 67-69.
- 6.14. R. A. Metzler, G. A. Tribello, M. Parrinello and P. Gilbert, Asprich peptides are occluded in calcite and permanently disorder biomineral crystals, *J. Am. Chem. Soc.*, 2010, **132**, 11585-11591.
- 6.15. J. Aizenberg, J. Hanson, T. F. Koetzle, S. Weiner and L. Addadi, Control of macromolecule distribution within synthetic and biogenic single calcite crystals, *J. Am. Chem. Soc.*, 1997, **119**, 881-886.
- 6.16. M. A. Shaibat et al., Characterization of Polymorphs and Solid-State Reactions for Paramagnetic Systems by ^{13}C Solid-State NMR and ab Initio Calculations, *J. Am. Chem. Soc.*, 2007, **129**, 10968-10969.
- 6.17. F. Gul-E-Noor et al., Effects of varying water adsorption on a $\text{Cu}_3(\text{BTC})_2$ metal-organic framework (MOF) as studied by ^1H and ^{13}C solid-state NMR spectroscopy, *Phys. Chem. Chem. Phys.*, 2011, **13**, 7783-7788.
- 6.18. H. Nebel, M. Neumann, C. Mayer and M. Epple, On the Structure of Amorphous Calcium Carbonates A Detailed Study by Solid-State NMR Spectroscopy, *Inorg. Chem.*, 2008, **47**, 7874-7879.
- 6.19. J. Baltrusaitis, C. R. Usher and V. H. Grassian, Reactions of sulfur dioxide on calcium carbonate single crystal and particle surfaces at the adsorbed water carbonate interface, *Phys. Chem. Chem. Phys.*, 2007, **9**, 3011-3024.
- 6.20. A. Achour, A. Arman, M. Islam, A. A. Zavarian, A. B. Al-Zubaidi and J. Szade, Synthesis and characterization of porous CaCO_3 micro/nano-particles, *Eur. Phys. J. Plus*, 2017, **132**, 267.
- 6.21. C. S. Gopinath, S. G. Hedge, A. V. Ramaswamy and S. Mahapatra, Photoemission studies of polymorphic CaCO_3 materials, *Mater. Res. Bull.*, 2002, **37**, 1323-1332.
- 6.22. M. E. Kunitake, L. M. Mangano, J. M. Peloquin, S. P. Baker and L. A. Estroff, Evaluation of strengthening mechanisms in calcite single crystals from mollusk shells, *Acta Biomater.*, 2013, **9**, 5353-5359.

Annexure-Chapter 6

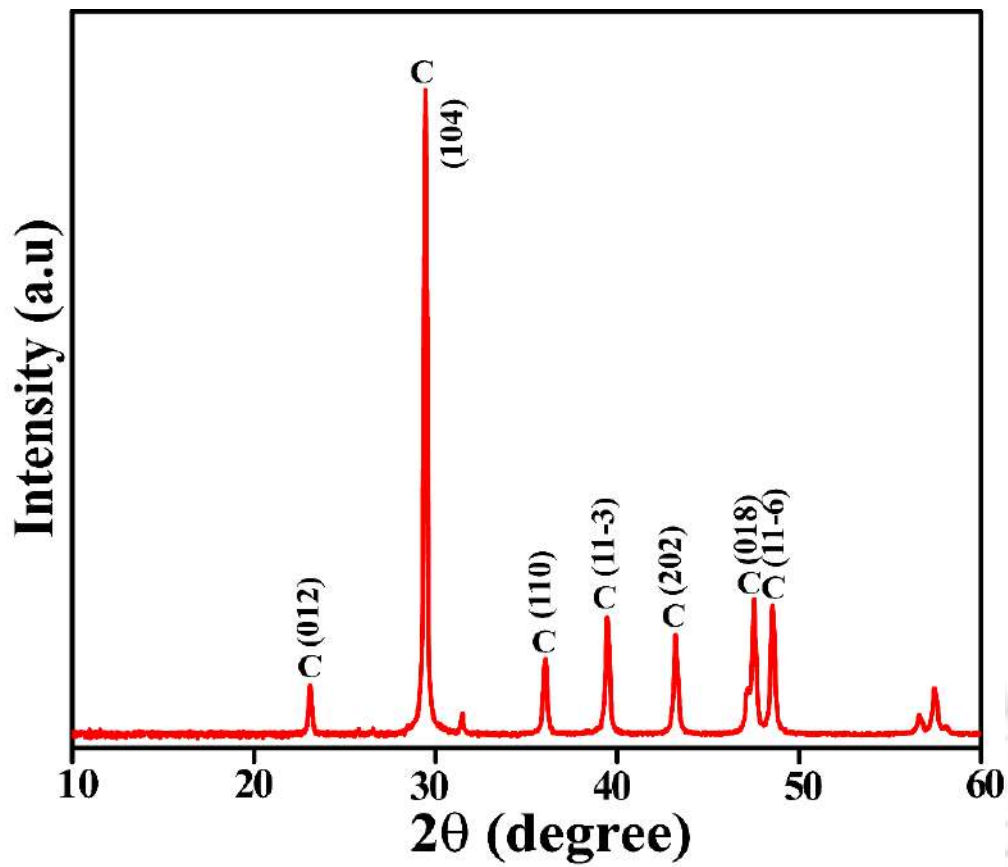


Figure A6.1: XRD patterns of CaCO_3 synthesized without any additive

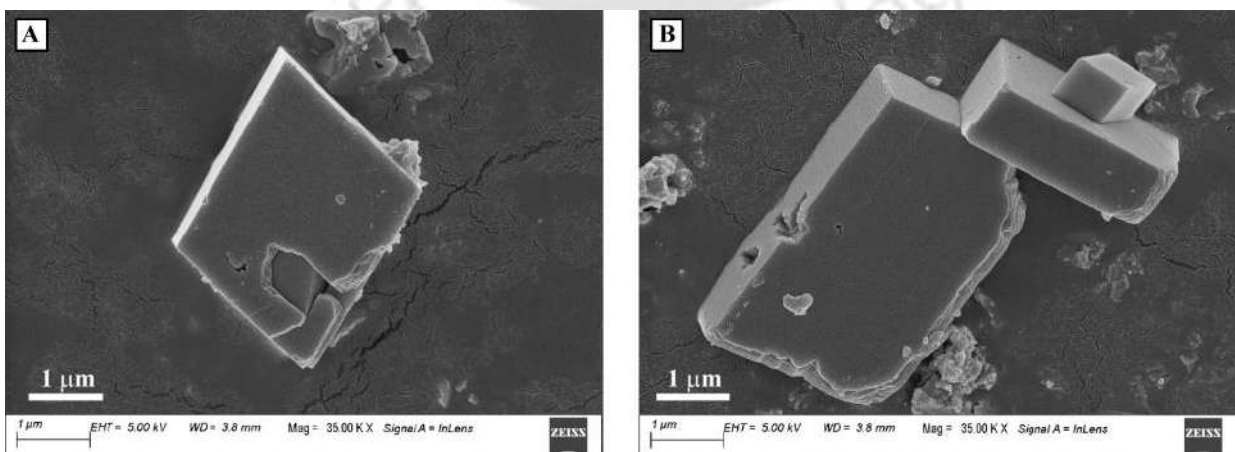


Figure A6.2: FESEM images of Calcite synthesized without any additive.

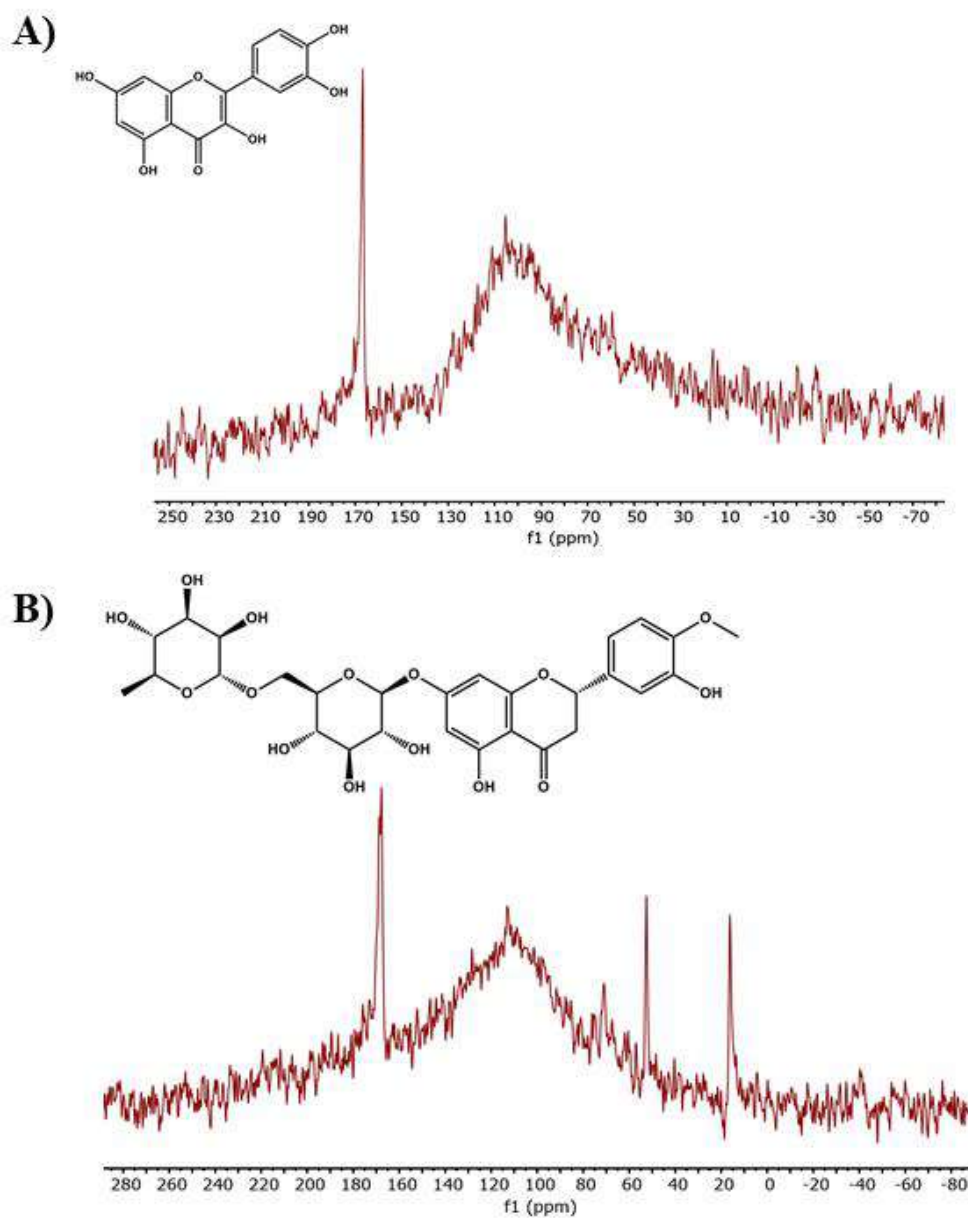


Figure A6.3: ^{13}C solid-state NMR of (A) Quercetin (3 mM) incorporated in CaCO_3 ; (B) Hesperidin (3 mM) incorporated in CaCO_3 .

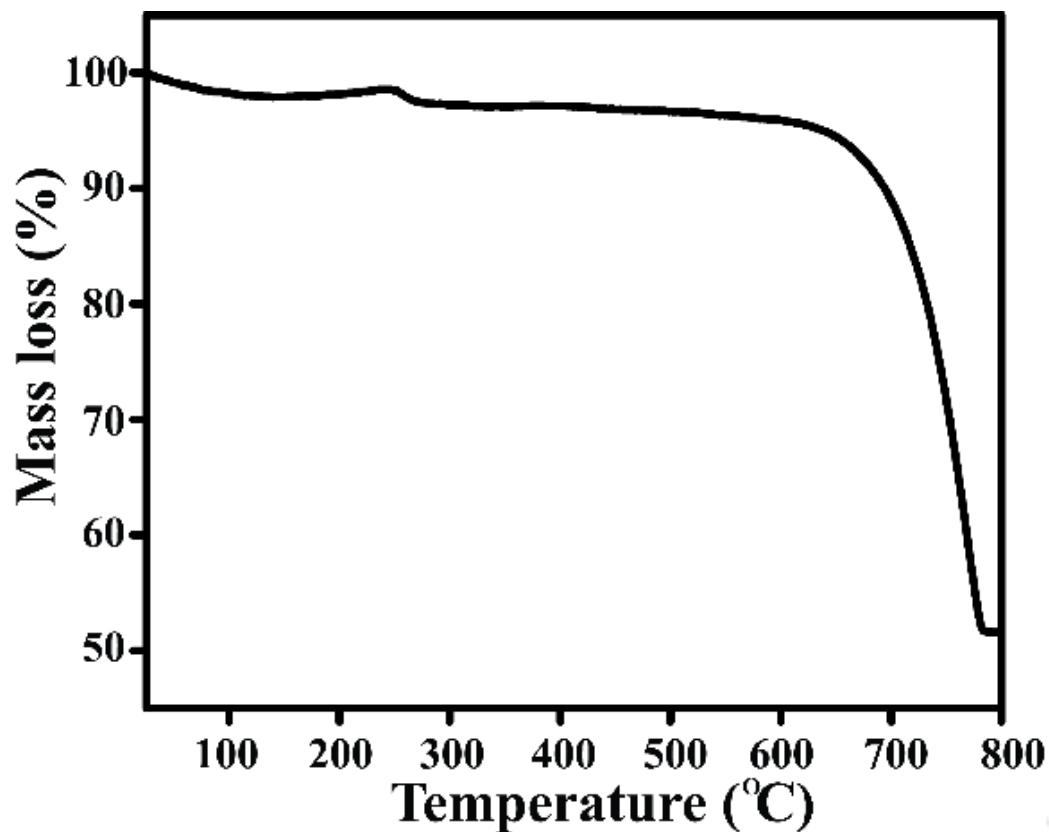


Figure A6.4: TGA pattern of CaCO_3 particles synthesized as a control.

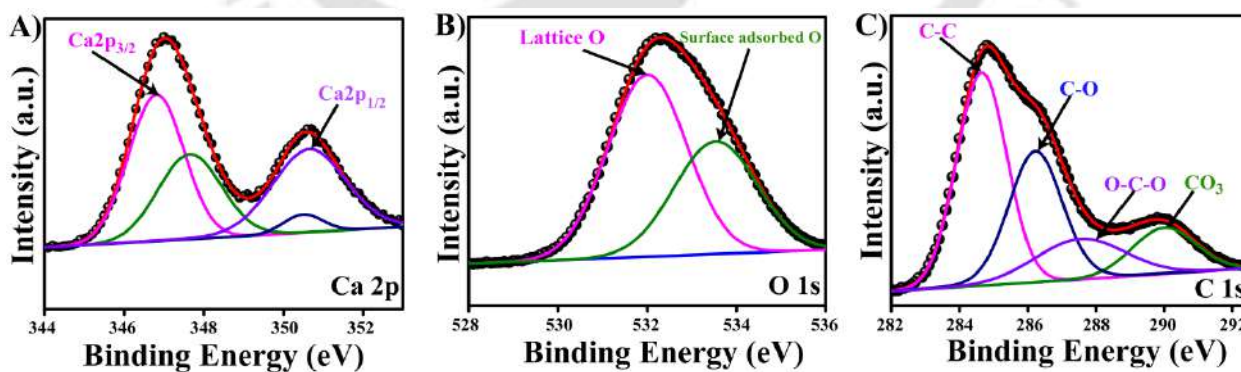


Figure A6.5: XPS analysis of bare CaCO_3 , (A) Ca 2p spectra; (B) O 1s spectra; (C) C 1s spectra.

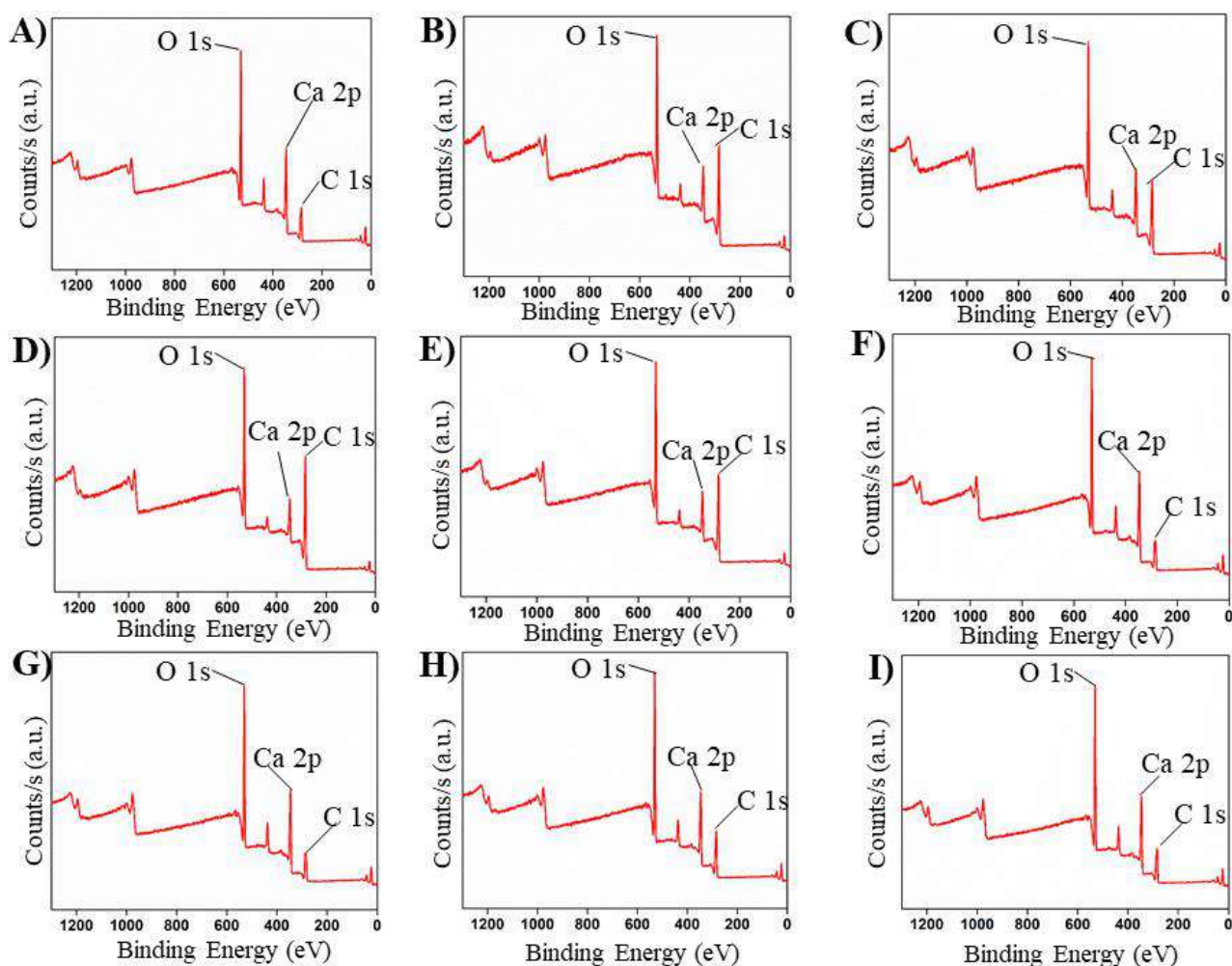


Figure A6.6: XPS Survey (A) Bare CaCO_3 ; (B) CaCO_3 incorporated with 1 mM Quercetin; (C) CaCO_3 incorporated with 2 mM Quercetin; (D) CaCO_3 incorporated with 3 mM Quercetin (E) CaCO_3 incorporated with 4 mM Quercetin; (F) CaCO_3 incorporated with 1 mM Hesperidin; (G) CaCO_3 incorporated with 2 mM Hesperidin; (H) CaCO_3 incorporated with 3 mM Hesperidin; (I) CaCO_3 incorporated with 4 mM Hesperidin.

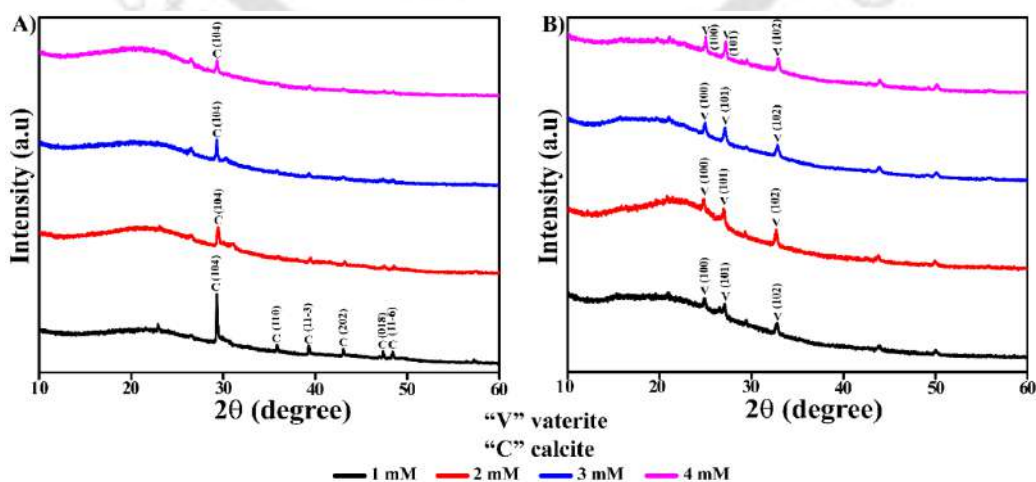


Figure A6.7: XRD patterns of (A) Gelatin films incorporated with CaCO_3 -Quercetin; (B) Gelatin films incorporated with CaCO_3 -Hesperidin.

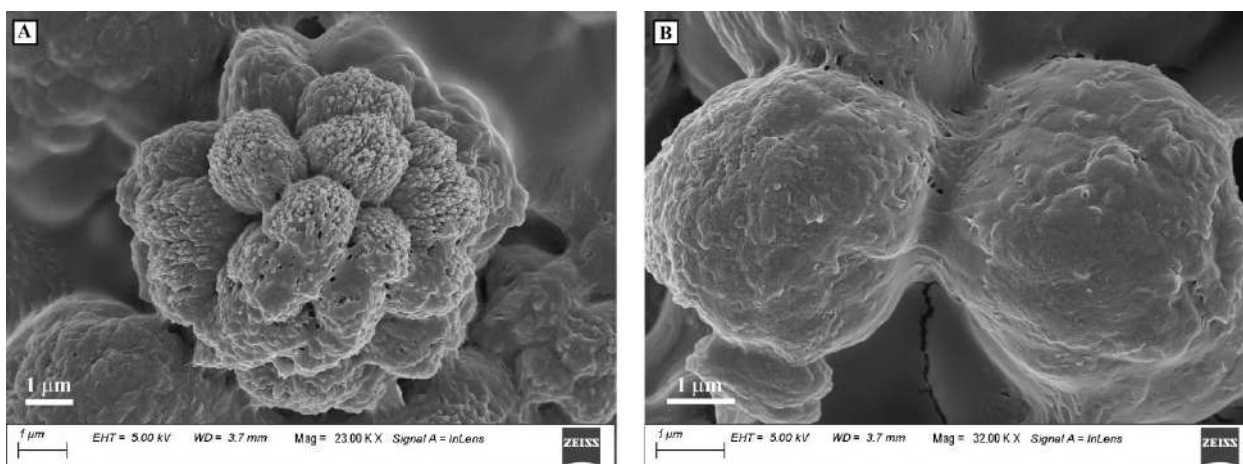


Figure A6.8: FESEM images of (A) Calcite-Quercetin (3 mM) within the fabricated gelatin film; (B) Vaterite-Hesperidin (3 mM) within the fabricated gelatin film.

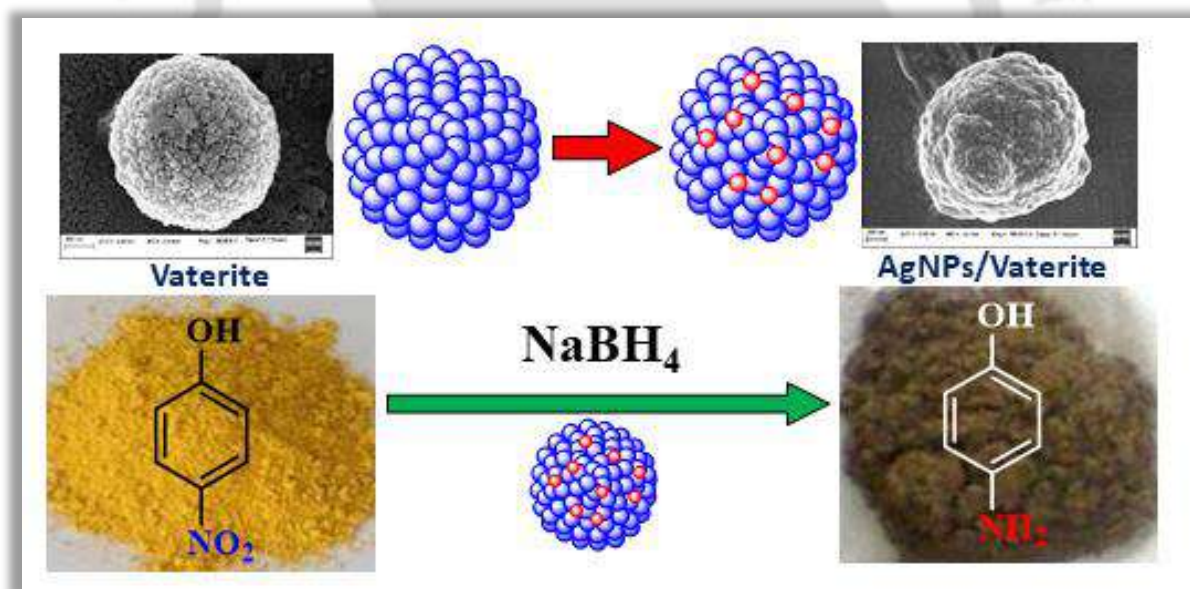
Table A6.1: Assignment of XPS binding energies in bare CaCO_3 and CaCO_3 incorporated with organic additives.

Composite material	Region	Assigned species	Binding energy (eV)
Bare CaCO_3	Ca 2p	Ca 2p _{3/2}	346.83
		Ca 2p _{1/2}	350.63
		Satellite	347.64
		Satellite	350.49
	O 1s	Lattice O	532.00
		Surface adsorbed O	533.54
	C 1s	C-C	284.64
		CO_3^{2-}	289.99
		C-O	286.22
		O-C-O	287.53
CaCO_3 -Quercetin (1 mM)	Ca 2p	Ca 2p _{3/2}	346.88
		Ca 2p _{1/2}	350.90
		Satellite	347.58
		Satellite	350.37
	O 1s	Lattice O	531.67
		Surface adsorbed O	533.29
	C 1s	C-C	284.79
		CO_3^{2-}	289.52
		C-O	286.20
		O-C-O	287.19
CaCO_3 -Quercetin (2 mM)	Ca 2p	Ca 2p _{3/2}	346.95
		Ca 2p _{1/2}	350.42
		Satellite	347.38
		Satellite	351.29
	O 1s	Lattice O	531.54

		Surface adsorbed O	533.12
	C 1s	C-C CO ₃ ²⁻ C-O O-C-O	284.59 289.45 285.78 286.96
CaCO ₃ -Quercetin (3 mM)	Ca 2p	Ca 2p _{3/2} Ca 2p _{1/2} Satellite Satellite	347.11 350.93 347.79 350.47
	O 1s	Lattice O Surface adsorbed O	531.45 532.04
	C 1s	C-C CO ₃ ²⁻ C-O O-C-O	284.65 289.37 285.49 286.39
CaCO ₃ -Quercetin (4 mM)	Ca 2p	Ca 2p _{3/2} Ca 2p _{1/2} Satellite Satellite	347.46 351.08 348.11 351.52
	O 1s	Lattice O Surface adsorbed O	531.33 532.88
	C 1s	C-C CO ₃ ²⁻ C-O O-C-O	284.43 289.36 285.67 286.83
CaCO ₃ -Hesperidin (1 mM)	Ca 2p	Ca 2p _{3/2} Ca 2p _{1/2} Satellite Satellite	346.60 350.03 346.99 350.76
	O 1s	Lattice O Surface adsorbed O	531.31 532.55
	C 1s	C-C CO ₃ ²⁻ C-O O-C-O	284.45 289.33 286.08 285.85
CaCO ₃ -Hesperidin (2 mM)	Ca 2p	Ca 2p _{3/2} Ca 2p _{1/2} Satellite Satellite	346.78 350.49 347.27 350.11
	O 1s	Lattice O Surface adsorbed O	531.30 532.46
	C 1s	C-C	284.42

		CO ₃ ²⁻	289.16
		C-O	285.62
		O-C-O	286.63
CaCO ₃ -Hesperidin (3 mM)	Ca 2p	Ca 2p _{3/2}	346.80
		Ca 2p _{1/2}	350.20
		Satellite	347.10
		Satellite	350.81
	O 1s	Lattice O	531.29
		Surface adsorbed O	532.58
	C 1s	C-C	284.34
		CO ₃ ²⁻	289.06
		C-O	25.64
		O-C-O	286.85
CaCO ₃ -Hesperidin (4 mM)	Ca 2p	Ca 2p _{3/2}	346.81
		Ca 2p _{1/2}	350.50
		Satellite	347.74
		Satellite	350.10
	O 1s	Lattice O	531.20
		Surface adsorbed O	532.62
	C 1s	C-C	284.52
		CO ₃ ²⁻	288.69
		C-O	285.21
		O-C-O	286.34

***In vitro* biomineralized vaterite as a solid-support for silver nanoparticles: A highly efficient catalyst for the reduction of 4-Nitrophenol**



7a.1 Introduction

The vaterite phase of CaCO_3 has been of great interest to researchers as its surface porosity and spherical morphology make it a versatile component for practical utility in commercial applications. However, the challenge lies in its isolation as it is the most unstable phase among the crystalline phases of CaCO_3 . In the previous chapters, we have explained how we were able to effectively isolate the unstable vaterite phase utilizing the different additives. In this work, we have used these biomineralized vaterite particles with porous surface texture to work as an inert and solid-support for silver nanoparticles (Ag NPs). The resulting Ag NPs/Vaterite particles were subjected as a heterogeneous catalyst to explore their efficiency in the reduction of 4-Nitrophenol (4-NP) to 4-Aminophenol (4-AP). Metal nanoparticle-based catalysts among others are highly promising as a heterogeneous catalyst for various industrial-based applications varying from the production of useful commercial products to the removal and *in situ* conversion of environmentally benign reaction by-products to their non-hazardous counterparts.^{7a.1-7a.6} These metal nanoparticles possess a high density of the active catalytic sites owing to their higher surface area compared to their bulk counterparts, hence showing a manifold increase in the catalytic activity.^{7a.7-7a.15} Silver nanoparticles (Ag NPs) have been a go-to candidate for many of organic catalytic reactions, preferably over other metal nanoparticle-based catalysts.^{7a.16-7a.17} The reason for this may be attributed to its low cost and high efficiency towards the catalytic activity. Therefore, the proper utilization of this noble catalyst in various industrial and environmental applications will be of great value. However, using free Ag NPs often leads to irreversible aggregation of the particles, changing their surface property and hence in most cases lowering their catalytic efficiency.^{7a.18} A lot of methods have been deployed to address this issue, such as the surface alteration of the Ag NPs using polymeric stabilizing agents.^{7a.19} But such methods have their limitations as the direct interaction between the substrate and the catalyst tends to be lowered due to the shielding by the protecting groups around the Ag NPs. Taking these into consideration, a recent study on exploring the possibility of the formation of metal nanoparticle-based composites by their deposition on inert surfaces is of great interest among the scientific community. In this study, we made a similar approach, using the biomineralized vaterite microspheres as the support for the Ag NPs. The use of the spherical vaterite particles is highly promising in elevating the catalytic activity of the Ag NPs and also their ability to run for a higher number of cycles when subjected as a catalyst in the reduction of 4-Nitrophenol.

4-Nitrophenol is a major contributor among the industrial pollutants released into the water bodies leading to severe water contamination. As a very common reagent used in industries

involved in pharmaceuticals, dyes, pesticides, etc., 4-NP is regularly released into the environment.^{7a.20-7a.25} This 4-NP poses a severe threat to the lives of both humans and animals. A lot of effort is being made to remove this toxic pollutant.^{7a.26} Even in trace amounts, it can be hazardous, causing potential damage to the human central nervous system, kidney, liver, etc.^{7a.27,7a.28} The challenge lies in its removal from contaminated water because of its high water stability and solubility. Most importantly, the upper limit of 4-NP is strictly restricted to 10 ppb by health regulating bodies across the world.^{7a.27,7a.29} Freshwater bodies serving the water needs for daily purposes, including drinking, are directly or indirectly contaminated by the release from industries and 4-NP being one such toxic pollutant. In this work, we have done a comprehensive study to check the usefulness of our catalyst by experimenting with water from different sources such that the catalyst, when used, serves the purpose not just in industrial treatment of water but also to render the water in the contaminated water bodies safe for consumption.

The catalytic route by using the noble metal Ag for the reduction of the toxic nitro-based compounds is considered an ideal process. It is being studied by scientific groups around the world for a few years now. But the challenge lies in designing a catalyst with high efficiency and the ability to run for several cycles, keeping in mind the cost of production and the ease with which it can be synthesized. Also, the tiny Ag NPs are highly susceptible to agglomeration. Resulting in an increase in their size and hence the deterioration in their performance.^{7a.30} Therefore, a platform to prevent them from agglomerating and also immobilizing is very important. This is where inert solid support comes into aid, as in this case, we made use of the spherical Vaterite particles. The platform or solid support can be varied, whereas the Ag NPs remain constant. The solid support, along with the method assigned for the fabrication of the NPs determines the size of the NPs, the efficiency and the catalytic activity. A number of materials have been subjected as the platform for immobilizing the Ag NPs, such as SiO₂, carbon nanofibers, graphene oxide, TiO₂, etc.^{7a.31-7a.33} The various crystalline phases of CaCO₃; calcite, aragonite and vaterite exhibit completely different properties including morphology and surface properties. The vaterite particles have never been used as a platform for Ag NPs to be used in the reduction of aromatic nitro compounds.

In this research work, we have performed the highly efficient fabrication of Ag NPs on spherical vaterite particles. The vaterite particles were biomineralized in the presence of whey protein as the directing template. The precipitation and subsequent fabrication of the Ag NPs on the vaterite surface were carried out in a simple, cost-effective and eco-friendly process. The porous texture of the biomineralized vaterite should ensure that the loaded Ag NPs should be stable for

several cycles of catalysis. The Ag/Vaterite particles were characterized by Powder X-Ray Diffraction (PXRD), the morphology of the particles was obtained by Field Emission Scanning Electron Microscope (FESEM). The Field Emission Transmission Electron Microscope (FETEM) analyses were done; where also the High-Resolution TEM analysis of an individual nanoparticle on vaterite was performed followed by subsequent mapping of the various elements involved. Thermogravimetric Analysis (TGA) of the Ag NPs/Vaterite composite was performed to confirm the presence of Ag NPs on the nanocomposite and also to determine the amount of loaded Ag NPs from the structural weight loss. The change in surface area of the vaterite particles before and after the fabrication of the Ag NPs was studied using Brunauer-Emmett-Teller (BET) surface area measurement. The Ag/Vaterite catalyst thus synthesized was subjected to catalyze the reduction of 4-NP to 4-AP and the efficiency and catalytic activity were studied.

7a.2 Results and discussion

7b.2.1 General characterizations of the materials

The vaterite phase synthesized by the template-directed biomineralization was characterized by X-Ray Diffraction analysis, where the pattern suggested the formation of the vaterite phase, Fig. A7a.1(A). The pattern was identical to the standard PDF data for the vaterite phase, ICSD 00-001-1033. From the FESEM images, we could see the formation of the spherical vaterite particles with a porous surface texture, Fig. A7a.1(B).

The crystalline structure of the Ag NPs/Vaterite was characterized by the PXRD analysis. The

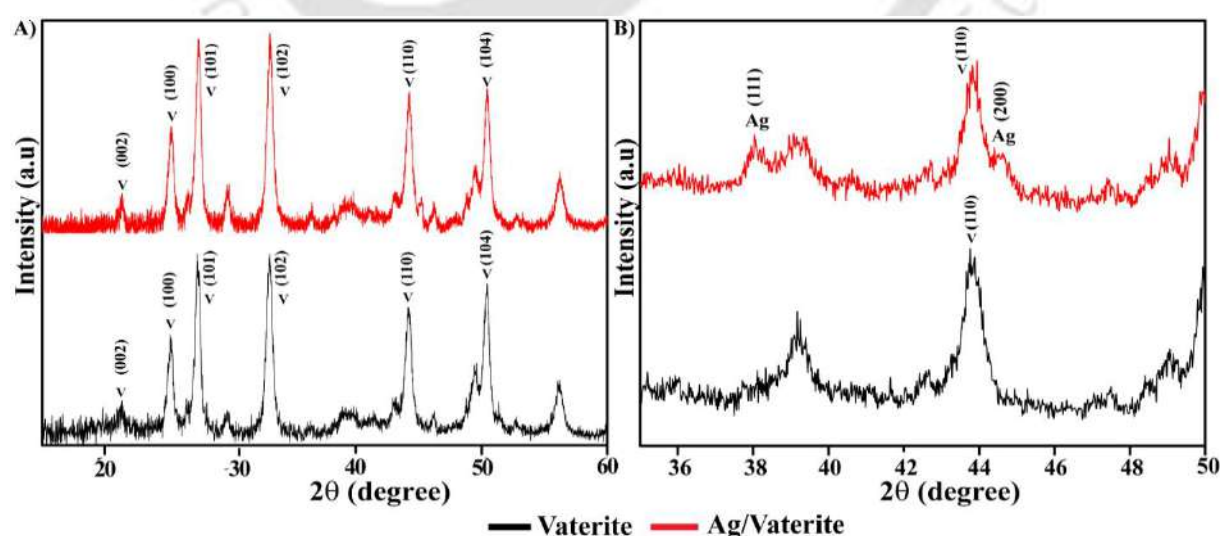


Figure 7a.1: XRD patterns of Vaterite and Ag NPs/Vaterite composite: (A) overall profiles; (B) magnification of Ag peaks.

pattern obtained was compared with that of the bare vaterite, Fig. 7a.1(A). Most of the peaks were identical such as the peaks at 2θ values equal to 20.98, 25.28, 27.28, 33.11, 43.83, 49.39, 50.41, 56.20 were identified as corresponding to (002), (100), (101), (102), (110), (112), (104), (202) respectively. These peaks were almost identical to the standard PDF data for the vaterite phase, ICSD 00-001-1033. In addition to these peaks, two additional peaks with 2θ values equal to 38.2 and 44.5 were observed only for the Ag NPs/Vaterite material, Fig. 7a.1(B). These two peaks are identical to the peaks for the (111) and (200) planes of Ag. This was verified by matching with the standard PDF data for Ag, ICSD 00-001-1164.

The morphology of the Ag/Vaterite composite can be observed from the FESEM images. The overall morphology of the resulting composite, Fig. 7a.2(E) and (F), is the same as that of the bare vaterite particles, Fig. 7a.2(A) and (B), that were biomineralized. Fig. 7a.2(C) and (D) show the FESEM images of the bare Ag NPs. They have a spherical morphology, analogous to the ones that are deposited on the surface of the nanocomposite Ag NPs/Vaterite, but the size of the bare ones are ~ 20 -50 nm, whereas those deposited on vaterite are of much smaller size. The small size of the deposited Ag NPs allows them to have the edge over their bigger counterparts in terms of functionality, such as catalytic activity. On comparing the surface texture of both the particles, we can clearly see that the vaterite particles before loading possessed a porous surface, which had changed after the fabrication of the Ag NPs. The surface texture was no longer porous, but we could see individual smaller sized particles, most of them bulging out from the surface, with some of them sitting smoothly on the surface. Most importantly, with no trace of porosity as that of the bare vaterite particles, indicating the deposition of the Ag NPs on their surface.

Field Emission Transmission Electron Microscope (FETEM) analysis was performed to understand the structure, size and morphology of the Ag NPs and also its distribution on the vaterite surface. From the low-resolution FETEM images, Fig. 7a.3(A), A7a.2(A) and (B), we can see the size and morphology of the Ag NPs. A large amount of deposition of the particles with no evident signs of aggregation can be seen. Although the nanoparticles are densely deposited, there is a clear spacing between each one of them. A comparison of the Ag NPs deposited on the solid support Vaterite with that of the bare Ag NPs is shown in Fig. A7a.2, where A7a.2(A) and (B) are that of the Ag NPs/Vaterite and A7a.2(C) and (D) is that of the bare Ag NPs. From the FETEM images, we can clearly see that the bare Ag NPs are much bigger in size and most importantly, the majority of the particles are agglomerated, which would hamper their functionality. Hence solid support like vaterite not only directs the size but also

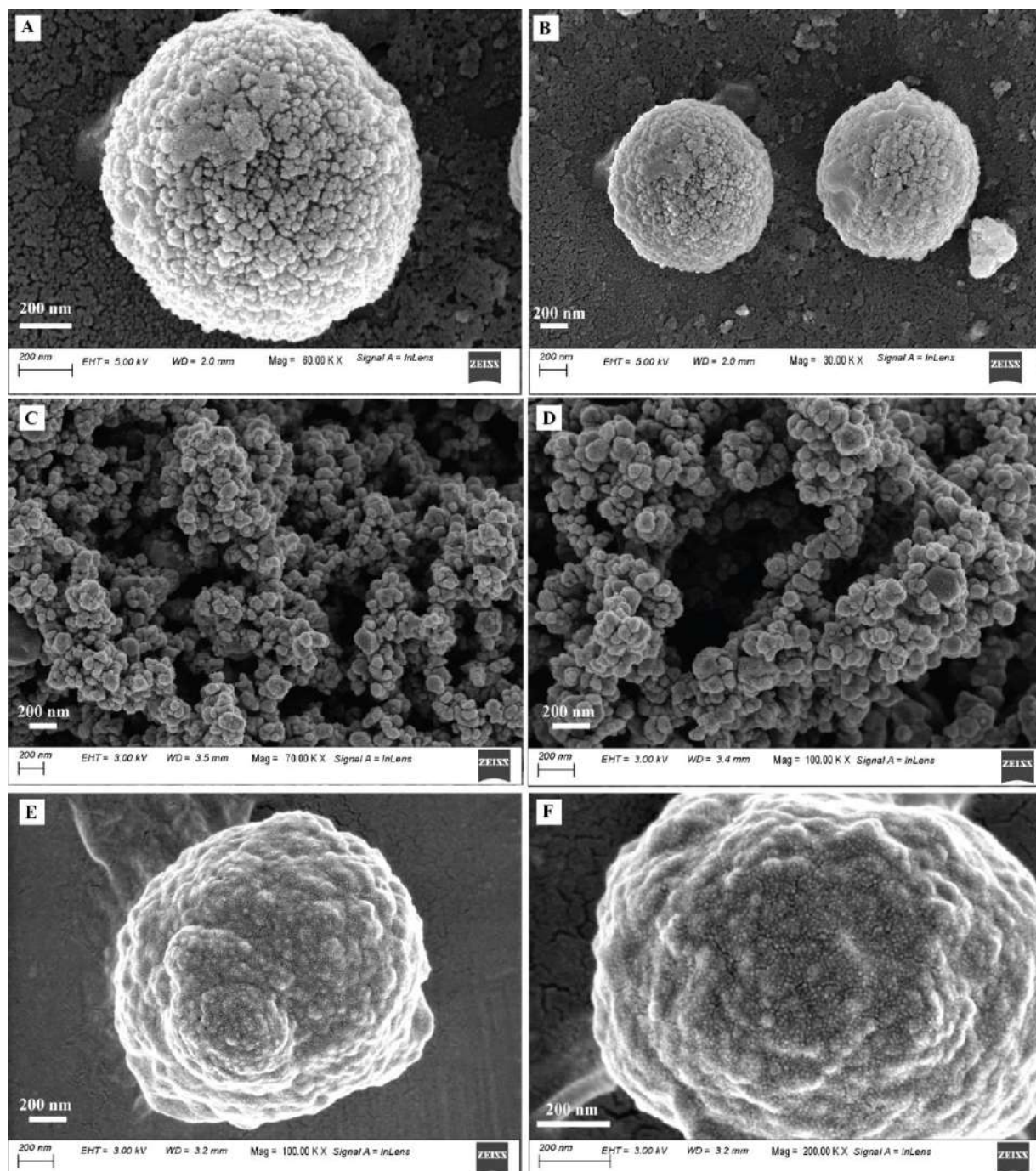


Figure 7a.2: FESEM images of (A) and (B) bare vaterite particles; (C) and (D) bare Ag NPs; (E) and (F) Ag NPs/Vaterite composite.

prevents the nanoparticles from agglomerating. This would allow each particle to discharge its role as a catalyst highly efficiently without any interference from the neighbouring particles, improving the overall catalytic activity of the catalyst by manifolds. The spherical morphology of vaterite directed the even distribution of the Ag NPs without any crowding. The size distribution was obtained, assuming all the particles to be nearly spherical and was calculated by analyzing 200 particles. The results revealed an intriguing fact as can be verified from the

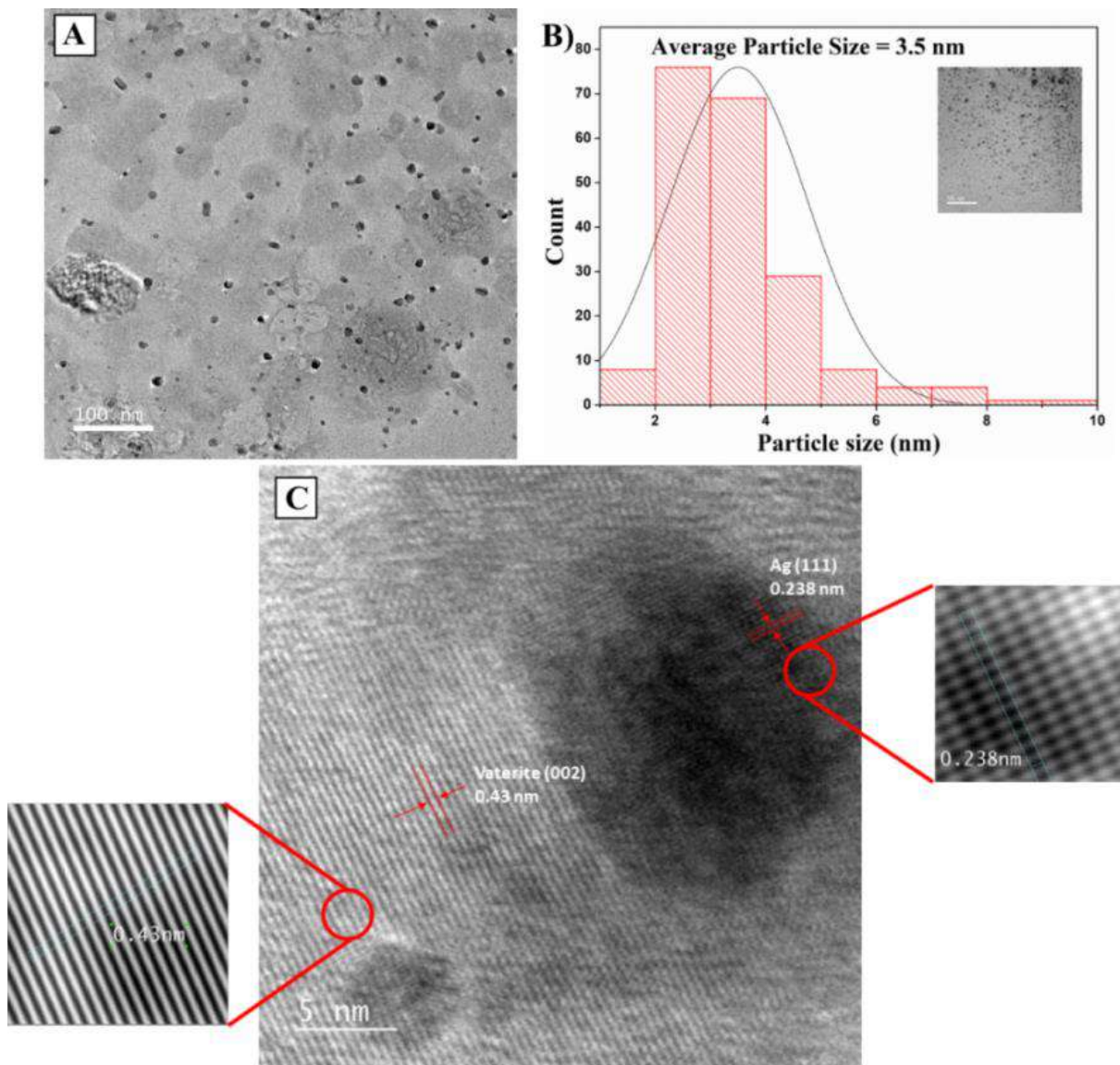


Figure 7a.3: (A) FETEM image of Ag NPs/Vaterite composite; (B) Particle size distribution of Ag NPs embedded on the biomineralized Vaterite; (C) HRTEM image of Ag NPs/Vaterite composite.

FETEM images that most of the particles fall in the range of 2-4 nm, with the average particle size being 3.5 nm, Fig. 7a.3(B). Hence the majority of the Ag NPs formed are of ultrafine size, which renders it to be an excellent component for catalysis. The formation of Ag NPs with the ultrafine size is due to the spatial confinement of the pores of vaterite particles. This poses constrictions for the growth of Ag NPs on the vaterite surface leading to their tiny size in the range of 2-4 nm. Hence it is the surface of the vaterite that dictates the dimensions of the embedding Ag NPs and also prevents them from agglomerating. The HRTEM imaging technique probably the best to visualize the fabrication of the Ag NPs on vaterite, evidently points out the distinct presence of both the phases, Fig. 7a.3(C). The measured fringe spacing values of 0.238 nm and 0.43 nm correspond to the inter-planar spacing of (111) plane of Ag and (002) of the Vaterite phase of CaCO_3 , respectively. The EDS mapping images show the uniform

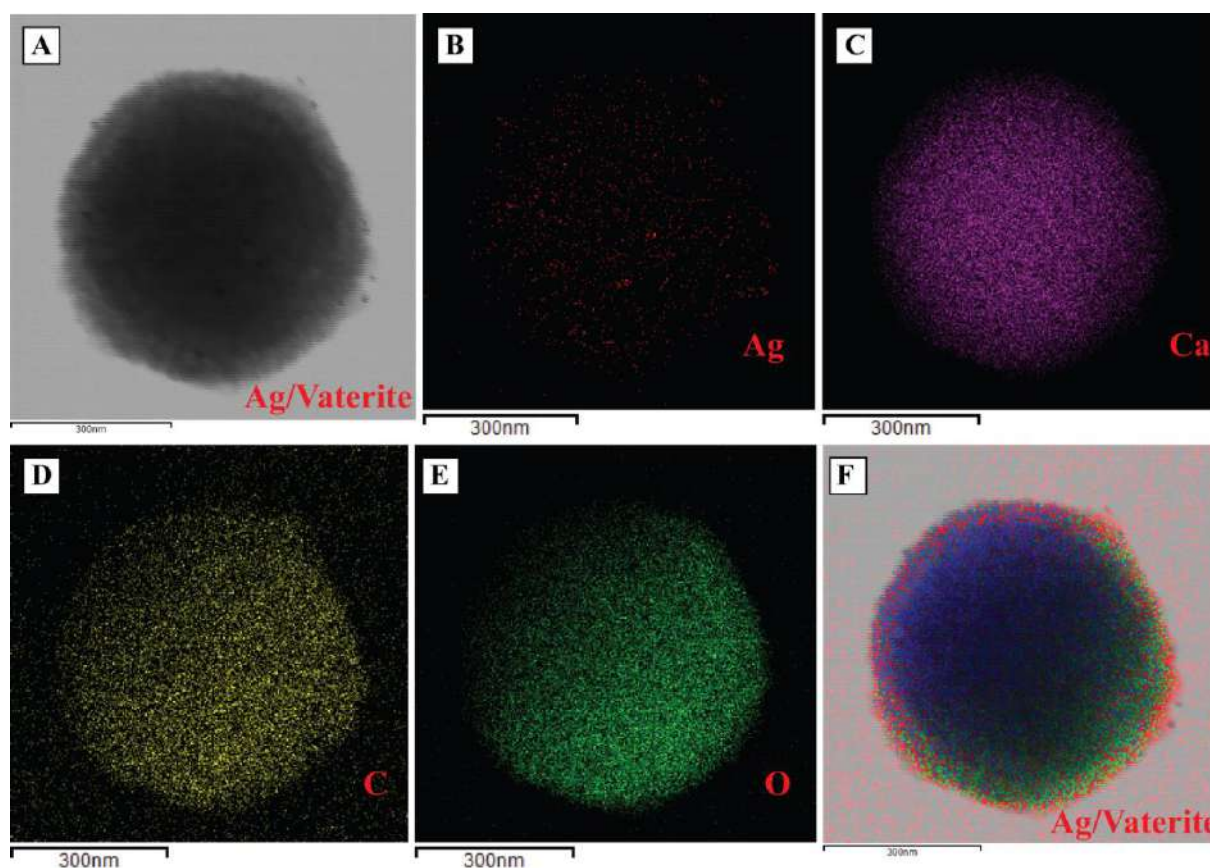


Figure 7a.4: (A) FETEM image of spherical vaterite fabricated with Ag/NPs; (B), (C), (D), (E) corresponding EDS elemental mapping of Ag, Ca, C and O respectively; (F) EDS mapping pointing out all the elements in the Ag NPs/Vaterite composite.

and dense distribution of Ag NPs on the spherical vaterite surface. The individual elements, Fig. 7a.4(B), (C), (D) and (E), and also the combination of all the elements, Fig. 7a.4(F), have been pointed out separately. Performing all the different analyses of the FETEM technique gave comprehensive information on the fabrication of Ag NPs on the spherical vaterite surface.

Thermogravimetric analysis (TGA) of the Ag NPs/Vaterite nanocomposite was performed to specify its composition by analyzing the percentage weight loss of the various components during the decomposition it undergoes when subjected to heating up to 800 °C, Fig. A7a.3(A). The first weight loss, 2-3% at around 100 °C is due to the physically adsorbed water. The ~5% weight loss at 200-300 °C is due to the loss of the Ag NPs.^{7a.34} The ~3% weight loss from 320-400 °C is due to the elimination of crystal water from vaterite. The transformation of vaterite to calcite takes place in the range of 400-500 °C. After which, the steep fall in the curve after 700 °C is due to the decomposition of calcite whereby the loss of CO₂ (decarbonization) to form CaO takes place.^{7a.35,7a.36} In this study, we were mainly focused on the region whereby the loss of Ag NPs occurred. Therefore, the region has been enlarged, Fig. A7a.3(B), where we can clearly see a weight loss of 5% which is due to the Ag NPs.

The surface area of the material before and after loading was derived from the BET specific surface area experiment obtained from the Nitrogen adsorption-desorption analysis, Fig. A7a.4(A) and (B). The average surface area of the bare vaterite and the composite material was 9.692 m²/g and 12.215 m²/g, respectively. The increase in the average surface area of the resulting composite material after loading may be attributed to the silver nanoparticles that have been added to the surface of vaterite. Nanoparticles are known to possess a greater surface area compared to their bulk counterparts. Hence their addition on the surface has led to an increase in the average surface area by approximately 21%.

7b.2.2 Reduction of 4-NP

The catalytic properties of the Ag NPs/Vaterite composite material were evaluated by its effectiveness in the reduction of 4-NP in the presence of an excess of NaBH₄. The addition of NaBH₄ to 4-NP led to the shift in its characteristic absorption peak from 317 nm to 400 nm, indicating the generation of 4-Nitrophenolate ions, Fig. A7a.5. This change could also be observed by the naked eye as the colour of the 4-NP solution changed from a very faint yellow colour to a dark yellow colour on the addition of NaBH₄. There was no change in the absorption intensity even after 30 minutes, Fig. A7a.5, indicating that NaBH₄ alone without the assistance of a catalyst is not enough to bring about the reduction of 4-NP. Also, on the addition of the bare vaterite particles to the mixture, no change was observed, Fig. 7a.5(A). In another similar experiment, we studied the role of the bare Ag NPs on the reduction of 4-NP in the presence of an excess of NaBH₄. On adding the Ag NPs, initially, the absorption intensity of the peak at 400 nm had diminished to approximately 50% within 1 minute with the simultaneous growth of a new peak at 298 nm due to the product 4-AP. But after this, the decrease in the peak intensity at 400 nm had slowed down significantly and there was hardly any change, Fig. 7a.5(B). This is due to the agglomeration of the Ag NPs in solution, because the exposure of the catalyst sites to be utilized by the substrate molecules was limited and hence, the rate of reduction had slowed down. However, in the experiment where the synthesized Ag NPs/Vaterite nanocomposite was used as the catalyst, the absorption intensity of the peak at 400 nm had started to diminish and simultaneously a new peak at 298 nm attributed to the product 4-AP had begun to appear. The peak at 400 nm gradually diminished with time and eventually, the peak had completely disappeared, whereas the peak at 298 nm had steadily increased, Fig. 7a.5(C). These changes in peak intensity indicated that the complete reduction of 4-NP to 4-AP had taken place.

The optimization experiments for the amount of catalyst to be used were studied at three different concentrations, 0.5 mg, 1 mg and 1.5 mg, Fig. A7a.6(A), (B) and (C). We observed that

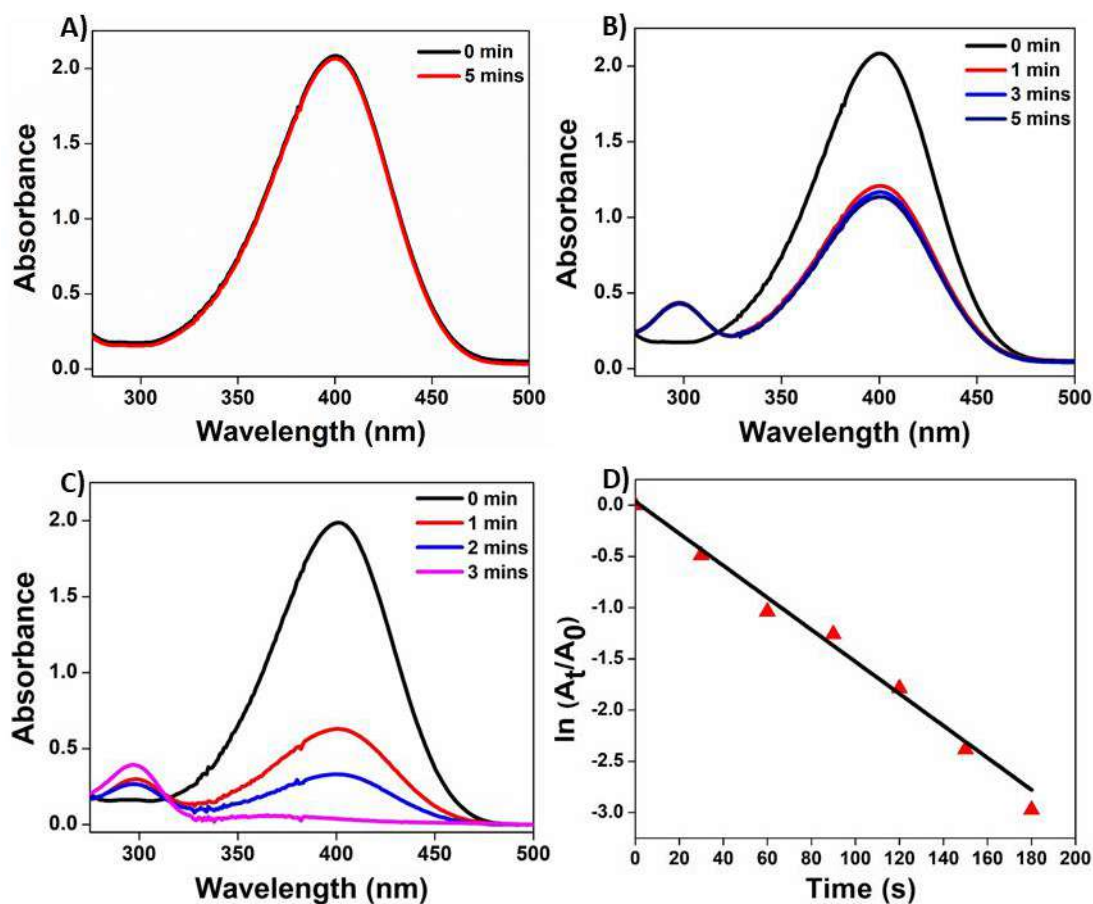


Figure 7a.5: UV/Vis absorption spectra for the catalytic reduction of 4-Nitrophenol in the presence of (A) Vaterite particles; (B) Ag NPs; (C) Ag NPs/Vaterite composite; (D) Plot of $\ln(A_t/A_0)$ versus reaction time [s].

when the amount of catalyst used was 0.5 mg, the time taken for the complete reduction was 5 minutes, whereas, for 1 mg of the catalyst, the time taken was 3 minutes. So from these two experiments, we can very easily say that the increase in the amount of catalyst increases the rate of reduction. But when we added 1.5 mg of the catalyst, the rate of reduction had gone down and it took 4 minutes for the process to be complete as compared to just 3 minutes for 1 mg of the nanocomposite. This decrease in rate on the addition of a comparatively higher amount of the catalyst can be explained in terms of the induction period. The induction period is the time taken by the surface atoms on the nanoparticles for restructuring in order to generate catalytically active sites.^{7a.37,7a.38} For a smaller amount of the catalyst, Ag NPs/Vaterite, with Ag NPs of ultrafine sizes, there is no question of agglomeration and hence a very short induction period. But an increase in dose may lead to agglomeration and hence slowing the rate of the reduction process. Therefore, after the optimization experiments, the amount of catalyst to be used was fixed to 1 mg. So the experiment using 1 mg of the nanocomposite catalyst was studied in detail. The UV-spectra of the reaction was taken in the range of 275-500 nm for every 1 minute (60s), Fig. 7a.5(C). It was observed that after 3 minutes (180 s), the peak at 400 nm due to 4-NP had

completely disappeared, whereas, the peak at 298 nm for the product 4-AP had gradually increased during the course of the reaction and attained its maximum, indicating complete reduction. The reaction can also be very easily monitored by the changes in the colour of the solution, from dark yellow to colourless at the end of 3 minutes. The decrease in the intensity of colour, every minute, was recorded, Fig. A7a.7.

The kinetics of the reaction was studied by observing the changes in the peak at 400 nm every 30 s. Since the initial concentration of NaBH₄ was significantly high as compared to 4-NP and it was assumed that it remained almost constant throughout the course of the reaction, hence we propose that the reaction follows pseudo first-order kinetics. Equation **7a.1** was used to calculate the apparent rate constant, k (s⁻¹), where A_t and A_0 are the absorption intensity at time t (s) and at the initial time ($t=0$). From the plot $\ln(A_t/A_0)$ versus time (s), Fig. 7a.5(D), an approximately linear relationship was observed. Considering the slope and intercept of the simulated straight line, the value of the apparent rate constant, k was found out to be 2.2×10^{-2} s⁻¹.

$$\ln(A_t/A_0) = -kt \quad (7a.1)$$

The turnover frequency (TOF, mmol mg⁻¹ s⁻¹) was calculated using equation **7b.2**. In equation **7b.2**, N_{4-NP} represents the concentration of 4-NP in mmol and $M_{Ag\ NPs}$ represents the specific amount of Ag NPs in mg that was present in 1 mg of the Ag NPs/Vaterite catalyst. The amount of Ag NPs loaded on 20 mg of the catalyst was determined from the AAS analysis, there we found out that the % of Ag NPs in 20 mg of the catalyst is 4.7%, Fig. A7a.8. From this, we calculated the specific amount of Ag NPs in 1 mg of the catalyst. The t (s) in equation **7b.2** represents the reaction time (180 s). Hence using equation **7b.2**, the TOF was calculated to be 2.36×10^{-2} mmol mg⁻¹ s⁻¹.

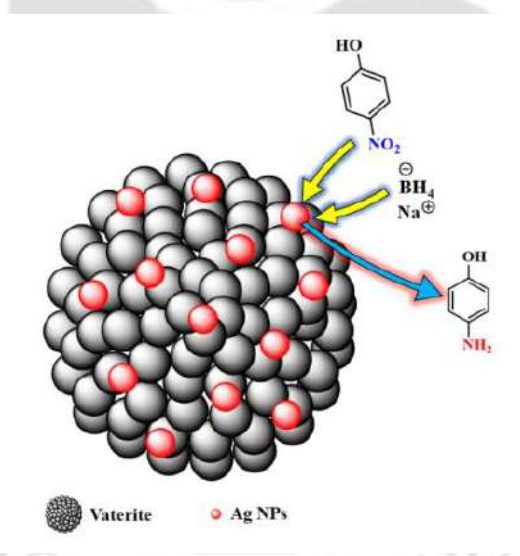
$$TOF = N_{4-NP} / M_{Ag\ NPs} \times t \quad (7b.2)$$

In **Table A7a.1**, we present a comparison, where we see the Ag NPs/Vaterite catalyst used in this work gives a higher value of the rate constant, k as compared to other reported Ag-based catalysts and also Au and Cu based catalysts used in the reduction of 4-NP. The high rate constant and turnover frequency proves that Ag NPs/Vaterite catalyst shows excellent catalytic activity towards 4-NP reduction.

A plausible mechanism of the catalytic activity of Ag NPs towards 4-NP reduction in the presence of an excess of NaBH₄ is shown in **Scheme 7a.1**. The metallic nanostructure of the Ag NPs provides a surface for the reduction to take place. The BH₄⁻ ions adsorb onto the surface of the nanocatalyst and transfer hydrogen ions on the surface. Simultaneously the substrate 4-NP

also gets adsorbed onto the surface and is reduced by the BH_4^- to 4-AP. Eventually, after the reduction process is complete, the product 4-AP leaves the surface of Ag, ready for the next catalytic cycle. The role of the solid support vaterite is to prevent the Ag NPs from agglomerating and also maintaining the distance between the neighbouring Ag NPs particles such that the reduction process on each Ag NPs surface takes place freely without any interference. As a result, the catalytic activity of the Ag NPs/Vaterite towards the 4-NP reduction was better than others.

The reusability of the catalyst, which is an issue for most support based metal catalyst was also addressed in this work. As a potential catalyst for industrial applications, it is very important that the catalyst synthesized should be able to maintain its characteristics for several cycles. The Ag NPs/Vaterite composite showed great ability to be reused at least for 5 consecutive cycles. From the UV-Visible spectroscopy, Fig. 7a.6(A), we were able to study the catalytic activity for several cycles and calculate the percentage of conversion from 4-NP to 4-AP in each cycle, Fig. 7a.6(B).



Scheme 7a.1: Plausible mechanism of 4-Nitrophenol reduction on the surface of the Ag NPs/Vaterite composite.

Here, we observed that the conversion efficiency was above 93.8% for five consecutive cycles. A major drawback faced during heterogeneous catalysis is the possible leaching of the metal from the solid support, but in this work, the Ag NPs embedded on vaterite remained unaffected even after five catalytic cycles. This was confirmed by the EDX technique, where the catalyst particles were isolated after the third, Fig. A7a.9(B), and the fifth cycle, Fig. A7a.9(C), and analyzed and compared with the unreacted catalyst particles, Fig. A7a.9(A). From the EDX data, we see that the amount of Ag in each case was identical and hence there is no question of leaching of the Ag NPs from the solid support vaterite. Additionally, it can be seen from the

FETEM image, Fig. A7a.10, of the catalyst taken after the fifth cycle, the nanoparticles were still free from agglomeration in the Ag NPs/Vaterite composite catalyst. Firstly, the immobilization of Ag NPs and then its ability to remain unaltered even after multiple cycles of catalysis justifies the role of the inert solid support vaterite. The porous texture of the vaterite surface allows the strong confinement of the embedded Ag NPs on its surface and hence prevents the Ag NPs from agglomerating and also from leaching out of the solid support.^{7a.39}

The effectiveness of the Ag NPs/Vaterite composite catalyst towards the reduction of 2-Nitrophenol (2-NP) was also studied, Fig. A7a.11. Keeping the initial concentration of 2-NP the same as that of 4-NP and using the same amount of catalyst in excess of NaBH₄. In this case, the % of conversion to 2-Aminophenol (2-AP) was low. After 30 minutes, only 23% of conversion had taken place. The lowering in the conversion % for 2-NP may be attributed to the intramolecular H-Bonding in 2-NP

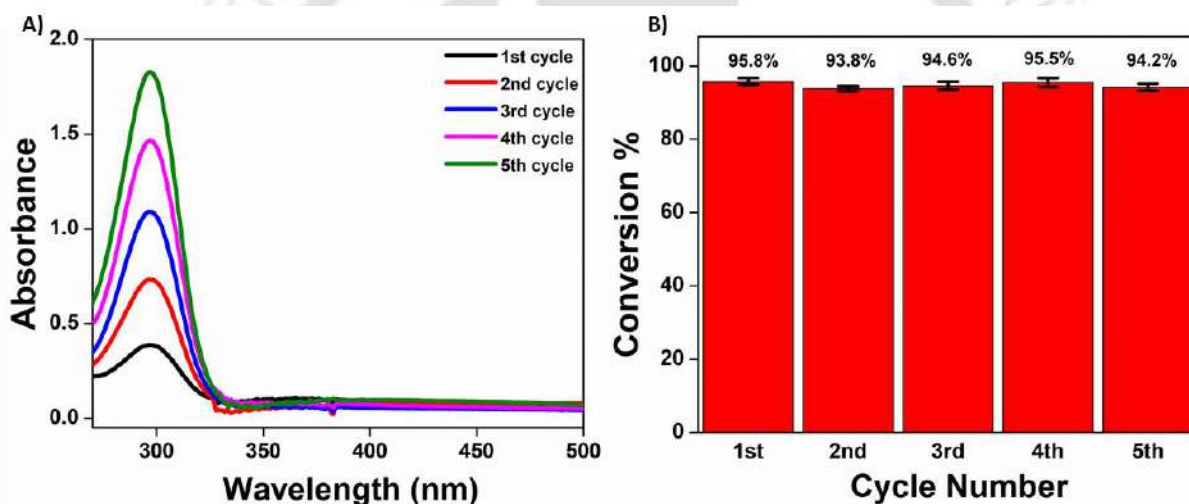
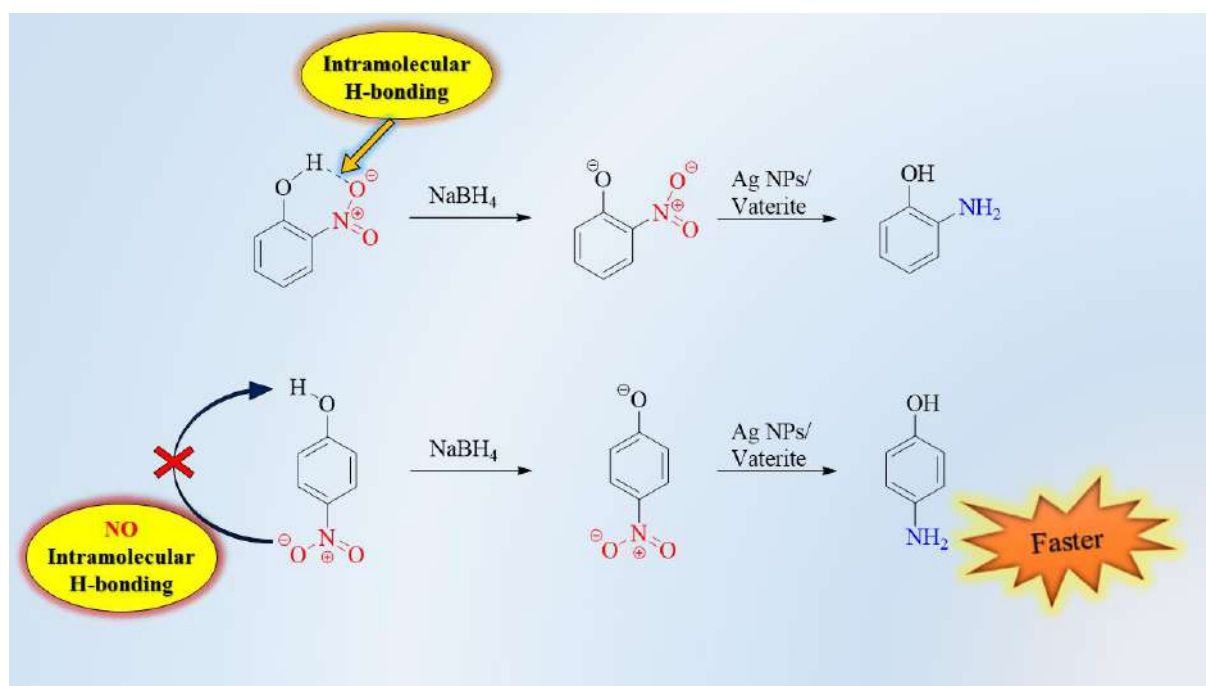


Figure 7a.6: (A) UV/Vis absorption spectra for the reusability experiments of the catalytic reduction of 4-Nitrophenol in the presence of Ag NPs/Vaterite catalyst; (B) Percentage conversion of 4-Nitrophenol in each catalytic cycle.

but this is not applicable in the case of 4-NP, **Scheme A7a.2**. For the reduction process of 2-NP to begin on the catalyst surface, it has to cross a higher activation energy barrier. Hence a slower rate is observed for the 2-NP compared to 4-NP. Additionally, to serve the goal of potential utilization of the Ag NPs based catalyst in industrial applications and wastewater treatment, we extended our work to study the efficiency of the catalyst in water from different sources such as tap water and lake water. It was observed that the catalyst performed excellently in those mediums too, Fig. A7a.12. In the case of tap water, the reduction of 4-NP, studied using



Scheme 7a.2: Schematic representation showing the difference in reaction mechanism of Ag NPs/Vaterite catalyzed reduction of 2-Nitrophenol and 4-Nitrophenol.

UV-Vis spectroscopy, maintaining all the concentrations as same, took 3 minutes (180 s) exactly as that of the deionized water, Fig. A7a.13(A). In the case of lake water, where there are high chances of other impurities being present and interfering with the substrate 4-NP, the time taken was 5 minutes (300 s) for the complete conversion, Fig. A7a.13(B). The ability of the Ag NPs/Vaterite catalyst to successfully convert the hazardous 4-NP in water from different sources proves its efficiency to be utilized for wastewater treatment.

7a.3 Conclusion

In this work, we were able to synthesize silver nanoparticle embedded biomineralized vaterite composite material. The intriguing points of this work include the highly-dense and even deposition of the nanoparticles with sufficient spacing between the neighbouring particles such that the question of agglomeration between particles can be satisfactorily neglected. Also, the silver nanoparticles deposited were mostly ultrafine particles of sizes in the range of 2-4 nm. The composite was subjected as a catalyst in the reduction of 4-Nitrophenol. It showed highly encouraging results in terms of catalytic activity and most importantly, remained unaltered for at least five consecutive cycles. The high rate constant of $2.2 \times 10^{-2} \text{ s}^{-1}$ and an impressive turnover frequency of $2.36 \times 10^{-2} \text{ mmol mg}^{-1} \text{ s}^{-1}$ are the highlights of this nanoparticle-based catalyst. Additionally, the effectiveness of this catalyst towards the reduction of 4-Nitrophenol was also studied in water from natural sources; tap water and lake water. The results attained were highly

impressive, suggesting that the material promises to be highly efficient as a potential catalyst for the industrial treatment of wastewater and can be deployed for large-scale purposes.

References

- 7a.1. I. Fechete, Y. Wang and J. C. Vedrine, The past, present and future of heterogeneous catalysis, *Catal. Today*, 2012, **189**, 2–27.
- 7a.2. R. Schlogl, Heterogeneous catalysis, *Angew. Chem. Int. Ed.*, 2015, **54**, 2–58.
- 7a.3. Z. Hajizadeh, K. Valadi, R. T. Ledari and A. Maleki, Convenient Cr(VI) Removal from Aqueous Samples: Executed by a Promising Clay-Based Catalytic System, Magnetized by Fe₃O₄ Nanoparticles and Functionalized with Humic Acid, *ChemistrySelect*, 2020, **5**, 2441-2448.
- 7a.4. A. Maleki, Z. Hajizadeh, V. Sharifi and Z. Emdadi, A green, porous and eco-friendly magnetic geopolymer adsorbent for heavy metals removal from aqueous solutions, *J. Clean. Prod.*, 2019, **215**, 1233-1245.
- 7a.5. A. Maleki, M. Mohammad, Z. Emdadi, N. Asim, M. Azizi and J. Safaei, Adsorbent materials based on a geopolymer paste for dye removal from aqueous solutions, *Arab. J. Chem.*, 2020, **13**, 3017-3025.
- 7a.6. M. Rouhi, M. Babamoradi, Z. Hajizadeh, A. Maleki and S. T. Maleki, Design and performance of polypyrrole/halloysite nanotubes/Fe₃O₄/Ag/Co nanocomposite for photocatalytic degradation of methylene blue under visible light irradiation, *Optik*, 2020, **212**, 164721.
- 7a.7. S. Wang, Z. Wang and Z. Zha, Metal nanoparticles or metal oxide nanoparticles, an efficient and promising family of novel heterogeneous catalysts in organic synthesis, *Dalton Trans.*, 2009, **2009**, 9363–9373.
- 7a.8. C.M. Friend and B. Xu, Heterogeneous catalysis: a central science for a sustainable future, *Acc. Chem. Res.*, 2017, **50**, 517–521.
- 7a.9. K. F. Kalz, R. Kraehnert, M. Dvoyashkin, R. Dittmeyer, R. Gl-ser, U. Krewer, K. Reuter and J. D. Grunwaldt, Future challenges in heterogeneous catalysis: understanding catalysts under dynamic reaction conditions, *ChemCatChem.*, 2017, **9**, 17-29.
- 7a.10. Q. L. Zhu and Q. Xu, Immobilization of ultrafine metal nanoparticles to high surface-area materials and their catalytic applications, *Chem.*, 2016, **1**, 220–245.
- 7a.11. C. Sarkar, S. Pendem, A. Shrotri, D. Q. Dao, P. P. T. Mai, T. N. Ngoc, D. R. Chandaka, T. V. Rao, Q. T. Trinh, M. P. Sherburne, J. Mondal, Interface engineering of graphene-supported Cu nanoparticles encapsulated by mesoporous Silica for size-dependent

- catalytic oxidative coupling of aromatic amines, *ACS Appl. Mater. Interfaces*, 2019, **11**, 11722–11735.
- 7a.12. J. Liu, K. He, W. Q. Wu, T. B. Song and M. G. Kanatzidis, In situ synthesis of highly dispersed and ultrafine metal nanoparticles from chalcogels, *J. Am. Chem. Soc.*, 2017, **139**, 2900–2903.
- 7a.13. Y. Shen, Z. H. Zhang, R. R. Long, K. J. Xiao and J. Y. Xi, Synthesis of ultrafine Pt nanoparticles stabilized by pristine graphene nanosheets for electro-oxidation of methanol, *ACS Appl. Mater. Interfaces*, 2014, **6**, 15162–15170.
- 7a.14. M. S. Esmaeili, Z. Varzi, R. E. Keihan, A. Maleki and H. Ghafuri, Design and development of natural and biocompatible raffinose-Cu₂O magnetic nanoparticles as a heterogeneous nanocatalyst for the selective oxidation of alcohols, *Mol. Catal.*, 2020, **492**, 111037.
- 7a.15. A. Maleki, Green oxidation protocol: Selective conversions of alcohols and alkenes to aldehydes, ketones and epoxides by using a new multiwall carbon nanotube-based hybrid nanocatalyst via ultrasound irradiation, *Ultrason. Sonochem.*, 2018, **40**, 460–464.
- 7a.16. K. D. Bhatte, P. J. Tambade, K. P. Dhake and B. M. Bhanage, Silver nanoparticles as an efficient, heterogeneous and recyclable catalyst for synthesis of β -enaminones, *Catal. Commun.*, 2010, **11**, 1233–1237.
- 7a.17. R. Poreddy, E. J. Garcia-Suarez, A. Riisager, S. Kegnæs, Silver nanoparticles supported on alumina—a highly efficient and selective nanocatalyst for imine reduction, *Dalton Trans.*, 2014, **43**, 4255–4259.
- 7a.18. X. Y. Dong, Z. W. Gao, K. F. Yang, W. Q. Zhang and L. W. Xu, Nanosilver as a new generation of silver catalysts in organic transformations for efficient synthesis of fine chemicals, *Catal. Sci. Technol.*, 2015, **5**, 2554–2574.
- 7a.19. A. K. Ilunga and R. Meijboom, Catalytic oxidation of methylene blue by dendrimer encapsulated silver and gold nanoparticles, *J. Mol. Catal. A*, 2016, **411**, 48–60.
- 7a.20. M. Chen, C. Xiao, C. Wang, H. Liu, H. Huang and D. Yan, Fabrication of tubular braid reinforced PMIA nanofiber membrane with mussel-inspired Ag nanoparticles and its superior performance for the reduction of 4-nitrophenol, *Nanoscale*, 2018, **10**, 19835–19845.
- 7a.21. D. Gao, S. Li, X. Wang, L. Xi, K. M. Lange, X. Ma, Y. Lv, S. Yang, K. Zhao, H. M. Loussala, A. Duan, X. Zhang and G. Chen, Ultrafine Pt Ru nanoparticles confined in hierarchically porous carbon derived from micro-mesoporous zeolite for enhanced nitroarenes reduction performance, *J. Catal.*, 2019, **370**, 385–403.

- 7a.22. T. Ji, L. Chen, M. Schmitz, F. S. Bao and J. Zhu, Hierarchical macrotube/mesopore carbon decorated with mono-dispersed Ag nanoparticles as a highly active catalyst, *Green Chem.*, 2015, **17**, 2515–2523.
- 7a.23. D. B. Jiang, X. Liu, Y. Yuan, L. Feng, J. Ji, J. Wang, D. Losic, H. -C. Yao and Y. X. Zhang, Biotemplated top-down assembly of hybrid Ni nanoparticles/N doping carbon on diatomite for enhanced catalytic reduction of 4-nitrophenol, *Chem. Eng. J.*, 2019, **383**, 123156.
- 7a.24. N. T. Ngoc Anh, P. -Y. Chang and R. -A. Doong, Sulfur-doped graphene quantum dot-based paper sensor for highly sensitive and selective detection of 4-nitrophenol in contaminated water and wastewater, *RSC Adv.*, 2019, **9**, 26588–26597.
- 7a.25. M. Rocha, P. Costa, C. A. D. Sousa, C. Pereira, J. E. Rodríguez-Borges and C. Freire, L-serine-functionalized montmorillonite decorated with Au nanoparticles: A new highly efficient catalyst for the reduction of 4-nitrophenol, *J. Catal.*, 2018, **361**, 143-155.
- 7a.26. M. Rabbani, H. Bathaee, R. Rahimi and A. Maleki, Photocatalytic degradation of *p*-nitrophenol and methylene blue using Zn-TCPP/Ag doped mesoporous TiO₂ under UV and visible light irradiation, *Desalin. Water Treat.*, 2016, **57**, 25848-25856.
- 7a.27. Y. Yang, K. Jiang, J. Guo, J. Li, X. Peng, B. Hong, X. Wang and H. Ge, Facile fabrication of Au/Fe₃O₄ nanocomposites as excellent nanocatalyst for ultrafast recyclable reduction of 4-nitrophenol, *Chem. Eng. J.*, 2019, **381**, 122596.
- 7a.28. B. Wang, X. L. Lv, D. Feng, L. H. Xie, J. Zhang, M. Li, Y. Xie, J. R. Li and H.C. Zhou, Highly stable Zr(IV)-based metal-organic frameworks for the detection and removal of antibiotics and organic explosives in water, *J. Am. Chem. Soc.*, 2016, **138**, 6204–6216.
- 7a.29. J. Zhang, T. Yao, H. Zhang, X. Zhang and J. Wu, Preparation of raspberry-like gamma-Fe₂O₃/crackled nitrogen-doped carbon capsules and their application as supports to improve catalytic activity, *Nanoscale* 8 (2016) 18693–18702.
- 7a.30. X.Y. Dong, Z.W. Gao, K.F. Yang, W.Q. Zhang and L.W. Xu, Nanosilver as a new generation of silver catalysts in organic transformations for efficient synthesis of fine chemicals, *Catal. Sci. Technol.*, 2015, **5**, 2554–2574.
- 7a.31. P. Zhang, C. Shao, Z. Zhang, M. Zhang, J. Mu, Z. Guo and Y. Liu, In situ assembly of well-dispersed Ag nanoparticles (AgNPs) on electrospun carbon nanofibers (CNFs) for catalytic reduction of 4-nitrophenol, *Nanoscale*, 2011, **3**, 3357–3363.

- 7a.32. M. Wang, D. Tian, P. Tian and L. Yuan, Synthesis of micron-SiO₂@nano-Ag particles and their catalytic performance in 4-nitrophenol reduction, *Appl. Surf. Sci.*, 2013, **283**, 389–395.
- 7a.33. M. Nasrollahzadeh, M. Atarod, B. Jaleh and M. Gandomirouzbahani, In situ green synthesis of Ag nanoparticles on graphene oxide/TiO₂ nanocomposite and their catalytic activity for the reduction of 4-nitrophenol, Congo red and methylene blue, *Ceram. Int.*, 2016, **7**, 8587–8596.
- 7a.34. M. A. M. Khan, S. Kumar, M. Ahamed, S. A. Alrokayan and M. S. AlSalhi, Structural and thermal studies of silver nanoparticles and electrical transport study of their thin films, *Nanoscale Res. Lett.*, 2011, **6**, 434.
- 7a.35. B. C. Chakoumakos, B. M. Pracheil, R. P. Koenigs, R. M. Bruch and M. Feygenson, Empirically testing vaterite structural models using neutron diffraction and thermal analysis, *Sci. Rep.*, 2016, **6**, 36799.
- 7a.36. T. Siva, S. Muralidharan, S. Sathiyarayanan, E. Manikandan and M. Jayachandran, Enhanced Polymer Induces Precipitation of Polymorphous in Calcium Carbonate: Calcite Aragonite Vaterite Phases, *J Inorg Organomet Polym.* 2017, **27**, 770-778.
- 7a.37. C. Kastner and A. F. Thunemann, Catalytic reduction of 4-Nitrophenol using silver nanoparticles with adjustable activity, *Langmuir*, 2016, **32**, 7383-7391.
- 7a.38. J. Mohanta, S. Satapathy and S. Si, Porous Silica-coated gold nanorods: a highly active catalyst for the reduction of 4-nitrophenol, *ChemPhysChem.*, 2016, **17**, 364-368.
- 7a.39. M. Saveleva, E. Prikhozhenko, D. Gorin, A. G. Skirtach, A. Yashchenok and B. Parakhonskiy, Polycaprolactone-Based, Porous CaCO₃ and Ag Nanoparticle Modified Scaffolds as a SERS Platform with Molecule-Specific Adsorption, *Front. Chem.*, 2020, **7**, 888.

Annexure-Chapter 7a

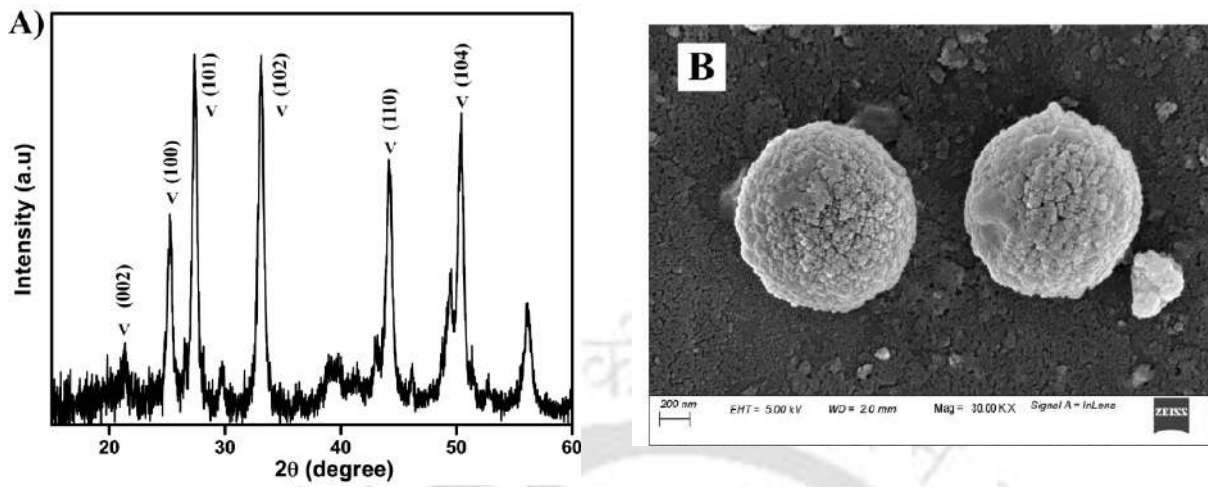


Figure A7a.1: (A) XRD patterns of biom mineralized Vaterite; and (B) FESEM image of biom mineralized Vaterite particles.

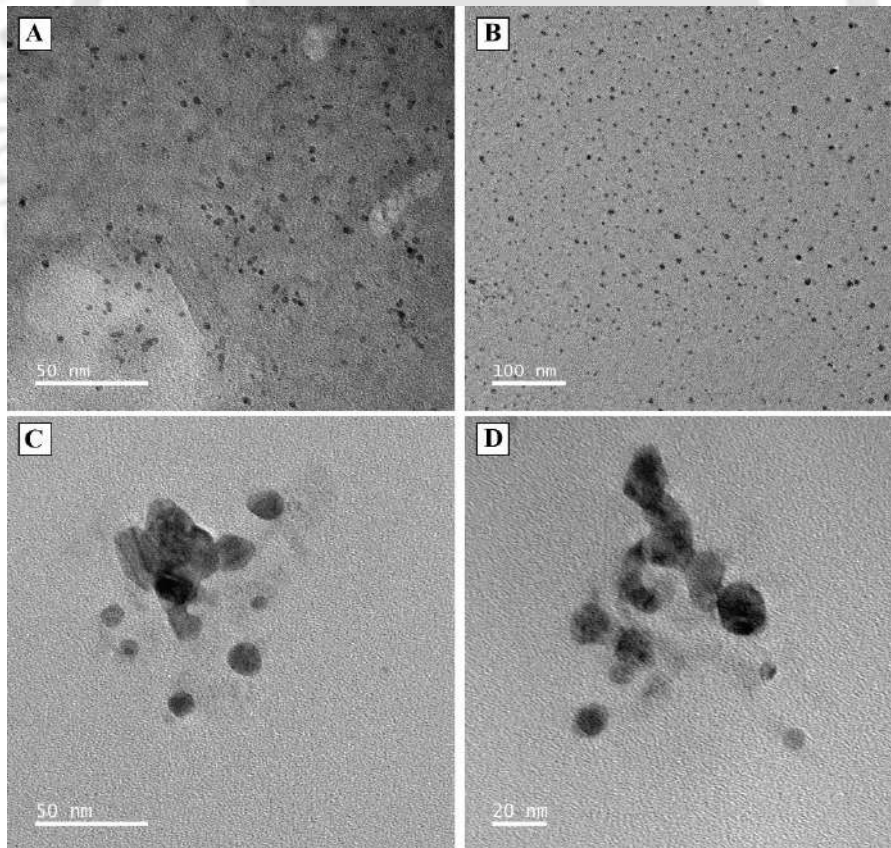


Figure A7a.2: FETEM images of (A) and (B) Ag NPs/Vaterite composite; (C) and (D) bare Ag NPs.

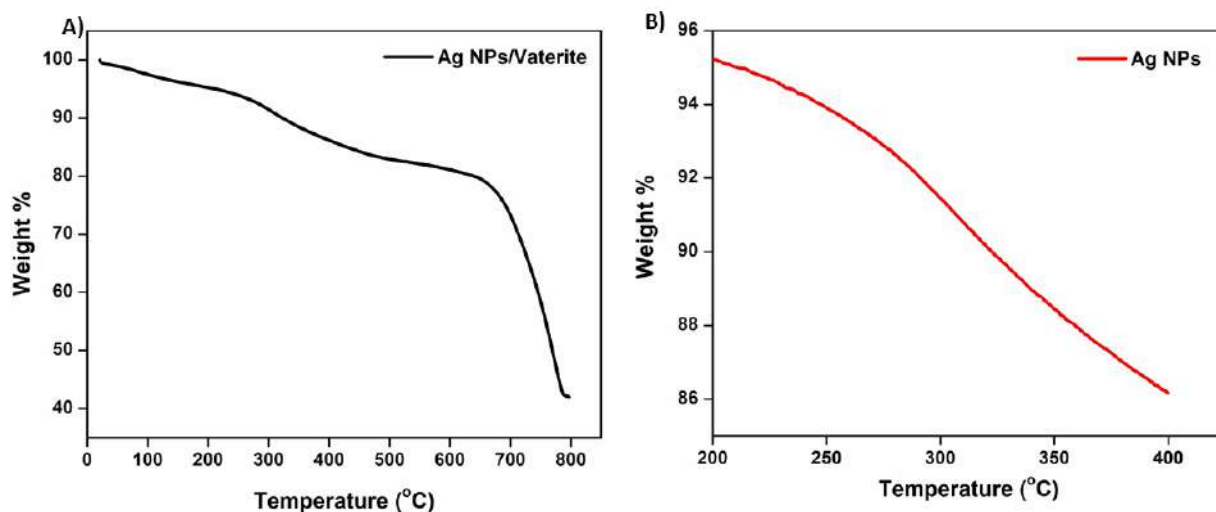


Figure A7a.3: TGA curve (A) Overall profile of Ag NPs/Vaterite composite; (B) Magnification of the region where Ag NPs decompose.

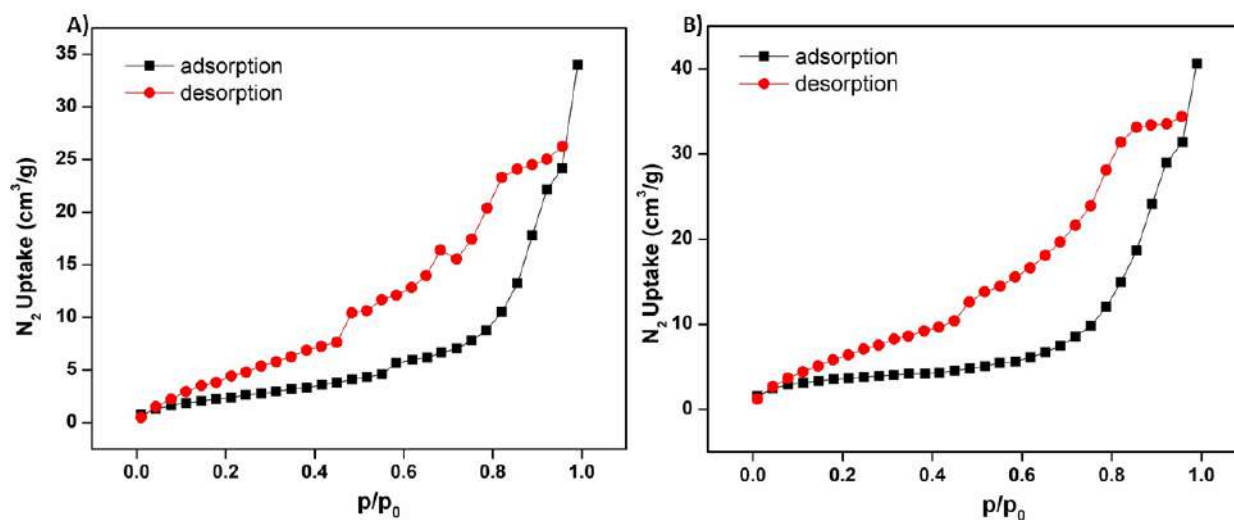


Figure A7a.4: Nitrogen adsorption-desorption BET isotherm (A) Vaterite; (B) AgNPs/Vaterite.

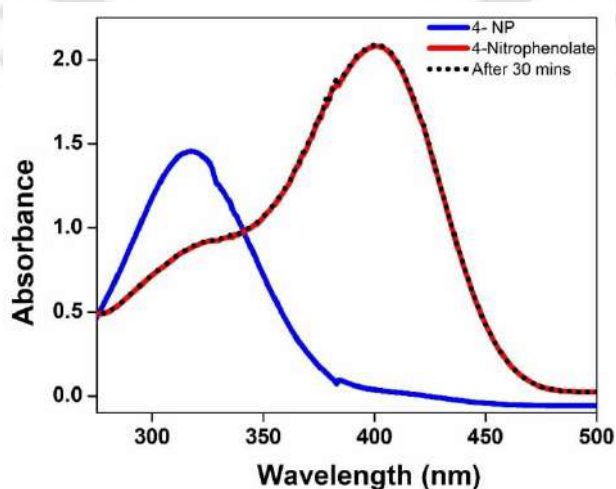


Figure A7a.5: UV/Vis absorption spectra of 4-Nitrophenol and of 4-Nitrophenolate generated by the addition of NaBH_4 .

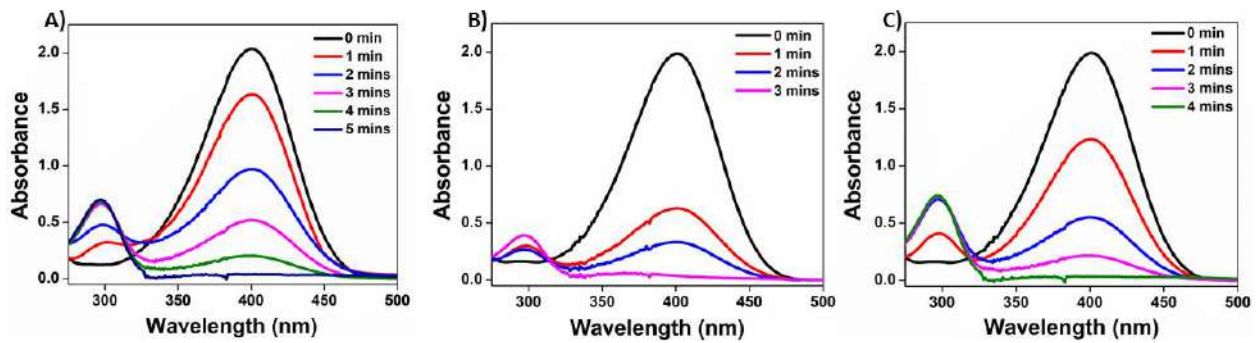


Figure A7a.6: UV/Vis absorption spectra for the catalytic reduction of 4-Nitrophenol in the presence of (A) 0.5 mg catalyst; (B) 1 mg catalyst and (C) 1.5 mg catalyst.

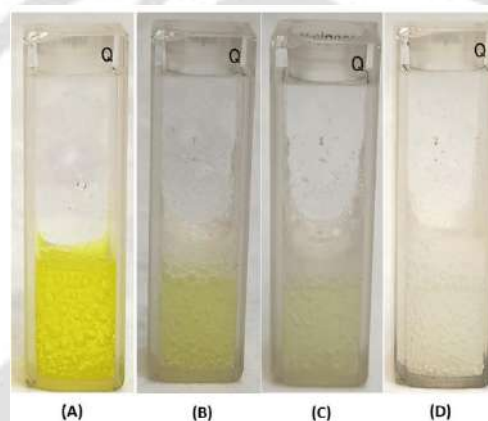


Figure A7a.7: Change in colour indicating the reduction of 4-Nitrophenol to 4-Aminophenol via 4-Nitrophenolate; (A) just before the addition of the AgNPs/Vaterite catalyst, (B) 1 min after the addition of the catalyst, (C) 2 mins after the addition of the catalyst, (D) 3 mins after the addition of the catalyst, a colourless solution indicating the complete reduction of 4-Nitrophenol.

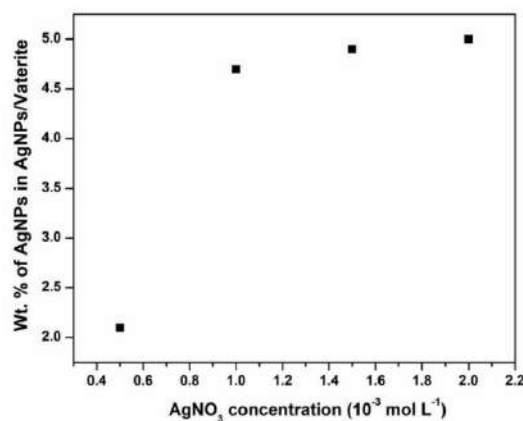


Figure A7a.8: Ag NPs loading on Vaterite microspheres at different AgNO₃ concentration.

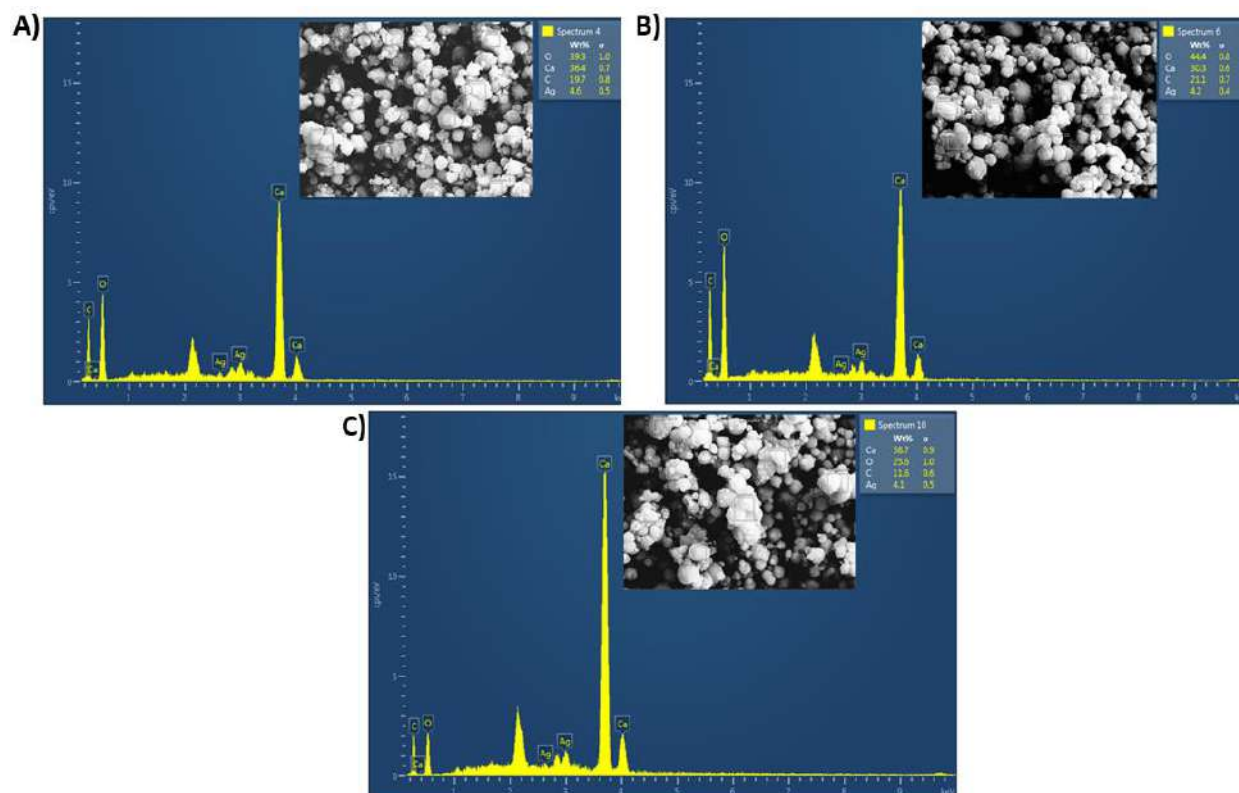


Figure A7a.9: EDX elemental analysis of (A) unreacted Ag NPs/Vaterite catalyst; (B) catalyst after the third cycle and (C) catalyst after the fifth cycle.

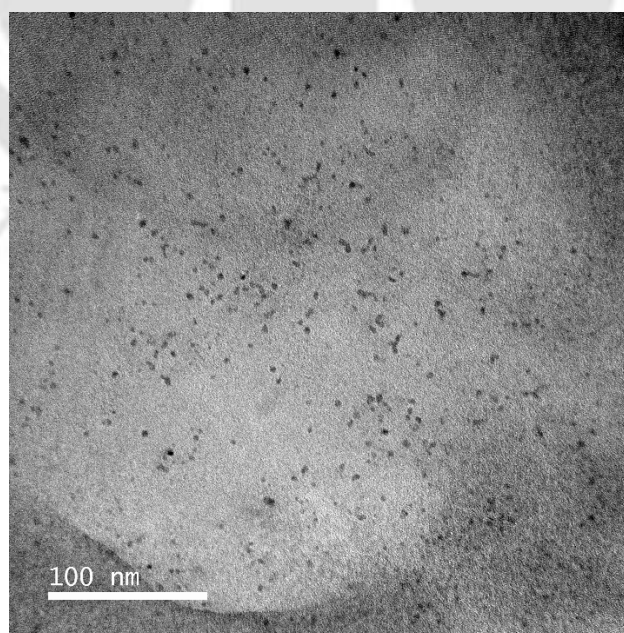


Figure A7a.10: FETEM image of the AgNPs/Vaterite after the fifth catalytic cycle.

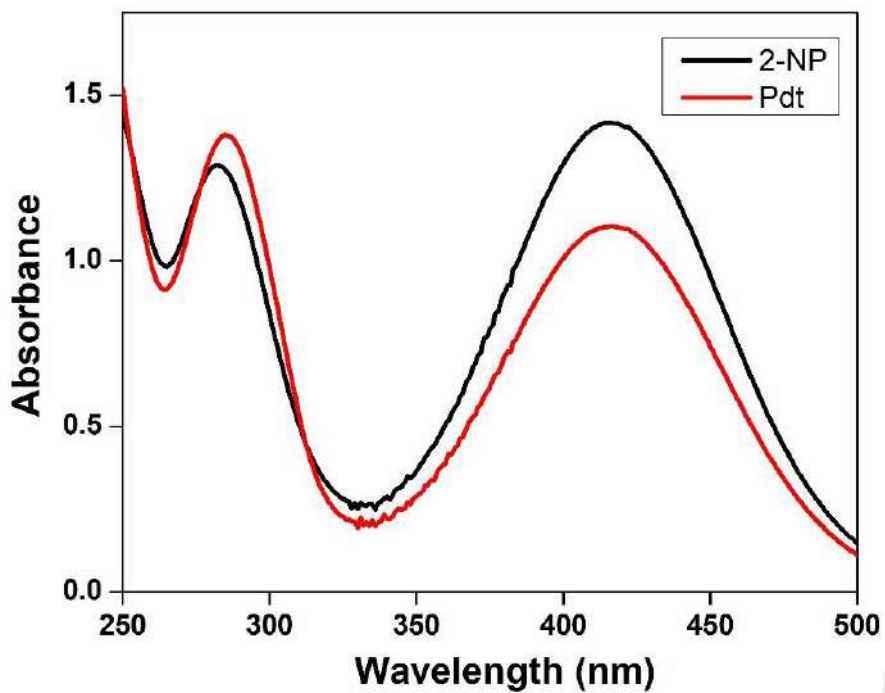


Figure A7a.11: UV/Vis absorption spectra for the catalytic reduction of 2-Nitrophenol in presence of Ag NPs/Vaterite catalyst.

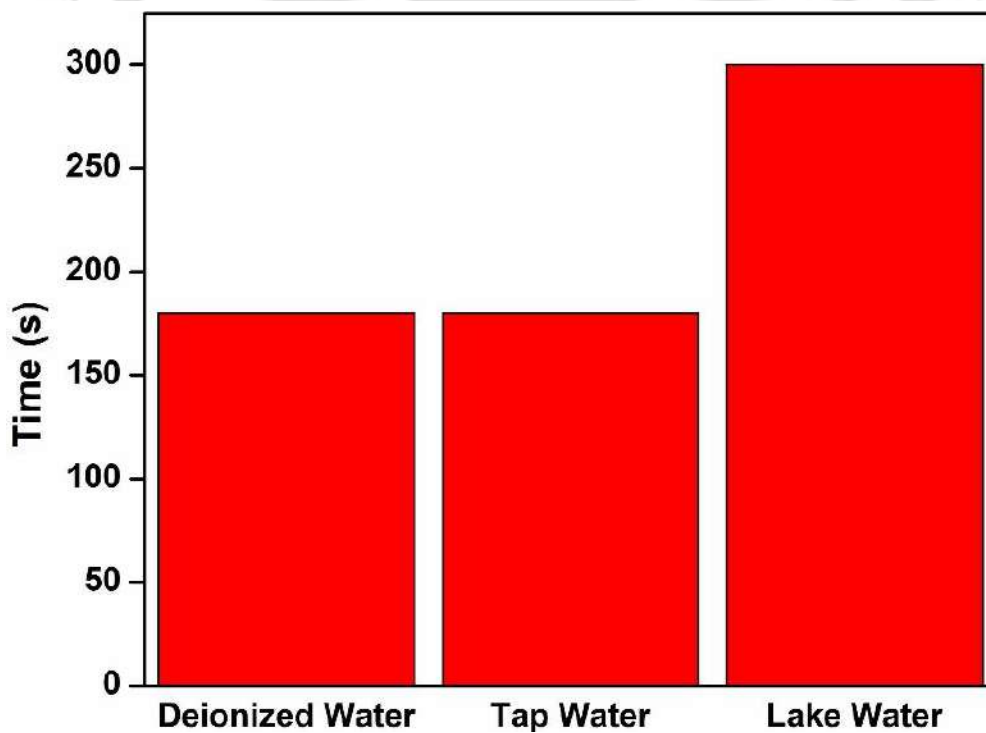


Figure A7a.12: Bar diagram showing the time taken (s) for the complete reduction of 4-NP in the presence of the Ag NPs/Vaterite catalyst when the reaction was performed in water from different sources.

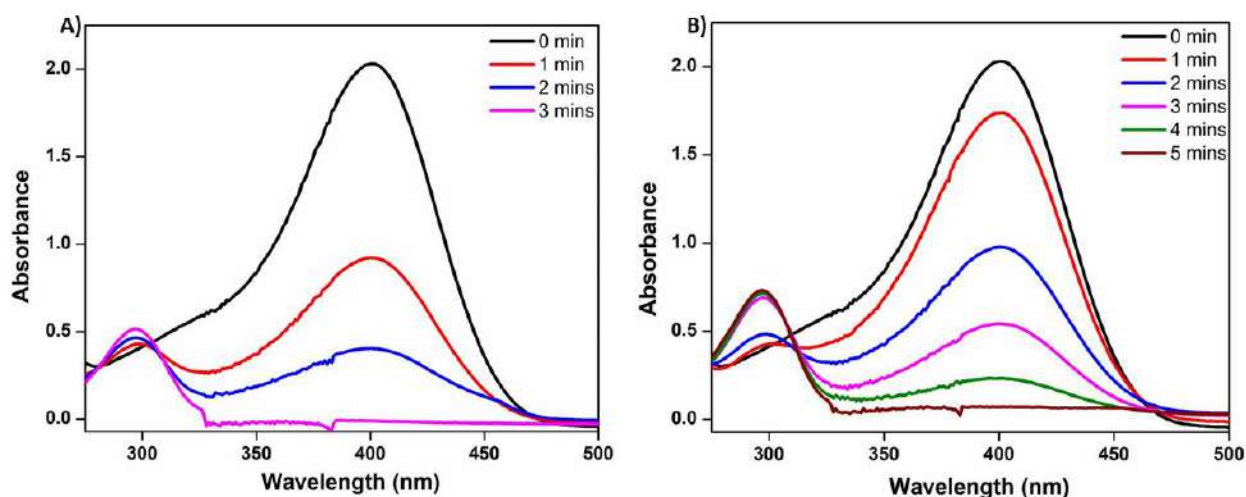


Figure A7a.13: UV/Vis absorption spectra for the catalytic reduction of 4-Nitrophenol in the presence of Ag NPs/Vaterite catalyst (A) in tap water and (B) in lake water.

Table A7a.1. Rate constant (k) of different metal-based catalysts towards 4-Nitrophenol reduction

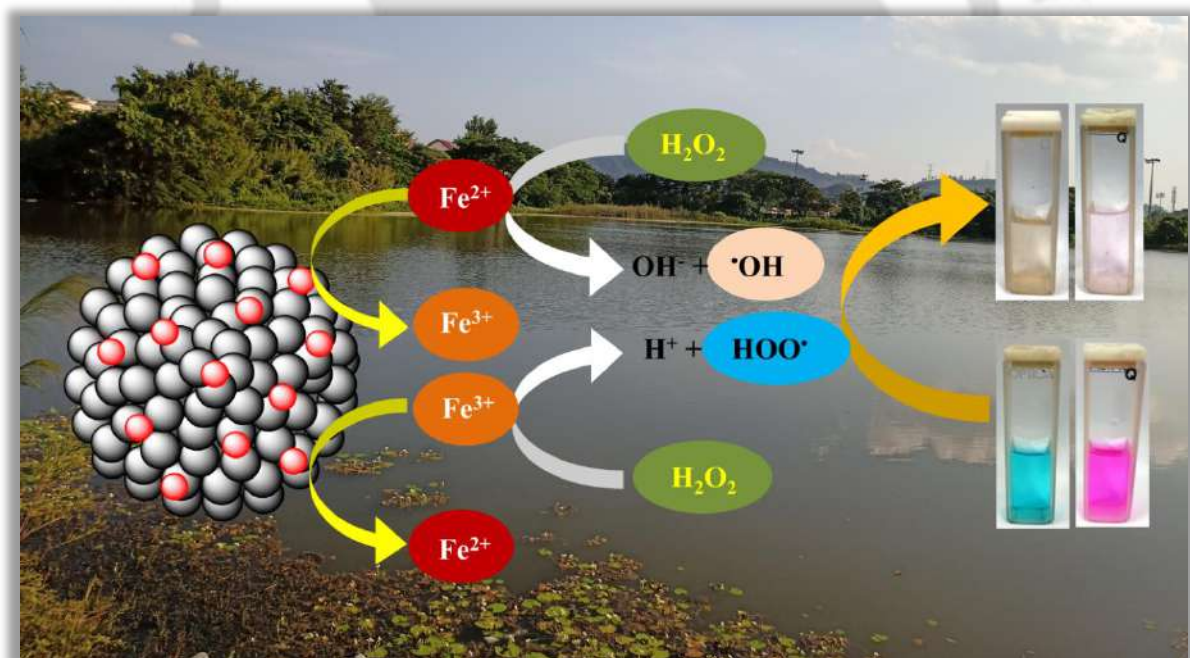
Sl No.	Catalyst	k (10^{-3} s^{-1})	References
1.	Spherical Ag NPs	1.87	Bhui et al. [1]
2.	Ag Nanoshell/Polystyrene	5.2	Jana et al. [2]
3.	Ag NPs/ Carbon nanofibers	6.2	Zhang et al. [3]
4.	Ag NPs/SiO ₂	1.24	Wang et al. [4]
5.	Ag NPs/CaCO ₃	3.1	Dash et al. [5]
6.	Au NPs/CaCO ₃	17.8	Ding et al. [6]
7.	Cu NPs/rGO	17.3	Yeh et al. [7]
8.	Ag NPs/Vaterite	22.0	This work

References

- 1 D.K. Bhui, A. Misra, Synthesis of worm like silver nanoparticles in methyl cellulose polymeric matrix and its catalytic activity, Carbohydr. Polym. 89 (2012) 830– 835.
- 2 S. Jana, S.K. Ghosh, S. Nath, S. Pande, S. Praharaj, S. Panigrahi, S. Basu, T. Endo, T. Pal, Synthesis of silver nanoshell-coated cationic polystyrene beads: A solid phase catalyst for the reduction of 4-nitrophenol, Appl. Catal. A: Gen. 313 (2006) 41–48.

- 3 P. Zhang, C. Shao, Z. Zhang, M. Zhang, J. Mu, Z. Guo, Y. Liu, In situ assembly of well-dispersed Ag nanoparticles (AgNPs) on electrospun carbon nanofibers (CNFs) for catalytic reduction of 4-nitrophenol, *Nanoscale*, 3 (2011) 3357–3363.
- 4 M. Wang, D. Tian, P. Tian, L. Yuan, Synthesis of micron-SiO₂@nano-Ag particles and their catalytic performance in 4-nitrophenol reduction, *Appl. Surf. Sci.* 283 (2013) 389–395.
- 5 S. Dash, S. Das, M.I. Khan, S. Sinha, B. Das, R. Jayabalan, P.K. Parhi, S.K. Tripathy, Sonochemically synthesized Ag/CaCO₃ nanocomposites: A highly efficient reusable catalyst for reduction of 4-nitrophenol, *Mat. Chem. Phys.* 220 (2018) 409–416.
- 6 Q. Ding, Z. Kang, L. Cao, M. Lin, H. Lin, D.P. Yang, Conversion of waste eggshell into difunctional Au/CaCO₃ nanocomposite for 4-Nitrophenol electrochemical detection and catalytic reduction, *Appl. Surf. Sci.* 510 (2020) 145526-145535.
- 7 C.C. Yeh, P.R. Wu, D.H. Chen, Fabrication and near infrared photothermally enhanced catalytic activity of Cu nanoparticles/reduced graphene oxide nanocomposite, *Mater. Lett.* 136 (2014) 274–277.

Vaterite and calcite based magnetite composites: A comparative study on the catalytic performance during spontaneous Fenton-like dye degradation



7b.1 Introduction:

The porous surface texture of the vaterite microspheres has been considered in several studies to introduce functionality to the otherwise inert CaCO_3 particles. In the previous chapter, we had discussed that owing to its surface porosity, the vaterite particles were subjected as an inert solid-support for silver nanoparticles.^{7b.1} The adsorption of CdSe, ZnS, and magnetite nanoparticles on porous vaterite and the subsequent applications of the functionalized materials has been reported.^{7b.2-7b.5} In this work, we present a convenient method where magnetite nanoparticles are embedded on the surface of vaterite microspheres. The resulting Fe_3O_4 /Vaterite particles were used to show enhanced catalytic activity towards the degradation of common environmental pollutant dyes; Methylene Blue (MB) and Rhodamine B (RhB), by a Fenton-like process. The calcite phase of CaCO_3 with a rhombohedral morphology was also used as solid support for the Fe_3O_4 nanoparticles to draw comparisons with the vaterite-supported Fe_3O_4 .

Industries such as textiles, cosmetics, plastics, leather, etc., use toxic organic dyes to impart color to their products. The wastewater discharged from these industries is polluted with toxic contaminants and this has been a major concern due to the potential threat it poses to aquatic life and also to human health.^{7b.6,7b.7} The contaminants pose a high chemical oxygen demand (COD) as they comprise significant concentrations of organic chemicals.^{7b.8} Current techniques involve adsorption,^{7b.9,7b.10} oxidation/reduction, etc., for removal of organic wastes from industrial wastewater, and in recent times, researchers are engaged in improvising and improving the AOPs such as Fenton and Fenton-like processes, photo-Fenton processes, and photocatalytic methods involving metal oxide photocatalysts.^{7b.11-7b.13} These processes involve the in-situ generation of reactive oxygen species (ROS), such as superoxide radical ($\cdot\text{O}_2$), hydroxyl radical ($\cdot\text{OH}$) and hydroperoxyl radical ($\cdot\text{OOH}$), these reactive species enhance the degradation process as a result of which the toxic organic molecules such as dyes are broken down into CO_2 , H_2O and mineral acids.^{7b.14,7b.15}

Among the recent works on the degradation of MB by AOPs, Ivanets et al. utilized magnesium ferrite doped with lanthanide ions as catalysts in the Fenton-like degradation of MB,^{7b.16} Yanushevska et al. performed the photocatalytic degradation of MB by using TiO_2 -based nanoparticles as catalyst.^{7b.17} Now, although the Fenton process catalyzed by Fe_3O_4 nanoparticles for the degradation of toxic organic compounds is already known.^{7b.18,7b.19} But in this study, we have introduced the use of solid supports for the Fe_3O_4 nanoparticles in the form of spherical vaterite and rhombohedral calcite particles to improve the catalytic activity by

reducing the amount of catalyst used in the degradation process as the use of solid support prevents the nanoparticles from agglomerating in the reaction mixture. The use of solid supports to improve the performances of Fe_3O_4 based heterogeneous catalytic reactions has been reported before. But the use of calcite and vaterite as supports and the competitive catalytic activity of the subsequently formed heterogeneous catalyst towards the Fenton-like process have never been reported. This modification would also help reduce the amount of H_2O_2 generally used as it would enhance the efficiency of the catalyst, thus promoting the generation of $\cdot\text{OH}$, which acts as the active species in oxidizing the pollutants.

7b.2 Results and Discussions

7b.2.1 General characterizations of the materials

The PXRD analyses were performed to obtain the diffraction pattern of the materials. The pattern obtained for bare Fe_3O_4 , Fig. 7b.1(A), included peaks at 2θ values equal to 30.56, 35.88, 43.52, 57.50, and 63.07 corresponding to (220), (311), (400), (511) and (440) planes, respectively, these values are identical to the standard PDF data for Fe_3O_4 , ICSD 01-071-6339. The PXRD pattern for $\text{Fe}_3\text{O}_4/\text{Calcite}$, Fig. 7b.1(A), included peaks at 2θ values equal to 29.57, 36.07, 39.52, 43.19, 47.82, and 48.67 were corresponding to (104), (110), (113), (202), (018) and (116) planes, respectively, identical to the standard PDF data for calcite, ICSD 01-071-1663 and the peaks at 30.29, 35.68, 43.52, 57.44 and 62.90 corresponding to (220), (311), (400), (511) and (440) planes, respectively and these values are identical to the standard PDF data for Fe_3O_4 , ICSD 01-071-6339.

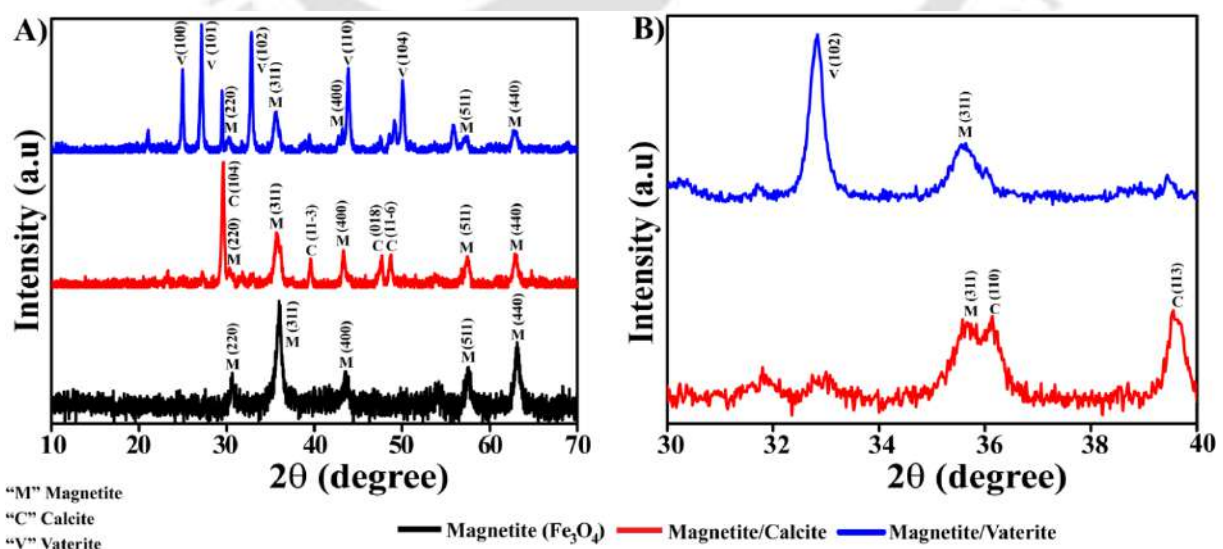


Figure 7b.1: XRD patterns of Magnetite, Magnetite/Calcite, and Magnetite/Vaterite: (A) overall profiles; (B) magnification of Magnetite/Calcite and Magnetite/Vaterite peaks.

The PXRD pattern was further magnified from 2θ value 30-40, Fig. 7b.1(B), where we could see the peak at 35.70 for Fe_3O_4 (311) and the peaks at 36.14 and 39.53 due to calcite (110) and (113). The PXRD pattern for $\text{Fe}_3\text{O}_4/\text{Vaterite}$, Fig. 7b.1(A), included peaks at 2θ values equal to 24.88, 27.11, 32.79, 43.89, and 49.95 corresponding to (100), (101), (102), (110), and (104) planes, respectively, confirmed the vaterite phase from the standard PDF data, ICSD 01-072-0506 and the peaks at 30.13, 35.50, 43.15, 57.29 and 62.80 corresponding to (220), (311), (400), (511) and (440) planes, respectively and these values are identical to Fe_3O_4 , ICSD 01-071-6339. Further, on magnifying the pattern from 2θ value 30-40, Fig. 7b.1(B), we could observe a peak at 32.83 for vaterite (102) and a peak at 35.57 for Fe_3O_4 (311).

The bare Fe_3O_4 appeared as tiny spherical nanoparticles, as seen from the FESEM image, Fig. 7b.2(C). The bare calcite particles exist as rhombohedral crystals, as seen from Fig. 7b.2(A), and the embedded Fe_3O_4 nanoparticles on the calcite crystal can be seen in Fig. 7b.2(B), where the loaded Fe_3O_4 have further been magnified. The FESEM image of bare vaterite showed the spherical morphology of the particle, Fig. 7b.2(D), and the uniform loading of the Fe_3O_4 nanoparticles around the spherical vaterite is shown in Fig. 7b.2(E), here also, the loaded nanoparticles have been magnified.

From the FETEM images, Fig. 7b.3(A) and (C), it can be seen how the Fe_3O_4 nanoparticles are embedded on the surface of calcite and vaterite, respectively. The HRTEM images of both the loaded materials further support the fabrication of the Fe_3O_4 nanoparticles on the surfaces of calcite and vaterite, respectively; Fig. 7b.3(B) and (D). The correlation between the fringe spacings in the HRTEM images and the inter-planar spacings of the diffraction planes of the materials was studied. For $\text{Fe}_3\text{O}_4/\text{Calcite}$, the measured fringe spacing values of 0.25 nm and 0.20 nm, Fig. 7b.3(B), correspond to the inter-planar spacing of (311) plane of Fe_3O_4 and (202) of calcite respectively and similarly for $\text{Fe}_3\text{O}_4/\text{Vaterite}$, the measured fringe spacing values of 0.25 nm and 0.33 nm correspond to the inter-planar spacing of (311) plane of Fe_3O_4 and (101) of vaterite, respectively, Fig. 7b.3(D). These findings and the subsequent matches with the inter-planar spacing give us comprehensive information on the loading of Fe_3O_4 on the solid supports.

XPS spectra of Fe 2p and O 1s were obtained for bare Fe_3O_4 and $\text{Fe}_3\text{O}_4/\text{Vaterite}$. In the spectrum for Fe 2p of bare Fe_3O_4 , Fig. 7b.4(A), six different peaks were obtained at 710.17 eV, 712.12 eV, 718.00 eV, 723.76 eV, 726.02 eV and 731.95 eV. The peak at 710.17 eV and 712.12 eV corresponds to the characteristic peak of Fe $2p_{3/2}$ core level electrons attributed to the Fe^{3+} and Fe^{2+} . For the other spin-orbit component, Fe $2p_{1/2}$, the peaks for Fe^{3+} and Fe^{2+} occurred at 723.76 eV and 726.02 eV, respectively.^{7b.20}

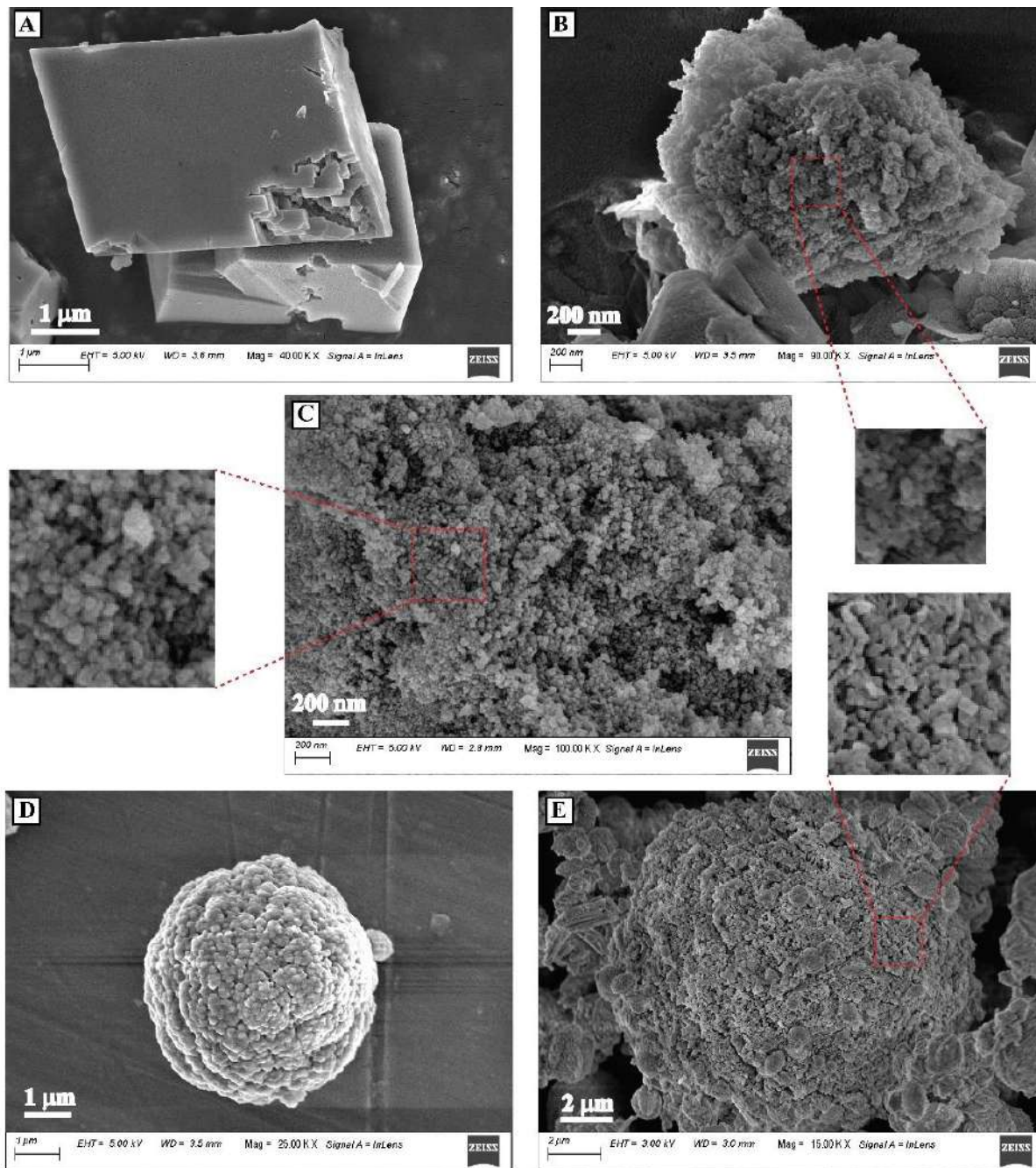


Figure 7b.2: FESEM images of (A) Calcite crystals; (B) Magnetite nanoparticles embedded on Calcite surface (Magnetite/Calcite); (C) Bare Magnetite nanoparticles; (D) Vaterite microsphere; (E) Magnetite nanoparticles embedded on Vaterite surface (Magnetite/ Vaterite).

The two peaks at 718.00 eV and 731.95 eV are the Fe^{2+} shake satellite peaks.^{7b.21} In the XPS spectra of Fe 2p of $\text{Fe}_3\text{O}_4/\text{Vaterite}$, Fig. 7b.4(B), also six different peaks were obtained. However, the binding energy values of all these peaks were slightly higher than those obtained for bare Fe_3O_4 . This may be attributed to the probable interactions between the Fe_3O_4 nanoparticles and the solid support vaterite. In this case, $\text{Fe}_3\text{O}_4/\text{Vaterite}$, the peak at 710.65 eV and 713.16 eV corresponds to the Fe 2p_{3/2} core level electrons attributed to the Fe^{3+} and Fe^{2+} ; an

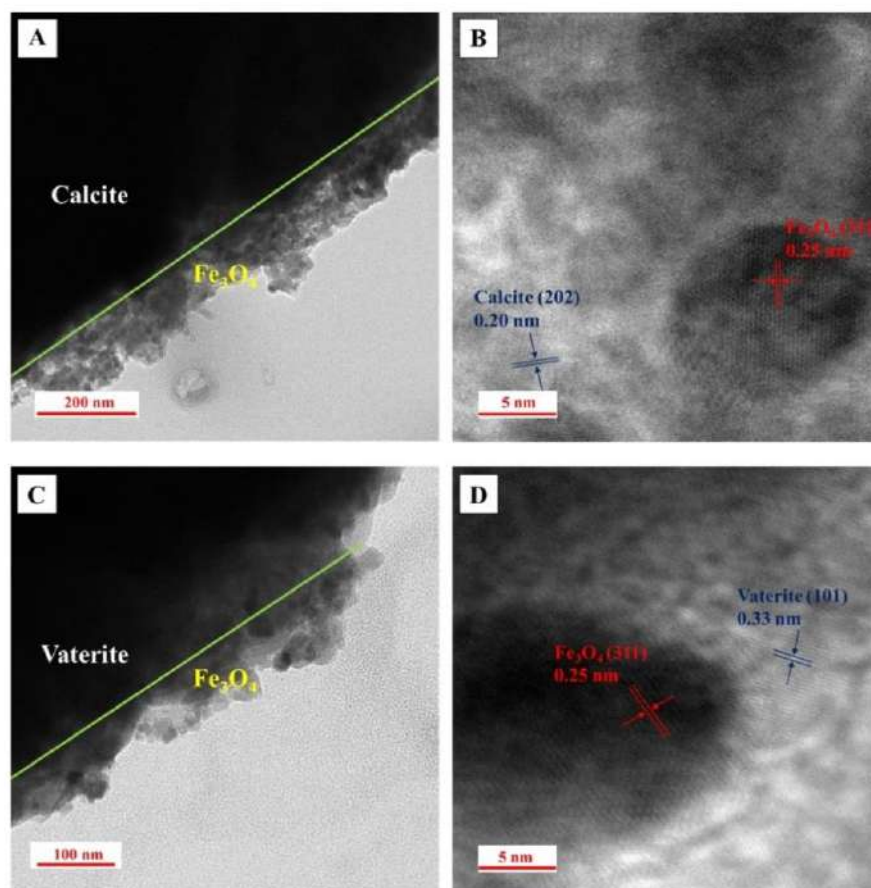


Figure 7b.3: (A) FETEM image of Magnetite nanoparticles embedded on Calcite surface (Magnetite/Calcite); (B) HRTEM image of Magnetite/Calcite; (C) FETEM image of Magnetite nanoparticles embedded on Vaterite surface (Magnetite/ Vaterite); (D) HRTEM image of Magnetite/ Vaterite.

increase of 0.48 eV and 1.04 eV, respectively, was observed. Again, two peaks for the other spin-orbit component, Fe 2p_{1/2} of Fe³⁺ and Fe²⁺, were observed at 724.03 eV and 726.61 eV (with an increase of 0.27 eV and 0.59 eV, respectively). Also, the Fe²⁺ satellite peaks were observed at 718.35 eV and 732.53 eV, greater than their bare Fe₃O₄ counterpart by 0.35 eV and 0.58 eV, respectively. Three peaks were obtained in the XPS spectra of O 1s for bare Fe₃O₄, Fig. 7b.4(C). The peak at 529.47 eV corresponds to Fe-O, the peak at 530.36 eV is contributed by the C-O and the peak at 531.88 eV may be attributed to the surface adsorbed oxygen.^{7b.20,7b.22} Similarly to the case of Fe 2p, the peak positions of O 1s have shifted slightly for Fe₃O₄/Vaterite, Fig. 7b.4(D), towards the higher side as a result of probable interactions between the bare nanoparticles and the solid support. The peak for Fe-O occurred at 530.29 eV with a shift of 0.78 eV, the peak for O 1s of C-O occurred at 530.97 eV with a shift of 0.61 eV, and the peak for the surface adsorbed oxygen appears at 532.49 eV with a shift of 0.61 eV. Additionally, for Fe₃O₄/Vaterite, we have one more peak at 531.70 eV, which is attributed to the oxygen in vaterite. Hence, from the XPS spectra of Fe 2p and O 1s, the presence of both the oxidation

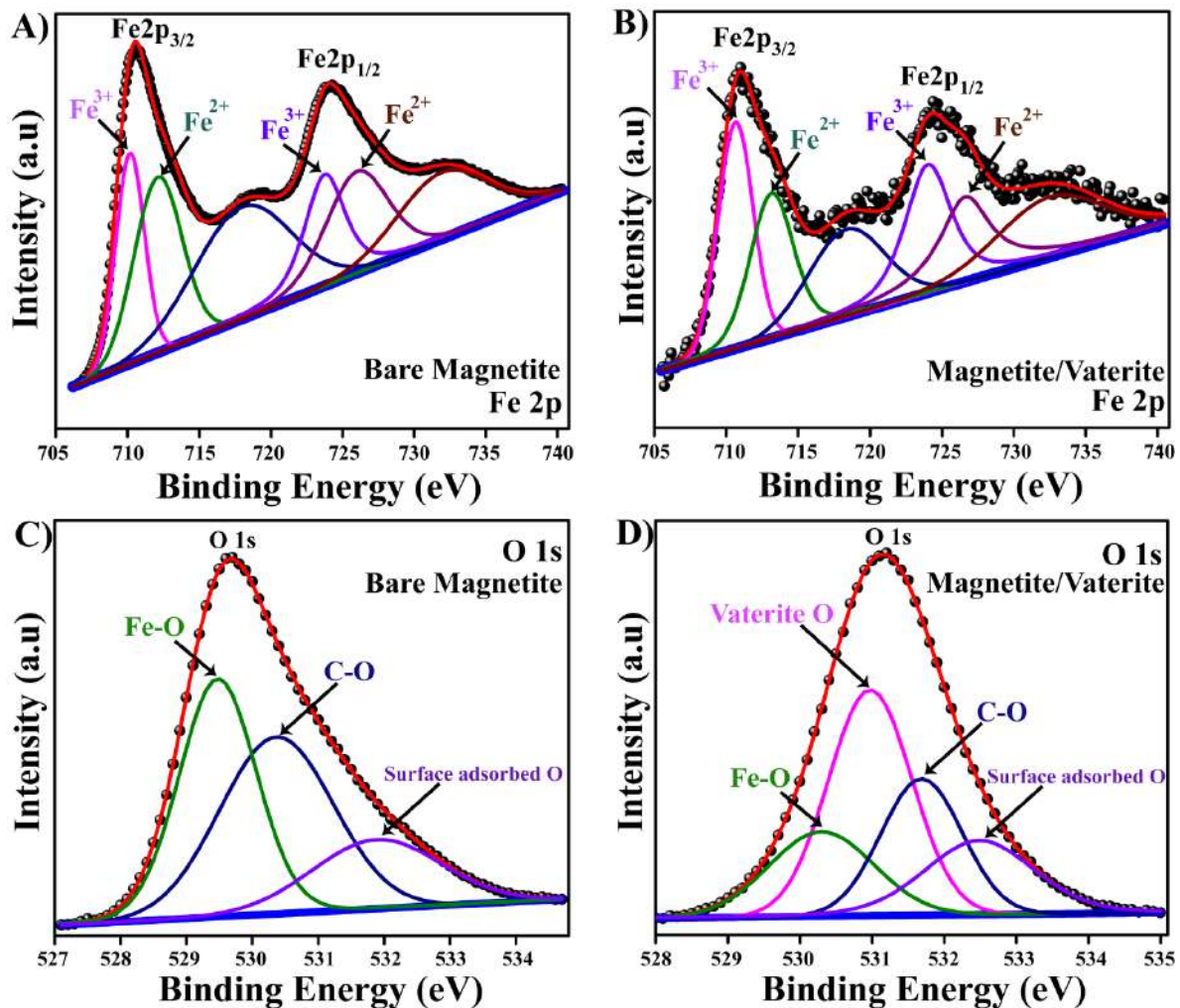


Figure 7b.4: XPS analysis. Fe 2p spectra of (A) Bare Magnetite; (B) Magnetite/Vaterite. O 1s spectra of (C) Bare Magnetite; (D) Magnetite/Vaterite.

states, +2 and +3 of Fe in the bare nanoparticles as well as in the loaded one and the presence of the O bonded to Fe in both the cases and the vaterite O in Fe₃O₄/Vaterite was evident. The XPS spectrum survey of both the materials indicating the presence of the corresponding element has been presented in Fig. A7b.1(A) and (B).

The specific surface area of Fe₃O₄/Calcite was found out to be 9.531 m²/g and that of Fe₃O₄/Vaterite was obtained as 13.284 m²/g, Fig. A7b.2(A) and (B). It is an important property in determining the ability of a material to perform applications involving the binding of substrate molecules on the material (catalyst) surface to initiate the possible transformation.^{7b.23} The rate of transformation of the substrates is directly proportional to the surface area of the catalyst.

On obtaining the zeta potential of the catalysts, Fe₃O₄/Calcite and Fe₃O₄/Vaterite and comparing them with bare Fe₃O₄, calcite, and vaterite, a change was observed. A positive value of zeta potential was observed for Fe₃O₄, 21.842 mV, Fig. A7b.3(A), whereas for the CaCO₃ phases,

negative values of -17.217 mV and -22.173 mV were observed for the calcite and vaterite phases, respectively, Fig. A7b.3(B) and (C). However, these negative values had come down on subsequent loading of the Fe_3O_4 nanoparticles, where a value of -14.662 mV and -19.354 mV was observed for $\text{Fe}_3\text{O}_4/\text{Calcite}$ and $\text{Fe}_3\text{O}_4/\text{Vaterite}$, respectively, Fig. A7b.3(D) and (E).

The materials were further analyzed by TG/DTG analysis; for bare Fe_3O_4 , a mass loss of 7% due to the nanoparticle stabilizer sodium lauryl sulphate was seen in the temperature range of 150-600 °C and accordingly, in the DTG curve, peaks at 120 °C and 330 °C due to loss of water/moisture and decarboxylation of the organic molecule was observed, Fig. A7b.4(A). For $\text{Fe}_3\text{O}_4/\text{Calcite}$, mainly two different mass losses, firstly, in the temperature range of 150-600 °C where a 6% loss due to the Fe_3O_4 nanoparticle stabilizer and the second mass loss of 39% due to the loss of CO_2 (decarbonization) from CaCO_3 were observed, Fig. A7b.4(B). In the DTG curve, Fig. A7b.4(B), peaks at 120 °C, 330 °C, and 730 °C corresponding to the dehydration, decarboxylation, and decarbonization processes, respectively was observed. However, for $\text{Fe}_3\text{O}_4/\text{Vaterite}$, a higher percentage of mass loss, 12%, was observed in the temperature range of 150-600 °C, Fig. A7b.4(C). Here, in addition to the loss of the nanoparticle stabilizer, the loss of organic groups from the template whey protein used in the mineralization of vaterite also occurred. Similar to the calcite phase, here, a loss of 35% mass in the range of 600-750 °C due to loss of CO_2 (decarbonization) from CaCO_3 used in the form of the vaterite phase was observed. Accordingly, in the DTG curve, Fig. A7b.4(C), peaks at 110 °C, 330 °C, and 720 °C corresponding to the dehydration, decarboxylation, and decarbonization processes, respectively was observed.

Both the loaded materials were then subjected to EDX elemental analysis and mapping. It was observed that in the calcite supported catalyst, Fig. A7b.5(F), in addition to the elements of CaCO_3 , Fe was present in weight percentage of ~7%, and in the vaterite supported catalyst, Fig. A7b.6(F), the percentage of Fe was ~9%. From the elemental mapping images, Fig. A7b.5(A), (B), (C), (D), (E) and Fig. A7b.6(A), (B), (C), (D), (E), we can very clearly see that the element Fe is evenly distributed across the solid support which is an indication of the distribution of the catalyst Fe_3O_4 on the calcite and vaterite surfaces. This even distribution explains how using solid support would prevent the agglomeration of the nanoparticles, which is very common in its bare form and contributes to the underperformance of the bare nanoparticles when subjected as catalysts.

7b.2.2 Dye degradation studies

The synthesized materials, bare Fe_3O_4 , $\text{Fe}_3\text{O}_4/\text{Calcite}$, and $\text{Fe}_3\text{O}_4/\text{Vaterite}$ were employed as catalysts to degrade the toxic organic dye MB in the presence of H_2O_2 by utilizing the generated $\cdot\text{OH}$ via the Fenton-like process. The dye degradation processes were performed by maintaining a fixed concentration of the dye (unless stated otherwise) and changing the other parameters. As already mentioned, the reaction catalyzed by $\text{Fe}_3\text{O}_4/\text{Vaterite}$ was used as the standard to optimize the reaction conditions. Initially, three different materials varying the ratios of the amount of Fe_3O_4 nanoparticles to vaterite as 0.5:10, 1:10, and 2:10 were synthesized and on performing the Fenton-like process of degradation of MB, the percentage of degradation obtained from the UV-vis spectroscopy study (absorption maxima, $\lambda_{\text{max}} = 663$) was 69%, 96%, and 89%, respectively, Fig. A7b.7(A), (B), and (C). It was observed that the solid-supported catalytic material synthesized in the ratio 1:10 showed the best result in terms of the degradation percentage. The lower percentage for 2:10 may be attributed to a certain degree of aggregation of the nanoparticles on increasing their concentration despite the presence of the solid-support vaterite. Hence, the catalysts prepared and subjected to the dye degradation studies were all in the ratio 1:10 ($\text{Fe}_3\text{O}_4/\text{support}$). To fix the amount of catalyst to be added for maximum degradation, the amount was varied as 10 mg, 20 mg, 30 mg, 40 mg, 50 mg, and 60 mg and the concentration of hydrogen peroxide was varied between 3-6 mM as shown in Fig. A7b.8(A) and (B), respectively. After performing the different sets of experiments, we considered that 50 mg of catalyst (1:10) and 5 mM of H_2O_2 was the optimum combination to perform the degradation as there was no significant enhancement in the reaction rate on further addition of the catalyst or H_2O_2 . For those reactions where bare Fe_3O_4 was subjected as the catalyst, the amount used was 4.5 mg, as in the other reactions involving the calcite and the vaterite supported nanoparticles, the ratio of Fe_3O_4 to calcite/vaterite was 1:10 and each 50 mg of it would contain 4.5 mg of Fe_3O_4 nanoparticles. The adsorption capacity of the catalysts and the solid support components, vaterite and calcite was determined by performing a series of experiments where 50 mg of a component was added to the dye solution (without the subsequent addition of H_2O_2) and allowed to interact under stirring condition for 2 hours. It was observed that the highest adsorption capacity was exhibited by bare vaterite particles where 24% of the dye was adsorbed whereas, the Fe_3O_4 nanoparticles showed the lowest adsorption capacity of merely 10%, Fig. A7b.9(A), (B), (C), (D) and (E). This difference may be attributed to the complementary relationship between the cationic nature of MB and the zeta potential values of the materials. The vaterite particles with the highest negative zeta potential exhibited greater affinity for the cationic dye molecules, as the magnitude of the negative zeta potential decreased, their adsorption capacity also declined and the lowest adsorption was observed for the bare Fe_3O_4 nanoparticles whose

zeta potential is positive. **Table A7b.1** represents the percentage of dye adsorbed on the materials along with their corresponding zeta potential values.

The Fenton-like degradation of MB was studied by UV-vis absorption spectroscopy (Fig. 7b.5A-C), where the decrease in intensity of the absorption maxima, λ_{\max} (663 nm) was observed. With Fe₃O₄/Vaterite as the catalyst, almost complete degradation (~96%) of the dye was attained in 2 hours (120 mins), whereas with the other two catalysts, bare Fe₃O₄ and Fe₃O₄/Calcite, a degradation of ~60% and ~81% was observed. To determine reaction kinetics in all three cases, $\ln(C_t/C_0)$ was plotted against time at λ_{\max} (663 nm) value for MB. The linear slope is seen in Fig. 7b.5(D), for the three different catalysts, indicating that the degradation processes follow first-order kinetics. The highest value of the rate constant (k) was observed for the reaction catalyzed by Fe₃O₄/Vaterite as $3.15 \times 10^{-2} \text{ min}^{-1}$, followed by Fe₃O₄/Calcite as $1.46 \times 10^{-2} \text{ min}^{-1}$, while bare Fe₃O₄ showed the minimum value of k as $7.77 \times 10^{-3} \text{ min}^{-1}$. The reaction kinetics and dye-degradation percentages were calculated using equations **7b.1** and **7b.2**, respectively.

Measurement of Reaction Kinetics

The following equation is used to evaluate the rate and the rate constant of the reaction;

$$\ln\left(\frac{C_t}{C_0}\right) = -kt \quad (7b.1)$$

where, C_0 is the initial concentration (mgL^{-1}) of the dye at the respective λ_{\max} value before the reaction starts, C_t is the concentration (mgL^{-1}) of the dye at 't' interval of time (min), k is the rate constant (min^{-1}). The linear relationship between $\ln\left(\frac{C_t}{C_0}\right)$ vs. t is evidence for the first-order reaction.

Calculation of dye-degradation percentage

The degradation percentage was determined by considering the absorbance, A_0 of the initial dye solution before the Fenton-like degradation to be 1 (absolute). The absorbance value of the degraded solution, A_t (at the end of time "t") was then subtracted from 1 to determine the extent of degradation.

To general equation to determine the percentage of degradation of the dye may be represented as

$$\text{Degradation \%} = \left(\frac{A_0 - A_t}{A_0}\right) \times 100 = \left(\frac{C_0 - C_t}{C_0}\right) \times 100 \quad (7b.2)$$

where, C_0 and C_t have their usual meaning as above.

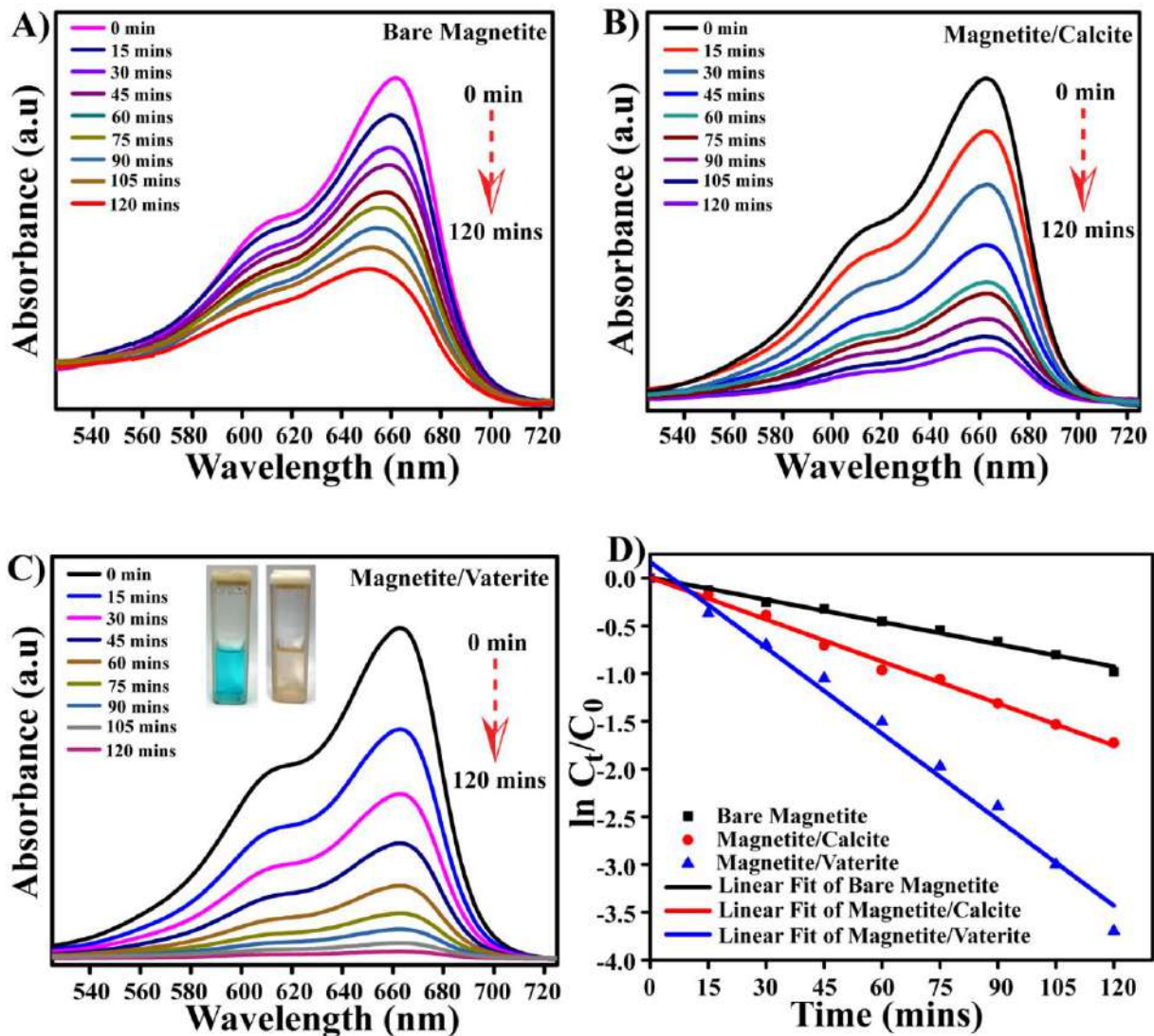


Figure 7b.5: UV-Vis spectra for the degradation of Methylene Blue catalyzed by (A) Bare Magnetite; (B) Magnetite/Calcite; (C) Magnetite/Vaterite; (D) Rate constant plots for the degradation of Methylene Blue in the presence of different catalysts.

The catalytic activity of $\text{Fe}_3\text{O}_4/\text{Vaterite}$ was studied by performing the degradation of MB at different pH conditions. Since the solid support CaCO_3 is unstable at low pH (acidic) conditions, hence in our study we performed the experiments starting from pH 5 and extending up to pH 9, Fig. A7b.10(A), (B), (C), (D) and (E). It was observed that at pH below the neutral level, the extent of degradation of MB had gone down, more so at pH 5 where the percentage of degradation was 84%, and at pH 6, the degradation, 92%, was almost similar to the one at neutral pH. The decline in percentage at pH 5 is possibly due to the instability of the solid support under acidic pH conditions, however, the decrease was not very significant and the result obtained was quite good. On increasing the pH above the neutral level, the results obtained was similar to the one obtained at the neutral condition. At pH 8, the degradation was 96% and at pH 9 it was 97%. Therefore, it can be inferred that the catalyst could facilitate the

Fenton-like degradation of MB at variable pH conditions. In another set of experiments, the concentration of the dye was varied in order to study the effect of the catalyst at different dye concentrations. As for all the experiments thus far, the concentration of MB taken was 1×10^{-5} M. In this set, the concentration was initially reduced to half, 0.5×10^{-5} M and then increased to 2×10^{-5} M and 3×10^{-5} M and the degradation was observed. For 0.5×10^{-5} M, it was observed that within 1 hour, more than 90% of degradation had taken place and for 2×10^{-5} M and 3×10^{-5} M the degradation percentage after two hours of treatment was 52% and 34%, respectively. From the extent of degradation observed it could be understood that the catalyst was suitable to perform its activity even at higher concentrations of the dye, however, a longer duration must be allotted for complete mineralization. The stability of the catalyst to perform for a longer period of time was proved in the subsequent section where we thoroughly studied the reusability of the catalyst.

To illustrate the versatility of the magnetite-based materials as catalysts in the Fenton-like process of degradation of dyes was further extended to another very commonly used industrial dye RhB. On performing the degradation process by maintaining similar conditions w.r.t the dye concentration (10^{-5} M) (50 ml), the catalyst amount (50 mg), and the concentration of H_2O_2 (5 mM), it was observed that here too, the vaterite supported catalyst (Fe_3O_4 /Vaterite) showed enhanced performance in terms of the extent of degradation. In 2 hours, ~86% of the dye had degraded, whereas with bare Fe_3O_4 and Fe_3O_4 /Calcite, a degradation of ~58% and ~73% was seen, Fig. 7b.6(A), (B), and (C). For this set of reactions, too, the reaction kinetics was determined by plotting $\ln(C_t/C_0)$ against time at λ_{max} (554 nm) value for RhB, Fig. 7b.6(D). The value of rate constants observed for the different reactions catalyzed by Fe_3O_4 /Vaterite, Fe_3O_4 /Calcite, and bare Fe_3O_4 were $1.82 \times 10^{-2} \text{ min}^{-1}$, $1.17 \times 10^{-2} \text{ min}^{-1}$, and $7.52 \times 10^{-3} \text{ min}^{-1}$, respectively. A comparison of the rate constants attained in the present work has been made with already reported results of dye degradation reactions catalysed by Fe_3O_4 based catalysts and presented in **Table A7b.2**.

The extent of decolorization obtained from the UV-Vis absorption study is not concrete to support the removal of dye from water. Therefore, to justify our findings obtained from the UV-Vis absorption study, chemical oxygen demand (COD) of the degradation of MB dye was determined. For the untreated dye solution, the COD value was obtained as 228 ppm, while the degraded solution after treatment showed a COD value of 18 ppm. Hence, the degradation of MB was accompanied by a ~92% decrease in the COD value. This value corresponds to the

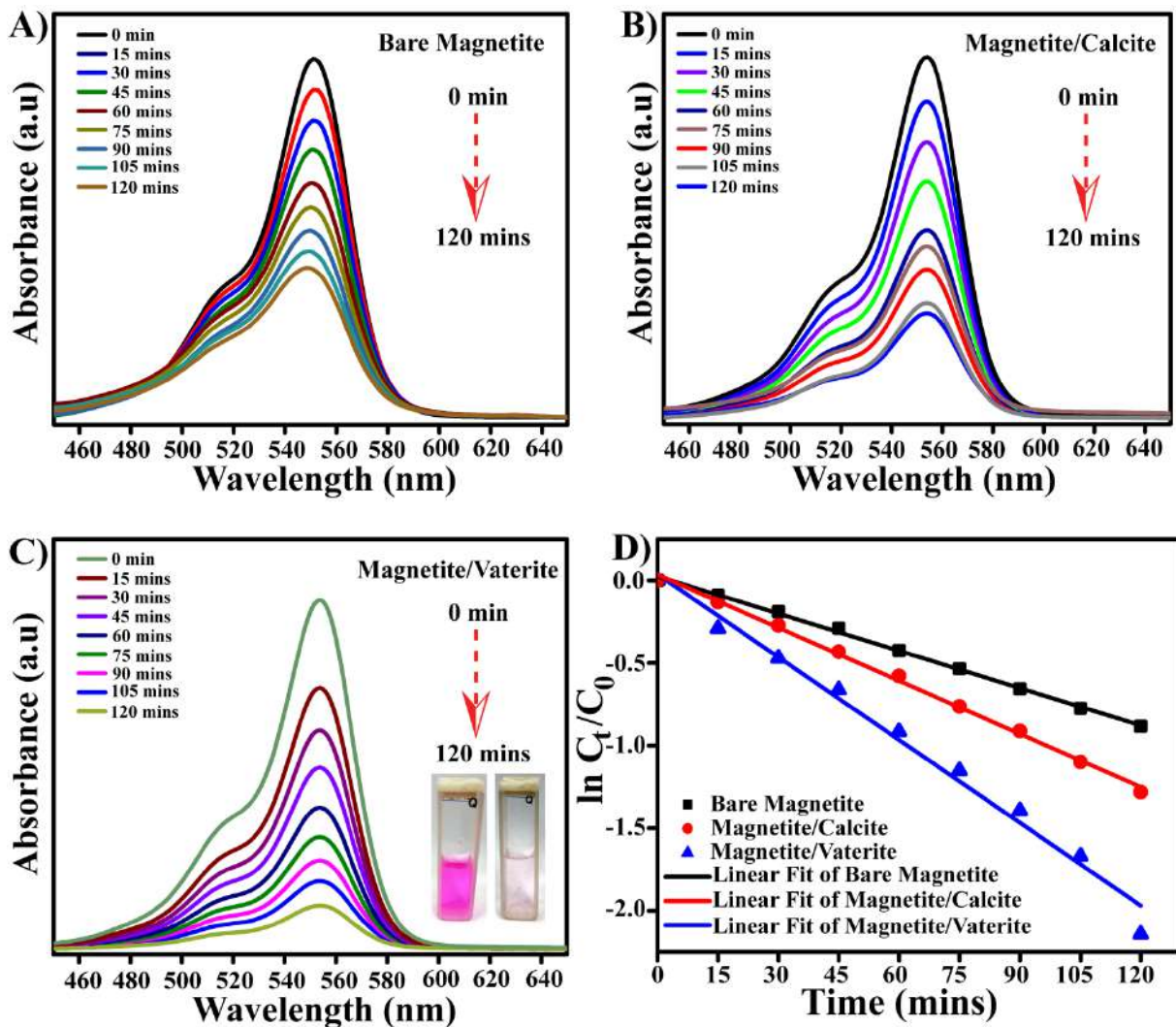


Figure 7b.6: UV-Vis spectra for the degradation of Rhodamine B catalyzed by (A) Bare Magnetite; (B) Magnetite/Calcite; (C) Magnetite/Vaterite; (D) Rate constant plots for the degradation of Methylene Blue in the presence of different catalysts.

toxicity level of the initial MB dye solution before the catalytic treatment and also the approximate percentage of mineralization after 2 hours. The TOC content of the pre-treated solution was 82 ppm while the post-treatment TOC content was found out to be 8 ppm. Thus, value obtained from the UV-Vis absorption study, 96%. Hence, it confirms the removal of the toxic organic dye from water. Additionally, the TOC measurements gave us an idea of the from the TOC measurements, it was proved that ~90% of the dye was mineralized in the Fenton-like degradation process catalyzed by $\text{Fe}_3\text{O}_4/\text{Vaterite}$.

7b.2.3 Resuability of the catalyst

Another important aspect that a catalyst needs to fulfil to be extended for large-scale and commercial applications, such as in industrial wastewater treatment, is the recyclability and reusability of the catalyst. One of the highlights of the Fe_3O_4 based heterogeneous catalyst for

the Fenton-like process was its magnetic nature which was determined from the VSM analysis. The magnetic properties of bare Fe_3O_4 , as well as the solid-supported materials, were obtained. The magnetization saturation (M_s) of the materials was found to be 24.170 emu/g, 1.7876 emu/g, and 2.1679 emu/g, respectively, Fig. A7b.11(A), (B), and (C). The small value of M_s for the supported materials is because these materials possess a small amount of the magnetic Fe_3O_4 , whereas the solid support calcite and vaterite are present in bulk. These materials subjected to VSM analysis were in the ratio 1:10 (Fe_3O_4 /support). Therefore, the M_s of the bare Fe_3O_4 is almost ten times that of the supported materials. Owing to the magnetic nature of the catalyst, its recovery at the end of a catalytic cycle becomes very convenient and ensures complete recovery without any loss of material. This enables an optimum catalytic activity over a period of cycles making the catalyst highly capable of being reused over many cycles. In this study, the vaterite-supported Fe_3O_4 catalyst was subjected to reusability with both the dyes, MB and RhB. It was found that the catalytic activity of the composite remained almost unaltered for five consecutive cycles. In both cases, the relative degradation percentage of $\geq 98\%$ was observed for the successive cycles w.r.t the first cycle (on normalizing the degradation percentages), Fig. A7b.12. Hence, in addition to the high rate constant, the ease of recovering the catalyst at the end of each cycle owing to its magnetic property and the excellent performance is shown by it on successive applications makes Fe_3O_4 /Vaterite a promising catalyst for commercial applications.

Additionally, to validate the effectiveness of Fe_3O_4 /Vaterite as a heterogeneous catalyst in wastewater treatment, the Fenton-like degradation of MB was carried out in the water from three different natural sources; tap water, lake water (IIT Guwahati), and river water (Brahmaputra, Assam). These water sources, especially the latter two, possess large amounts of contaminants, notably the river water as it is being subjected as a dumping yard for industrial effluents and city sewage. The characteristics of water from the different sources have been presented in **Table A7b.3**. The Fenton-like degradation of MB in tap water, lake water, and river water showed impressive results with 93%, 87%, and 84% degradation, respectively in two hours (Fig. 7b.7A-C). The degradation percentages do not differ much from the degradation performed in Millipore water (96%), suggesting that the catalyst can be utilized in large-scale wastewater treatment (Fig. 7b.7D).

7b.2.4 Mechanism of the Fenton-like dye degradation

It is known that in the Fenton and Fenton-like processes, the degradation mechanism undergoes a free radical pathway.^{7b.24-7b.26} Therefore, to illustrate the mechanism of degradation catalyzed by Fe_3O_4 /Vaterite one must know the active species (ROS) involved and hence, the dye-

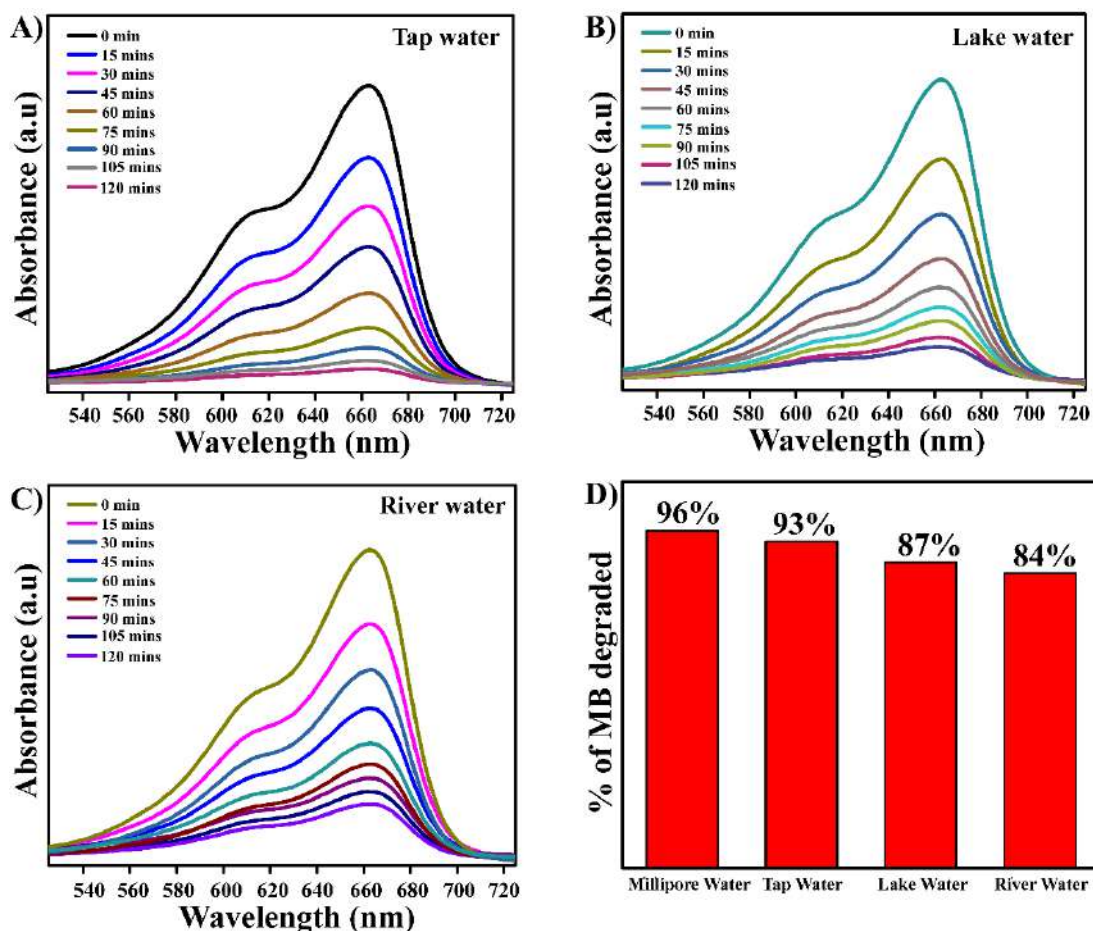
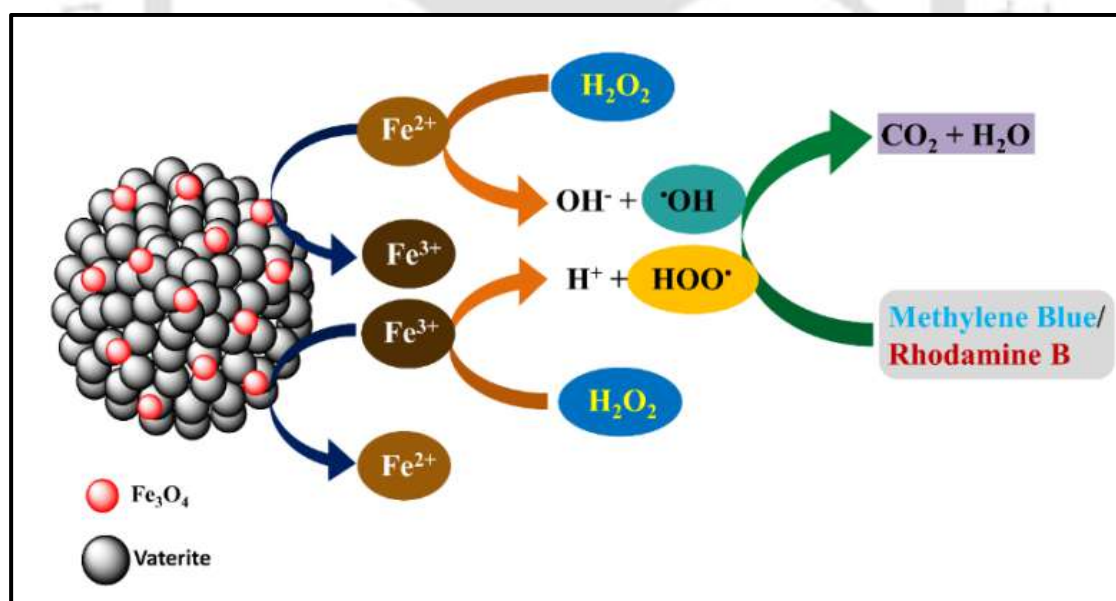


Figure 7b.7: UV-Vis spectra for the degradation of Methylene Blue catalyzed by Magnetite/Vaterite (A) in tap water; (B) in lake water; (C) in river water; (D) percentage degradation of Methylene Blue in the different water sources.

degradation process of MB was performed in the presence of free radical scavengers. Three different scavengers, NaN_3 , $t\text{-BuOH}$, and $p\text{-benzoquinone}$, were used for singlet oxygen, $\cdot\text{OH}$ and $\cdot\text{OOH}$, respectively, Fig. A7b.13. On evaluating the reaction kinetics for the degradation process using NaN_3 it was observed that the rate constant value was almost equal to the one performed without any scavenger. Thus, confirming that the ROS involved in the process was not singlet oxygen. However, on performing the reaction in the presence of the $\cdot\text{OH}$ and the $\cdot\text{OOH}$ scavengers and evaluating the reaction kinetics, a drastic fall in the rate constant values were observed. While introducing $t\text{-BuOH}$ to the reaction medium, the degradation process was quenched as the active $\cdot\text{OH}$ species were rendered inactive. Similarly, the introduction of $p\text{-benzoquinone}$ to the reaction mixture rendered the $\cdot\text{OOH}$ inactive, thereby quenching the degradation process. Hence, confirming that the active species involved in the dye-degradation process are $\cdot\text{OH}$ and $\cdot\text{OOH}$. Also, it was experimentally observed that the generation of ROS results from the combination of the catalyst and H_2O_2 , as can be seen in Fig. A7b.14; when the individual components were used, the extent of degradation was very minimal, $\leq 18\%$. Fe_3O_4

contains both Fe^{2+} and Fe^{3+} and exists as an inverse spinel where Fe^{2+} ions occupy half the octahedral sites and the Fe^{3+} ions are evenly split across the remaining octahedral sites and the tetrahedral sites. In the Fenton-like reaction involving Fe_3O_4 in the presence of H_2O_2 , the oxidation of Fe^{2+} to Fe^{3+} liberates $\cdot\text{OH}$ and subsequently, the regeneration of Fe^{2+} from Fe^{3+} in the presence of H_2O_2 , liberates $\cdot\text{OOH}$. This self-redox cycle between Fe^{2+} to Fe^{3+} generates the ROS species, which attacks the dye molecule and ultimately oxidizes it to the degradation products CO_2 , H_2O , etc. A schematic representation of the Fenton-like dye degradation mechanism catalyzed by $\text{Fe}_3\text{O}_4/\text{Vaterite}$ composite has been illustrated in **Scheme 7b.1**. The ability of Fe_3O_4 to catalyze the degradation of dye is already known but, the presence of the inert solid support here prevented the agglomeration of the nanoparticles. Both the dyes used in the study were cationic; therefore, the solid supports vaterite and calcite with a negative zeta potential (-22.173 mV and -17.217 mV) attracted the dye molecules to its surface, thereby facilitating the Fe_3O_4 embedded on its surface to catalyze the degradation more effectively and in the process, resulted in the improvement of the overall catalytic performance.^{7b.27,7b.28} The vaterite microspheres, due to their spherical morphology and a greater negative value of the zeta potential, resulted in better solid support as compared to the calcite particles when judged in terms of the catalytic activity of the respective Fe_3O_4 composites.



Scheme 7b.1: Plausible mechanism for degradation of organic dyes by a Fenton-like process catalyzed by Magnetite/Vaterite composite catalyst.

7b.3 Conclusion

To summarise, Fe_3O_4 nanoparticles were embedded on *in vitro* biomineralized vaterite, and the resulting composite material, $\text{Fe}_3\text{O}_4/\text{Vaterite}$ was used as a heterogeneous catalyst in the Fenton-

like degradation of the model dyes MB and RhB. *In vitro* biomineralized vaterite as support improved the catalytic performance of Fe₃O₄ as compared to bare Fe₃O₄ and also Fe₃O₄/Calcite. With 50 mg of the catalyst Fe₃O₄/Vaterite, both the dyes (50 ml, 10⁻⁵ M) were degraded in 2 hours in the presence of a minimal amount of H₂O₂ (5 mM). The degradation processes had taken place via first-order rate kinetics, where a rate constant value of 3.15 × 10⁻² min⁻¹ was observed for MB and 1.82 × 10⁻² min⁻¹ for RhB. The versatility of the catalyst was proven by its ability to perform the degradation in water from natural sources as they usually contain other forms of pollutants. Also, the magnetic nature of the composite enables its easy separation from the medium, making it a suitable candidate to be reused for multiple catalytic cycles without losing its activity. Hence, the nature of the composite material and the improved catalytic activity suggests a potential utilization of the catalyst to large-scale wastewater treatment.

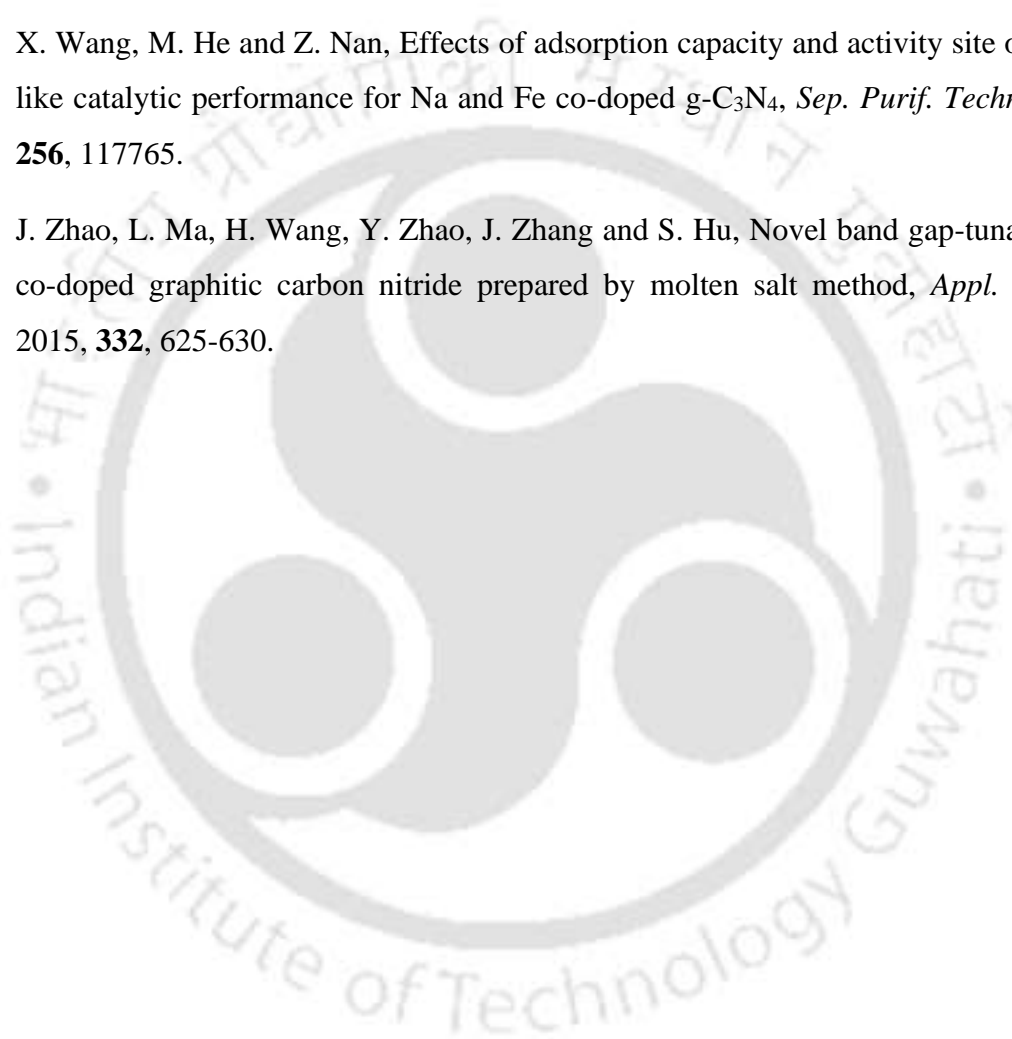
References

- 7b.1. D. Paul, D. Sachan, S. De and G. Das, Modulation of the CaCO₃ phase and morphology by tuning the sequence of addition: an insight into the formation of monohydrocalcite, *New J. Chem.*, 2021, **45**, 18337–18348.
- 7b.2. Yi-Y. Kim, A. S. Schenk, D. Walsh, A. N. Kulak, O. Cespedes and F. C. Meldrum, Bio-inspired formation of functional calcite/metal oxide nanoparticle composites, *Nanoscale*, 2014, **6**, 852-859.
- 7b.3. A. N. Kulak, M. Semsarilar, Yi-Y. Kim, J. Ihli, L. A. Fielding, O. Cespedes, S. P. Armes and F. C. Meldrum, One-pot synthesis of an inorganic heterostructure: uniform occlusion of magnetite nanoparticles within calcite single crystals, *Chem. Sci.*, 2014, **5**, 738-743.
- 7b.4. Y. H. Won, H. S. Jang, D. W. Chung and L. A. Stanciu, Multifunctional calcium carbonate microparticles: Synthesis and biological applications, *J. Mater. Chem.*, 2010, **20**, 7728-7733.
- 7b.5. D. Walsh, Yi-Y. Kim, A. Miyamoto and F. C. Meldrum, Synthesis of Macroporous Calcium Carbonate/Magnetite Nanocomposites and their Application in Photocatalytic Water Splitting, *Small*, 2011, **7**, 2168-2172.
- 7b.6. V. K. Saharan, M. P. Badve and A. B. Pandit, Degradation of reactive red 120 dye using hydrodynamic cavitation, *Chem. Eng. J.*, 2011, **178**, 100–107.

- 7b.7. U. G. Akpan and B. H. Hameed, Parameters affecting the photocatalytic degradation of dyes using TiO₂-based photocatalysts: a review. *J. Hazard. Mater.*, 2009, **170**, 520–529.
- 7b.8. J. E. Kumar, T. Mulai, W. Kharmawphlang, R. N. Sharan and M. K. Sahoo, Decolourisation, mineralisation and detoxification of mixture of azo dyes using Fenton and Fenton-type advanced oxidation processes, *Chem. Pap.*, 2020, **74**, 3145–3159.
- 7b.9. T. A. Dontsova, E. I. Yanushevskaya, S. V. Nahirniak, O. V. Makarchuk, A. I. Ivanets, M. Y. Roshchina, A. S. Kutuzova and L. M. Kulikov, Directional Control of the Structural Adsorption Properties of Clays by Magnetite Modification, *J. Nanomater.*, 2018, **2018**, 6573016.
- 7b.10. H. Wang, Z. Li, S. Yahyaoui, H. Hanafy, M. K. Seliem, A. Bonilla-Petriciolet, G. L. Dotto, L. Sellaoui and Q. Li, Effective adsorption of dyes on an activated carbon prepared from carboxymethyl cellulose: Experiments, characterization and advanced modelling, *Chem. Eng. J.*, 2021, **417**, 128116.
- 7b.11. E. Kusiak-Nejman and A. W. Morawski, TiO₂/graphene-based nanocomposites for water treatment: a brief overview of charge carrier transfer, antimicrobial and photocatalytic performance, *Appl. Catal. B: Environ.*, 2019, **253**, 179–186.
- 7b.12. D. He, H. Yang, D. Jin, J. Qu, X. Yuan, Y. Zhang, M. Huo and W. J. G. M. Peijnenburg, Rapid water purification using modified graphitic carbon nitride and visible light, *Appl. Catal. B: Environ.*, 2021, **285**, 119864.
- 7b.13. S. O. Ganiyu, M. Zhou and C. A. Martínez-Huitle, Heterogeneous electro-Fenton and photoelectro-Fenton processes: a critical review of fundamental principles and application for water/wastewater treatment, *Appl. Catal. B: Environ.*, 2018, **235**, 103–129.
- 7b.14. S. S. Xin, G. C. Liu, X. H. Ma, J. X. Gong, B. R. Ma, Q. H. Yan, Q. H. Chen, D. Ma, G. S. Zhang, M. C. Gao and Y. J. Xin, High efficiency heterogeneous Fenton-like catalyst biochar modified CuFeO₂ for the degradation of tetracycline: economical synthesis, catalytic performance and mechanism, *Appl. Catal. B: Environ.*, 2021, **280**, 119386.
- 7b.15. P. Baldrian, V. Merhautova, J. Gabriel, F. Nerud, P. Stopka, M. Hruby and M. J. Benes, Decolorization of synthetic dyes by hydrogen peroxide with heterogeneous catalysis by

- mixed iron oxides, *Appl. Catal. B: Environ.*, 2006, **66**, 258–264.
- 7b.16. A. Ivanets, V. Prozorovich, V. Sarkisov, M. Roshchina, I. Grigoraviciute-Puroniene, A. Zarkov, A. Kareiva, V. Masindi, C. Wang, V. Srivastava and M. Sillanp, Effect of magnesium ferrite doping with lanthanide ions on dark-, visible-and UV-driven methylene blue degradation on heterogeneous Fenton-like catalysts, *Ceram. Int.*, 2021, **47**, 29786-29794.
- 7b.17. O. I. Yanushevskaya, N. V. Vlasenko, G. M. Telbis, E. V. Leonenko, O. Z. Didenko, V. G. Prozorovich, A. I. Ivanets and T. A. Dontsova, Acid–base and photocatalytic properties of TiO₂-based nanomaterials, *Appl Nanosci.*, 2021, **12**, 691-700.
- 7b.18. N. N. N. Mahasti, Yu-J. Shih and Y. H. Huang, Recovery of magnetite from fluidized-bed homogeneous crystallization of iron-containing solution as photocatalyst for Fenton-like degradation of RB5 azo dye under UVA irradiation, *Sep. Purif. Technol.*, 2020, **247**, 116975.
- 7b.19. H. Jiang, Y. Sun, J. Feng and J. Wang, Heterogeneous electro-Fenton oxidation of azo dye methyl orange catalyzed by magnetic Fe₃O₄ nanoparticles, *Wat Sci Technol.*, 2016, **74**, 1116–1126.
- 7b.20. L. Wan, D. Yan, X. Xu, J. Li, T. Lu, Y. Gao, Y. Yao and L. Pan, Self-assembled 3D flower-like Fe₃O₄/C architecture with superior lithium ion storage performance, *J. Mater. Chem. A*, 2018, **6**, 24940–24948.
- 7b.21. X. Li, X. Huang, D. Liu, X. Wang, S. Song, L. Zhou and H. Zhang, Synthesis of 3D Hierarchical Fe₃O₄/Graphene Composites with High Lithium Storage Capacity and for Controlled Drug Delivery, *J. Phys. Chem. C*, 2011, **115**, 21567-21573.
- 7b.22. T. Yamashita and P. Hayes, Analysis of XPS spectra of Fe²⁺ and Fe³⁺ ions oxide materials, *Appl. Surf. Sci.*, 2008, **254**, 2441-2449.
- 7b.23. M. Rochkind, S. Pasternak and Y. Paz, Using dyes for evaluating photocatalytic properties: a critical review, *Molecules*, 2015, **20**, 88–110.
- 7b.24. S. Bhowmick, C. T. Moi, N. Kalita, A. Sahu, S. Suman and M. Qureshi, Spontaneous Fenton-like dye degradation in clustered-petal di-manganese copper oxide by virtue of self-cyclic redox couple, *J. Environ. Chem. Eng.*, 2021, **9**, 106094.

- 7b.25. T. Zhou, Y. Xu, X. Wang, S. Huang, M. Xie, J. Xia, L. Huang, H. Xu and H. Li, Construction of solid–liquid interfacial Fenton-like reaction under visible light irradiation over etched $\text{Co}_x\text{Fe}_y\text{O}_4$ –BiOBr photocatalysts, *Catal. Sci. Technol.*, 2018, **8**, 551-561.
- 7b.26. W. Zhao, C. Liang, B. Wang and S. Xing, Enhanced Photocatalytic and Fenton-like Performance of CuO_x -Decorated ZnFe_2O_4 , *ACS Appl. Mater. Interfaces*, 2017, **9**, 41927–41936.
- 7b.27. X. Wang, M. He and Z. Nan, Effects of adsorption capacity and activity site on Fenton-like catalytic performance for Na and Fe co-doped g- C_3N_4 , *Sep. Purif. Technol.*, 2021, **256**, 117765.
- 7b.28. J. Zhao, L. Ma, H. Wang, Y. Zhao, J. Zhang and S. Hu, Novel band gap-tunable K–Na co-doped graphitic carbon nitride prepared by molten salt method, *Appl. Surf. Sci.*, 2015, **332**, 625-630.



Annexure-Chapter 7b

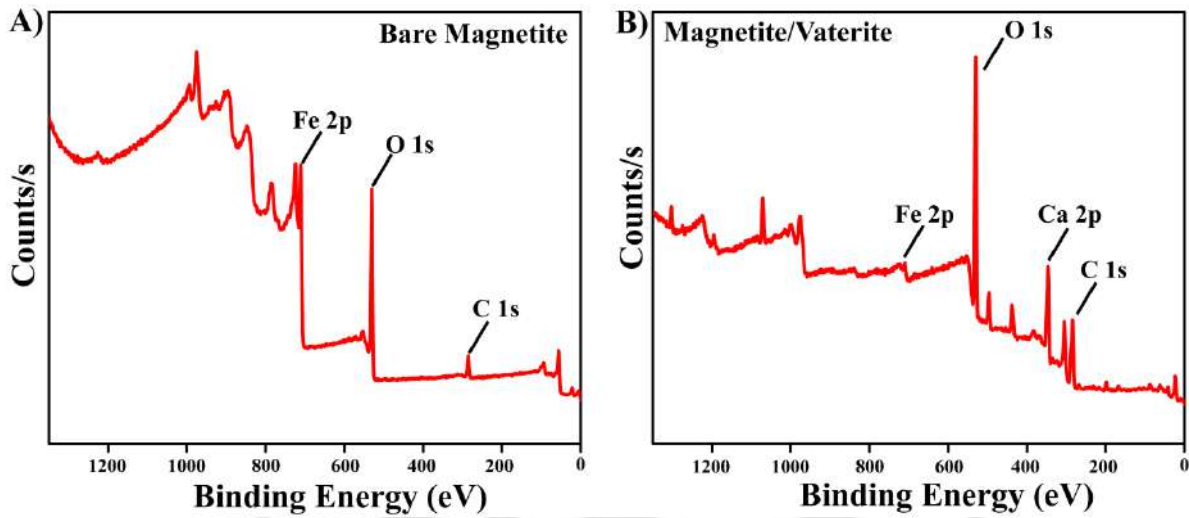


Figure A7b.1: XPS Survey (A) Bare magnetite; (B) Magnetite/Vaterite.

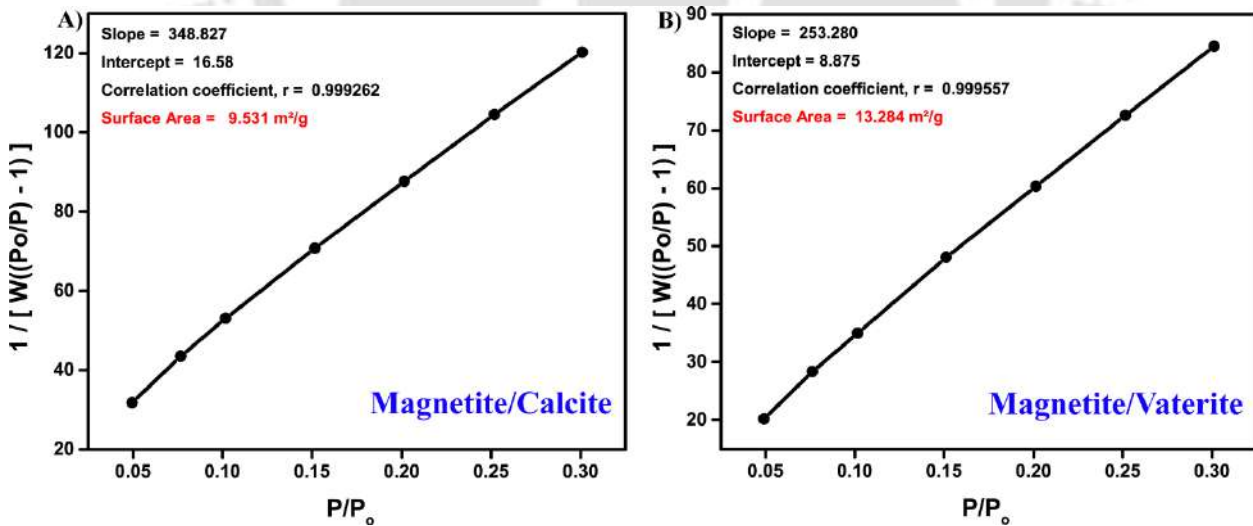


Figure A7b.2: Nitrogen adsorption-desorption BET isotherm (A) Magnetite/Calcite; (B) Magnetite/Vaterite.

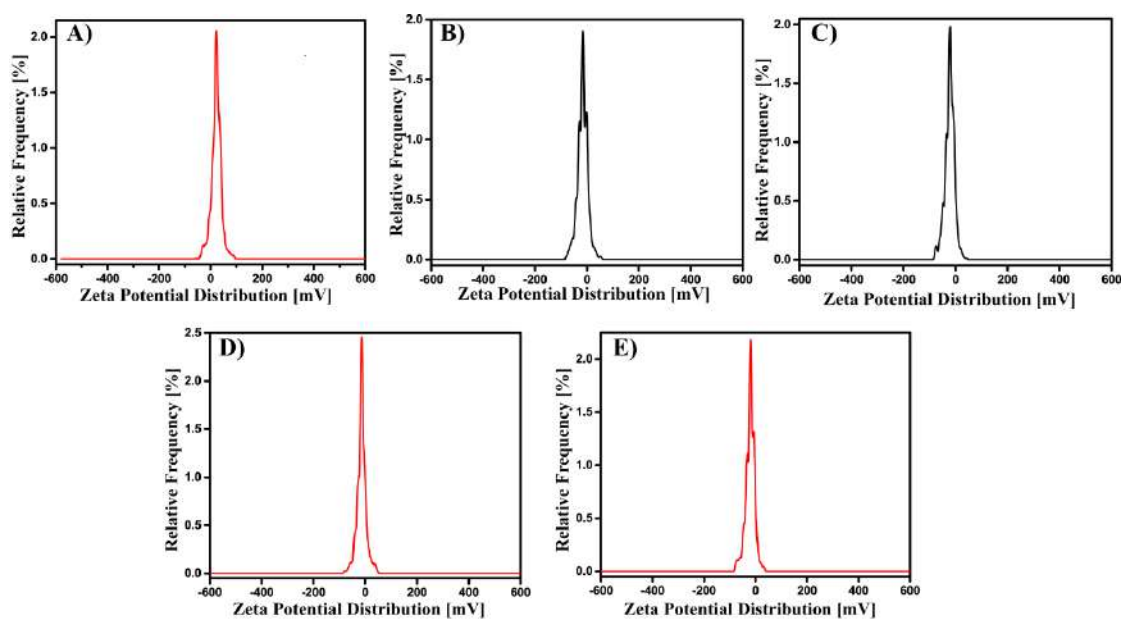


Figure A7b.3: Zeta Potential of (A) Bare magnetite; (B) Bare Calcite; (C) Bare Vaterite; (D) Magnetite/Calcite; (E) Magnetite/Vaterite.

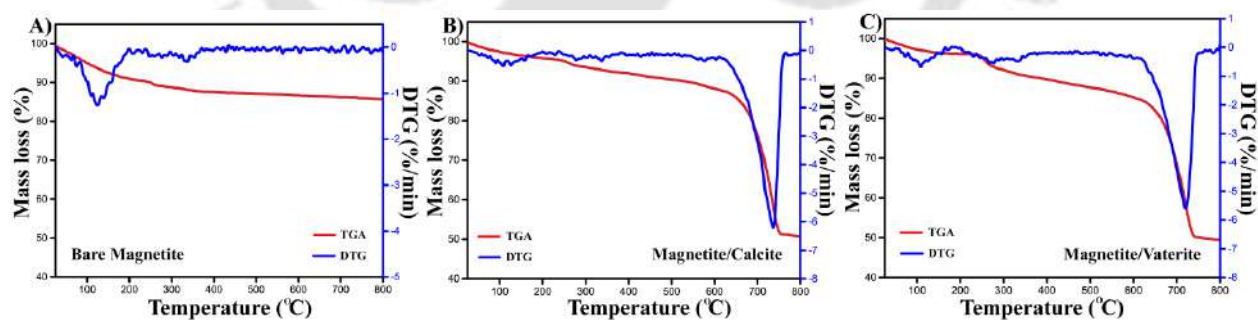


Figure A7b.4: TGA/DTG curve of (A) Bare Magnetite; (B) Magnetite/Calcite; (C) Magnetite/Vaterite; in the temperature range of 25-800 °C.

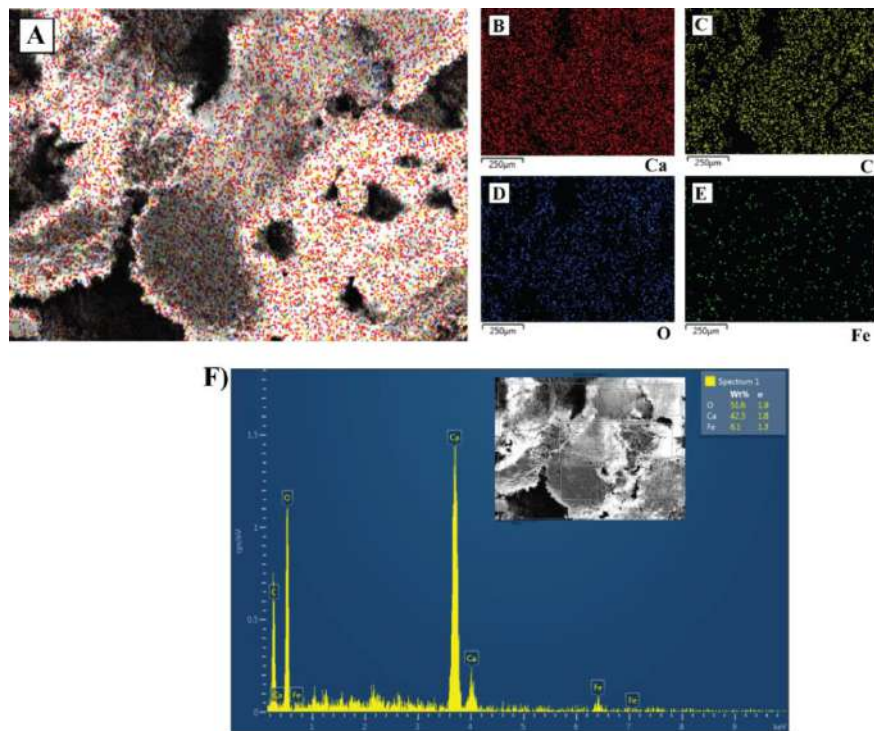


Figure A7b.5: (A) EDX mapping of Magnetite/Calcite particles highlighting all the elements; (B), (C), (D), (E) highlighting the individual elements Ca, C, O, Fe, respectively; (F) EDX elemental analysis of Magnetite/Calcite.

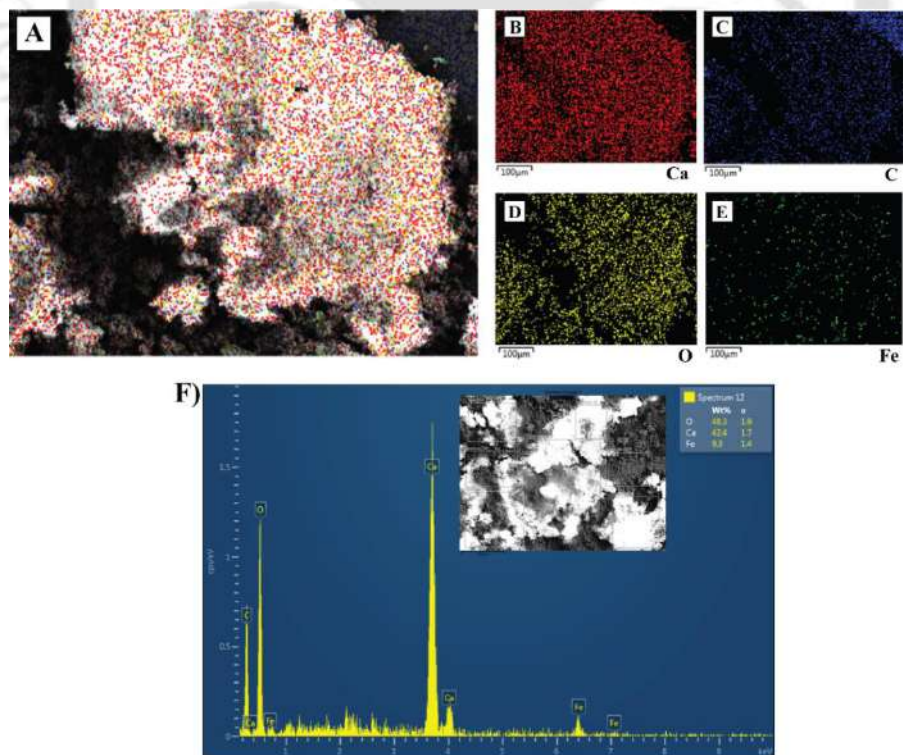


Figure A7b.6: (A) EDX mapping of Magnetite/Vaterite particles highlighting all the elements; (B), (C), (D), (E) highlighting the individual elements Ca, C, O, Fe, respectively; (F) EDX elemental analysis of Magnetite/Vaterite.

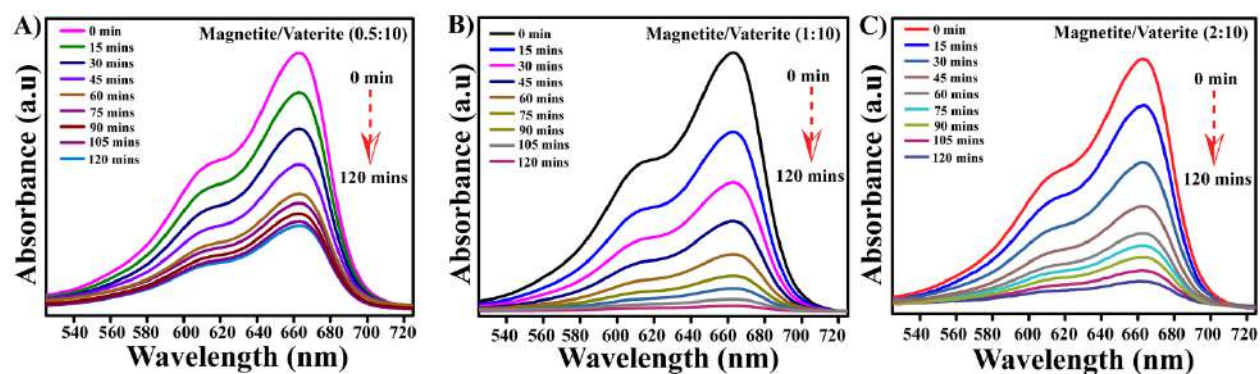


Figure A7b.7: UV-Vis absorption spectra of the degradation of Methylene Blue catalyzed by (A) Magnetite/Vaterite (0.5:10); (B) Magnetite/Vaterite (1:10); and (C) Magnetite/Vaterite (2:10).

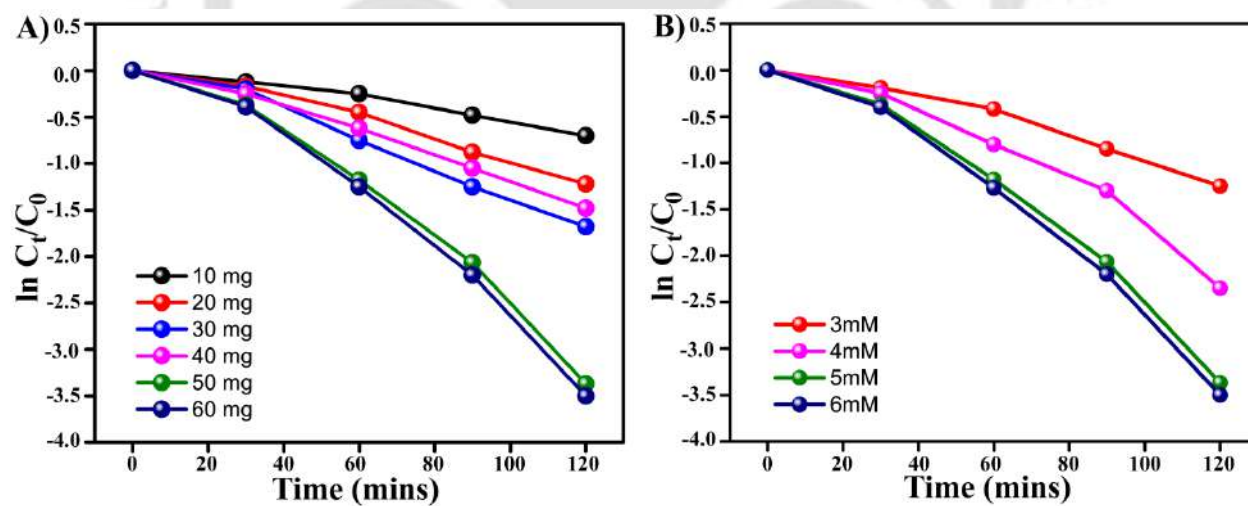


Figure A7b.8: The dependence of rate of the reaction on (A) the amount of catalyst, and (B) the concentration of H_2O_2 added to the system keeping the other constant.

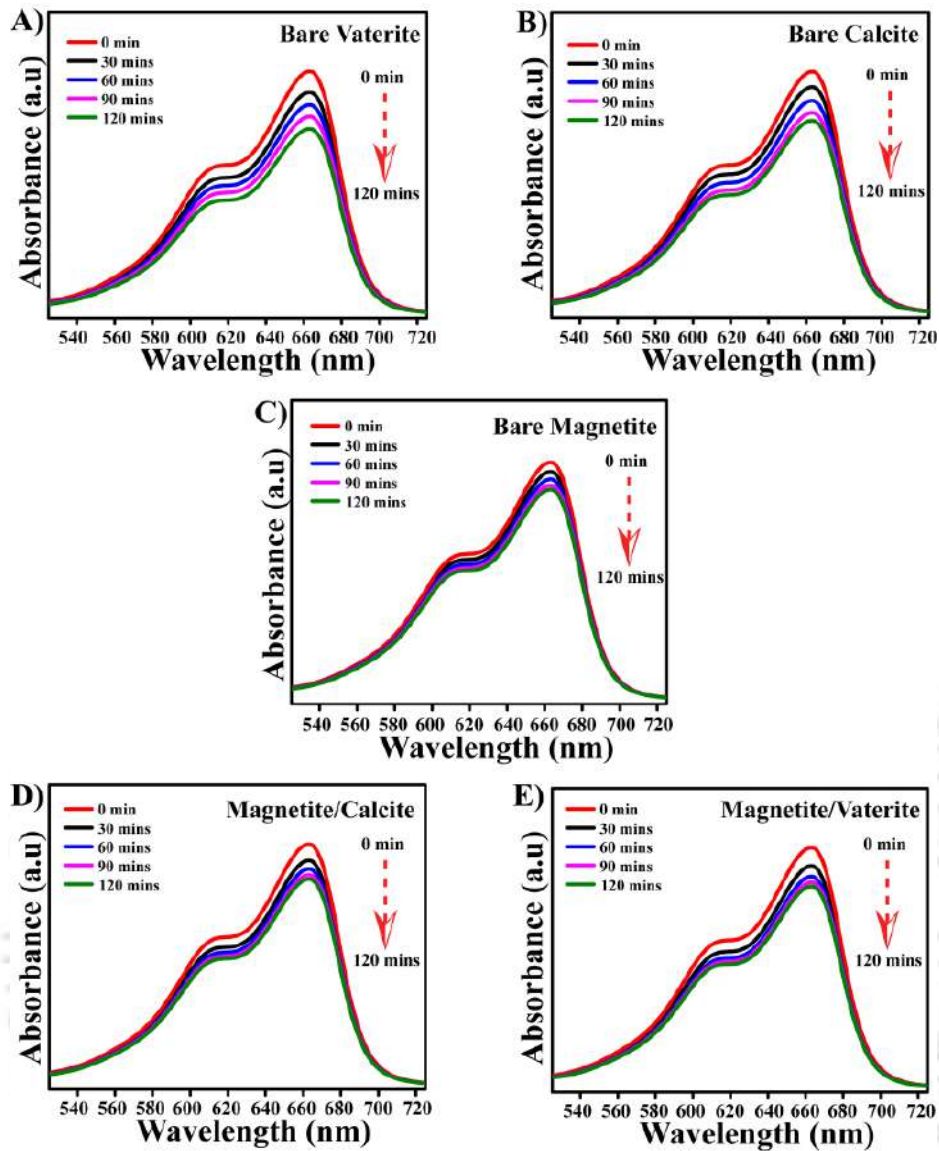


Figure A7b.9: UV-Vis spectra for the adsorption of Methylene Blue on (A) Bare Vaterite; (B) Bare Calcite; (C) Bare Magnetite; (D) Magnetite/Calcite; (E) Magnetite/Vaterite.

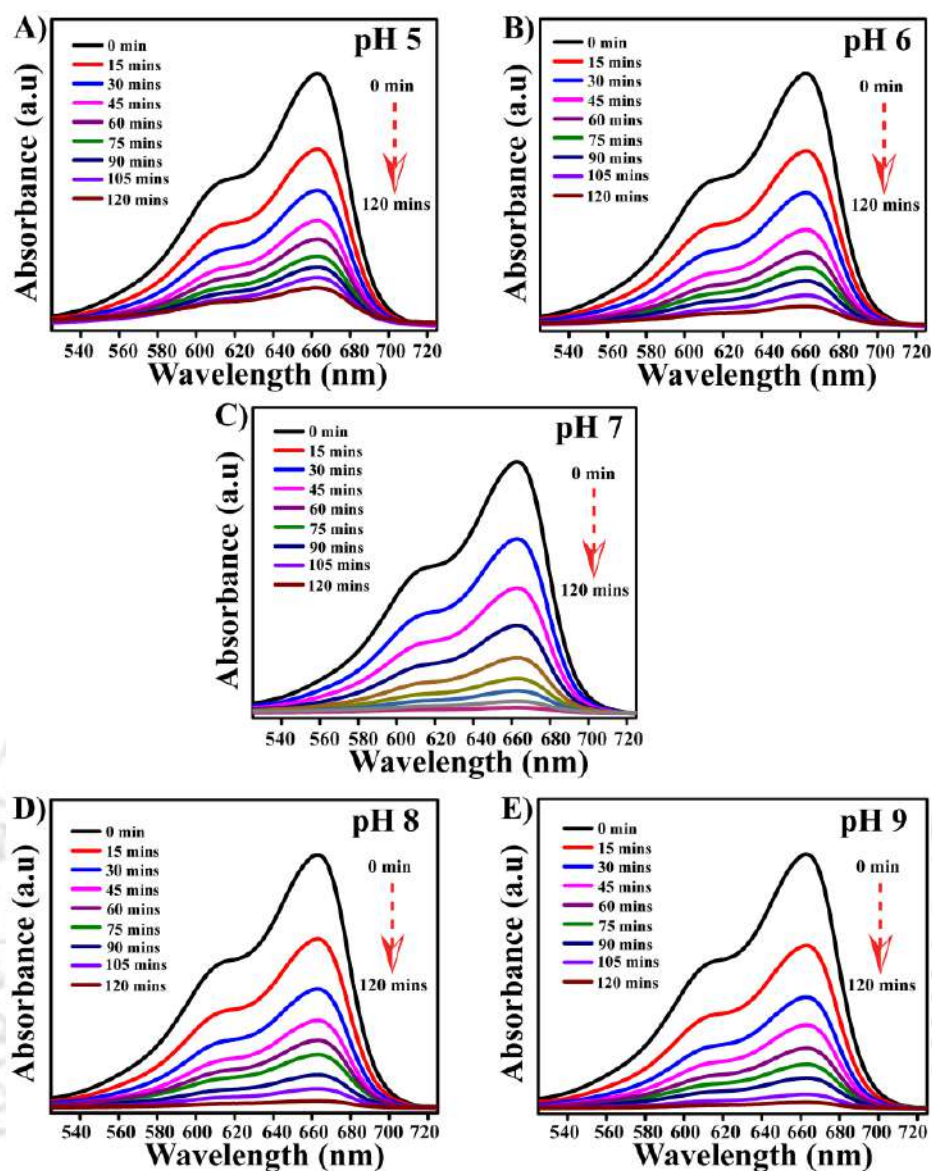


Figure A7b.10: UV-Vis spectra for the degradation of Methylene Blue catalyzed by Magnetite/Vaterite at different pH conditions (A) pH 5; (B) pH 6; (C) pH 7; (D) pH 8; (E) pH 9.

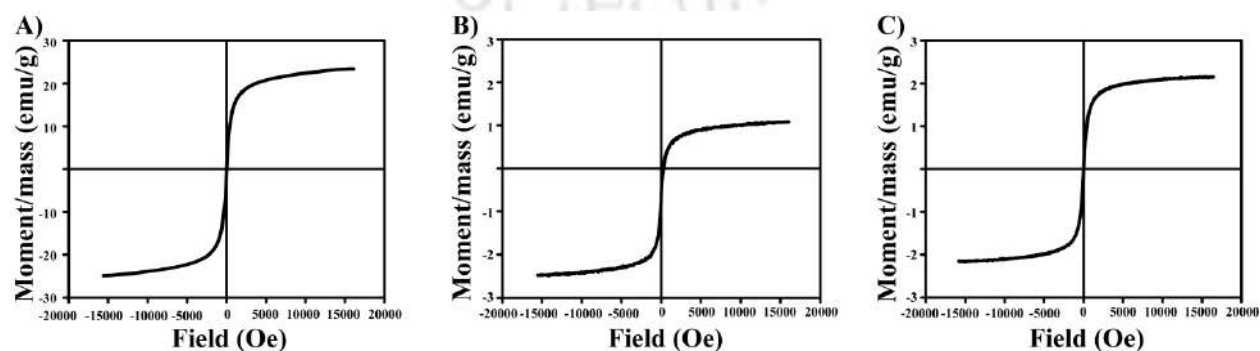


Figure A7b.11: VSM spectra of A) Bare Magnetite; (B) Magnetite/Calcite; (C) Magnetite/Vaterite.

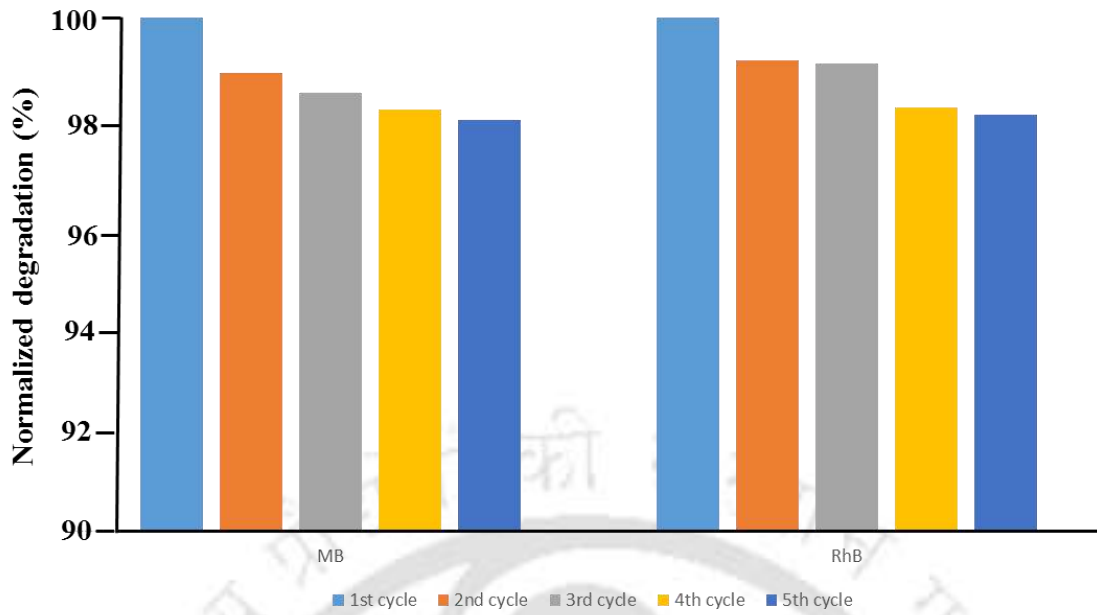


Figure A7b.12: Normalized dye-degradation percentages of the different dyes upon reusability of the catalyst Magnetite/Vaterite.

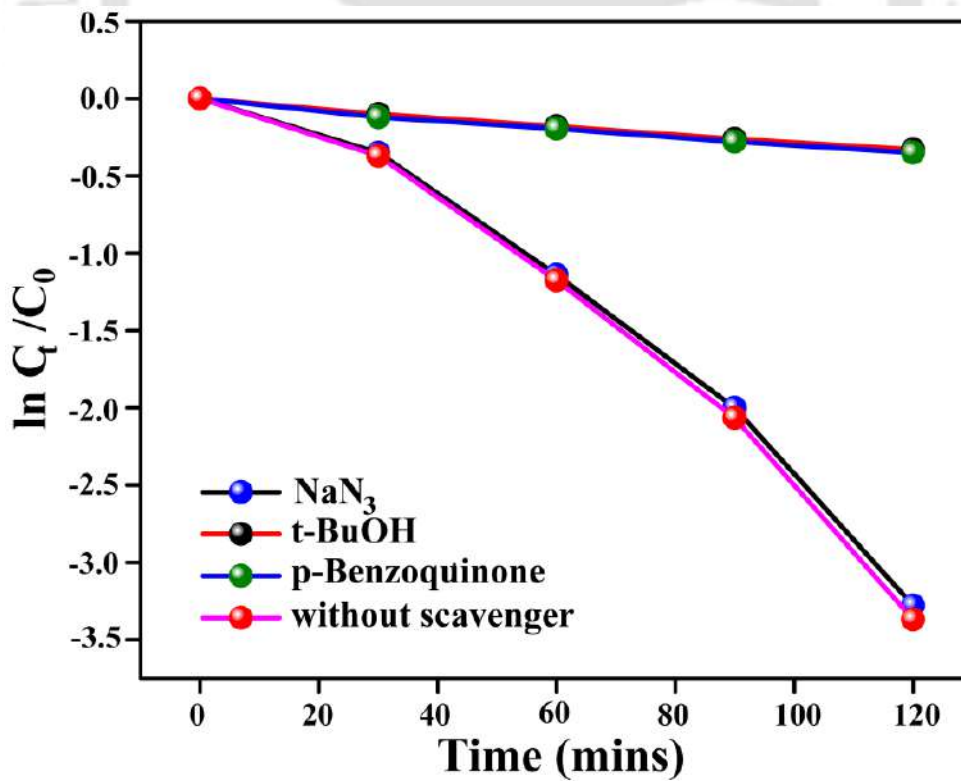


Figure A7b.13: Rate constant plot for Methylene Blue degradation in presence and absence of free radical scavengers.

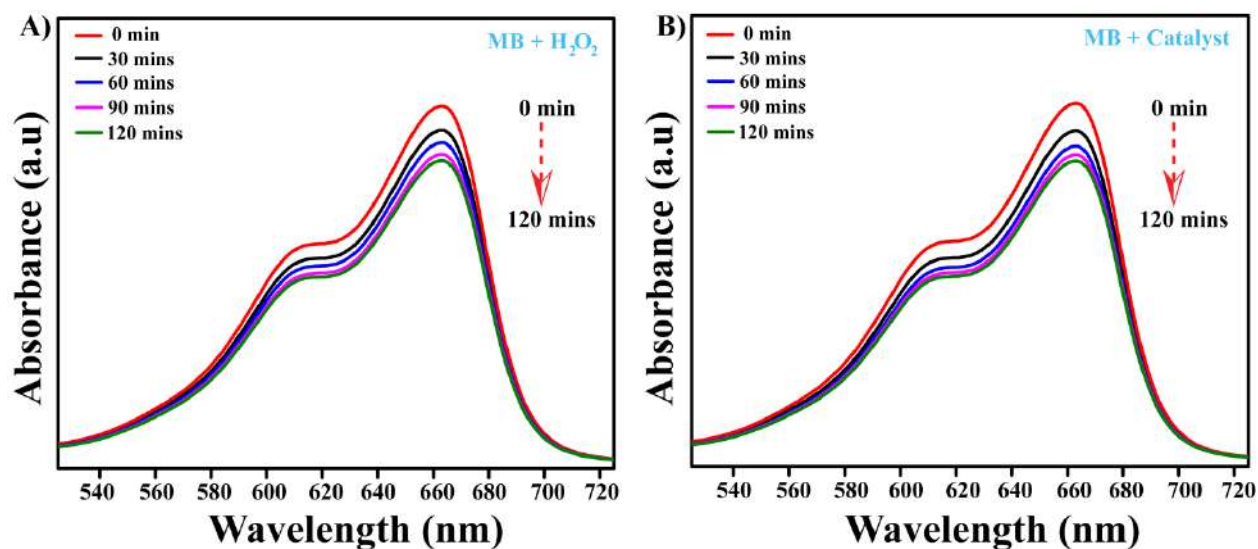


Figure A7b.14: UV-Vis absorption spectra of the degradation of Methylene Blue in the presence of (A) only H_2O_2 ; (B) only catalyst (Magnetite/Vaterite).

Table A7b.1: Adsorption capacity of the materials and their zeta potential

Sl. No.	Material	Zeta Potential (mV)	Amount of dye adsorbed in 2 hours (%)
1	Bare Vaterite	-22.173	24
2	Bare Calcite	-17.217	20
3	Bare Fe_3O_4	+21.842	10
4	Fe_3O_4 /Calcite	-14.662	14
5	Fe_3O_4 /Vaterite	-19.354	16

Table A7b.2: A comparison of the rate constant of dye degradation reactions catalysed by Fe_3O_4 based catalysts

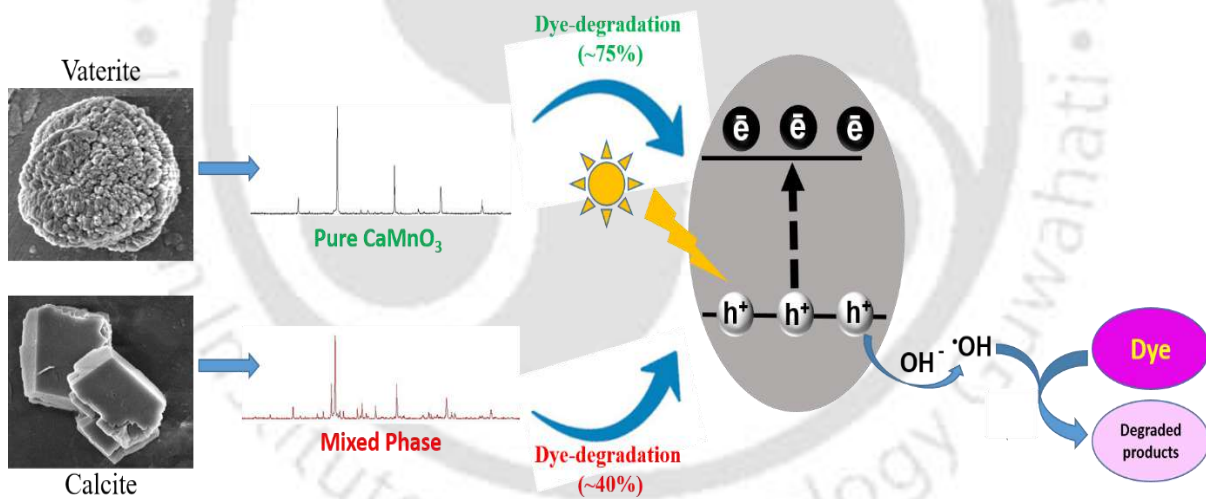
Reference	Catalyst	Dye	Rate constant (min^{-1})
<i>Catalysts</i> 2016 , 6, 146	$\text{Fe}_3\text{O}_4/\text{TiO}_2/\text{C}$	Methylene Blue	1.9×10^{-2}

<i>Water Sci. Eng.</i> 2017 , 10,326-333	Fe ₃ O ₄ -MnO ₂	Acid orange	2.9 x 10 ⁻²
<i>Sep. Purif. Technol.</i> 2019 , 210, 563-573	Fe ₃ O ₄ /ZnO/graphene (visible light irradiation)	Methylene Blue Congo Red	1.8 x 10 ⁻² 2.5 x 10 ⁻²
<i>Mater. Chem. Phys.</i> 2019 , 227, 302-312	Fe ₃ O ₄ /SiO ₂	Rhodamine B	2.6 x 10 ⁻²
<i>Int. J. Biol. Macromol.</i> 2020 , 152, 242-249	cellulose-based hydrogel coated Fe ₃ O ₄	Acid red 73	1.9 x 10 ⁻²
Present work	Fe₃O₄/Vaterite	Methylene Blue Rhodamine B	3.1 × 10 ⁻² 1.8 × 10 ⁻²

Table A7b.3: The characteristics of water from the various sources

Sl. No.	Parameters	Tap water	River water	Lake water	Millipore water
1	pH	7.91	7.64	7.78	6.75
2	Conductivity (µS/cm)	273	247	262	15.05
3	Salinity (%)	0.13	0.12	0.11	0
4	TDS (mg/L)	130.4	117.7	124.3	0.015
5	D.O (mg/L)	8.86	8.42	8.42	8.42

In vitro biomineralized vaterite derived efficient solid-state synthesis of pure CaMnO_3 perovskite as a useful photocatalyst



8.1 Introduction

The perovskite materials, represented as ABO_3 , where A is an alkali, or rare-earth metal and B is a transition metal, are of great interest to the researchers due to their intrinsic catalytic activity.^{8.1,8.2} Their low bandgap energy, the high flexibility of their elemental composition, and rich electronic/defect structure permit the easy tuning of their intrinsic activity.^{8.3,8.4} Perovskite materials owing to the presence of transition metals that have variable oxidation states, such as Mn, Co, Fe, or Ni, facilitates electron movement and are, therefore, utilized in designing electro or photocatalyst.^{8.5,8.6}

Photocatalysis is an effective method for various environmental remediation applications, including the neutralization of pollutants from water and air.^{8.7} In the past few years, especially considering the increasing threat posed by the dreadful pollutants, photocatalysts are considered one of the best remedies. Accordingly, photocatalysis researchers have reciprocated positively by putting forward many approaches to address environmental issues. Many photocatalysts have been designed based on the fundamental principle of utilizing light energy to initiate the processes. Eventually, every photocatalyst is designed to maintain its uniqueness to perform its task more efficiently and, most importantly, showcase widespread utility towards applications ranging from removing toxic organic compounds and dyes in water^{8.8,8.9} to the moderation of obnoxious gases and volatile organic compounds in the air.^{8.10-8.12} Calcium manganese oxides (CMOs), among other photocatalytic materials, are an emerging class of biomimetic redox catalysts. Their utilization in applications across multiple fields has become highly demanding due to their abundant and environment-friendly chemical compositions. But what makes them more intriguing is the similarity in their structure to the μ -oxo- Mn_4Ca group present in Photosystem-II protein. This group is responsible for water-splitting in the natural photosynthesis process.^{8.13-8.15} Recently, photocatalytic properties of CMOs and their application on dye degradation under visible light irradiation have been studied. Due to their structural similarities to perovskite materials, they have shown excellent photocatalytic abilities.^{8.16-8.18} This opens up the scope for us to explore their photocatalytic properties and utilize them for various applications. The usual methods adopted to synthesize the CMOs involve sol-gel,^{8.19} hydrothermal,^{8.20} and electrospinning methods.^{8.21} All these methods are solution-based, and the use of organic solvents has always been a cause of concern as it poses a severe threat to the environment. Moreover, when these materials are utilized in industrial and commercial-based applications, the production of the materials in bulk raises the threat posed to the manifold. Hence using a method to limit or absolutely nullify the use of solvents would reduce such risks.

The solid-state synthesis methods have thus been adopted whereby the Ca and Mn precursors are mixed in stoichiometric amounts and heated at elevated temperatures.^{8.22,8.23} Also, in addition to addressing the ecological concern, it is essential to adhere to cost-effective processes such that they can be adopted for practical purposes.

Industrial wastewater discharge into water bodies has always been a severe cause of concern for the environment and eventually posing severe health hazards. Among the most common pollutants that are being expelled, the dyes constitute a large percentage of it.^{8.24,8.25} These dyes are highly soluble in water, making them very difficult to be removed by conventional methods.^{8.26} The colour associated with the dyes prevents the penetration of light through water and, therefore, hinders the photosynthesis process in aquatic plants, which disturbs the ecological balance.^{8.27} In short, based on recent reports, the major threats posed by the dyes that are discharged into the water bodies include lowering the aesthetic quality of water bodies, increasing the biochemical and chemical oxygen demand (BOD and COD), impairment of photosynthesis, making way into the food chain and thereby posing the threats of toxicity and carcinogenicity.^{8.28} Rhodamine 6G (Rh 6G) is very often used as a colorant in textile industries and is among the toxic pollutants that are being regularly used and discharged into the water bodies. It is a dark reddish-purple-colored compound, which is highly soluble in water and is non-volatile.

Additionally, it also has some other applications in biochemistry where it is used as a diagnostic tool for detecting antigens in liquid samples.^{8.29} Exposure to water contaminated with Rhodamine dyes, which also includes Rhodamine B (RhB), irritates the eyes and skin and is toxic for the respiratory system in humans. Drinking water contaminated with Rhodamine dyes is highly carcinogenic and hazardous to living organisms.^{8.30,8.31} In addition to the Rhodamine dyes, Methylene Blue (MB) and Methyl Orange (MO) are also commonly used in textile, leather, and paper industries and are constantly expelled by these industries into the environment. While MB is known to be carcinogenic, MO also poses serious health issues with symptoms such as nausea, dizziness, abdominal pain, etc., if consumed in trace amounts.^{8.32,8.33} Hence, pre-treatment of these dyes to convert them to harmless products before discharging them into the environment is very important. Over the years, various methods have been adopted for the treatment of dyes, the photocatalytic method being one of them.^{8.34-8.36}

As already mentioned, the vaterite particles have been utilized. They have shown tremendous results in applications across various fields, but their versatility has never been explored in the generation of perovskite materials. This study used biomaterialized vaterite as the calcium

precursor for calcium manganese oxide, CaMnO_3 . We tried to attain the target perovskite material in the pure phase. Despite the challenges in synthesizing and isolating the vaterite phase, due to its unstable nature, in our recent works, we were successfully able to isolate this metastable phase in the template-directed *in vitro* biomineralization of CaCO_3 .^{8,37,8,38} In this work, we have used different Ca precursors to make a comparison with biomineralized vaterite. The materials were synthesized by a solid-state synthesis method using elevated temperatures. The factors such as solvent-free conditions and economic viability were kept in focus while performing the syntheses. The role of CaMnO_3 synthesized using biomineralized vaterite was studied in detail in the photocatalytic degradation of Rh 6G and compared with the one synthesized using commercially available CaCO_3 (Calcite). The radical initiated photocatalytic dye-degradation was further analyzed to understand the plausible mechanism and specify the reactive species responsible for the degradation process. Additionally, the degradation of RhB, MB, and MO was also performed with pure CaMnO_3 .

8.2 Results and Discussions

8.2.1 General characterizations of the materials

The vaterite particles synthesized by curcumin-directed *in vitro* biomineralization were characterized by PXRD analysis, and the pattern suggested the formation of the vaterite phase, Fig. 8.1(A). The peaks obtained at 2θ values equal to 20.97, 25.29, 27.29, 33.12, 43.82, 49.37, 50.42, and 56.21 were corresponding to (002), (100), (101), (102), (110), (112), (104) and (202) planes respectively, confirmed from the standard PDF data for the vaterite phase, ICSD 01-072-0506. From the FESEM images, we could see the formation of the spherical vaterite particles, Fig. 8.1(D) and (E). Similarly, the commercially available CaCO_3 was analyzed using the PXRD technique, and here we attained a pattern identical to the calcite phase, Fig. 8.1(A). The peaks obtained at 2θ values equal to 23.03, 29.37, 35.86, 39.32, 43.19, 47.42, and 48.53 were corresponding to (012), (104), (110), (11-3), (202), (018) and (11-6) planes respectively, identical to the standard PDF data for calcite, ICSD 00-001-0837. In the FESEM images of the calcite phase, we could see cubic crystalline particles, Fig. 8.1(B) and (C). Both these phases, vaterite and calcite were used as Ca precursors in the synthesis where we targeted the exclusive formation of only the perovskite material CaMnO_3 . The Mn precursor used was $\text{Mn}(\text{OH})_2$, and in addition to the two CaCO_3 phases, we also used $\text{Ca}(\text{OH})_2$ as a Ca precursor to draw a comparison. The CMOs obtained in each case were initially characterized by the PXRD analysis, which gave us the idea with regards to the phases that have formed. In the case where

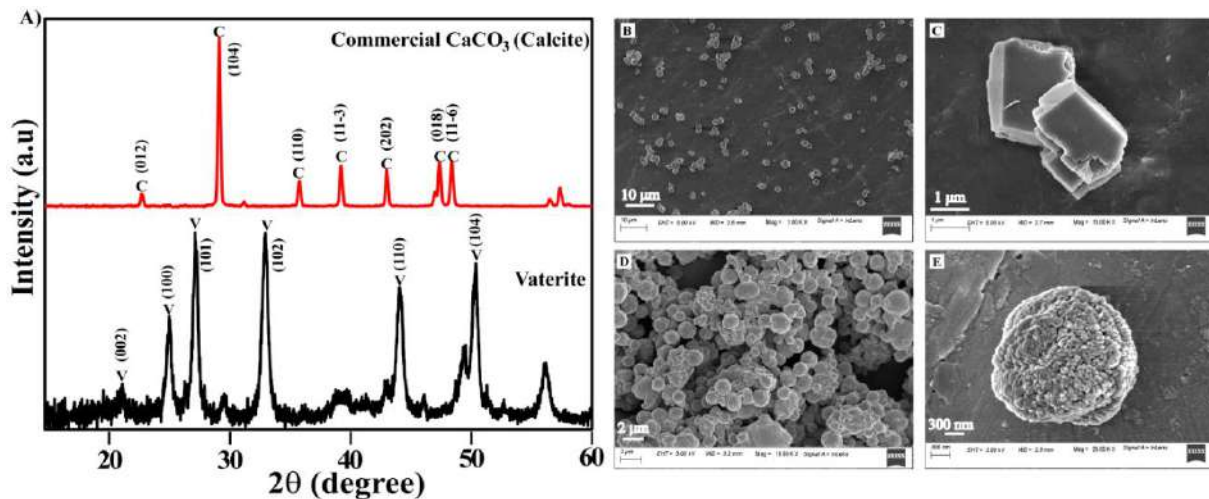


Figure 8.1: (A) XRD Patterns of Biom mineralized Vaterite and Commercial CaCO₃ (Calcite); (B) and (C) FESEM images of Commercial CaCO₃ (Calcite); (D) and (E) FESEM images of Biom mineralized Vaterite.

biom mineralized vaterite was used, the peaks were obtained at 2θ values equal to 23.93, 34.08, 48.95, 60.92, and 71.53, Fig. 8.2(A)(i). These peaks were corresponding to (101), (121), (202), (123), and (242) planes, respectively, identical to the standard PDF data of CaMnO₃, ICSD 00-063-0466. In the second case, where calcite was used as the Ca precursor, in addition to the peaks for CaMnO₃ at 23.81, 33.95, 48.64, 60.80, and 71.44 corresponding to the (101), (121), (202), (123) and (242) planes respectively, we also obtained peaks at 32.99, 39.27, 40.36 and 43.50, Fig. 8.2(A)(ii). These additional peaks correspond to the (023), (130), (131), and (132) planes of Marokite, CaMn₂O₄, confirmed by matching with the standard PDF data of Marokite, ICSD 01-070-4889. Again, when Ca(OH)₂ was used as the Ca precursor, in addition to the peaks at 23.96, 34.20, 48.95, 60.86, and 71.69 corresponding to the (101), (121), (202), (123), and (242) planes of CaMnO₃, we obtained peaks at 33.11, 39.46, 40.61 and 43.81 corresponding to (023), (130), (131) and (132) planes of Marokite as was obtained with calcite, Fig. 8.2(A)(iii). But here, one more peak was obtained at 2θ equal to 34.73. This peak is almost identical to the (200) plane of dicalcium manganate, Ca₂MnO₄, confirmed from the standard PDF data of dicalcium manganate, ICSD 01-070-5606. From the PXRD analysis, we can clearly see that the biom mineralized vaterite, when used as the Ca source, has led to the specific formation, 100%, of the target perovskite material CaMnO₃, whereas with the calcite phase and the Ca(OH)₂ as the precursors, we obtained a mixed-phase of CMOs where along with CaMnO₃, CaMn₂O₄ and Ca₂MnO₄ were also obtained. Although in this work, we are focused on the role of the different phases of CaCO₃ in the synthesis of CaMnO₃; the experiment with Ca(OH)₂ was performed to give a conclusive idea that following the solvent-free solid-state synthesis route and the vaterite phase is the most suitable Ca source to attain only the specific phase.

The morphologies of the materials synthesized using vaterite and calcite were obtained from the FESEM technique. The pure CaMnO_3 , synthesized using vaterite, exhibited a definite and near-spherical (oval-shaped) morphology, as can be seen in Fig. 8.2(D) and (E). For the mixed-phase, obtained from calcite and consisting of both CaMnO_3 and CaMn_2O_4 , however, the FESEM images, Fig. 8.2(B) and (C), revealed no definite morphology, the presence of several different and random shaped particles can be observed, which in all likelihood denotes the mixed-phase. The sizes of the particles were obtained in both cases by taking into consideration a total of 15 particles in each case. In the case of pure CaMnO_3 where the particles are nearly spherical, the average size was obtained as 414 nm, with the maximum and minimum size being ~ 260 nm and ~ 700 nm, respectively, Fig. A8.1(A). In the second case, where the particles were of random morphology, eventually, after considering particles of diverse shapes, the average size was found out to be 710 nm and here, the maximum and minimum size of particles were ~ 450 nm and ~ 1050 nm, respectively, Fig. A8.1(B).

The HRTEM analysis was performed to confirm the formation of CaMnO_3 using vaterite. Fig. 8.2(F) represents the HRTEM image and the fringe patterns obtained have been magnified and illustrated in Fig. 8.2(H) and the corresponding selected area electron diffraction (SAED) pattern is shown in Fig. 8.2(G). The measured fringe spacing of 0.263 nm corresponds to the interplanar spacing of (121) plane of CaMnO_3 . The specific surface area of the materials was obtained from the BET surface area study obtained from the Nitrogen adsorption-desorption analysis, Fig. A8.2(A) and (B). The specific surface area of CaMnO_3 was found out to be $11.040 \text{ m}^2/\text{g}$ and that of the mixed oxides, CaMnO_3 and CaMn_2O_4 , was $4.75 \text{ m}^2/\text{g}$. The lowering in specific surface area of the mixed-phase is mainly attributed to the smaller specific surface area of CaMn_2O_4 and additionally, the irregular-shaped morphology and the bigger size of the particles compared to pure CaMnO_3 contributed to the lowering.^{8,18,8.39,8.40} The comparatively larger specific surface area of the single-phase CaMnO_3 makes it highly favorable towards diverse applications such as water-splitting, dye degradation, etc. In such applications, the material's surface plays a pivotal role whereby the substrate molecules bind to and then undergo the possible transformation.^{8.41} Greater the specific surface area of the catalyst, the higher the substrate's rate of transformation. The optical bandgap energy of the materials was attained from the Tauc plot, Fig. 8.3(A) and (B). The Tauc plot in the form of $(\alpha h\nu)^2$ versus $h\nu$ was obtained from the absorption spectra (UV-vis diffuse reflectance spectroscopy), Fig. A8.3, of the materials. The intercepts of the extrapolated straight lines on the X-axis, the energy axis, give us the optical bandgap energy of the materials. The values were equal to 1.21 eV and 1.26 eV for pure CaMnO_3 and the mixed-phase, respectively. These values are comparable to the

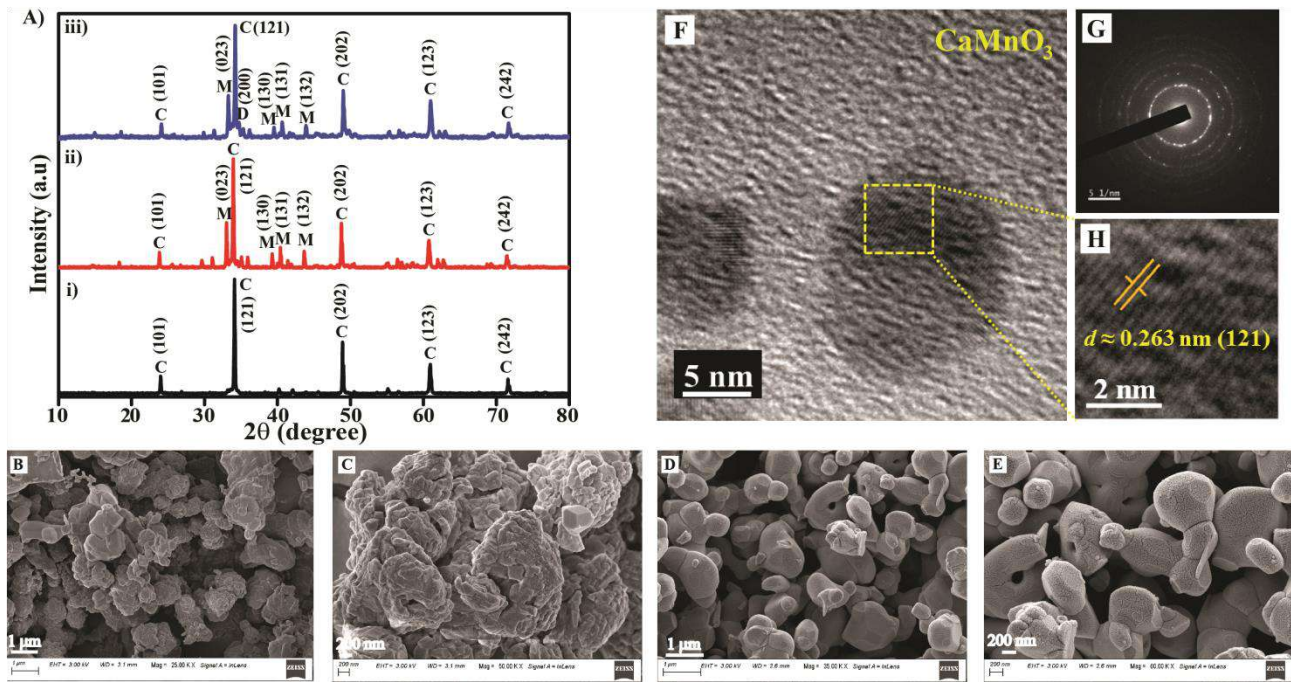


Figure 8.2: (A) XRD Patterns of (i) pure CaMnO_3 synthesized using Vaterite, (ii) Mixed-phase calcium manganese oxide synthesized using Calcite, (iii) Mixed-phase calcium manganese oxide synthesized using $\text{Ca}(\text{OH})_2$; (B) and (C) FESEM images of mixed-phase calcium manganese oxide synthesized using Calcite; (D) and (E) FESEM images of CaMnO_3 synthesized using Biomineralized Vaterite; (F) HRTEM image of pure CaMnO_3 ; (G) SAED pattern; (H) Magnified HRTEM image.

previously reported values for CMOs.^{8,16,8.17} The low value of the bandgap energy makes them highly favorable to absorb visible light and renders them highly functional towards photocatalytic applications.

8.2.2 Photocatalytic dye-degradation

The degradation of Rh 6G during the photocatalytic reaction was studied using UV-vis absorption spectroscopy, Fig. 8.4(A, B, C), by observing the decrease in the intensity of the absorption maxima, λ_{max} (526 nm). Both the materials, pure CaMnO_3 , and the mixed-phase CMOs induced the photolytic degradation of Rh 6G. On two hours of light irradiation, ~16% of the dye had decolorized without the presence of any catalyst. Upon introducing the catalyst CaMnO_3 , the dye degraded was ~72% within the same two hours of irradiation. In contrast, when the mixed-phase calcium manganese oxide was used, the percentage had gone down to ~46%. All the dye-degradation experiments, direct photolysis, and in the presence of the catalysts were performed three times, and the percentage of degradation obtained in each case was almost identical with an error of ~1.5-2%. The percentage degradation along with the error bars have been graphically represented in Fig. 8.5(A). The photolytic processes followed the

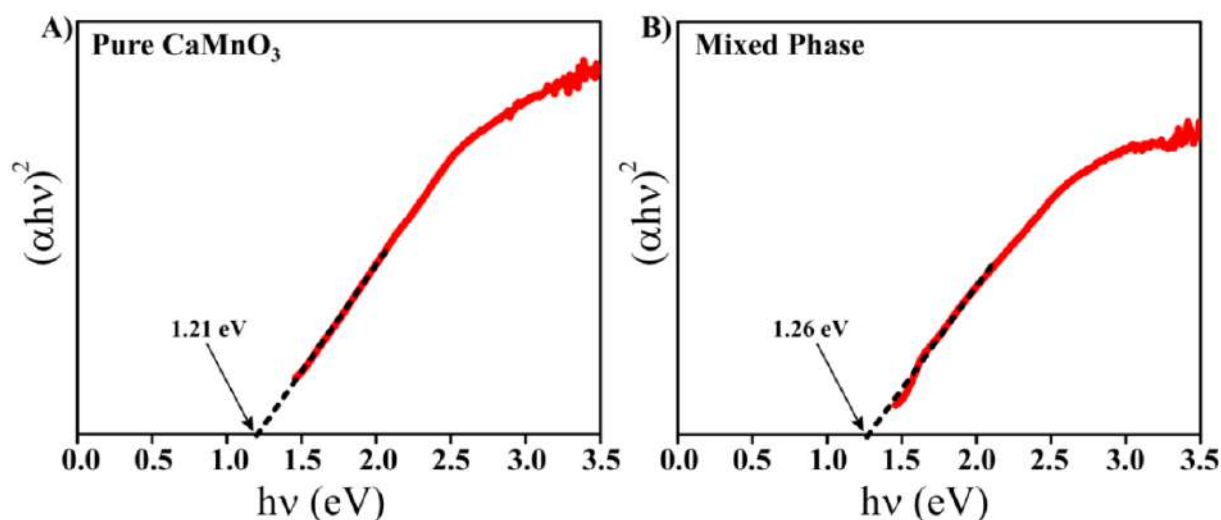


Figure 8.3: Tauc plot of (A) pure CaMnO_3 ; (B) Mixed-phase calcium manganese oxides.

first-order kinetics as can be seen from the plot of $\ln(A_t/A_0)$ vs. Time (minutes), Fig. 8.5(B), where A_t represents the absorbance of Rh 6G at the wavelength of 526 nm at various time intervals and A_0 represents the absorbance (at 526 nm) at $t = 0$ min (just before the irradiation). From these experiments, we can conclude that both the synthesized materials act as photocatalysts. The mere 16% degradation in the case of direct photolysis has increased manifold in the presence of the CMOs. Between the two materials, the pure CaMnO_3 and the mixed-phase CMO, there is a significant difference in the photocatalytic activity, which was recorded in terms of percentage degradation of Rh 6G. After two hours of photo-irradiation, a difference in degradation of Rh 6G by 26% was observed between the two materials, pure CaMnO_3 being a superior photocatalyst than the mixed-phase CMO. The superiority of CaMnO_3 over the mixed-phase CMO was observed from the various characterizations of the materials that were performed and eventually proven by their better activity in the photocatalytic dye-degradation. It was a well-established fact in material research that the particles of smaller

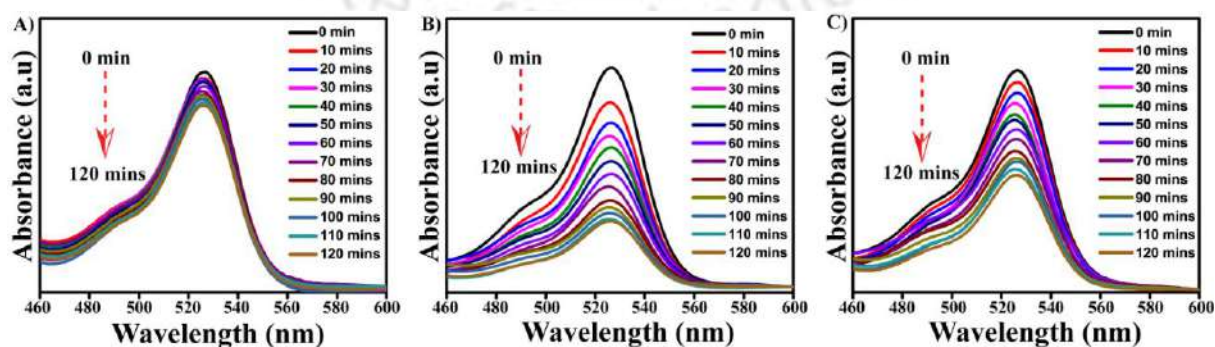


Figure 8.4: UV-vis absorption spectra of the photolytic degradation of Rhodamine 6G (A) without any catalyst; (B) catalyzed by CaMnO_3 ; (C) catalyzed by mixed-phase calcium manganese oxides.

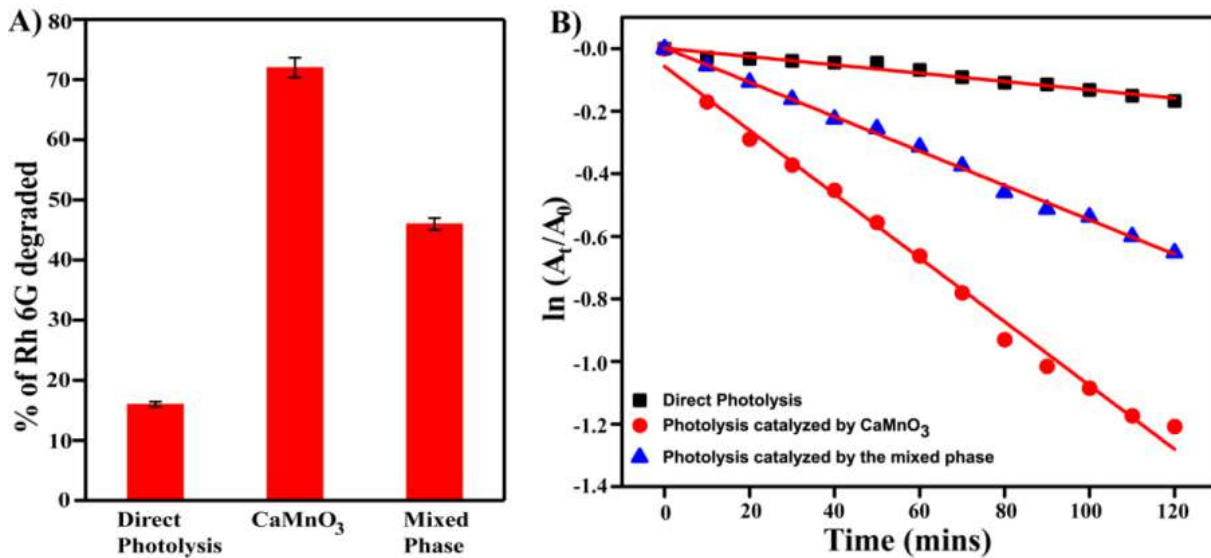


Figure 8.5: (A) Percentage degradation of Rhodamine 6G under different photolytic conditions; (B) Plot of $\ln(A_t/A_0)$ versus Time [mins].

dimensions have the edge over their bigger counterparts in terms of their activity. The average particle size of CaMnO₃ was calculated to be 414 nm, and that of mixed-phase CMO was 710 nm. Hence, there is a significant difference, 300 nm in their average sizes. The pure CaMnO₃ has a well-defined near spherical morphology, whereas the mixed-phase lacks a specific morphology. The adsorption of the dye on the surface of the catalyst is of utmost importance for the mechanism leading to degradation. The spherical morphology and the greater specific surface area of pure CaMnO₃ make it highly favourable for the effective catalyst and substrate interaction which is a prerequisite for initiating the photocatalytic degradation. And eventually, after this interaction, it is the optical bandgap energy of the materials that come into consideration on exposure to light. The optical bandgap energy of both the materials was good enough to absorb visible light. Hence on photo-irradiation, there would be an excitation of electrons from the valence to the conduction band, leading to the generation of charged species. Eventually, this charge transfer leads to the degradation of Rh 6G by the oxidation/reduction pathway. The bandgap energy of pure CaMnO₃ was found out to be 0.05 eV lower than that of the mixed-phase, suggesting comparative ease of charge transfer. All these factors combined account for the better performance of pure CaMnO₃ over the mixed-phase CMO as a photocatalyst. From the literature survey, we have seen that the theoretical density functional theory (DFT) studies have predicted that the CMOs vary in their adsorption configurations, resulting in the difference in their photocatalytic strength.^{8,42} Therefore, this supports the result that we have obtained in terms of the difference in the efficiency of dye-degradation shown by the pure CaMnO₃ and the mixed-phase. **Table A8.1** presents a comparison, where we see that

the biomineralized vaterite-based CaMnO_3 shows better photocatalytic activity in terms of the percentage of Rh 6G degradation compared to other CMOs.

In order to understand the mechanism of the dye-degradation and the role of the photocatalyst, it is important that we know the species that are involved in initiating the process. Photocatalysis involves the generation of radicals and charged species that are responsible for initiating the process. In the degradation of Rh 6G, the usual active species are $\cdot\text{OH}$ and h^+ . To better understand this, the scavengers of these species were introduced in the reaction mixture before the light irradiation. The scavengers used for the purpose were tert-butanol and potassium oxalate for $\cdot\text{OH}$ and h^+ respectively. The reaction involving the photocatalyst CaMnO_3 was studied in the presence of the scavengers for 60 minutes. Like the previously studied photolytic processes, the effect of the scavengers was also studied by UV-vis absorption spectroscopy. In Fig. A8.4(A), we could see the slight decrease in the intensity of Rh 6G absorption maxima (at 526 nm) on the introduction of the $\cdot\text{OH}$ scavenger, and similarly, in Fig. A8.4(B) we could see the decrease in the presence of the h^+ scavenger. Although the catalyst was present in both cases, it was observed that the extent of dye-degradation was comparable to that of the direct photolysis without any catalyst, Fig. A8.4(C).

From this, we can infer that the photo-generated $\cdot\text{OH}$ and h^+ are the species responsible for the degradation of Rh 6G. Although h^+ is not directly involved in the photolysis process, it is responsible for the generation of the active radical species $\cdot\text{OH}$, which in turn are responsible for the initiation of Rh 6G degradation, $\text{h}^+ + \text{H}_2\text{O}/\text{OH}^- = \cdot\text{OH}$. The generated $\cdot\text{OH}$ are capable of oxidizing the organic molecule which leads to the degradation of the compound into simpler fragments. The degradation of Rh 6G was also confirmed by mass spectrometry. The mass spectrum of the dye before the irradiation process was compared with that after the degradation process. Before the photocatalytic reaction, Rh 6G was detected by the base peak at $m/z = 443$ (Fig. A8.5A). However, after two hours of irradiation in the presence of CaMnO_3 , the peak at 443 was reduced to a very faint one, and prominent peaks were observed at $m/z = 415, 387, 371, 345,$ and 331 , Fig. A8.5(B). These peaks represent the by-products that were formed as a result of the degradation and the molecular formula of the by-products has been shown in Fig. A8.5(B), representing their m/z values in the mass spectrum.

The role of CaMnO_3 as a catalyst in photolytic degradation was extended to three other dyes, known to undergo degradation initiated by a similar $\cdot\text{OH}$ radical pathway. The three other dyes used in this study were Rh B, MB, and MO. Upon 2 hours of irradiation in the presence of the catalyst CaMnO_3 , these dyes were degraded by 65%, 62%, and 68%, respectively. The

degradation of these dyes was also studied by the UV-vis spectroscopy, and the decrease in the intensity of the λ_{\max} was observed, Fig. 8.6(A), (B) and (C). The slight variations in the degradation % of the dyes may be attributed to the differences in their relative reaction rates in the presence of the photocatalyst, CaMnO_3 . We were mainly focused on studying the photocatalytic degradation of Rh6G, and in two hours, a degradation of 72% was observed. Hence keeping the time of observation constant, we performed the degradation of the other dyes under similar conditions, but as it can be assumed that the interaction between the photocatalyst and the different dyes will vary; hence their relative reaction rates will also differ and as such, the percentage of degradations in a particular time period (2 hours) has slightly varied. From the point of view of the mechanistic pathway, the active species that are responsible for the degradation of dyes are h^+ , $\cdot\text{OH}$ and $\text{O}_2^{\cdot-}$. In the case of Rh 6G, we have experimentally proven that the $\cdot\text{OH}$ and h^+ are the species that are responsible for the degradation, and literature reports suggest that in the case of MB and MO, it is the generation of superoxide anion radical ($\text{O}_2^{\cdot-}$) and for Rh B, it is $\cdot\text{OH}$ that is responsible.^{8.29,8.30,8.43}

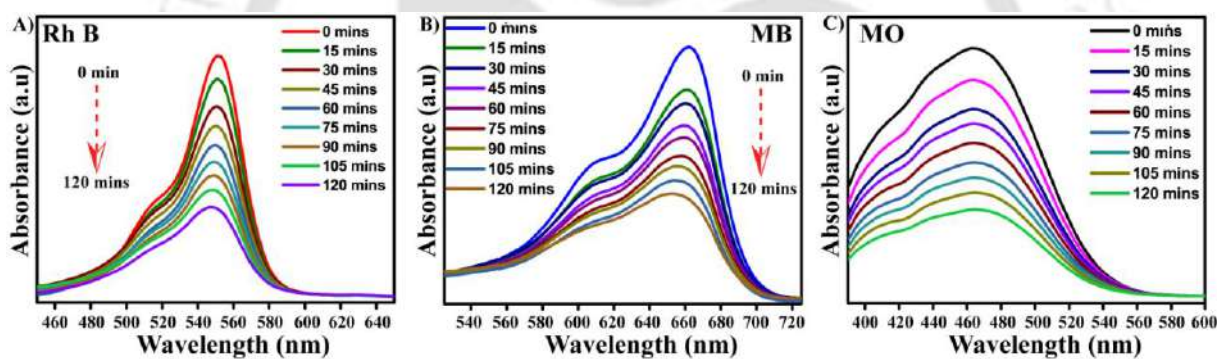
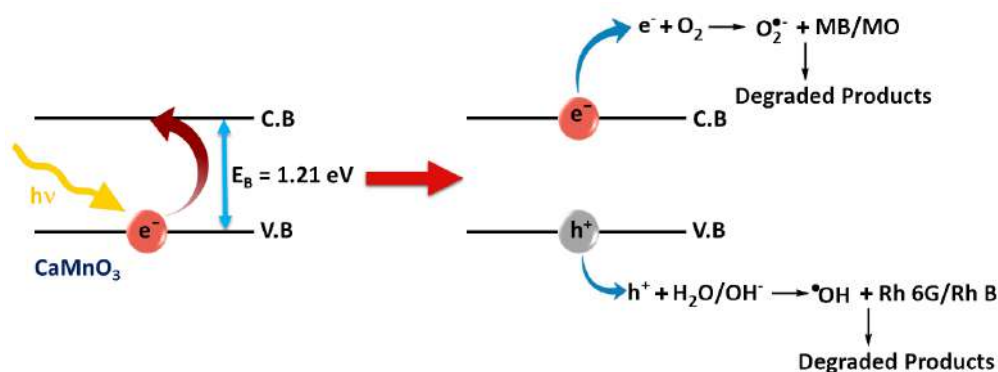


Figure 8.6: UV-vis absorption spectra of the photocatalytic degradation of (A) Rhodamine B; (B) Methylene Blue; (C) Methyl Orange.

With CaMnO_3 as the photocatalyst, considering the low optical bandgap energy (1.21 eV), the generation of all these species were equally feasible and hence we were able to perform the degradation of four different dyes quite convincingly. A schematic representation for the plausible mechanism of the CaMnO_3 catalyzed photolytic degradation of the dyes is shown in **Scheme 8.1**. The changes that were taking place in the course of the degradation of the dyes could be easily observed visually by the naked eyes. The intensity of the dye-solution was diminishing with time, and such a change has been recorded for each dye. It can be seen in Fig. 8.7(A-D). The importance of CaMnO_3 as a photocatalyst was strongly justified by its ability to degrade several dyes, which are among the most commonly used ones in the commercial industries and are known to cause severe health issues. The recyclability and reusability of a



Scheme 8.1: Schematic representation of the CaMnO_3 catalyzed photolytic dye-degradation.

catalyst are of utmost importance. These are the properties that render the catalyst highly functional in the field of applications. In the case of CaMnO_3 , on performing the reusability experiments with all the four dyes, we found out that the material remained almost unchanged for five consecutive cycles, Fig. A8.6. We found out that the relative percentages of the successive cycles w.r.t the first cycle were above $\geq 98\%$ in all the four cases on normalizing the dye-degradation percentages. The excellent reusability added to the photocatalytic activity makes CaMnO_3 a highly promising material for large-scale applications.

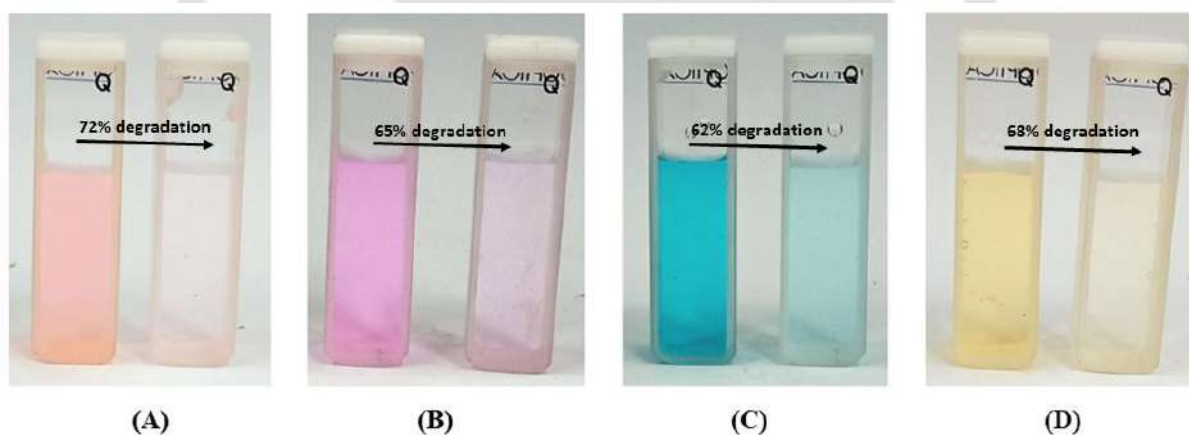


Figure 8.7: Decrease in the intensity of colour after 2 hours of irradiation in presence of the catalyst CaMnO_3 , (A) Rhodamine 6G; (B) Rhodamine B; (C) Methylene Blue; (D) Methyl Orange.

To validate the usefulness of CaMnO_3 towards wastewater treatment, the photocatalytic degradation of Rh 6G was performed in water from two natural sources, lake water (IIT Guwahati) and river water (Brahmaputra, Assam). Water from both these sources possesses significant amounts of contaminants, especially the water from the river Brahmaputra, a dumping yard for city sewage and industrial effluents. The photocatalytic degradation of Rh 6G in lake water and river water, Fig. A8.7(A) and (B) yielded impressive results with 70% and 67% degradation, respectively in two hours, the percentage of degradation almost equal to the

degradation performed in Millipore water (72%). These results indicate that the material can be subjected to wastewater treatment and considering its cost-effectiveness, it can be considered as a prospect for commercial applications.

8.3 Conclusion

Biomaterialized vaterite was used as the calcium source in the synthesis of calcium manganese oxide, and most importantly, we were able to synthesize pure CaMnO_3 , a perovskite material. The bandgap energy of the material was found out to be 1.21 eV. This low value suggested that the material would easily absorb visible light, rendering it highly suitable to be used as a photocatalyst. To draw a comparison, the use of calcite as the calcium source led to the formation of a mixed-phase, where along with CaMnO_3 , CaMn_2O_4 was also present. The pure CaMnO_3 has a higher specific surface area than the mixed-phase, and also, the morphology of both the materials was different. They were eventually subjected as catalysts in the photolytic dye-degradation of Rh 6G. Under similar irradiation conditions, the use of the biomaterialized vaterite-based CaMnO_3 resulted in 72% of the dye-degradation, whereas with the calcite-based mixed-phase, only 46% was observed. Additionally, three other dyes, Rh 6G, MB, and MO were also degraded by photolysis in the presence of the catalyst CaMnO_3 . To validate the effectiveness of the catalyst towards wastewater treatment, the degradation experiments were performed in lake water and river water, and the results obtained were impressive. Hence, to summarize, we have developed a convenient method to synthesize the perovskite CaMnO_3 , which showed impressive photocatalytic activity towards the degradation of several toxic and hazardous dyes.

References

- 8.1. H. Sun, X. Xu, Z. Hu, L. H. Tjeng, J. Zhao, Q. Zhang, H. -J. Lin, C. -T. Chen, T. -S. Chan, W. Zhou and Z. Shao, Boosting the oxygen evolution reaction activity of a perovskite through introducing multi element synergy and building an ordered structure, *J. Mater. Chem. A*, 2019, **7**, 9924–9932.
- 8.2. L. Etgar, The merit of perovskite's dimensionality; can this replace the 3D halide perovskite, *Energy Environ. Sci.*, 2018, **11**, 234–242.
- 8.3. X. M. Xu, Y. B. Chen, W. Zhou, Z. H. Zhu, C. Su, M. L. Liu and Z. P. Shao, A Perovskite Electrocatalyst for Efficient Hydrogen Evolution Reaction, *Adv. Mater.*, 2016, **28**, 6442–6648.

- 8.4. X. M. Xu, C. Su, W. Zhou, Y. L. Zhu, Y. B. Chen and Z. P. Shao, Co-doping Strategy for Developing Perovskite Oxides as Highly Efficient Electrocatalysts for Oxygen Evolution Reaction, *Adv. Sci.*, 2016, **3** (2), 1500187.
- 8.5. Y. Yan, B. Y. Xia, B. Zhao and X. Wang, A review on noble-metal-free bifunctional heterogeneous catalysts for overall electrochemical water splitting, *J. Mater. Chem. A*, 2016, **4**, 17587–17903.
- 8.6. L. Han, S. J. Dong and E. Wang, Transition-Metal (Co, Ni, and Fe)- Based Electrocatalysts for the Water Oxidation Reaction, *Adv. Mater.*, 2016, **28** (42), 9266–9291.
- 8.7. K. Kabra, R. Chaudhary and R. L. Sawhney, Treatment of hazardous organic and inorganic compounds through aqueous-phase Photocatalysis: A review., *Ind. Eng. Chem. Res.*, 2004, **43**, 7683–7696.
- 8.8. M. Li, C. Song, Y. Wu, M. Wang, Z. Pan, Y. Sun, L. Meng, S. Han, L. Xu and L. Gan, Novel Z-scheme visible-light photocatalyst based on CoFe₂O₄/BiOBr/Graphene composites for organic dye degradation and Cr(VI) reduction, *Appl. Surf. Sci.*, 2019, **478**, 744-753.
- 8.9. A. Behera, S. Mansingh, K. K. Das and K. Parida, Synergistic ZnFe₂O₄-carbon allotropes nanocomposite photocatalyst for norfloxacin degradation and Cr (VI) reduction, *J. Colloid Interface Sci.*, 2019, **544**, 96-111.
- 8.10. M. Ghosh, J. Liu, S. S. C. Chuang and S. C. Jana, Fabrication of Hierarchical V₂O₅ Nanorods on TiO₂ Nanofibers and Their Enhanced Photocatalytic Activity under Visible Light, *ChemCatChem*, 2018, **10**, 3305 – 3318.
- 8.11. S. Weon, F. He and W. Choi, Status and challenges in photocatalytic nanotechnology for cleaning air polluted with volatile organic compounds: visible light utilization and catalyst deactivation, *Environ. Sci.: Nano*, 2019, **6**, 3185-3214.
- 8.12. R. Zouzelka and J. Rathousky, Photocatalytic abatement of NO_x pollutants in the air using commercial functional coating with porous morphology, *Appl. Catal. B*, 2017, **217**, 466-476.
- 8.13. M. M. Najafpour, Mixed-valence manganese calcium oxides as efficient catalysts for water oxidation, *Dalton Trans.*, 2011, **40**, 3793–3795.
- 8.14. F. Rong, J. Zhao, Z. Chen, Y. Xu, Y. Zhao, Q. Yang and C. Li, Highly active water oxidation on nanostructured biomimetic calcium manganese oxide catalysts, *J. Mater. Chem. A*, 2016, **4**, 6585–6594.

- 8.15. M. M. Najafpour, S. Nayeri and B. Pashaei, Nano-size amorphous calcium-manganese oxide as an efficient and biomimetic water oxidizing catalyst for artificial photosynthesis: back to manganese, *Dalton Trans.*, 2011, **40**, 9374–9378.
- 8.16. B. Barrocas, S. Sérgio and M. E. M. Jorge, Hierarchically Grown CaMn_3O_6 Nanorods by R.F. Magnetron Sputtering for Enhanced Visible-Light-Driven Photocatalysis, *J. Phys. Chem. C*, 2014, **118**, 41, 24127–24135.
- 8.17. S. Khanahmadzadeh, N. Mikaeili and S. Hasanpour, Facile synthesis of CaMn_2O_4 nanoparticles and investigation of photocatalytic activity, optical and magnetic properties and its influence on the thermal stability of polymeric nanocomposite, *J. Mater. Sci. Mater. Electron.*, 2017, **28**, 4521–4529.
- 8.18. A. Gagrani, S. Sousa, O. C. Monteiro and T. Tsuzuki, Solid state synthesis and photocatalytic activity of bio-inspired calcium manganese oxide catalysts, *J. Solid State Chem*, 2020, **288**, 121390.
- 8.19. J. Kim, X. Yin, K. -C. Tsao, S. Fang and H. Yang, $\text{Ca}_2\text{Mn}_2\text{O}_5$ as oxygen-deficient perovskite electrocatalyst for oxygen evolution reaction, *J. Am. Chem. Soc.*, 2014, **136**, 14646–14649.
- 8.20. M. M. Najafpour, T. Ehrenberg, M. Wiechen and P. Kurz, Calcium manganese(III) oxides ($\text{CaMn}_2\text{O}_4 \cdot x\text{H}_2\text{O}$) as biomimetic oxygen-evolving catalysts, *Angew. Chem. Int. Ed.*, 2010, **49**, 2233–2237.
- 8.21. R. Nakh Wong, Preparation and characterization of calcium manganese oxide (CaMnO_3) nanofibers by electrospinning, *Mater. Lett.*, 2016, **163**, 222–225.
- 8.22. J. Hadermann, A. M. Abakumov, L. J. Gillie, C. Martin and M. Hervieu, Coupled cation and charge ordering in the CaMn_3O_6 tunnel structure, *Chem. Mater.*, 2006, **18**, 5530–5536.
- 8.23. B. D. White, C. A. M. dos Santos, J. A. Souza, K. J. McClellan and J. J. Neumeier, Crystal growth and characterization of Marokite $\text{CaMn}_2\text{O}_{4+\delta}$, *J. Cryst. Growth*, 2008, **310**, 3325–3330.
- 8.24. V. K. Saharan, M. P. Badve and A. B. Pandit, Degradation of reactive red 120 dye using hydrodynamic cavitation, *Chem. Eng. J.*, 2011, **178**, 100–107.
- 8.25. U. G. Akpan and B. H. Hameed, Parameters affecting the photocatalytic degradation of dyes using TiO_2 -based photocatalysts: a review, *J. Hazard. Mater.*, 2009, **170**, 520–529.
- 8.26. M. M. Hassan and C. M. Carr, A critical review on recent advancements of the removal of reactive dyes from dye house effluent by ion-exchange adsorbents, *Chemosphere*, 2018, **209(1)**, 201-219.

- 8.27. M. Imran, D. E. Crowley, A. Khalid, S. Hussain, M. W. Mumtaz, and M. Arshad, Microbial biotechnology for decolorization of textile wastewaters, *Reviews in Environmental Science and Biotechnology*, 2015, **14**(1), 73-92.
- 8.28. B. Lellis, C. Z. Fávaro-Polonio, J. A. Pamphile and J. C. Polonio, Effects of textile dyes on health and the environment and bioremediation potential of living organisms, *Biotechnol. Res. Innov.*, 2019, **3**, 275-290.
- 8.29. M. N. Ghazzala, H. Kebaili and M. Joseph, Photocatalytic degradation of Rhodamine 6G on mesoporous titania films: combined effect of texture and dye aggregation forms, *Appl. Catal. B Env.*, 2012, **115**, 276–284.
- 8.30. R. Jain, M. Mathur, S. Sikarwar and A. Mittal, Removal of the hazardous dye Rhodamine B through photocatalytic and adsorption treatments, *J. Environ. Manage.*, 2007, **85**, 956–964.
- 8.31. T. F. Robinson, G. McMullan, R. Marchant and P. Nigam, Remediation of dyes in textile effluent: a critical review on current treatment technologies with a proposed alternative, *Bioresour. Technol.*, 2001, **77**, 247–255.
- 8.32. Z. Z. Vasiljevic, M. P. Dojcinovic, J. D. Vujancevic, I. Jankovic-Castvan, M. Ognjanovic, N. B. Tadic, S. Stojadinovic, G. O. Brankovic and M. V. Nikolic, Photocatalytic degradation of methylene blue under natural sunlight using iron titanate nanoparticles prepared by a modified sol–gel method, *R. Soc. Open Sci.*, 2020, **7**, 200708.
- 8.33. P. Dey and R. Das, Enhanced photocatalytic degradation of methyl orange dye on interaction with synthesized ligand free CdS nanocrystals under visible light illumination, *Spectrochim. Acta A*, 2020, **231**, 118122.
- 8.34. S. Rajoriya, S. Bargole and V. K. Saharan, Degradation of a cationic dye (Rhodamine 6G) using hydrodynamic cavitation coupled with other oxidative agents: Reaction mechanism and pathway, *Ultrason. Sonochem.*, 2017, **34**, 183–194.
- 8.35. R. Kaur, K. Vellingiri, K. Kim, A. K. Paul and A. Deep, Efficient photocatalytic degradation of Rhodamine 6G with a quantum dot-metal organic framework nanocomposite, *Chemosphere*, 2016, **154**, 620-627.
- 8.36. F. Zheng and Z. Zhu, Flexible, Freestanding, and Functional SiO₂ Nanofibrous Mat for Dye-Sensitized Solar Cell and Photocatalytic Dye Degradation, *ACS Appl. Nano Mater.*, 2018, **1**, **3**, 1141-1149.

- 8.37. D. Paul, S. Halder and G. Das, Whey protein directed in vitro vaterite viomineralization: Influence of External Parameters on Phase Transformation, *Colloids Interface Sci. Commun.*, 2020, **36**, 100255.
- 8.38. D. Paul and G. Das, Curcumin and quercetin as templates in the in vitro biomineralization of CaCO_3 : A comparative study on phase modulation, *Ceram. Int.*, 2021, **47**, 12334-12341.
- 8.39. J. Du, Y. Pan, T. Zhang, X. Han, F. Cheng and J. Chen, Facile solvothermal synthesis of CaMn_2O_4 nanorods for electrochemical oxygen reduction, *J. Mater. Chem.*, 2012, **22**, 15812-15818.
- 8.40. A. Gagrani, M. Alsultan, G. F. Swiegers and T. Tsuzuki, Photo-Electrochemical Oxygen Evolution Reaction by Biomimetic CaMn_2O_4 Catalyst, *Appl. Sci.*, 2019, **9**, 2196.
- 8.41. M. Rochkind, S. Pasternak and Y. Paz, Using dyes for evaluating photocatalytic properties: a critical review, *Molecules*, 2015, **20**, 88–110.
- 8.42. X. Han, T. Zhang, J. Du, F. Cheng and J. Chen, Porous calcium-manganese oxide microspheres for electrocatalytic oxygen reduction with high activity, *Chem. Sci.*, 2013, **4**, 368–376.
- 8.43. M. Sundararajan, V. Sailaja, L. J. Kennedy and J. J. Vijaya, Photocatalytic degradation of rhodamine B under visible light using nanostructured zinc doped cobalt ferrite: Kinetics and mechanism, *Ceram. Int.*, 2017, **43**, 540-548.

Annexure-Chapter 8

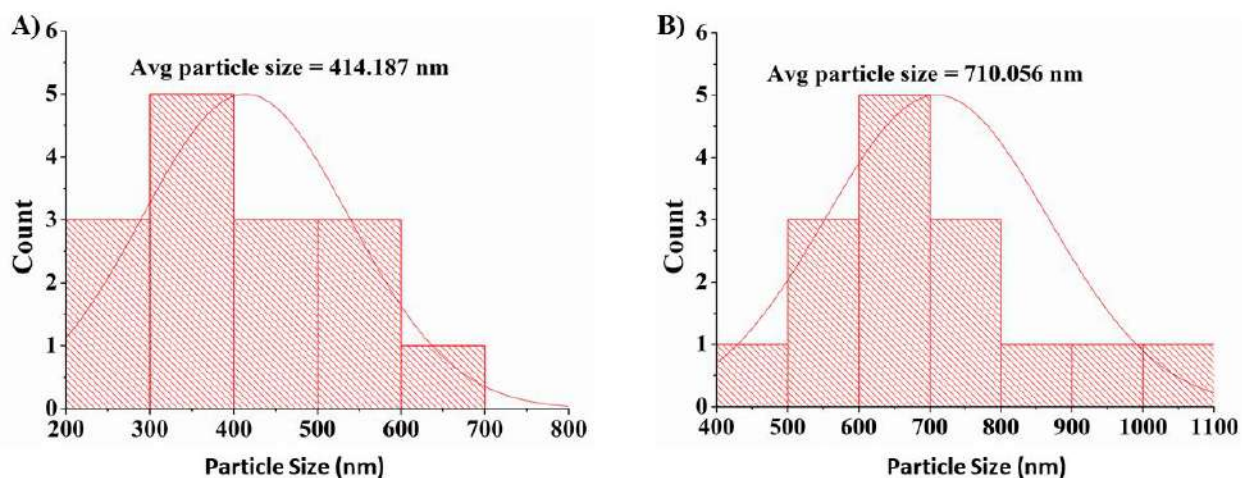


Figure A8.1: Average particle size of (A) pure CaMnO_3 particles; (B) Mixed phase CMOs.

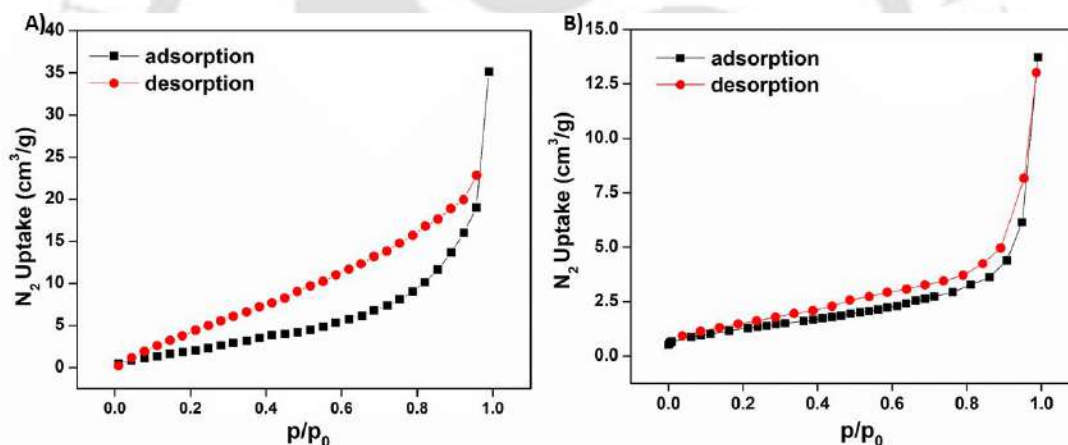


Figure A8.2: Nitrogen adsorption-desorption BET isotherm (A) CaMnO_3 ; (B) Mixed Phase.

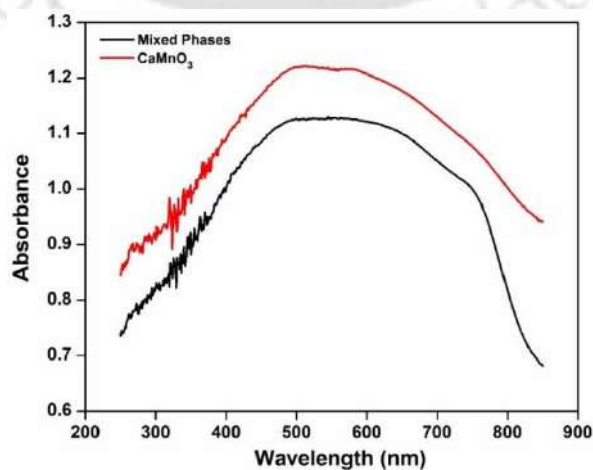


Figure A8.3: UV/visible diffuse reflectance spectra of CaMnO_3 and the mixed phase CMOs.

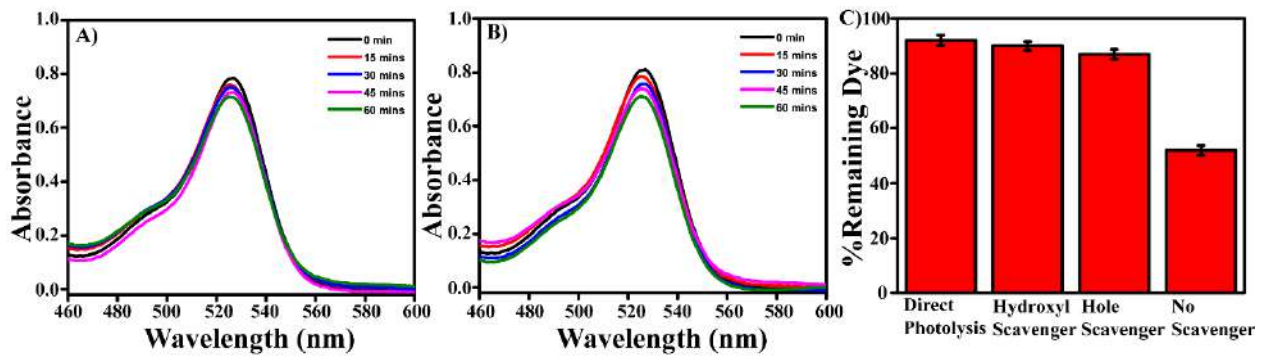


Figure A8.4: UV/Vis absorption spectra of the photolytic degradation of Rhodamine 6G catalyzed by CaMnO_3 in the presence (A) $\cdot\text{OH}$ scavenger; (B) h^+ scavenger; and (C) Percentage degradation of Rhodamine 6G in the presence and absence of the scavengers.

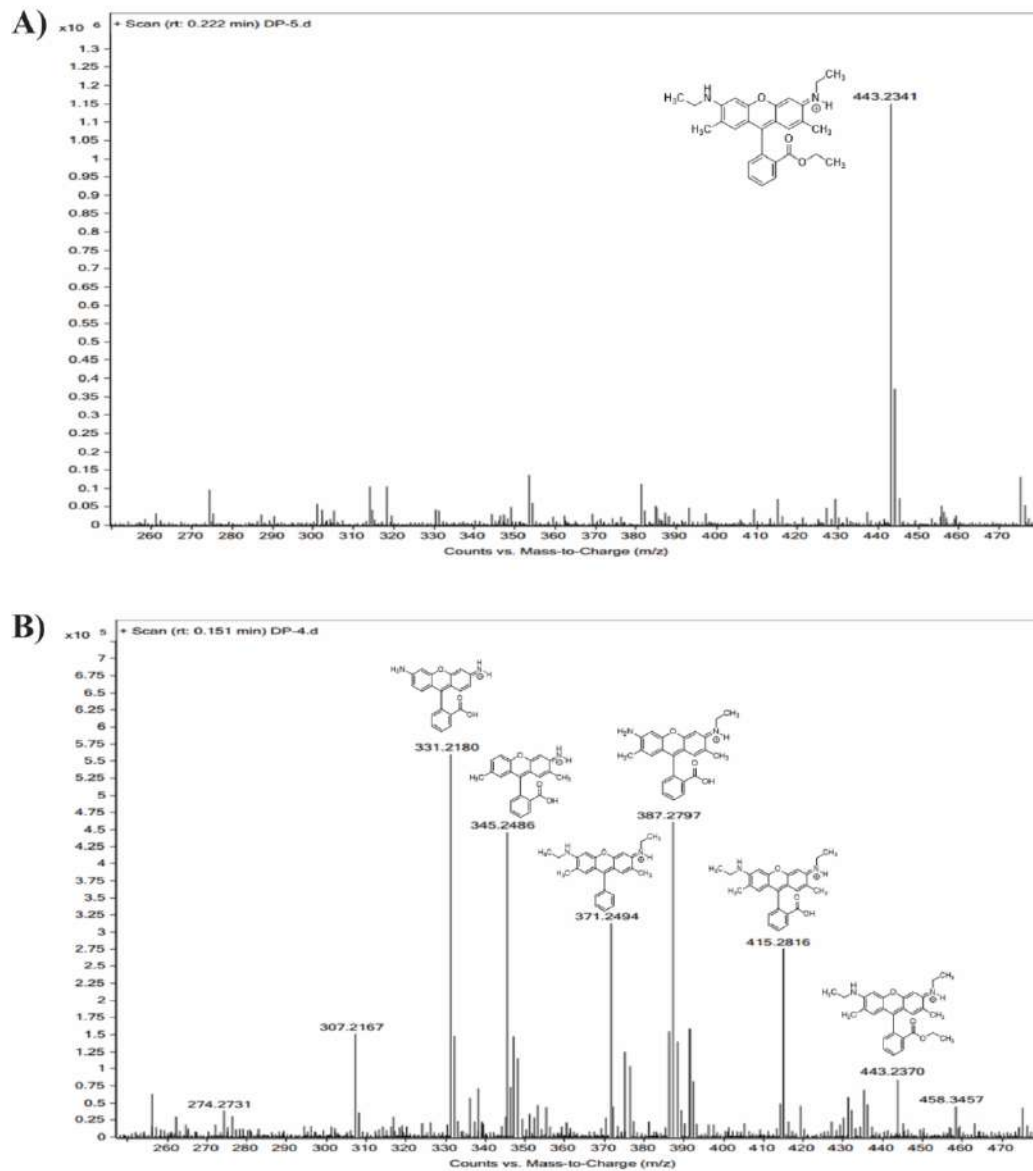


Figure A8.5: Mass spectrum of Rh 6G (A) before light irradiation; (B) after 2 hours of light irradiation.

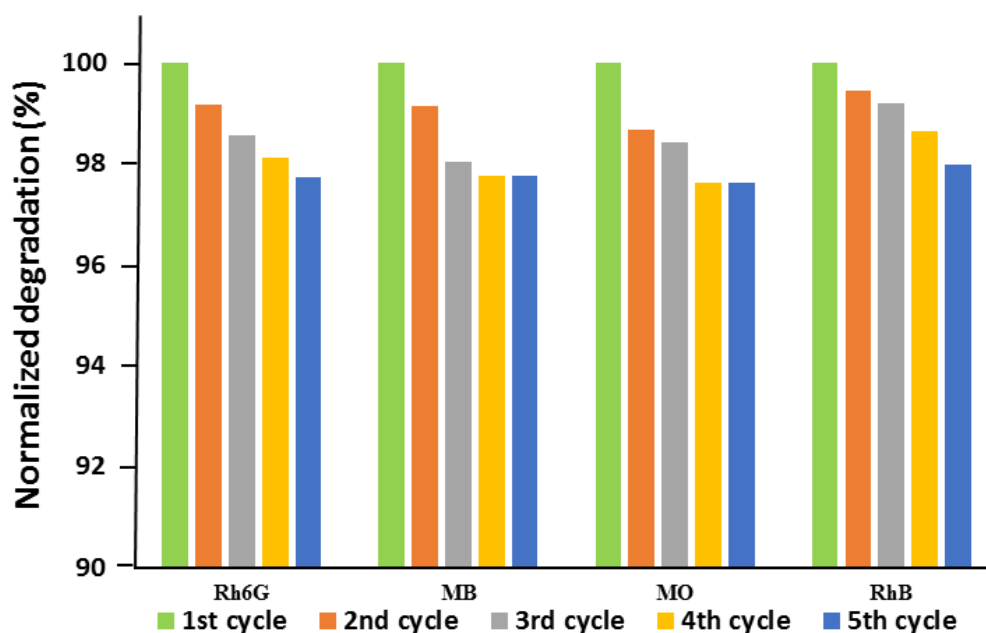


Figure A8.6: Normalized dye-degradation percentages of the different dyes upon recyclability and reusability.

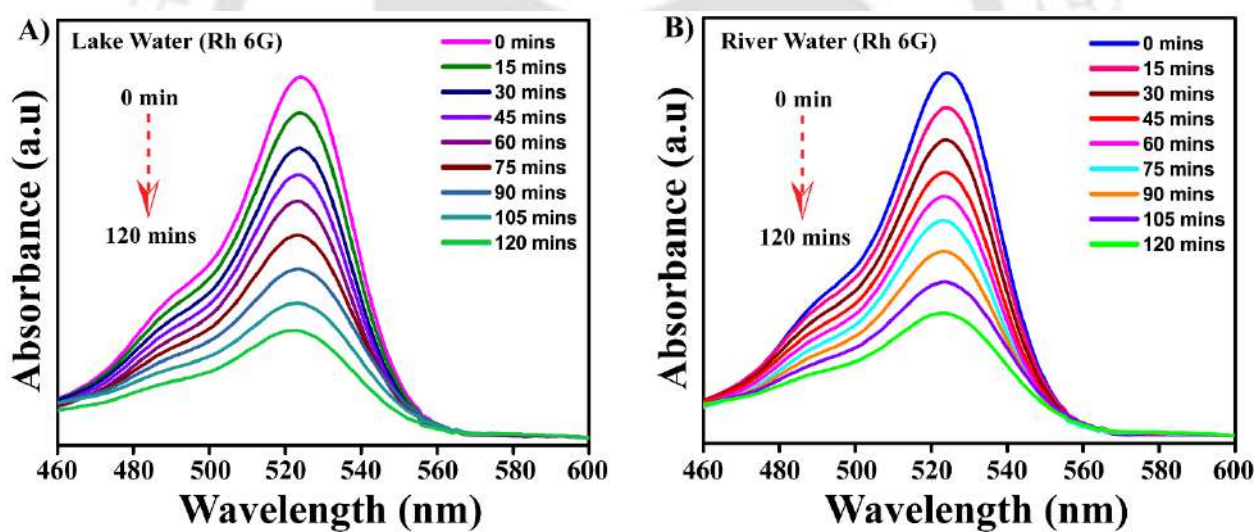


Figure S8.7: UV/Vis absorption spectra of the photocatalytic degradation of Rhodamine 6G catalyzed by CaMnO_3 performed in (A) Lake water and (B) River water.

Table A8.1: Photocatalytic activity of calcium manganese oxides towards the degradation of Rhodamine 6G

Reference	Photocatalyst	Time (mins)	Percentage of Degradation (%)
<i>J. Phys. Chem., C</i> 2014, 118 , 41 , 24127–24135	CaMn_3O_6	240	82

<i>J. Solid State Chem.</i> , 2020, 288 , 121390	CaMnO ₃	180	62
	CaMn ₂ O ₄	180	61
	Ca ₂ Mn ₃ O ₈	180	32
This work	CaMnO₃	120	72



Conclusion and Future Perspective

To summarise, in the course of work performed in preparation of the thesis, all the aspects of biomineralization covered under chemistry have been addressed. The aspects include the characterization of the crystallography and composition of the materials to study the phase and morphology of the biominerals; *in vitro* model systems to understand biomineralization where both low and high molecular weight species, as well as natural sources such as plant extracts, were used as additives; and in the development of new methods to improve the material properties, the incorporation of flavonoids to improve the mechanical strength was performed, also the biomineralized materials synthesized were utilized as solid supports to form functionalized materials composites upon doping of metal-based nanoparticles.

In the third chapter, we have discussed the impact of a large molecular weight molecule, **whey protein**, on the *in vitro* biomineralization of CaCO_3 and in the fourth chapter, we have seen the influence of two small molecular weight molecules, **curcumin** and **quercetin**, when a comparative mode study of the role of these two molecules on the *in vitro* biomineralization of CaCO_3 was performed. In both these chapters, in addition to simply observing the role of these additives, the influence of several other parameters such as sequence of addition, temperature, pH, additive concentration, ionic strength, etc., were studied. In the fifth chapter, the leaf extracts of two naturally and commonly available plants of biological and medicinal values, **Tulsi** and **Green tea** were subjected as additives in the *in vitro* biomineralization of CaCO_3 . The first part of this work consisted of a comparative mode of study between the additives, where we were successfully able to isolate some highly elegant morphologies of calcite. In the second part of the work, we demonstrated how by reversing the sequence of addition of the constituent ions and subjecting the methanol extract of tulsi, the highly unstable amorphous phase and the hydrated monohydrocalcite phase were obtained. Additionally, we were able to show the transition of CaCO_3 from the amorphous precursor to the stable calcite phase via the monohydrocalcite phase. In the sixth chapter, in addition to studying the phase and morphology of the biomineralized CaCO_3 , the mechanical properties of the composites were studied post the incorporation of additives, **quercetin** and **hesperidin**. It was observed that the mechanical strength of the CaCO_3 composites would increase with an increase in the degree of incorporation until it reaches a certain limiting value. Interestingly, with quercetin, it was the calcite phase whose properties were tuned and with hesperidin, it was the metastable vaterite phase.

The seventh chapter is divided into two parts and this chapter discusses the utilization of CaCO_3 , the vaterite microspheres and the rhombohedral calcite as solid supports for metal nanoparticles. In the first part of this chapter, we demonstrated how *in vitro* biomineralized vaterite with spherical morphology and a porous surface texture was subjected as a solid-support for silver nanoparticles to form a composite material which was eventually utilized as a catalyst for efficient reduction of 4-Nitrophenol. In the second part, we discussed the utilization of vaterite and calcite as solid-support in the comparison mode, where both these particles were subjected as a solid-support for magnetite nanoparticles. The resulting composites were then utilized as catalysts in the Fenton-like degradation of common water-polluting dyes MB and Rh B. The results obtained suggested that the solid-supported composites behaved more efficiently as catalysts when compared with bare magnetite nanoparticles; and the vaterite microsphere-based catalyst exhibited the best catalytic activity. In the final chapter, we demonstrated the solid state synthesis of the perovskite material CaMnO_3 where *in vitro* biomineralized vaterite was used as the calcium precursor and for the comparison mode study; the commercially available CaCO_3 was also used (as the precursor). The material synthesized using biomineralized vaterite resulted in the formation of pure perovskite CaMnO_3 , whereas with the other Ca source, we attained a mixed-phase calcium manganese oxide. The low bandgap energy of the materials made them highly suitable for photocatalytic activities. Hence, these materials were subjected as photocatalysts, irradiated by visible light and used in the degradation of common water-polluting dyes Rh 6G, MB, MO and Rh B. The catalytic activity of the pure perovskite material obtained using the biomineralized vaterite was observed to be much better than that of the mixed oxides.

The results attained through the course of work show how biologically useful molecules and plant extracts can participate in Ca-based biomineralization, also, generating scope for their utilization in the broader picture concerning the applications of calcium biominerals. The polymorphs of CaCO_3 synthesized in this work can be utilized in the field of bio-medicines such as in drug delivery vehicles, bone grafting, etc., and in environmental applications such as removal of heavy metals and other toxic impurities apart from the applications performed here. As CaCO_3 is a model system for understanding the mineralization of other Ca-based minerals, the methods used for studying CaCO_3 mineralization in this thesis can be employed for studying systems such as hydroxyapatite, calcium silicate hydrate (C-S-H), etc.

Curriculum Vitae

DEBOJIT PAUL

Date of Birth: 26/02/1993

Nationality: Indian

Phone No.: +91 70053 66929 +91 73087 40630

Email id: debojitpaul97@gmail.com paul176122026@iitg.ac.in

Address: Department of Chemistry, Indian Institute of Technology Guwahati,
North Guwahati-781039, Assam, India



Academic Summary

2017-present: Ph.D. student at Indian Institute of Technology Guwahati, India.

Thesis title: “Effect of additives on bio-inspired mineralization of CaCO_3 and application of its composites”.

Supervisor: Prof. Gopal Das

2016: Master of Science in Chemistry (86.10%, 1ST RANK) from North-Eastern Hill University, Shillong, Meghalaya, India.

Project title: “A study on nucleophilic addition of nitroalkanes to nitroolefins”

Supervisor: Prof. G. Bez

2014: Bachelor of Science (Hons.) in Chemistry (86.5%, 1ST RANK) from St. Edmund’s College (North-Eastern Hill University), Shillong, Meghalaya, India.

2011: Higher Secondary (10+2) in Science (73%) from St. Edmund’s College (Meghalaya Board of School Education), Shillong, Meghalaya, India.

2009: Secondary Education (86.5%) from All Saints’ Diocesan Higher Secondary School (Meghalaya Board of School Education), Shillong, Meghalaya, India.

Awards and Achievements

- Qualified GATE (Graduate Aptitude Test in Engineering) 2017.
- Selected for DST Inspire Fellow (2017) by DST, New Delhi.

- Awarded ONGC Scholarship (2016) by ONGC, Dehradun.
- Received DST Inspire Scholarship (2011-2016) from DST, New Delhi.
- Awarded President of India, Dr. Shankar Dayal Sharma Gold Medal (2016), North-Eastern Hill University, Shillong, Meghalaya, India.
- Awarded Gold Medal, Department of Chemistry (Master of Science) (2016), North-Eastern Hill University, Shillong, Meghalaya, India.
- Awarded Best Student of the Year (Edmundian of the Year 2013, St. Edmund's College, Shillong).

Skills and Experiences

- Basic computer knowledge: Microsoft office, Origin, Chemdraw, Adobe Illustrator.
- Lab skills: Spectroscopic techniques (PXRD, UV, FT-IR, NMR, DLS, XPS, CD) and microscope imaging (FESEM, FETEM) analysis (TGA/DSC, BET) chromatographic techniques (thin-layer chromatography, column chromatography).
- Trained and authorized operator of TGA/DSC instrument (Netzsch, STA449F3A00) as a part of teaching assistantship duty in central Instrument Facility (CIF), IIT Guwahati from January 2018 to present.
- Teaching assistantship at IIT Guwahati: Inorganic Tutorial Courses for undergraduate students (July-Nov, 2019).
- Co-supervised one M.Sc. final year project student (2021) on *In vitro* Biomineralization of Calcium Carbonate.

Research Interests

Additive assisted synthesis of biominerals to obtain unstable phases and minerals with unusual morphology followed by the study of mechanistic pathways of polymorph transformation and the utilization of the synthesized minerals in applications across various fields.

List of Publications

1. **D. Paul**, S. Halder, G. Das, Whey Protein Directed *in vitro* Vaterite Biomineralization: Influence of External Parameters on Phase Transformation, *Colloid Interfac. Sci. Comm.*, 2020, **36**, 100255.
2. **D. Paul** and G. Das, Curcumin and quercetin as templates in the *in vitro* biomineralization of CaCO₃: A comparative study on phase modulation, *Ceram. Int.*, 2021, **47**, 12334-12341.
3. **D. Paul**, D. Sachan, G. Das, Silver Nanoparticles embedded on *in-vitro* biomineralized Vaterite: A highly efficient catalyst with enhanced catalytic activity towards 4-Nitrophenol reduction, *Mol. Catal.*, 2021, **504**, 111433.
4. **D. Paul** and G. Das, Efficient solid-state synthesis of biomineralized vaterite-derived pure CaMnO₃ Perovskite as an effective photocatalyst, *CrystEngComm.*, 2021, **23**, 4050-4058.
5. **D. Paul**, D. Sachan, S. De and G. Das, Modulation of the CaCO₃ phase and morphology by tuning the sequence of addition: an insight into the formation of monohydrocalcite, *New J. Chem.*, 2021, **45**, 18337–18348.
6. **D. Paul** and G. Das, Bio-inspired synthesis of flavonoids incorporated CaCO₃: Influence on the phase, morphology and mechanical strength of the composites, *Colloids Surf. A: Physicochem. Eng. Asp.*, 2022, **642**, 128720.
7. **D. Paul**, A. Singhanian and G. Das, Catalytic activities of the vaterite and the calcite based solid supported catalysts for spontaneous Fenton-like dye degradation: A comparative study, *J. Environ. Chem. Eng.*, 2022, **10**, 107558.
8. Book chapter “Biomineralization of CaCO₃: A biomimetic approach using *in vitro* model systems” in **Advances in Material Research and Technology**, Springer (Submitted).

Conferences/Workshop attended

1. Oral presentation on “**Whey Protein Directed *In vitro* Vaterite Biomineralization: Influence of External Parameters on Phase Transformation**” in Modern Trends in Inorganic Chemistry-XVIII, 2019, Department of Chemistry, Indian Institute of Technology Guwahati.
2. Oral presentation on “**Silver Nanoparticles embedded on *in-vitro* biomineralized Vaterite: A highly efficient catalyst with enhanced catalytic activity towards 4-Nitrophenol reduction**” in Progress and Challenges in Modern Day Science (PCMDS), 2021, Department of Chemistry, B. Borooah College, Guwahati.

3. Oral presentation on “**Efficient solid-state synthesis of biomineralized vaterite derived pure CaMnO_3 Perovskite as an effective photocatalyst**” in Recent Advances and Innovation in Solar Energy (RAiSE), 2021, DST Solar Energy Harnessing Centre, Indian Institute of Technology Madras.
4. Poster Presentation on “**Silver Nanoparticles embedded on *in-vitro* biomineralized Vaterite: A highly efficient catalyst with enhanced catalytic activity towards 4-Nitrophenol reduction**” in 20th National Conference on Surfactants, Emulsions and Biocolloids (NATCOSEB XX), 2021, Department of Chemistry, Indian Institute of Technology Guwahati.
5. Flash Talk Presentation on “***In vitro* biomineralized Vaterite derived efficient solid-state synthesis of pure CaMnO_3 Perovskite as an effective photocatalyst**” in 7th International Conference on Advanced Nanomaterials and Nanotechnology (ICANN), 2021, Centre for Nanotechnology, Indian Institute of Technology Guwahati.
6. Oral Presentation on “**Modulation of CaCO_3 Phase and Morphology by Tuning the Sequence of Addition: An Insight into the Formation of Monohydrocalcite**” in 58th Annual Convention of Chemists & International Conference on Recent Trends in Chemical Sciences (ACC-RTCS), 2021 Indian Chemical Society, Kolkata.
7. Poster Presentation on “***In vitro* biomineralized Vaterite derived efficient solid-state synthesis of pure CaMnO_3 Perovskite as an effective photocatalyst**” in Research and Industrial Conclave, 2022, Indian Institute of Technology Guwahati.
8. Poster Presentation on “**Modulation of CaCO_3 Phase and Morphology by Tuning the Sequence of Addition: An Insight into the Formation of Monohydrocalcite**” in 28th Chemical Research Society of India National Symposium in Chemistry, 2022, Department of Chemistry, Indian Institute of Technology Guwahati.
9. Poster presentation on “**Efficient solid-state synthesis of biomineralized vaterite derived pure CaMnO_3 Perovskite as an effective photocatalyst**” in International Conference on Advances in Chemical and Material Science (ACMS), 2022, Indian Institute of Chemical Engineers (IChE).
10. Participation in online workshop on **Powder X-Ray Diffraction Techniques and its Applications**, 2021, North East Centre for Biological Sciences and Healthcare Engineering (NECBH), Indian Institute of Technology Guwahati.